Open Research Online

The Open University's repository of research publications
and other research outputs

Generation and Characterization of Energetic Neutral Beams for Surface Modification

Thesis

oro.open.ac.uk

The Open University

Generation and Characterization of Energetic Neutral Beams for Surface Modification

Author:
Adetokunbo Ayilaran

Supervisor:
Prof. Nicholas. St. J. Braithwaite

A thesis submitted in fulfillment of the requirements
for the degree of Doctor of Philosophy

Plasmas

School of Physical Sciences

June 6, 2018

Abstract

The aim of this research is to explore ways in which energetic neutral beams can be generated and characterized for modifying polymer substrates in a charge-less etching environment, without profile distortion.

A modified inductively coupled plasma source was constructed to characterize processing plasmas and generate a source of energetic neutral particles based upon the resonant gas phase charge-exchange mechanism. A combination of probe diagnostics and plasma imaging was used to study the electron temperature, electron density and electromagnetic structure in the capacitive and inductive modes of operation. Measured average energies in the tail of the electron energy distribution function ranged between 7 and 9 eV in a pressure range of 1 - 100 mTorr, indicating suffiecient ionization. Characteristics such as an E-H transition, electron densities of up to 10^{18} m^{-3} and plasma uniformity were measured to show that the plasma source was ideal for plasma processing.

An electrostatic quadrupole mass/energy analyzer was used to determine the energy of charge-exchanged neutral particles in the range of 10 - 70 eV. It was shown that the charge-exchanged neutral energy distribution function mirrored the energy of the parent ions. Validation of these results involved the use of electron emission current modulation and the dissociative electron attachment mechanism on fast, energetic O$_2$. It was shown that the O$^-$ anion fragment carried away approximately half the energy of the fast O$_2$ molecule. Ion flux probe measurements determined a gas phase charge-exchange neutralization efficiency of 36% along a neutralization path corresponding to half the mean free path for charge-exchange collisions.

Finally, an inductively coupled plasma etcher tool was used to ignite plasma with tailored parameters as those studied within the modified source.

Ions were extracted and neutralized via surface or gas phase charge-exchange. The neutral beam etching of polymers with a reactive mixture of O_2/SF_6 produced initial etch rates of up to 30 nm min^{-1} in a single extractor arrangement and up to 14 nm min^{-1} using a wafer neutralizer. Atomic force microscopy and x-ray photoelectron spectroscopy was used to measure the physical and chemical profiles of the substrates post etch. It was determined that the presence of vacuum ultraviolet photons assisted the neutral beam etching mechanism and improved the etch rate of a fluorocarbon polymer from 3.5 nm min^{-1} up to 4.5 nm min^{-1}. In the case of a hydrocarbon polymer, photo-chemistry hardened the surface which suppressed the etch rate. Roughness profiles indicated smooth features in the presence of reactive chemical etching whilst profiles were rougher when the main etching mechanism was mechanical. The smoothness of the substrate surfaces post etch wass comparable to polished silicon, indicating neutral beam etching as a suitable technique for surface polishing and the patterning of smooth profiles.

Acknowledgments

I'd like to first thank my supervisor Prof. Nicholas St. J. Braithwaite for his continued support, tutelage and for giving me the oppurtunity to undertake this research. Under him, I have become a more intelligent, critical thinking human being. You certainly are a cut above the rest. I'd like to thank Dr. Daniil Marinov for being my secondary supervisor at the beginning of my PhD and for Russian 'contacts'. I'd like to thank Dr. Alex Nomine for his fruitful discussions and his encouragement during his stay at the OU. I thank Claire Greenwood of Hiden Analytical for fruitful discussions. I thank Dr. Yvonne Sutton for her support and her invaluable input. I'd like to thank Chris Hall for his amazing support, his fruitful discussion and for his presence at the OU. A toast to you my friend! Moreover, his team of innovative engineers; Andrew and Michael, I thank them for their unwavering support. I'd like to thank Dr. Sam Eden for his contributions in the last year of my PhD. I'd especially like to thank Dr. James Bowen. You are THE man! I thank you appearing at my time of need and lendin your time and expertise. I'd like to thank Mohammed Shabbir for the pep talk he gave earlier this year when things looked hopeless. I'd like to also thank the SNM Project and Oxford Instruments for funding and supporting this research.

I'd like to thank my best friends Jay, Ridwan, Abdul and Brian for being amazing. Ghost I might be, but you guys never forgot. I want to thank Kian for his long term support since my undergraduate studies. I want to thank my family, most especially my sisters Tinu, Kemi and my brother Deji for supporting me. I'd also like to thank my cousins Made and Banji, Toyin and Tunrayo for believing in me. I want to thank my grandparents Big Mummy and Big Daddy for their constant love. I want to thank my Uncle for raising me and for giving me the Father to Son talks along the years. Last but certainly not the least, I want to thank my Mother. She put me on this path, she made sure I walked it. She made sure I finished it.

Contents

List of Figures

List of Tables

List of Abbreviations

APPJ   Atmospheric Pressure Plasma Jet

CCD   Charge Coupled Device

CCP   Capacitively Coupled Plasma

CW   Continuous Wave

DEA   Dissociative Electron Attachment

EBEP   ElectronBeam Excited Plasma

ECR   Electron Cyclotron Resonance

EM   Electro Magnetic

EEDF   Electron Energy Distribution Function

EQP   Electrostatic QuadruPole

FAB   Fast Atom Beam

FCP   FluoroCarbon Polymer

HCP   HydroCarbon Polymer

ICP   Inductively Coupled Plasma

IEDF   Ion Energy Distribution Function

NBE   Neutral Beam Etching

OES   Optical Emission Spectroscopy

QMS   Quadrupole Mass Spectrometer

RF   Radio Frequency

RFA   Retarding Field Analyzer

RGA   Residual Gas Analysis

SIMS   Seconday Ion Mass Spectrometry

SNM   Single Nano Metre

SWP   Surface Wave Plasma

UV   Ultra Violet

VUV   Vacuum Ultra Violet

List of Symbols

c	Speed of light in vacuum
e	Electronic charge
f_0	Vacuum resonance frequency of hairpin probe
f_r	Immersed resonance frequency of hairpin probe
k_B	Boltzmann constant
m_e	Mass of electron
M_i	Mass of ion
T_x	Temperature of species
P	Power
n_x	Density of species
c_s	Bohm speed
x_s	Sheath size
V_p	Plasma potential
V_b	Plasma bias
k	Wave number
r	Radius / Distance
E_x	Electric field
B_x	Magnetic field
α	Ionization ratio
ω	Radiofrequency (RF)
ω_x	Angular Frequency
ϵ_0	Vacuum permitivity
μ_0	Vacuum permeability
μ	Mass ratio / mobility
ϕ	Potential
λ_D	Debye length

λ_x Mean free path

σ Conductivity

v_m Collision frequency

δ Skin depth

Γ Flux

v Mean velocity

c_s Bohm velocity

To my Mother, who Sacrificed for me. And so I Served diligently...

Chapter 1

Introduction

The main objective of this research is to explore ways in which energetic neutral particles can be used for surface modification and possibly the fabrication of ultrananoscale devices. Although primarily applied in plasma etching, the properties of energetic neutral particles can also be exploited in lithography, atomic layer etching/deposition and fusion plasmas [1]. In this work, energetic ions are extracted from a low pressure plasma source, neutralized and then characterized. This is done within a bespoke reactor modified for diagnostic measurements. Energetic neutral particles are then deployed in the etching of polymer substrates in an attempt to assess their viability as an alternative method to conventional plasma etching that can smooth vertical features without the damaging effects of surface charging at the single nanometre (SNM).

Plasma etching has been used for several decades as a way to modify the surface properties of various materials, most especially the patterning of silicon wafers for electronic circuitry. There is a need to innovate as the dimensions of these patterned features have continued to decrease over the years (a Moore's Law observation) and plasma damage at these dimensions becomes a concern [2]. To understand why conventional plasma etching has has become problematic at the SNM scale, the representation of a single nanometre must be considered. A nanometre is about 10 times the inter-atomic distance of a hydrogen molecule. At these scales, matter does not appear continuous and becomes granular; etched features would now have

a thickness of only a few atoms. In the etching process, ions transfer their energy onto the substrate in order to contribute to the breaking of bonds. Electrons from the plasma are available to neutralize ionic charging of the substrate. However at the SNM scale, quantum mechanical effects such as electron tunneling become magnified and contribute to feature damage. Furthermore, it becomes more difficult to control localized current and charging effects. The current approach in the SNM regime also presents difficulties for patterning via lithography as the patterning of photo-resist by use of light and masking suffers from diffraction effects. Shorter wavelength light or electron beam techniques are required together with considerable artifice. The application of neutral beams for charge-less, damage free patterning is to be explored in this context. The work was influenced by the SNM project (Single Nanometer Manufacturing for beyond CMOS Devises - FP7-ICT) and involved pushing the limits of nano-manufacturing down to the SNM by investigating novel methods for surface patterning and plasma etching.

The first section of this chapter introduces important plasma parameters that define etching from the plasma perspective. The second section introduces conventional plasma etching, problems that have arisen due to downscaling of dimensions and research undertaken to highlight or tackle issues. The last section of this chapter contains a summary of challenges and possible solutions. The general layout of the thesis is as follows:

- Neutral Beam Etching Review (**Chapter 2**); A literature review that discusses Neutral Beam Etching as an alternative method to standard plasma etching. The research questions are also set out.

- The Experimental Setup (**Chapter 3**); physically characterizes the bespoke inductively coupled plasma setup that was designed and created as a diagnostic tool to study processing plasmas that are identical to those in an industrial plasma etcher (PL-80).

- Characterization of the ICP (**Chapter 4**); discusses the characterization of the setup from the plasma perspective.

- The Electrostatic Quadrupole Mass spectrometer (**Chapter 5**); introduces the Electrostatic Quadrupole (EQP) as the main diagonostic instrument of the setup and characterizes it using COMSOL 3D modelling.

- Neutral Beam Energy Measurement (**Chapter 6**); discusses the detection and characterization of fast, energetic neutral species from argon and oxygen plasmas using the EQP. Measurements were then validated.

- Neutral Beam Processing (**Chapter 7**); discusses methods of surface analysis such as Atomic Force Microscopy, Ellipsometry and X-ray Photoelectron Spectroscopy used to characterize the substrates post-etch in a charge-less environment.

- Conclusions and Future Work (**Chapter 8**); summarizes the thesis and then proposes future work to extend this research.

1.1   Plasmas

FIGURE 1.1: Collage of natural and industrial plasmas: Aurora, Lightning, Arc Welding, Nebula, Neon Lights and Coronal Flares. *Wikipedia images, 2017*

A plasma is an ionized gas containing free moving charges as well as neutrals, metastable species and photons. This exoticness also leads to non-equilibrium properties. Being of a gaseous nature, a plasma exhibits many of the properties of an ideal gas containing particles moving in random directions with a mean speed corresponding to their collective distribution. A plasma is quasi-neutral where the negative and positive charge densities are very nearly equal. In bounded plasmas however (which this research concerns itself with), this cannot be sustained in boundary regions where there are regions of positive space charge. Electrically conducting gas was first discovered [3] as a state of matter by Sir William Crookes in 1879 after he ionized air in an electrical discharge tube using a high voltage source. The nature of this matter was further probed by the British physicist Sir J.J Thompson in 1897. It was eventually termed a 'plasma' in 1928 by Irving Langmuir [4].

Most of the known visible universe is composed of plasma and mankind has used plasma in numerous ways, including surface modification, materials processing and arc welding. The main interest in this research involves the use of low pressure/temperature processing plasmas. Many types of

plasma show differing characteristics such as ionization ratio, charged particle and neutral density, particle energy and chemistry. Low temperature plasmas have the definition that they are non-equilibrium; electrons and heavier species have dissimilar distribution functions. This leads to potentially complex chemistry that is utilized for micro-fabrication.

It is necessary to establish the parameters that serve to characterize these kind of plasmas. Most of the underlying theory has been summarised thoroughly by Pascal & Braithwaite [5] and Lieberman & Litchenberg [6] and these textbooks are referred to in some detail in the following sections.

1.1.1 Plasma parameters

Plasma Pressure

The effect of gas pressure on the behaviour of a low temperature is important. Although plasmas can operate up to atmospheric pressure (760 Torr) in atmospheric plasma pressure jets (APPJs), the plasmas concerned in this research are typically operated at low gas pressures between 1 and 100 mTorr. The gas pressure refers to the kinetics of the massive species within the plasma (ions and neutrals). According to ideal gas law, they are related via:

$$p = \frac{n_g m \bar{v}^2}{3} \tag{1.1}$$

Where p, n_g, m and $\bar{v}^2$ are the gas pressure, gas density, particle mass and the root mean square velocity respectively. This gas kinetic energy is proportional to the gas temperature:

$$\frac{1}{2} m \bar{v}^2 = \frac{3 k_B T_g}{2} \tag{1.2}$$

Where T_g is the gas temperature and k_B is the Boltzmann constant. The gas pressure can therefore be expressed as:

$$p = n_g k_B T_g \tag{1.3}$$

The pressure becomes important because its variation changes the balance between production and loss of species in the plasma due to energy density and the frequency of collisions. Pressure also indicates average particle density and velocity, which then relates to ionization ratio and the composition of plasma species.

Ionization Ratio

Ionization ratio in an electropositive plasma is expressed in terms of the ion density (n_i) and the neutral gas density (n_g) by the relation:

$$\alpha = \frac{n_i}{n_g + n_i} \tag{1.4}$$

Which is the ratio of the density of ions to all heavy species in the plasma. In most low temperature electrical discharges, this ratio is generally $\ll 0.1$. In the case of fusion plasmas, it is expected that this ratio approaches 1. Some processing plasmas (Helicon plasmas and extremely high density inductively coupled plasmas) aim for an ionization ratio approaching 10%. Quasi-neutrality is expressed in terms of electron density n_e.

$$n_i - n_e \sim 0 \tag{1.5}$$

The plasmas used in this research are not extremely high power density discharges so ionization ratios $\ll 0.1$ are expected. Thus, most of the plasma population will be neutral gas. A ratio is quantifed at the end of **Chapter 4**.

Electron Density

Electron density is a key parameter as many of the important events such as ionization, dissociation and attachment that define plasma chemistry have rates that are dependent on the electron density. Before ignition, stray electrons are accelerated by electromagnetic fields that begin ionization. An electron must attain energy greater than or equal to the ionization potential

of the feed gas to ionize, which produces more electrons. The mean electron density characterizes the steady state condition where the loss of charges matches their creation and it scales naturally with the population density of ionized gas. Processing plasmas typically have electron densities in the range $10^{14} \leq n_e \leq 10^{18}$ m^{-3}. These arguments are for principle monatomic gases but similar results hold for molecular gases which are also studied in this thesis as at low pressure.

Electron Temperature and Energy

Electrons can have energies that markedly differ from the heavier species, often having temperatures upwards of a few thousand kelvin. Their energies are described using an electron energy distribution function (EEDF) with the temperature T_e as a measure of the thermal energy of a population of electrons when the distribution of energies takes the shape of a Maxwellian distribution:

$$f_e(v) = n_e \left(\frac{m}{2\pi k_B T_e} \right)^{\frac{3}{2}} \exp \left(\frac{m\bar{v}^2}{2k_B T_e} \right) \tag{1.6}$$

The electrons sit at a much higher temperature than the rest of the plasma species due to their low mass and high mobility. They predominantly undergo elastic collisions although ionization and dissociation are the result of inelastic collisions. Typical bulk electron energies are between 2 - 6 eV ($T_e \sim 45000$ K) in the plasmas studied in this thesis whilst the neutral gas in the plasma bulk are thermalized and have temperatures close to 0.025 eV (room temperature). Ions themselves have temperature $T_i \sim 500$ K (slightly above room temperature) in the central plasma region. However due to acceleration mechanisms in the sheath, they gain drift speeds significantly larger than thermal speed. Since $T_i \neq T_e$, the plasma is non-equilibrium. Although, the average electron energy mentioned appears lower than what is necessary for mechanisms such as ionization and dissociation, the tail of the EEDF contains electrons of sufficient energy for these mechanisms.

The electron temperature is essential for much of the plasmas characteristics such as the ionization ratio, plasma scale lengths and even the Bohm speed c_s which determines the energy with which ions enter the sheath.

Debye Length

Although plasmas are described as quasi-neutral, local fields and space charge can exist. The Debye length λ_D indicates the effective scale length of these local fields. Consider the space potential ϕ which becomes more negative closer a surface in a bounded plasma using Poission's equation:

$$\nabla^2 \phi = -\frac{e(n_i - n_e)}{\epsilon_0} \tag{1.7}$$

Where ϵ_0 is the vacuum permittivity. In one spatial dimension (x), one can obtain a simplified second order differential in Cartesian coordinates:

$$\frac{d^2\phi}{dx^2} = -\frac{e(n_i - n_e)}{\epsilon_0} \tag{1.8}$$

The assumption is that within the bulk (where this length scale is important), potential fluctuations are much less than thermal ($\phi \sim \frac{k_B T_e}{e}$) over the distance x that will be defined as the Debye length. This assumption works because large fields are not expected within the bulk plasma, so pockets of mono-charge densities do not occur. **Equation 1.8** reduces to:

$$\frac{d^2(\frac{e\phi}{kT})}{d(\frac{x}{\lambda_D})^2} \sim \frac{(n_e - n_i)}{\epsilon_0} \frac{e^2}{k_B T} \lambda_D{}^2 \tag{1.9}$$

At the boundaries where $n_e \ll n_i$:

$$\frac{d^2\eta}{d\xi^2} \approx \left(\frac{n_e - n_i}{n_e}\right) \frac{e^2 n_e}{\epsilon_0 k_B T} \lambda_D{}^2 \sim 1 \tag{1.10}$$

Where η is the dimensionless potential $\frac{e\phi}{kT}$ and ξ is the dimensionless distance $\frac{x}{\lambda_D}$. Local fields do not exist beyond a scale length λ_D:

$$\lambda_D = \left(\frac{\epsilon_0 k_B T_e}{n_e e^2}\right)^{\frac{1}{2}} \tag{1.11}$$

Plasma Frequency

Plasma frequency describes the response time for oscillations of charged species as they move on the scale of Debye lengths. If a small cloud of electrons are perturbed from a region of neutral charge density, a temporary field will caused them to oscillate about the ions. The oscillations will continue until they are damped by collisions back to their equilibrium state. A derivation of this frequency can be found from the Debye length as the natural scale length and the thermal speed as a natural velocity scale:

$$\omega_p \sim \frac{\bar{v}}{\lambda_d} \tag{1.12}$$

Where $\bar{v}$ is the mean particle speed of electrons which are considered here. Using **Equation 1.11**, the electron plasma frequency can be derived:

$$\left(\frac{n_e e^2}{m \epsilon_0}\right)^{\frac{1}{2}} = \omega_p \tag{1.13}$$

An analogous ion plasma frequency contains M as the ion mass instead of m.

Plasma Potential

A plasma sits at a potential V_p with respect to a nearby surface that depends upon the electron and ion transport to that surface. Essentially, it is the potential difference between the bulk plasma and nearby surface which causes current to travel through a sheath on an insulating surface. In the previous section, the Debye length referred to small scales within the bulk. In this section, larger scales are considered, especially in the sheath region where there is positive space charge. When the plasma is first ignited, the low mass high mobility electrons are the first to leave the bulk plasma which creates a charge imbalance due to ions drifting much more slowly out of the plasma. This creates a potential in the plasma which sets up an electric field sufficient to force ions out of the plasma and to slow the rate of electron loss. Due to their higher mobility, electrons will keep escaping nonetheless until

an equilibrium between the loss of electrons and ions is reached when the plasma potential is such that on average, ions leave the plasma at the same rate as the electrons. This is also an equilibrium corresponding to ion and electron creation. Quasi-neutrality is obeyed as the electric field actively supports the expulsion of ions out the plasma. The loss of electrons on the other hand is mitigated by the growing negative potential at the boundary with respect to the bulk of the plasma. The diffusion of the charge carriers due to their interaction with the electric field is defined as ambipolar diffusion – a condition which describes the average diffusion rate of electrons and ions out of the bulk as equal.

A related potential V_f describes the potential assumed by a conductor such that the net current on it (when immersed in a plasma) is zero. Due to typical differences between the fluxes of electrons and that of the ions, V_f is necessarily more negative than than V_p. V_f is particularly of interest in electrostatic probe theory.

The Plasma Sheath

The basic sheath is composed primarily of positive space charge (**Figure 1.2**) and serves to match the plasma from nearby surfaces.
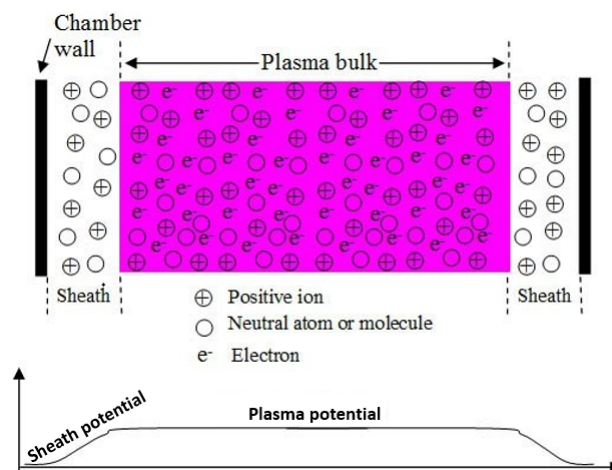
FIGURE 1.2: Variation of charge density and potential from the bulk of the plasma to the wall. *Credit: Pie Scientific*

The sheath's relationship with the Debye length and its dependence on the plasma potential is important. Due to its elegance and the information it provides, it is worth a detailed analysis of the Child-Langmuir relation which considers the electric currents and potentials within the plasma boundary. Poisson's equation was defined in **Equation 1.7**, where electron density is now ~ 0 within the (non-zero space charge) sheath region. There are two quantities which must be conserved as the flow of species from the bulk to the sheath region is monitored. Flux conservation:

$$\Gamma = n_s c_s = n_i v_i \tag{1.14}$$

Hence:

$$n_i = \frac{n_s c_s}{v_i} \tag{1.15}$$

Where ions enter the sheath with a flux $n_s c_s$ and n_s is the ion density at the sheath – plasma boundary. $c_s = \sqrt{kT_e/M_i}$ is the Bohm speed and describes the velocity of ions entering the sheath. In fact, the Bohm speed is the result of a pre-sheath forming in the plasma bulk (**Figure 1.3**). The other quantity that must be conserved is energy - that is the total energy of each ion within the sheath is a combination of its kinetic energy on entering the sheath and energy gained by the sheath potential ϕ:

$$\frac{1}{2} M v^2 = -e\phi + \frac{1}{2} M c_s{}^2 \tag{1.16}$$

Hence:

$$v_i = \left(\frac{-2e\phi}{M} + c_s{}^2 \right)^{\frac{1}{2}} \tag{1.17}$$

Expressing n_i as a function of the potential, Poisson's equation then becomes:

$$\frac{d^2\phi}{dx^2} = -\frac{en_s c_s}{\epsilon_0} \left(\frac{2e}{M} \right)^{-\frac{1}{2}} (-\phi)^{-\frac{1}{2}} \tag{1.18}$$

Where it has been assumed that $c_s{}^2 \ll \frac{2e\phi}{M}$, that is the ion energy quickly exceeds the initial kinetic energy at the sheath boundary . Solving this requires integrating between the limits of the plasma sheath $x = x_s$ and the

bounded surface $x = x_0$, giving the Child-Langmuir relation:

$$\phi_0^{\frac{3}{4}} = \frac{3}{2}\left(\frac{ec_s n_s}{\epsilon_0}\right)^{\frac{1}{2}}\left(\frac{2e}{M}\right)^{-\frac{1}{4}} x_s \tag{1.19}$$

Dividing both sides by the Debye length yields:

$$\left(\frac{e\phi}{k_B T_e}\right)^{\frac{3}{4}} = \frac{3}{2}\frac{x_s}{\lambda_D} \tag{1.20}$$
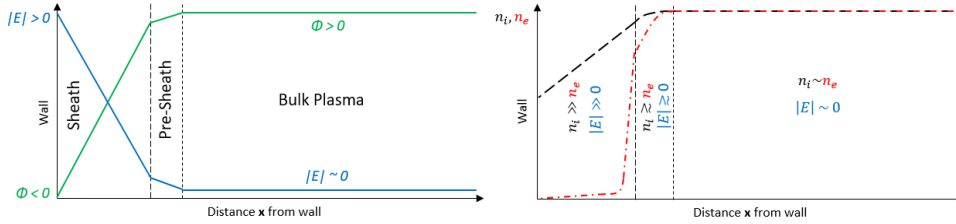
FIGURE 1.3: **Left** Absolute field values increase from the bulk to the sheath. Actual field is negative as potential falls. **Right** number density of ions and electrons from the bulk to the sheath. *Credit: adapted from [5]*

$c_s n_s$ is the current density J_i for ions into the sheath. This result works for sheaths where $\phi \gg \frac{k_B T_e}{e}$ and the potential is generally more than a few V. The size of the sheath can be estimated in Debye lengths and depends on the potential across the sheath. The result is especially consequential in the extraction of positive ions in order to form collimated neutral beams in plasma processing where the plasmas are often biased.

The RF plasmas used for this research project are relatively low temperature and pressure. The electron densities are of order $n_e \sim 10^{17}$ m^{-3}. Pressures are between 1 - 100 mTorr and bulk electron temperatures are between 2 - 6 eV, typical values for plasma parameters at 1 mTorr are debye length $\lambda_D = 4$ x 10^{-5} m, ionization ratio $\alpha \sim 0.004$ and plasma frequency $\omega_{pe} = 17$ x 10^9 s^{-1}.

1.2 Plasma Sources

This section will cover common processing chambers that are primarily used for plasma processing rather than pure research interest. For plasma etching, a source must be able to provide a high particle density, control over the ion energies, high uniformity and scalability. It should also be relatively straight forward to study and characterize. The merits and short-comings of each source will be briefly discussed. It will be explained why the Inductively Coupled Plasma (ICP) source is the most appropriate for the present research.

1.2.1 DC Discharge Plasmas

DC discharges are the oldest form of plasma discharge and may be as simple as a parallel plate arrangement between a cathode and an anode in a gas at reduced pressure. Historically, they are known as glow discharges or Crookes tubes, provided the current remains low enough to avoid excessive gas heating – hence operating in the non-equilibrium regime. A continuous current through the low pressure volume generates plasma that primarily recombines on surrounding surfaces, while ion bombardment of the cathode ensures sufficient electron emission to sustain the discharge at the electrodes.
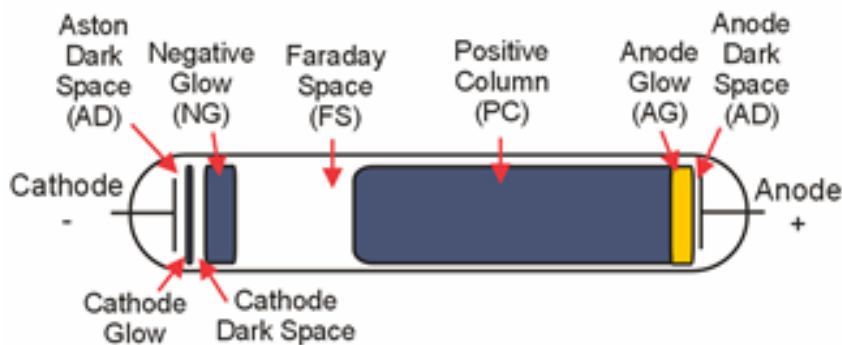
FIGURE 1.4: Schematic of a Glow Discharge with gas flow.
Wikipedia images, 2017.

The pressure range of operation is generally between 10 mTorr and 10 Torr. In an electropositive discharge, the discharge itself is sustained by

a spatially localized region around the cathode where ions are driven towards the cathode and electrons towards the anode. There is secondary electron emission by positive ions bombarding the cathode for electron emission; ion bombardment also leads to atoms from the cathode being released which is called sputtering. Populations of electrons and ions are maintained as long as electrons gain sufficient energy from the weak field in the plasma to sustain loss. As seen in **Figure 1.4**, the discharge is structured with parallel bright and dark regions. An account of the electrical structure and characteristics of a glow discharge is given by Garamoon *et al.* [7].

DC discharges are primarily used for sputter deposition of metallic thin films. DC discharges are unsuitable for plasma etching in the microelectronics industry due to scaling issues, constraints on the ion energy and the damaging nature of the sputtering process (DC Magnetrons are now a superior method of sputter deposition due to this issue). Furthermore, DC sources are not compatible with processing of semi-conducting and insulating substrates where these are placed on electrodes; this has led to RF sources such as capacitively coupled plasmas being investigated.

1.2.2 Capacitively Coupled Plasmas (CCP)

CCPs are a common form of discharge used for processing. A standard low pressure CCP arrangement is based on a pair of parallel plate electrodes with one being grounded and the other driven by RF power through a coupling capacitor to block DC. Another feature is the fact that a CCP is unmagnetized. Capacitive sheath systems develop a DC component from the RF by rectification, owing to the nonlinear current-voltage relationship of the sheath. The plasma is heated via collisional ohmic heating in the bulk and stochastic sheath heating which describes the momentum transfer from high voltage sheaths varying along the RF cycle. CCP heating modes are described in Sahu *et al.* [8] whilst a treatment of stochastic power is described in reference [6]. A GEC reference cell (a universal CCP reactor) is

shown in **figure 1.5**:

$$V(t) = \tilde{V}_{rf} \cos \omega t$$
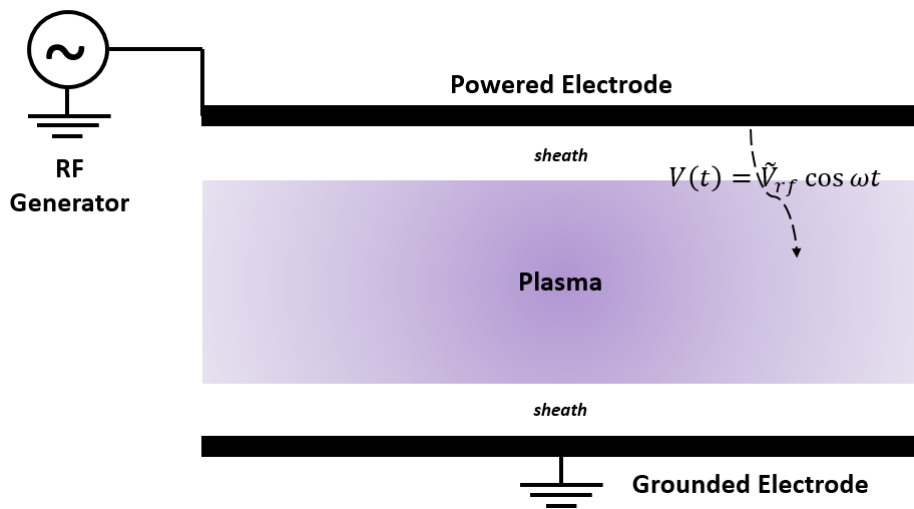
FIGURE 1.5: Schematic of a simple CCP. RF power is coupled through a plasma sheath.

When an RF voltage is applied between the plates of a CCP chamber, an RF current I_{rf} flows between the parallel plates – initially as a displacement current but after breakdown there is also a conduction component. Electrons are accelerated within the electric field. As the plasma volume increases, this field becomes more localized near to the electrode. The positive ions gain energy in passing through the sheath. The rectification of RF by the nonlinear sheath produces a DC bias which superimposes itself onto the alternating RF power to repel electrons away from the walls and maintain both the quasi-neutrality of the plasma and the plasma density. When the two electrode sheaths are of different areas, the DC biases at each electrode and the plasma are different resulting in a net bias that can be measured externally.

CCPs are relatively simple to make and therefore contribute to a large portion of process plasmas used in industry. However, this arrangement has limited ability to control ion energy separately without affecting discharge characteristics. There is also a constraint on the minimum pressure required for a sustained discharge, meaning that CCPs typically cannot be

ignited at less than 10 mTorr. Although the DC provides a way to give ions energy sufficient to directionally bombard the substrate and enhance the etching mechanism, the inability to control this bias without affecting the plasma parameters such as plasma density introduces limitations. These include decreasing the selectivity of the resist mask and substrate and increasing surface roughness of the material being etched.

Energetic neutral beam production requires a high density plasma to ensure a high flux of neutral beams, without sacrificing the ability to tailor the energy of the beam. In a CCP, the plasma density is tied directly to the ion energy and this is restrictive. The use of a second (higher) frequency component [9] can be introduced to provide additional control so that the lower frequency sets the ion energy while the higher frequency sets the plasma density. Also, the geometry makes the extraction of neutral beams from a CCP non-trivial such that the CCP is unsuited for this research. This has made it necessary to investigate other forms of discharge that can combine a high density plasma with low pressure and controllable ion energies.

1.2.3   Wave Heated Plasmas

Magnetic plasma confinement has been explored in capacitively coupled plasmas during magnetic field enhanced reactive ion etching studies (MERIE) and is associated with DC magnetrons as a way to increased plasma density by setting up a stationary magnetic field. Wave heated sources such as electron cyclotron resonance (ECR) plasmas have taken magnetic confinement further as their principle of operation. They are also considered 'electrodeless' plasmas as the source electrode is not in direct contact with the plasma. The principle of operation involves the coupling of a microwave electric field to electrons with a stationary magnetic field. This has the consequence of reducing plasma movement perpendicular to the magnetic field lines thereby increasing the plasma density. Electrons gyrate around stationary magnetic field lines with a characteristic cyclotron frequency. When this

stationary field is superimposed with the microwave electric field, electrons circling the magnetic field continuously absorb energy from the electric field during the cycle (generally driven at microwave frequency, 2450 MHz). The microwave frequency is chosen to match the electron cyclotron frequency of the magnetic field and this hits a resonance to ensure that the collisional frequency of the electrons (typically around 1×10^7 s^{-1}) is such that the ionization efficiency is very high. This leads to a high density given that the operational pressure is within range of 1 Torr. **Figure 1.6** shows a schematic of an ECR source:
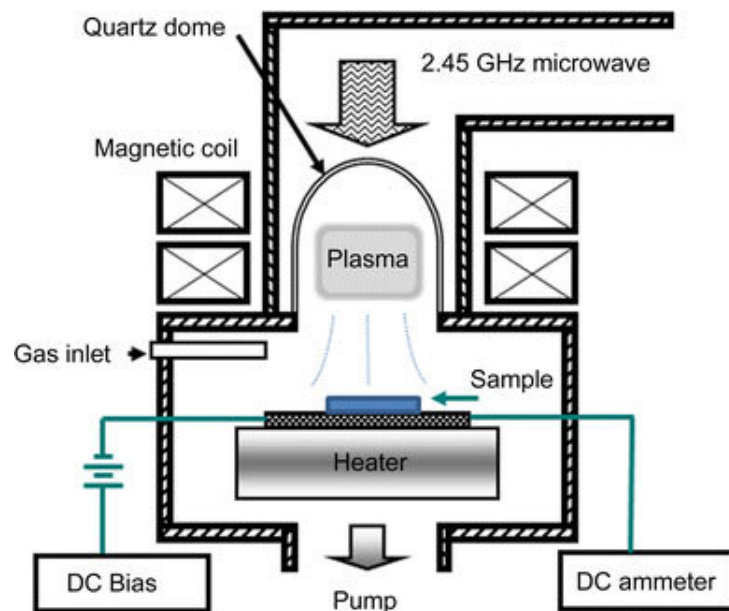
FIGURE 1.6: Schematic of an ECR plasma setup. Resonance occurs in specific regions of the plasma thus requiring restrictions on wafer and reactor size. *Credit: Tseng, 2008 [10]*

ECRs demonstrated high plasma densities and etch rates when studied by Sung *et al.* [11] and Sung *et al.* [12] in 1993 and 1994. But the constraint of substrate size has encouraged the study of similar sources such as the Helicon source which is another type of wave-heated discharge. Helicons were first used by Boswell in 1970 and work by driving a whistler wave mode down an axially, magnetized plasma column. Helicon/whistler waves are launched from an external RF antenna driven at 13.65 MHz and the plasma absorbs the wave energy downstream of the launch point. By

contrast, energy is absorbed in CCPs close to the plasma boundary and, as will be shown next, in inductively coupled discharges, the energy absorption occurs within a skin depth of the plasma. The Helicon sources achieve high ionization efficiencies and therefore high plasma densities. The magnetic fields in Helicon discharges are smaller than those in ECRs and are therefore less costly – requiring less magnetic confinement or magnetic arrangement. Because power is absorbed into helicon via combinations of capacitive, inductive and wave absorption modes, it is a complex source to deploy for high uniformity/high throughput processing. This is contrasted to other plasma sources which have defined capacitive and inductive modes, whereas Helicons transition through all 3 and may experience extra resonances in the helicon mode which can cause sudden jumps in power and density. Its advantage of high plasma density and short process times does not appear to have outweighed the difficulties of configuring it for processing.

1.2.4   Inductively Coupled Plasmas (ICP)

The requirements mentioned at the end of the last section have led to the ICP becoming a major workhorse and this is the plasma source chosen for this work on diagnostic and etching studies. In ICPs, the power coupling is driven by electromagnetic induction. An RF current is passed along a non-resonant coil which creates a time varying, axially symmetric solenoidal magnetic field that penetrates the dielectric walls of the chamber. This field induces azimuthal electrical currents within the chamber gas at reduced pressure to cause successive electron impact ionization collisions which ignite a plasma (**Figure 1.7**). The power absorption occurs within a skin depth. The development of the ICP began as early as 1884 [13]when Hittorf reported work on an electrodeless ring discharge. Subsequent iterations in the 1970s and 1980s resulted in two configurations (planar and helical) that could drive a high density plasma discharge in either low pressure or high pressure regimes. In practice the initial mode of a coil-driven discharge is a low power, low density capacitive mode (*E-mode*) which is characterized

by low ionization efficiency (low light emission) and therefore low plasma density. Much of the power absorption occurs within the electric field between the live end and grounded end of the coil. The high density inductive mode (*H-mode*) is characterized by brighter emission due to greater ionization efficiency and plasma density. The ICP can enter H-mode almost instantaneously at the required power and can maintain this high density and because it is not magnetized, there are no other resonant modes. This makes the source viable for consistent industrial use.
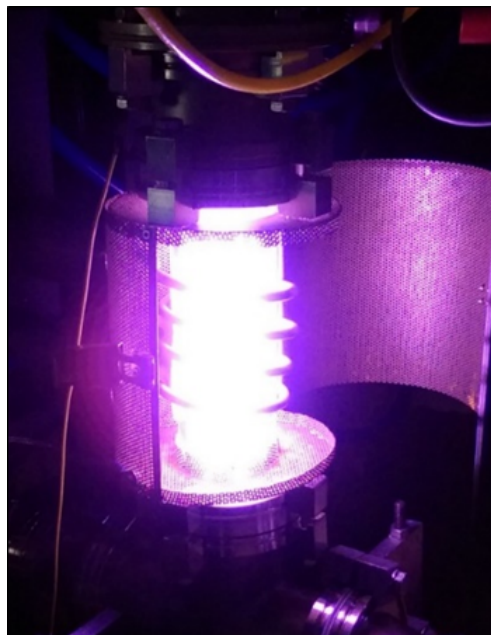
FIGURE 1.7: Photograph of the experimental ICP (used in this thesis) operating in H-Mode

There are clear advantages to using ICPs for plasma processing as separating plasma density from ion energy is trivial. This is usually achieved in ICPs by providing a separate capacitive biasing (which could be in another region of the plasma) for the substrate that is independent of the density-controlling ICP. As the ICP is nominally within a geometrically symmetric dielectric envelope, it is straightforward to extract ions with controlled energy. ICPs are able to sustain plasma densities up to $n_e = 10^{18}$ m^{-3} with high uniformity whilst being able to work at a tenth of the pressure of the limit of a CCP. Even at these pressures, etch rates have been reported to be

as high as 1 μm min^{-1} as reported by Paranjpe *et al.* [14]. Although planar geometry is the more common for industry, a cylindrical geometry is also used in industry (and also in this research due to axial symmetry for ion extraction and probe diagnostics). ICPs are ubiquitous throughout the study of etching despite varying modifications. This thesis investigates the characteristics of an experimental ICPs and how it can be used in the production and extraction of energetic neutral beams. **Chapters 3 & 4 provide a detailed characterization of an experimental ICP source**.

1.3 Applications of Discharge Plasmas

Plasmas have a wide variety of commercial applications listed below:

- Plasmas for Micro Electronics. The semiconductor industry was worth $335.2 billion in 2015 and has steadily grown. [15]. Process plasmas are essential for the sub-micron scale etching of semi-conductor wafers into fine features enabling the production of integrated circuits and transistors for almost all microelectronics from smart phones to intelligent sensors.

- Plasmas for Medicine. This field is emerging rapidly as plasma sources are widely applied to disinfection, healing wounds and cancer therapy within the medical field. Most applications in medicine involve direct application of the source onto the human body for both dermatology and wound/cancer treatment. Other emerging applications are in dentistry.

- Plasmas for Materials Processing. Materials processing by plasma interaction is very diverse. It includes the activation of surfaces which improve adhesive properties or the production of polymers following the fragmentation of gaseous monomers within a discharge. It also includes the application of plasmas in the engineering automotive industry where thermal plasmas are used for arc welding and re-melting of metals. The diversity of application is attributed to the variation in plasma conditions, discharge geometries and methods for activation and excitation. Some of the plasmas in this field (such as those for arc welding) are not of the low temperature variety whereas the etching of semiconductors is also an example of materials processing and this exclusively uses low temperature plasmas.

- Entertainment and homeware. Gas discharges have been used as light sources and although they replaced the filament lamps as the primary light source in many homes, presently LEDs bulbs have proved far more energy efficient and cost effective and are steadily replacing

them in their turn. Other common entertainment applications include plasma televisions which use small cells containing low temperature plasmas or the production of the components used for liquid crystal displays.

1.3.1   Plasma Etching in the Semi-Conductor Industry

Plasma etching describes processes in which chemically active species derived from a plasma are incident on semi-conductor wafers where material is removed through chemical reactions to produce volatile products which are carried away. The nature of the plasma discharge depends on the feed gas; noble gas discharges will form electropositive plasmas whilst molecular discharges will create chemically diverse discharges. The plasma is also characterized by the power absorbed, the chamber pressure before the discharge, particle densities, the flow rate and plasma bias. These parameters modify the behavior of the etching process while the introduction of different semi-conductor substrates with different chemical susceptibility to plasma species can make their monitoring and control quite complex.

Plasma ion "assisted" etching exploits synergistic relationships between the actions of the ionic and neutral species in the plasma. This is well documented in Coburn & Winters [16]. Observations of the etching of silicon with beams of Ar ions and XeF_2 gas illustrated a relationship between the physical impact of the Ar ions and the spontaneous chemical reactions of the XeF_2 coverage on the surface. Etching with just XeF_2 gas or Ar^+ gave low etch rates of approximately 0.5 nm s^{-1} each. When both beams were combined, the etch rate increased to about 7 nm s^{-1}. Energetic ions bombard and deposit energy onto the surface to weaken the lattice structure, the neutral flux then experiences a lower activation energy needed to chemically remove material and create volatile products. Etching via this method is characterized by a high etch rate without necessarily sacrificing a vertical, anisotropic etch characteristic. Plasma ion assisted etching is now the preferred method of fabrication in the industry Donelly *et al.* [17]. Synergies

in etching are further discussed in **Chapter 7** where VUV/UV radiation is investigated in its role within the neutral beam etching process.

The plasma etching mechanism is parameterized by etch rate, directionality, selectivity, profile quality, uniformity, scalability and reproducibility and an illustration of these parameters is given in **Figure 1.8**:

- Etch Rate. This is the speed at which material is removed from the substrate and is usually measured in nm per second/minute or the number of atoms removed from the surface per second/minute. Etch rates can reach up to 600 nm s^{-1} depending on the size of the features being etched and the plasma process. At the SNM scale, single digit etch rates are acceptable to avoid damage to the features on a comparable scale with the feature size.

- Directionality. This parameter describes the anisotropy of the incident species direction of incidence onto the substrate. It is desirable for plasma sources to extract ions with a low angular distribution which protects the sidewalls and reduces lateral etching.

- Profile Quality. This describes shape and physical dimensions of etched features. Good profile quality is characterized by high aspect ratio, vertical side walls that do not persist past the etch stop material and the absence of deformity which affects performance.

- Selectivity. Describes the tendency for etching species to etch different materials (photoresist mask and substrate) which will also have different etch rates. It is desirable in a plasma process for the mask (or other layers) to experience different responses to plasma [18].

- Uniformity. This is a measure of how homogenous the etching process is and depends on both the geometry of the plasma source and the size of the substrate features. Substrates of smaller dimensions are able to maintain a constant etch rate across the entire surface, but

larger substrates (as often used in industrial batch processes) place high demands on uniformity.

- Scalability and Reproducibility. Scalability is important if it is expected that research plasma etching sources can be applicable to an industrial setting. Reproducibility describes whether the same etching process can be performed in batch processes which are standard for industrial etching.
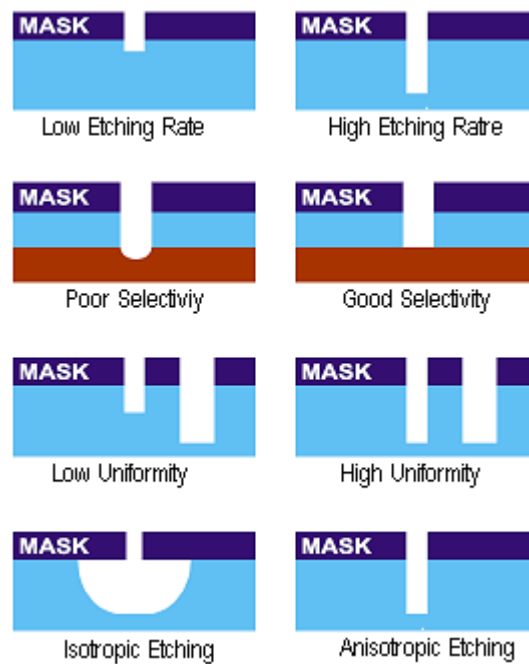
FIGURE 1.8: Visualization of common etching parameters.
Credit: Adapted from O'tell, 2014

1.3.2   Disadvantages of Plasma Etching

Limitations in Etch Profiles

The downsizing of features at the SNM scale has highlighted the necessity to preserve feature quality as surface charging and lateral etching become more significant. These phenomena produce a range of structural defects such as bowing, notching, undercut and even microtrenches (**Figure 1.9**). The main effect of surface charging is to cause directional ions to experience a lateral deflection whilst entering the vertical side wall regions. Charging

on the resist mask also displaces directional ions on approach, giving the impression of undesirably large angular distributions that cause scattering within the sidewalls.
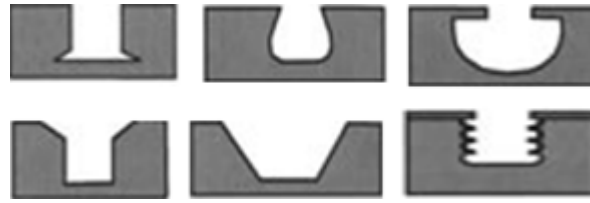
FIGURE 1.9: **Top** notching/microtrench, bowing, undercut. **Bottom** faceting, sloped sidewalls and roughened sidewalls. *Credit: Molecular Foundry*

The problem of bowing and undercut can also be attributed to the selectivity of species entering the trenches. The passivation layer describes a thin resistive mask layering the side walls to prevent lateral etching. The passivation layer is usually formed by reactive plasma species creating oxides and this oxide being naturally inert to plasma exposure Meng *et al.* [19]. Insufficient passivation or excessive bombardment by scattered ions/neutrals will break down this passivation layer and contribute to a bowed profile. On the other hand, too much passivation (encouraged by the difficulty of neutral species being transported out of the sidewalls) will produce gradually narrowing profiles. Notching and microtrenches are caused by charging at the deep end of the vertical trench. The accumulation of electrons in the trenches contributes to a charge imbalance as ions enter the trenches and are diverted to the corners to create micro trenches and notched features.

Early instances of surface charging were observed by Murakawa *et al.* [20] using a 13.65 MHz ECR generated SF_6/Cl_2CF_4 plasma to etch single crystal silicon and polycrystalline silicon. Profile tilt of the vertical sidewalls and bowing were observed in the etching of silicon whilst undercut was observed in the poly-Si both with insulating (photoresist) masks and with metallic (conductive) masks in the absence of significant charging. The

potential differences between the masks and substrates were measured using a surface potential probe. The results, when combined with modeled ion trajectories, indicated that the presence of charged surfaces caused the defects seen in the etched profile and were dependent on the pattern of the masks. A permanent 8×10^{-3} T magnet was placed below the substrate in order to affect the trajectories of incoming charged species and make the local plasma non-uniform. This effect was seen to magnify surface charging for further characterization of this phenomenon.

Charging mechanisms and effects have been modeled in detail by Ishchuck *et al.* [21] and experimentally investigated using a CCP as a way to identify plasma parameter effects on the quality of side walls in etched trenches. The presence of locally varying electric fields due positive charge build-up on the oxide layer via positive ion bombardment and negative charge on the mask due to electron absorption was observed. These effects were also modeled using a numerical simulation integrated in the ViPER (Virtual Plasma Etch Reactor) software [22]. The work highlights the evolution of etch profile dynamics, in greater detail from Murukawa, 1994 [20], and estimates the effects of differing mask configurations or oxide layers.

Bogart *et al.* [23] suggested that mask charging was not the main cause of ion deflection when etching silicon using an ICP Cl_2 plasma. In the investigation, two masks were used, an insulating SiO_2 mask and a conductive Si mask and it was found that the effects of tapered sidewalls and microtrenches were identical between the two masks suggesting the effects of surface charging to not be very significant in this case. It was concluded that that deformation was due to the larger angular distribution of ions incident into the region which draws parallels with Murakawa, 1994, and their attempt to affect the local plasma species via magnetic deflection. Bogart, 2000 also observed that increasing RF source power deepened the microtrenches whilst increase of substrate bias power magnified the effect of

bowing, suggesting that local potentials within the features perturb ion trajectories. Furthermore, they reported large effects on the etch profile when the gas pressure was varied from 10 mTorr down to 2 mTorr. Facets forming on the top of masked and maskless substrate wafers appeared to direct incident ions onto the sidewalls, contributing to large ion angular distribution. This is enhanced by a higher ion flux at low pressures.

Efforts to control these structural effects were attempted by Grangeon *et al.* [24] when using an ICP and O_2/SF_6 gas mixtures. Using a cryogenic etching method, high aspect ratio trenches were etched at the μm level with slopes varying between 88 degrees and 90 degrees. Local bowing however still remained an issue especially with longer process durations and very low or very high pressures. It was reported that the building up of a sidewall passivation layer may be a solution to reducing local bowing. This passivation layer usually forms towards the top of the trench and any found at the bottom can be attributed to higher passivation layers being sputtered by energetic ions. Passivation generally does not form at the bottom of the trench as it is removed by ion impact as quickly as it is formed. In this investigation, over-passivation however occurred as a result of too much oxygen and decreased sidewall quality via gradually narrowing, sloping vertical sidewalls. The effect and study of undercut was not undertaken although it was mentioned. Using an ICP and etching sub micron holes into Si(100) wafers, a later investigation by Pike *et al.* [25] suggested channel size (aspect ratio of vertical sidewalls) also being a contributor to sidewall quality. A scanning electron microscopy (SEM) examination showed that narrow channels of 100 μm or less were found to be smooth but with some over-etching and local bowing due to ion damage. Wider channels reduced local bowing via the passivation layer but smoothness of the etch profile was degraded due to a decrease in polymer coverage – possiblly due to plasma non-uniformity. Another investigation that highlighted these issues was the etching of high aspect ratio contact holes as reported by Masaru *et al.*

[26] using an ECR discharging $C_4F_8/Ar/O_2$ plasma. Bowing of the side-walls was confirmed to be encouraged by the etching and faceting of the mask which suggests poor selectivity between the mask and substrate and caused large angular distributions in incident ions. Minimizing the production of oxygen radicals by controlling the O_2 gas flow helped to reduce the effect of bowing.

Various investigations have identified surface charging and large ion angle distributions as the main cause of structural deformities such as bowing which affect the profile and integrity of etched features. Other investigations indicated the presence of passivation layers having a marked effect on the integrity of the etched profile. This research notes these issues but does not attempt to study them outside of observation during the etch process as etching with fast neutrals provides some solution to these issues.

Limitations in Plasma Sources and Chemistry

The need for greater control and profiles of etched features also includes studies on modified sources and resulting discharge kinetics. Etching yield has been used in several investigations as an indicator to monitor the chemistry and kinetics of the plasma discharge. Vitale *et al.* [27] observed Si etching yields in high density halogen discharges using a planar ICP source. Etching yields of Si were observed to vary approximately as the square root of the ion energy when measured using a quartz crystal mass (QCM) balancer and a mass spectrometer in the same position. Etching yields in a HBr plasma were enhanced compared to Br_2 due to the neutral coverage of the substrate surface by H atoms (suggesting activation of the Si substrate). When raising the temperature of the Si substrate, the etching yield decreased suggesting the inability of H atoms to adsorb onto the Si surface at higher temperatures. A study of discharge kinetics was repeated by Mahorowala *et al.* [28] using an ICP to etch poly-Si. A combination of oxide and photo-resist masked poly-Si substrates were etched in order to obtain evolution profiles which might show dependence on the type of mask used

along with the discharge chemistry. Some observations include a delayed microtrenching in a Cl_2 discharge when using a photo-resist mask although this was offset by instances of bowing. Microtrenches were absent in all HBr discharge results and this was attributed to a lower angular dispersion of ions in the HBr discharge.

The study and applications of pulsed power discharges rather than continuous wave (CW) discharges have also been done. Economou reported a review of work done with pulsed power discharges [29]. Pulsed Plasma etching was investigated as early as 1985 by Boswell *et al.* [30]; high etch rates of Si were linked to high densities of F atoms in the afterglow of the discharge. Further work by Samukawa reported a decrease in notching and an enhanced etch rate when using a pulsed source combined with a biased substrate [31]. Pulsed power generally has had positive consequences for plasma etching. Surface charging is eliminated due to neutralization and negative ion formation in the afterglow to make neutral atoms and negative ions. The identical mobilities of positive and negative ions from the plasma means that there is no charge buildup on the substrate surface or within the trench. In a molecular discharge, negative ions are also able to be extracted due to the relaxation of the plasma potential. A pulsed power source (**Figure 1.10**) can be as simple as turning the power on and off - very quickly in controlled time steps. Typically, these times steps can be separated into two regions; active glow and afterglow. The active glow begins with a ramp up of RF power and a subsequent increase in plasma potential which is soon followed by ignition and a plasma sheath is formed. When the power is briefly turned off, the plasma enters the after glow stage and the initially high electron energy begins to fall off as no more power is absorbed by the electrons and they dissipate energy in collisions. The late afterglow sees the cross-section for electron impact dissociation/ionization drop rapidly and an increase in the cross-section for attachment and recombination which has the potential for the extraction of ions and reactive neutral species for etching without surface charging.
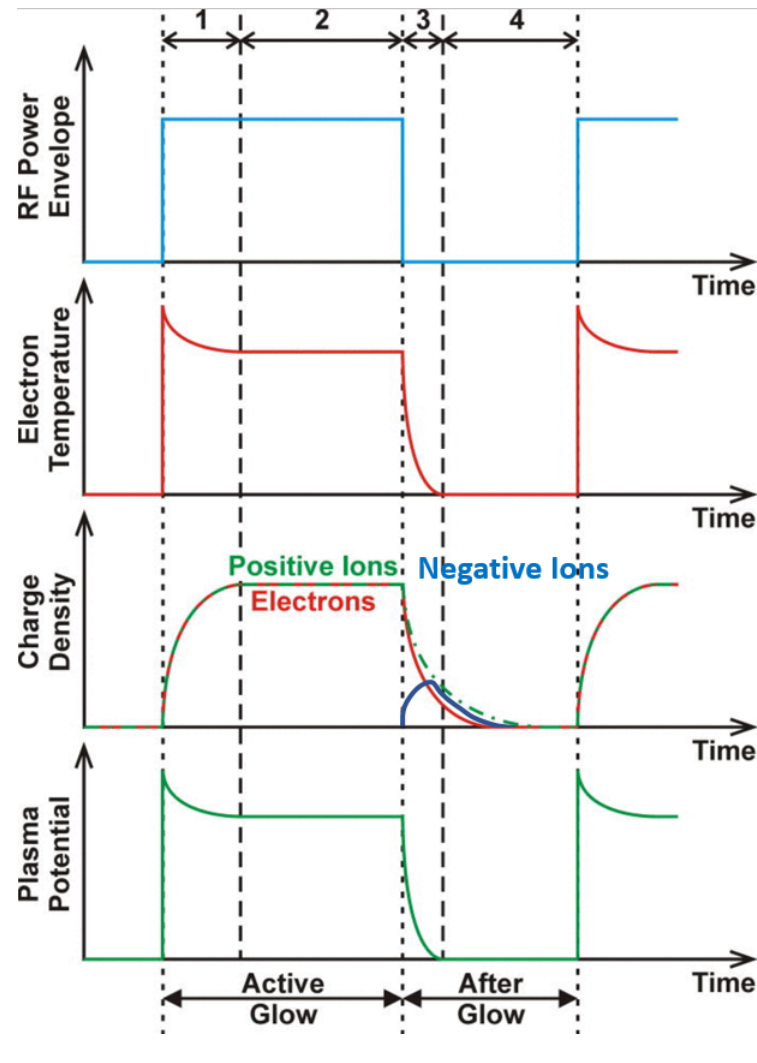
FIGURE 1.10: Evolution of a pulsed plasma. Negative ions
(blue) begin to form via attachment and recombination in
the afterglow stage. *Credit:Adapted from [32]*

Examples of dual frequency pulsing were investigated in a CCP setup
by Jun Kim *et al.* [33] using an Ar/C_4F_8 discharge. The etch rate was con-
trolled by using a high frequency whilst the ion energy was controlled by
a lower frequency. A similar experiment was carried out using an ICP by
Seok Seo *et al.* [34]. They observed a marked increase in plasma uniformity
in pulsed plasma when compared to CW sources. A pulsed power source
encourages plasma uniformity as the plasma can diffuse across space dur-
ing pulse off time. In spite of early results, the continued use of pulsed
power in nanoscale etching has encountered low etch rates. Methods to
counter-act the lowered etch rate were modeled by Agarwal *et al.* [35] us-
ing a Hybrid Plasma Equipment Model (HPEM) code. In general, source

only biasing whilst increasing the power seemed to increase the etch rate, but this introduced greater feature damage via ion bombardment due to coupling of the ion energy with ion flux. A review of pulsed power was given by Banna *et al.* [36].

Gas chemistry in a pulsed setup can be controlled by varying plasma parameters and this translates to improved etch rates and vertical sidewalls in halogen based plasmas such as HBr discharges. However, lateral etching was still observed and it was increased in Cl_2 discharges. The use of pulsed power in electronegative discharges eliminates the problem of surface charging, allowing the extraction of energetic ions and diffuse neutrals to etch fine features. Etch rates were still low however and increasing the etch rate via the ion energy caused damage to the features. Attempts to recoup etch rate were furthered by Dorf *et al.* [37] using an electron beam excited plasma (EBEP) that produced high ratio ion-radical beams for atomic layer etching on silicon. Chlorine ions are known to effectively remove material but the ions suffer from large ion angle distributions which produce lateral etching. This was reduced by increasing the ion energy to make them more directional, but this caused damage at the etch stop for < 20 eV ions. A protocol of switching between continuous Cl radical bombardment and exposure to Ar/N_2 was promising in order to lower damage, but it was difficult to control the energies of both ions and neutral radicals effectively.

The objective to produce consistent etch profiles that have minimal profile distortion require efforts in investigating ways to control the plasma source, kinetics and plasma to substrate interaction. Despite significant research effort, the persistence of structural deformities and consistently low etch rates make current methods still unsuitable for industrial batch processing at the SNM scale. Improvement of the etch rate usually results in greater surface damage along with non-trivial plasma kinetics.

1.4   Summary

This chapter has reviewed the key physical concepts that underpin plasma etching. Furthermore, a brief review of plasma etching as the modern and conventional method of etching has been undertaken whilst discussing the problems associated with it. This sets the scope of the research carried out in this project with the intention to study and characterize etching plasmas using an ICP source and to also provide an alternative method to conventional plasma etching that can produce vertical high aspect ratio SNM features whilst minimizing structural deformities. It has been previously proposed that a chargeless, energetic neutral beam can be applied in a process called neutral beam etching (NBE) and could be a viable alternative to conventional plasma ion etching to produce damage-free fine etched features. The ways in which energetic neutral beams can be created and extracted will be investigated, requiring both a detailed study of the plasma phenomena and methods of extraction and characterization. The neutral beams will then be applied to the modification of polymer substrates within a geometrically identical plasma etcher, characterizing the etch depth, etch rate, surface roughness and chemical profiles.

Chapter 2

Neutral Beam Etching Review

This chapter reviews the development of NBE. Over the past three decades, many investigations have focused on the creation of fast directed, energetic neutrals which can be aimed at a substrate and etch without charging or excessive substrate damage at the nanometre scale. This requires (1) utilization of a convenient plasma source, (2) an ion extraction mechanism which includes a basis for energy control and (3) a process that can neutralize the ions into a beam of energetic neutrals which have the same energy characteristics and direction as the parent ion beam. In order to be an industrially viable alternative to conventional plasma ion etching, neutral beam etching must also achieve competitive etch rates.

This literature review will show that over the last 30 years, neutral beams have been demonstrated to achieve vertical profiles combined with low profile damage. However, their industrial use remains minimal due to low etch rates and the understanding of neutral beams being partial due to the inability to measure them directly or control them to the degree of ions. As discussed at the final section of this chapter, this thesis aims to fill this gap in the literature by proposing a method for measuring and characterizing fast neutral energy and investigating ways to increase the etch rate using photochemistry. The importance of this entire research is therefore to provide a more complete understanding of the neutral beam etching/surface modification mechanism for the purposes of integrated circuit component fabrication in industry.

2.1 Gas Phase Neutralization

The first reported investigations into a neutral beam source came in the form of fast atom beam (FAB) (**Figure 2.1**) sources that took advantage of the A. H. McIlraith Cold Cathode (1972). A cold cathode is voltage driven and produces electrons with a quantity that surpasses that which could be produced from thermionic emission. Secondary electrons from the cathode surface ionize neutral gas which then bombard the cathode to produce more electrons in a self sustaining discharge. One such source was investigated by Shimokawa *et al.* [38] where a reactive Cl_2 discharge was used to generate energetic neutral beams to etch GaAs wafers.
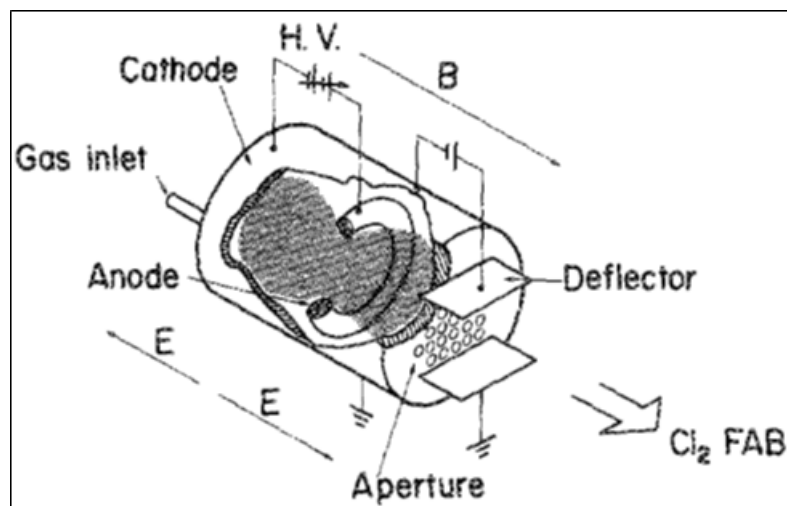
FIGURE 2.1: McIllraith Cold Cathode Fast Atom source.
Credit: Shimokawa, 1989 [38]

Vertical deflector plates swept any residual ion current to produce a beam composed entirely of directed neutrals. The discharge chamber was composed of an electromagnetically enhanced ringed anode and a cylindrical cathode. The enhancement enabled electrons to perform long oscillation paths which improved plasma density. Cl_2 ions extracted with 1.5 – 1.8 kV engaged in charge-exchange collisions with neutral Cl_2 gas within the apertures to produce a beam of energetic neutrals and reactive Cl which diffused naturally through the apertures. The apertures of the cathode and

the anode were made of graphite as it is relatively inert to Cl_2. At pressure between 10^{-2} - 100 Pa (0.07 – 7.5 mTorr), an etch rate of 10 – 60 nm min^{-1} was recorded which was up to a 100 times greater than when an Ar discharge was used. This enhancement was attributed to the chemical reactivity of Cl_2 molecules on the substrate surface. Low radiation damage was reported and this was associated with the absence of charged particles and UV photons.

Following interest in FAB sources, a number of investigations focused on a gas phase charge-exchange mechanism. In particular, Mizutani *et al.* [39] used an ECR plasma to produce energetic neutral Ne beams via the gas phase charge-exchange mechanism. Ne ions were extracted from the plasma using multi-aperture electrodes. The ions then engaged in resonant charge-exchange collisions with the neutral gas (with minimal energy loss) to produce a directed energetic neutral beam onto a Cu substrate. Under pressure conditions of 9.8 x 10^{-2} Pa (0.7 mTorr) and a neutralization path length of 13 cm, 50% of the total extracted ions were neutralized by the charge-exchange mechanism. Most ions that were not neutralized were removed via retarding potential grids. The plasma was electrically separated from the neutral gas due to the aperture electrodes such that there was no plasma activity within the neutralization region. Using a Faraday cup, the residual ion beam flux densities were reported up to 10^{20} ion m^{-2} s^{-1} with the neutral beam flux densities being measured by a calorimeter and measured up to 3 x 10^{18} atoms m^{-2} s^{-1}. The etch rate of the sputtered Cu substrate was measured at 10.8 nm min^{-1}.

Mizutani *et al.* [40] revisited this work in 1990 with the aim to etch rather than physically bombard/sputter the substrate. Ion beams in the range of 200 – 700 eV were generated from an Ar plasma using a Kaufman ion source which then produced neutral beams via the charge exchange mechanism beyond multiaperture electrodes which etched an SiO_2 substrate (**Figure 2.2**). Neutral F and CF radicals from a CHF_3 discharge were also present

in the chamber created using an ECR source similar to previous research [39]. The authors report a neutralization efficiency of around 50% along a path of 13 cm within the background gas of pressure $0.09 - 0.1$ Pa ($0.67 - 0.7$ mTorr). Four cases of plasma etching were presented in this research:

1. Ion beam etching, where the retarding grids were set to 0 V to encourage full exposure of an energetic Ar ion beam and the microwave source was not switched on to produce a CHF_3 plasma that would produce radicals.

2. Neutral beam etching, where the retarding grids were set at a potential higher than the ion energy and again the CHF_3 was not excited.

3. Ion beam assisted etching, where both the Ar ion and neutral beams were incident on the specimen with the simultaneous excitation of the CHF3 plasma as a source of radicals.

4. Neutral beam assisted etching, where any and all charged particles are prevented from reaching the specimen via the application of appropriate potential to the retarding grids.

Etch rates for neutral beam etching were shown to be about half of those for ion beam etching (case 1) - 18 nm min^{-1} for the ion beam and 9 nm min^{-1} at maximum extraction voltage. These etch rates were then doubled with the assistance of radicals from CHF_3 (cases 3 & 4) which again illustrates the earlier conclusion of radical and energetic particle synergy as mentioned in [16]. The etch rates of Si were noticeably lower than SiO_2 and this was concluded to be caused by polymerization on the substrate surface which suppressed the Si etch rate. A quartz crystal oscillator (a sensitive piezo-electric) measured the neutral beam flux density as 3.12 x 10^{18} atoms m^{-2} s^{-1} which was identical with [39] as described above. Profile studies were not undertaken in Mizutani's research.
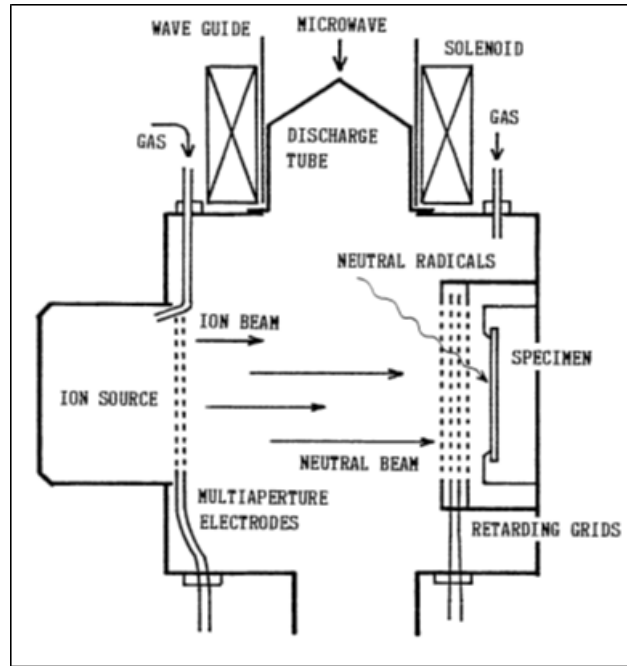
FIGURE 2.2: ECR/Kaufman Ion source and Charge-exchange chamber. *Credit: Mizutani, 1990* [40]

Higher etch rates using a neutral beam assisted plasma were reported by Yunogami *et al.* [41] where ions from a Kaufman source were extracted to charge-exchange in the gas phase. Diffuse CHF_3 radicals were provided by a microwave source similar to earlier investigations. Although the dependence of ion beam divergence on chamber pressure was recorded and the neutral beam was assumed to have the same characteristic. The Ar ion beam divergence angle in the neutral beam assisted case was recorded as 5 – 6 degrees at a pressure between 0.5 and 1 mTorr which was larger than the conventional ion beam etching at 2 - 3 degrees. The neutral energy distribution (neutrals were ionized) was measured as 500 ± 20 eV using time of flight (TOF) mass spectroscopy. The enhancement effect of neutral beams assisted with neutral radicals resulted in an etch rate of 60 nm min^{-1} on SiO_2 with critical dimensions of 1 μm thickeness and 0.25 μm line patterns. No charging effects were recorded. Tsuchuzawa *et al.* [42] on the other hand reported low damage Si etch rates of up to 10 nm min^{-1} when using a mixture of SF_6 and Cl_2 extracting in the energy range of 10 – 20 eV.

2.2   Surface Phase Neutralization

As an alternative to gas-phase charge-exchange, surface phase charge-exchange
was developed as a means to produce energetic and directed neutral beams
in the late 1990's. The production of energetic neutral beams using sur-
face charge-exchange involves the Auger process. Samukawa *et al.* [43]
extracted ions from a pulsed ICP through a DC biased carbon plate with
many apertures/high aspect ratio holes (dimensions 1 mm and 10 mm for
diameter and length respectively) which where then neutralized via surface
collisions (**Figure 2.3**).
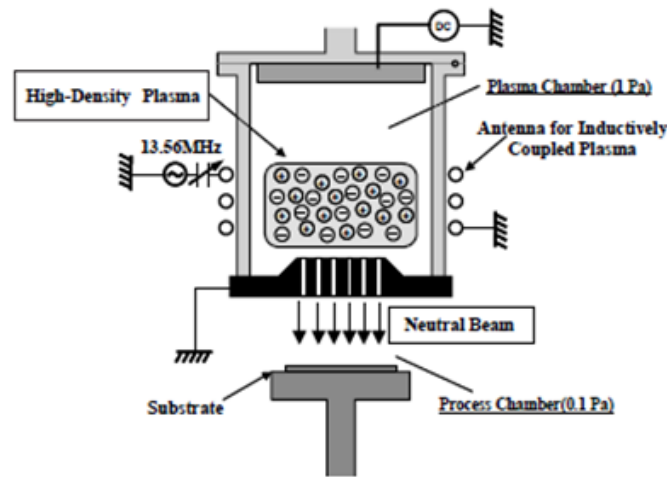
FIGURE 2.3: Pulsed ICP with a carbon neutralizer for neu-
tral beam extraction. *Credit: Samukawa, 2001* [43]

The ion and neutral energies were restricted to between $10 - 20$ eV rather
than the energies of 100+ eV used in earlier experiments and this was pro-
posed to further mitigate surface damage. The extraction of negative ions
in the afterglow for charge-exchange on the surface was preferred rather
than the conventional neutralization of positive ions. The authors state
their reasoning for this as the neutralization efficiency for negative ions was
higher than that of positive ions for the same bias voltages. However, at
very low bias voltages, these differences were negligible. It also happens
that positive ion formation is more efficient than that of negative ions. The
work showcased the possibility of extracting negative ions and neutraliz-
ing them efficiently to produce neutral beams capable of etching without

profile distortion. Although the authors stated that they used a quadrupole mass/energy analyser (QMS), there was no recorded neutral beam characterization or determination of energy. This was instead assumed to be similar to the energy of residual negative ions. The neutralization efficiency was reported to be almost 100% with a maximum neutral flux density of 1.75×10^{20} atoms $m^{-2} \, s^{-1}$. However the surface charge-exchange process is not without energy loss and this was not highlighted. The volume of the reactor was approximately 2×10^{-3} m^3 whilst the RF power was fixed at 500 W. This gives a power per unit volume of 25×10^4 W m^{-3}. Although no dimensions are given, it is assumed that wave plasma sources such as those used by Mizutani *et al.* [39, 40] are larger in volume with comparatively lower power (microwave source was based on a model that did not discharge far beyond 80 W). Therefore, it can be seen why the flux density measured by Samukawa is signifcantly greater.

A similar surface charge exchange investigation within the same year was conducted by Panda *et al.* in 2001 [44], this time using hyperthermal O_2 neutrals (100s of eV). Ions were extracted from an ICP through aluminium neutralization apertures to produce an energetic beam of neutrals that etched polymer films. The authors state that due to the lack of differential pressure control (the discharge was 10 mTorr at minimum pressure), the gas phase charge-exchange mechanism would not be sufficient to contribute to a neutral stream. Very high etch rates of up to 400 nm min^{-1} were reported with anisotropic features and no undercut to the etch profile.

Other groups have investigated the possibilities of employing forward angle reflector plate neutralizers (**Figure 2.4**) as a means to control the direction a an energetic neutral stream. Lee and co-workers [45, 46] in 2002 used an ICP to extract various ionic species of reactive discharges (SF_6, NF_3, CF_4 and Ar) through forward angle (5 degrees) aluminium reflector plates in order to produce an anisotropic, energetic neutral stream. The authors reported a decrease in residual ion flux density when the reflectors were
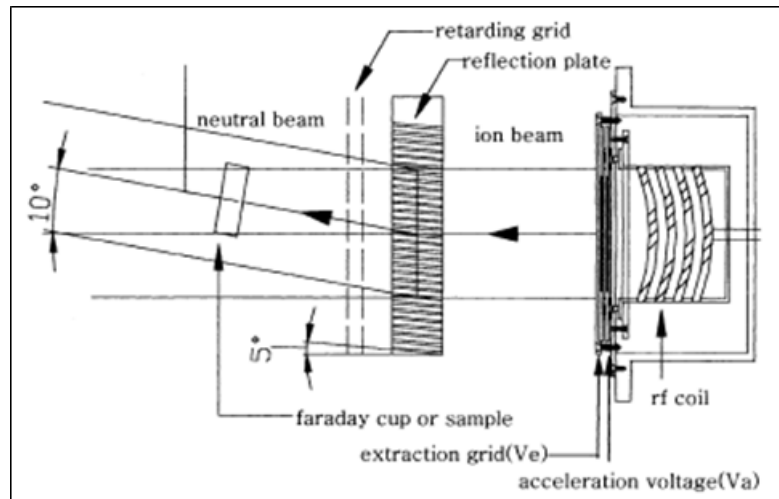
FIGURE 2.4: ICP source with forward angle reflectors
(wafer neutralizers). *Credit: Lee, 2001* [45]

installed, suggesting a high neutralization efficiency of the ion beams into
an energetic neutral stream. Although not greatly dependent, an increase
in acceleration voltage gave a small increase in ion flux density at 5 and 15
degrees, suggesting a small dependency of species energy on the process
of surface neutralization. In general, using a reactive discharge (SF_6, NF_3)
produced more etching of the SiO_2 substrate than the other gases such as
electropositive Ar discharges. This suggests neutral beam assisted etching
with radicals to increase the removal of material from the substrate. Etch
rates were reported to be in range of $0.5 - 7$ nm min^{-1}. In further studies by
Kim *et al.* [47] and Nam *et al.* [48] performed simulations of these forward
angle reflectors in order to optimize the neutral stream based upon varying
the reflector hole size, retardation grid gaps and their respective voltages.
They found that neutral stream generation depended on the ion flux, inci-
dent ion energy and angular distribution. Increasing the hole size would in
theory increase the ion flux and therefore the neutral flux, but the ion angu-
lar divergance becomes broader, weakening the direction of any resultant
neutral stream. The molding of the plasma potential in the apertures were
also discussed and this was said to have a marked effect on the anisotropy
of the neutral beam.

2.3 Neutral Beam Characterization

Investigations returned to gas phase charge-exchange with Ichiki *et al.* [49] in 2008, using a cold cathode FAB source to etch SiO_2. The authors report etch rates of 30 nm min^{-1} but no direct characterization of the neutrals. Characterization of neutral beams have been made previously [41], but the general lack of characterization in other studies has contributed to the partial understanding of the NBE process. A characterization of a neutral beam source was undertaken by Hara *et al.* [50] in 2008, using a surface wave plasma (SWP) (**Figure 2.5**) to produce directed ion beams which transitioned into a neutral beam (a little less than 100 eV) via the charge-exchange process in gas phase. Ionic N_2 and Ar species were accelerated by dual carbon electrode grids and charge-exchanged without energy loss in a neutralization region of length 50 mm. The chamber was electrically connected to the top carbon electrode, so the plasma potential was set by that electrode. The pressures of the main plasma chamber and the neutralization region were independently controlled to be 9.25 Pa in the main chamber and 0.25 Pa in the neutralization region. A QMS was set beyond the neutralization region 50 mm from the bottom electrode, in order to characterize the ionic and neutral energies. The energy of the neutral beams was determined by modulating the ionization filaments of the QMS and was found to mirror the IED of the residual ions, indicating charge-exchange without energy loss. The authors reported a secondary low energy ion peak in the nitrogen plasma which was removed by placing a ceramic spacer between the two carbon electrodes. This suggested that plasma was created by secondary electrons formed by the collisions of ions within the electrode space. A neutral beam flux density was estimated as 2.3 x 10^{18} atoms m^{-2} s^{-1}.
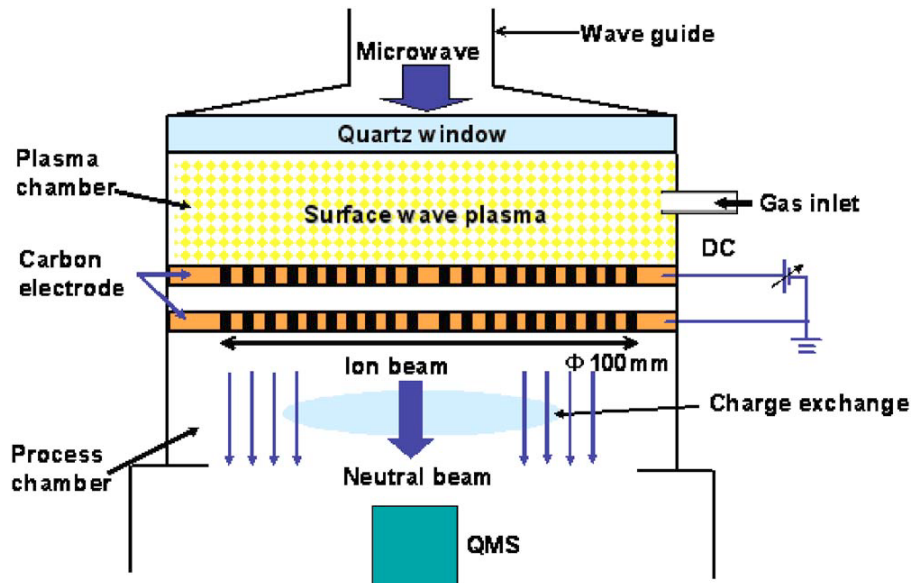
FIGURE 2.5: Surface Wave source with charge-exchange
volume to create an energetic neutral beam *Credit: Hara,
2008* [50]

Further work by Hara *et al.* [51] in 2011, saw the use of an Electron Beam
Excited Plasma in order to produce a neutral stream. A DC discharge re-
gion emitted electrons which were accelerated via means of a double grid-
ded structure to produce a uniformly dense plasma via ionization collisions
on feed gas by said electrons. Plasma ions were then extracted using accel-
eration electrodes (similar to that of Hara, 2008 [50]) to engage in charge-
exchange collisions in the neutralization region. It was reported that Ar
ion beam uniformity was improved and the variation of the ion energy dis-
tribution function varied only in a narrow band of 2.5 eV although con-
tributions from the resolution of the diagnostic were not discussed. This
translated into a greater control of the ion energy and therefore the produc-
tion of a more uniform and monoenergetic neutral beam. Low etch rates of
Si were reported however and only at 140 V extraction voltage did the etch
rate surpass 4 nm min^{-1}.

2.4 Pulse Modulation of an ICP to Produce Neutral Beams

At the Open University in 2013, Marinov *et al.* [52] established a protocol where electron free ion-ion plasmas can be formed in the afterglow of a pulsed ICP source and both positive and negative ionic species can be extracted and neutralized using solid neutralizer apertures similar to Samukawa, 2001 [43]. **Figure 2.6** illustrates the schematic of the commercial PL-80 etching system setup used by Marinov.
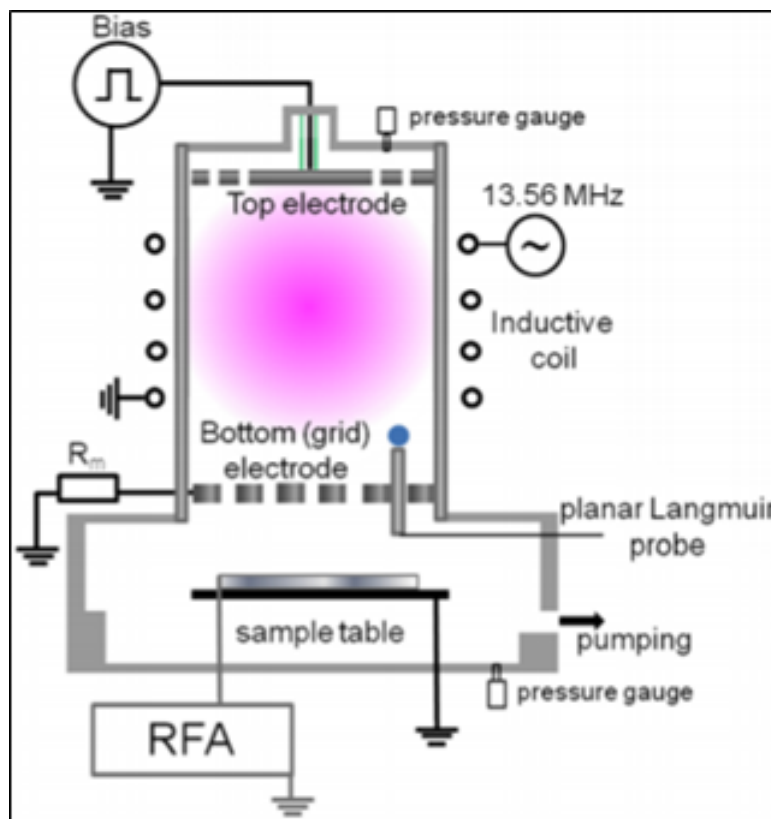
FIGURE 2.6: PL-80 ICP source and extraction of positive and negative ions on high aspect ratio carbon apertures to create a neutral stream. *Credit: Marinov, 2015* [52]

Control of the ion energy was achieved by use of a top 'pusher' carbon electrode and was also pulsed synchronously with the RF modulation. The ion energy and residual ion flux was measured using a retarding field analyzer (SEMION RFA). The energy of the neutral particles and their flux

were not directly measured. Instead, these were inferred from the charac-
teristics of the residual ion beam. The simultaneous extraction and neutral-
ization of positive and negative ions from an ion-ion plasma formed in the
afterglow was demonstrated. Although no mass resolution was available,
biasing of the afterglow implies a neutral beam assisted mechanism where
neutral radicals (created via recombination during the afterglow phase) can
be extracted along with a tuned energetic neutral beam as low as 10 eV for
charge-less, etching without profile distortion. Further etching trials how-
ever did not succeed in suppressing other mechanisms so that etch depths
could not completely be attributed to an energetic, neutralized component.
Furthermore, it was found that positive ions were not that much harder
to neutralize than negative ions and since they are always available in a
continuous wave setup, any lowered efficiency of neutralization is com-
pensated by avoiding the duty cycle factors of pulsed arrangements. This
was the context in which the present work was established, using a new
ICP source designed to enable diagnostic access.

2.5   Overview of Neutral Beam Sources

NBE has demonstrated processing in a charge-free environment and surface profiles are absent of distortion. An incidental, but important consequence of etching with extracted beams is that substrates are protected to some degree from exposure to plasma generated UV. Challenges for deepening understanding of neutral beam approaches are centered around the direct characterization of the beams. Often, the presence of an energetic neutral beam is inferred from the observation of residual ions and surface profiles of the substrate. However, the neutral beam itself has rarely been successfully characterized directly. Hara [50] used a QMS to measure neutral energy, Yunogami [41] used a TOF approach, but no report was made of the exact neutralization efficiency and total neutral flux. Other methods to measure the energy of neutral particles include calorimetry, where the temperature rise of a known material is directly proportional to the power deposited over its area. These methods are complicated by a number of effects including the fact that neutrals will deposit only a fraction of their energy on the surface of the material due to relatively low sticking coefficients. Trottenberg *et al.* [53] reviewed various non-electrostatic diagnostics for the measurement of energetic neutrals present in ion beams. Alongside calorimetric studies, force probes, falling micro-particles and sputter emission. Other techniques include the production of secondary electrons in an absorption plate whose energies and fluxes are measured such that neutral beam energy and flux can be extrapolated [54]. Whereas the angular distributions of energetic ion beams have been measured, the neutral beam distributions have not been directly measured; [41]. In absence of direct measurements, it is often assumed that the neutral beam should maintain the same direction as the parent ion beam due to the charge-exchange mechanism. **Table 2.1** provides an overview of the sources mentioned in this chapter.

Reference	Year	Author	Source	Neutralizer	Gas	Pressure	Etch Rate	Neutral Detection
[39]	1988	Mizutani, T.	ECR	Gas	Ne	1 mTorr	n/a	Calorimetry
[38]	1989	Shimokawa, F.	Cold Cathode	Gas	Cl_2	0.5 mTorr	600 nm min^{-1}	No
[40]	1990	Mizutani, T.	ECR/Kaufman	Gas	Ar/CHF_3	0.75 mTorr	4 nm min^{-1}	No
[42]	1994	Tsuchizawa, T.	ECR	Gas	SF_6/Cl_2	0.6 mTorr	60 nm min^{-1}	No
[54]	1994	Iijima, Y.	Kaufman	Gas	Ar	1 mTorr	1.6 nm min^{-1}	No
[41]	1995	Yunogami, T.	ECR/Kaufman	Gas	Ar/CHF_3	1 mTorr	60 nm min^{-1}	ToF-MS
[49]	2008	Ichiki, K.	Cold Cathode	Gas	SF_6	75 mTorr	30 nm min^{-1}	No
[50]	2008	Hara, Y.	SWP	Gas	Ar/N_2	70 mTorr	n/a	QMS
[51]	2008	Hara, Y.	EBEP	Gas	Ar	0.7 mTorr	4.5 nm min^{-1}	QMS
[43]	2001	Samukawa, S.	ICP-Pulse	Surface	SF_6	7.5 mTorr	n/a	No
[44]	2001	Panda, S.	ICP-CW	Surface	O_2	50 mTorr	600 nm min^{-1}	No
[45]	2001	Lee, D.	ICP-CW	Surface	O_2	n/a	7 nm min^{-1}	No
[46]	2002	Chung, M.J.	ICP-CW	Surface	$SF_6/NF_3/CF_4/Ar$	1 mTorr	7 nm min^{-1}	No
[47]	2004	Kim, S.J.	Ion Gun	Surface	n/a	0.1 mTorr	n/a	No
[52]	2015	Marinov, D.	ICP-Pulse	Surface	SF_6	30 mTorr	n/a	No
Present	2017	Ayilaran, A.	ICP-CW	Gas/Surface	$Ar/O_2/He/SF_6$	30 mTorr	30 nm min^{-1}	QMS

TABLE 2.1: Historical Review of Neutral Beam Sources

2.6 Research Objectives

The main objective of this research is to characterize energetic neutral beams as with the exception of Yunogami (ToF mass spectroscopy) and Hara (QMS) [41, 50], direct neutral beam characterization has not been attempted over the course of 30 years. Furthermore, ways in which the neutral beam etch rate can be adjusted will be investigated. The research can be split into three parts:

- **Development of a system capable of producing a source of energetic, directed neutral species**

    - Chosen plasma source (ICP) based on PL-80 (Marinov, OTell and Bowden) [52]

    - Diagnostic measurements to characterize the plasma

    - Neutral beam source

- **A protocol for measuring these neutral particles**

    - Use of modelling techniques to characterize an electrostatic quadrupole

    - Characterization of neutral beam with paramaterization of plasma

    - Validation of neutral energy measurements

- **A protocol for surface modification of polymers**

    - Etching of polymer substrates in a charge-free environment

    - Study and quantification of UV photons within the etch process

    - Ellipsometry, Atomic Force Microscopy and X-ray Photon Spectrometry to characterize physical and chemical characteristics of polymer substrates post etch

    - Strategies for enhancing etch rates

    - Investigation of potential benefits of processing with controlled exposure to plasma UV

2.7   Summary

This chapter has reviewed some of the main discoveries and innovations following the study of energetic neutral beams for plasma etching. This is done in the low process pressure range of 1 mTorr - 100 mTorr and has the main advantage of being immune to the charging effects mentioned in detail in **Section 1.3.2**. Efforts in NBE began with fast atom beam sources using cold cathodes at hyperthermal energies and also with electron cyclotron resonance plasmas that featured a separated gas phase neutralizer. Surface phase neutralization in neutral beam etching and the work on creating directed neutral beams with high aspect ratio apertures or small grazing angle reflectors was discussed. It was found that issues with the method have been mainly in the lack of neutral beam characterization, which has only been addressed in part. This has contributed to a partial understanding of the process and situations where an energetic neutral beam component has been indistinguishable from an ion or radical component during the etch process. Therefore, a protocol for neutral beam etching being formed that provides a clear benefit over conventional plasma ion etching has yet to be formulated. However, for polymer etching (which are used as dielectrics in integrated circuit fabrication) where mass reduction via chemical reactions may benefit from a controlled energetic beam of neutrals, NBE could provide a low damage environment that is not possible with ion etching. The work in this thesis will attempt to characterize neutral beams and then apply neutral beams to modify the surfaces of polymer substrates in a charge-free etching environment. It is noted that low etch rates may be in part of processing outside the UV rich environment of an active plasma.

Chapter 3

The Experimental Setup

This chapter introduces the bespoke experimental environment, the design considerations and engineering that went into its creation. In order to create a plasma environment that can be directly compared with the PL-80 commerical etcher used in the underlying project, the experimental setup must satisfy criteria regarding size shape, materials and power coupling. It must also be compatible with diagnostic access (which the PL-80 is not). It must achieve plasma discharge densities of order 10^{17} m^{-3}. **Chapter 4** deals with the rigorous characterization of the plasma with various parameterization, whilst **Chapter 3** deals with the structural design and effectiveness of the setup.

3.1 Physical Design Considerations

3.1.1 Coupling Power from a 4-turn Coil into a Plasma

The high density, low pressure regime is of particular interest for plasma processing. The densities needed for this regime are achieved in inductive mode with high power absorption. The configuration of the experimental setup (like the industrial PL-80) is simple and features a non-resonant inductive coil of 4 turns (**Figure 3.1**) wrapped around an evacuated dielectric tube (ceramic or glass) and powered by RF_f = 13.56 MHz:
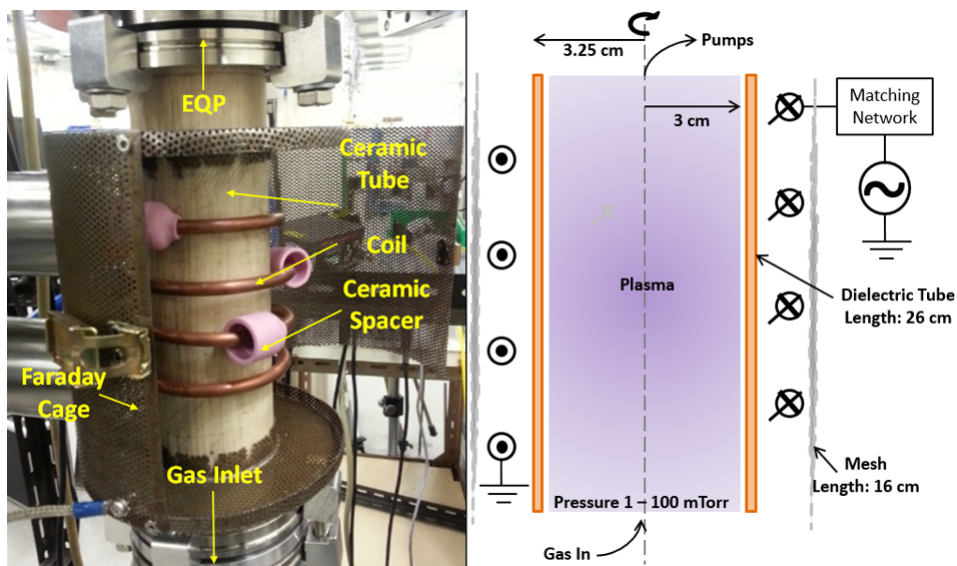
FIGURE 3.1: Picture of the 4 turn Inductive Coil used in this thesis with dimensions.

A high number of turns for an inductive coil will give rise to an excessive voltage across the coil and a consequently a substantial capacitive coupling. Low aspect ratio discharges avoid this complication, but high aspect ratio cylindrical discharges do not. The fewer the turns, the higher the coil current must be for a given power input and the smaller the coupled volume. The PL-80 and this bespoke source use a 4 turn coil. The 4 turn primary coil is formed from a 6 mm copper tube of length 1.34 m with a wall thickness of 1.5 mm. Tubing was used instead of wire due to the skin depth

and to enable water cooling. A 'long' coil has a characteristic inductance:

$$L = \frac{\mu_0 N^2 A}{l} = \frac{4\pi \times 10^{-7} \times 4^2 \times \pi \times (42.5 \times 10^{-3})^2}{10 \times 10^{-2}} = 1.14 \times 10^{-6} \, \text{H} \quad (3.1)$$

Where N is the number of turns, A is the cross-sectional area of the coil and l is the length of the coil. The RF resistance of the copper coil was calculated using the EM skin depth δ:

$$\delta = \left(\frac{2}{\omega \sigma \mu_0} \right)^{\frac{1}{2}} = \left(\frac{2}{8\pi^2 \times 13.65 \times 10^6 \times 5.67} \right)^{\frac{1}{2}} = 1.76 \times 10^{-5} \, \text{m} \quad (3.2)$$

Where σ is the conductivity of copper. Noting that the current only flows in a small cross-sectional area of $1.76 \times 10^{-5} \times 2\pi \times 0.003$ (skin depth δ x thickness of copper tube). Using the resistivity expression, the total RF resistance of the coil is therefore:

$$R = \frac{\rho l}{A} = \frac{1.677 \times 10^{-8}}{3.317 \times 10^{-7}} = 0.067 \, \Omega \quad (3.3)$$

Capacitive coupling to the conducting material (i.e. plasma) within the coil arises due to the electrostatic field associated with the voltage across the coil that is required to drive the current. This electrostatic coupling is responsible for initial gas breakdown. This phenomenon is further quantified in **Chapter 4**. At sufficiently high coil current, an inductive coupling takes over which leads to a higher density. Although the discharge is initiated in low capacitive mode, the power associated with capacitive coupling should be much less than that of the inductive coupling. The consequences include severe interactions with the ion energy distribution. In this regard, the distance and dielectric material between the coil and the plasma serve to limit the electrostatic coupling. The coil voltage can be estimated as:

$$|\tilde{V}_{coil}| = \omega L_{ind} |\tilde{I}_{coil}| = 2\pi \times 13.65 \times 10^6 \times 1.14 \times 10^{-6} \times 15 = 1466 \, \text{V} \quad (3.4)$$

Assuming a high density mode where the coil current is $\sim$ 15 A. The efficiency of the discharge is maintained by only having a fraction of this coil

voltage appearing across the plasma sheath. This is simply modeled by treating the sheath and the dielectric tube as a capacitive potential divider:

$$V_{sheath} = |\tilde{V}_{coil}| \left(\frac{x_s}{\frac{r_c - r_0}{\epsilon_r} + x_s} \right) \tag{3.5}$$

Where r_c is the coil radius and r_0 is the radius of the dielectric tube and ϵ_r is the relative permittivity of the dielectric tube. The average thickness of the sheath x_s was derived in **Chapter 1** and was noted to be of order a few Debye lengths based on a 1 mTorr plasma with an average plasma potential of 20 V and plasma density 10^{17} m^{-3}:

$$V_{sheath} = 1466 \left(\frac{1.13 \times 10^{-4}}{0.0425 - 0.03 + 1.13 \times 10^{-4}} \right) = 13.13 \, \text{V} \tag{3.6}$$

Lieberman has shown that increasing the number of coil turns leads to a rapid increase in x_s [6]. If x_s increases, capacitive coupling becomes large. This is avoided by keeping the number of turns low $(3-4)$.

3.1.2 Transformer Model, Impedance and Matching Network

A description of an ICP using the transformer model had been presented by Piejak *et al.* [55]. That analysis can be applied to this system. In inductive mode, the experimental setup is considered as a primary coil with 4 turns, coupled through mutual inductance with a 1 turn secondary (the plasma) **Figure 3.2**:
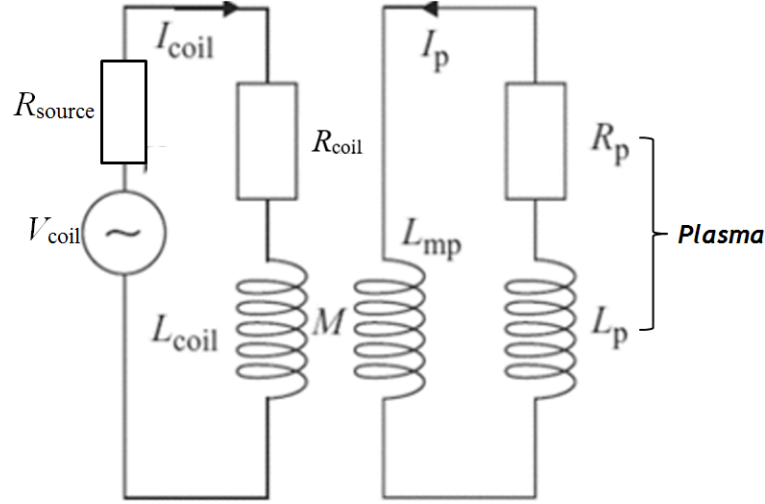
FIGURE 3.2: Primary and Secondary circuits of the ICP Transformer Model. *Credit: Piejak, 1992* [55]

When RF voltage is applied across the coil, potential is developed across the effective resistance (R$_{coil}$) and inductive load (L$_{coil}$) that mutually couple with the plasma with a numerical factor M. On the secondary side, the voltage induced across the plasma against the impedence of a plasma resistance (R_p) and a plasma inductance (L_p). The induced current travels in the opposite direction to that of the current in the primary coil. -The description of potential can be expressed in terms of Kirchoff's laws:

$$|\tilde{V}_{coil}| = i\omega L_{coil}|\tilde{I}_{coil}| + i\omega L_{mp}\tilde{I}_p \tag{3.7}$$

$$\tilde{V}_p = i\omega L_p \tilde{I}_p + i\omega L_{mp}|\tilde{I}_{coil}| \tag{3.8}$$

Where L_{mp} is a mutual inductance term and enables an induced voltage to drive current in the plasma. This second equation can be re-expressed to account for the direction of the induced current and the resultant plasma resistance as:

$$\tilde{V}_p = -\tilde{I}_p R_p - i\tilde{I} R_p \left(\frac{\omega}{v_m}\right) \tag{3.9}$$

Which can be used to solve for the impedance at the coil terminals:

$$Z_s = \frac{|\tilde{V}_{coil}|}{|\tilde{I}_{coil}|} \tag{3.10}$$

Where $Z_s = R_s + i\omega L_s$. R_s is a combination of the real coil resistance R_{coil} and the real part of the plasma resistance R_p. L_s is the inductive load L_{ind} as shown in **Figure 3.3**:
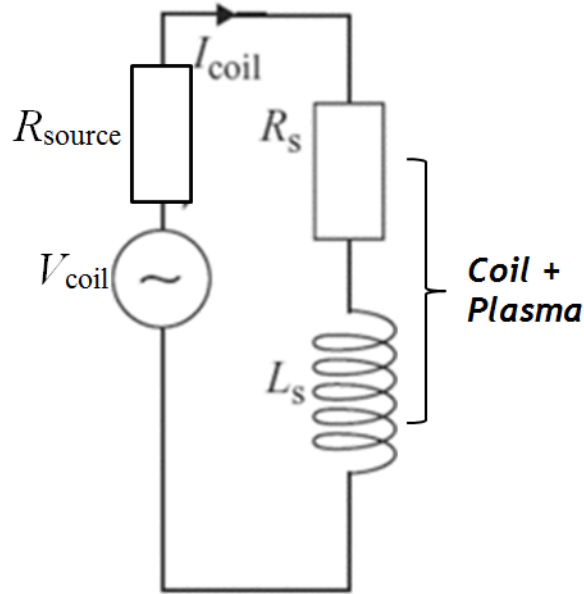
FIGURE 3.3: The equivalent series circuit of the transformer model. *Credit: [55]*

Because the coil and plasma are both mutually coupled inductors, their resistances and inductances can be expressed as:

$$Z_s = R_{ind} + i\omega L_{ind} \tag{3.11}$$

The coils are driven by a 13.65 MHz RF source which has a 50 Ω output impedance (Z_s). This is a real impedance and power must be coupled efficiently to the ICP. Not being able to sufficiently match the source to this load results in reflections that reduce the power absorbed into the plasma and may cause damage along the current path. **Equation 3.11** matches the source to the load in the form of a capacitive matching network as shown in **Figure 3.4**:
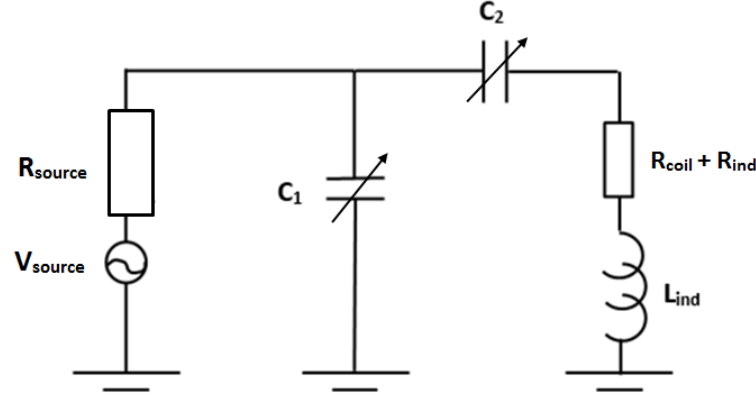
FIGURE 3.4: Schematic of the capacitive L-type matching network used to couple power into the experimental ICP with minimal reflection.

An L-shaped matching network with 2 tuneable capacitors was designed. The range was chosen to be 80 – 230 pF. The air-spaced capacitors exhibit low to negligible loss so that $Z_c = -jX$. Matching is achieved by cancelling the inductive reactance of the load by the capacitive reactance of the tuning circuit. It is expected that a combination of low capacitive coupling and suitable matching sets a high inductive power transfer efficiency for the system. This can be calculated by determining a value of the coil's Q-factor. The individual Q-factor of the coil is therefore measured as:

$$Q = \frac{\omega L_{coil}}{R_{coil}} = \frac{2\pi \times 13.65 \times 10^6 \times 1.13 \times 10^{-6}}{0.067} = 1449.67 \tag{3.12}$$

This describes the inductive power delivered divided by the resistive losses in the coil. The Q-factor allows the calculation of a quantity called the power transfer efficiency which is the fraction of power from the coil that is absorbed into the plasma. In the low-pressure regime, the power transfer efficiency [5] in a pure inductive discharge is taken as:

$$\zeta_{m,lp} = \left[1 + \frac{2}{Q} \frac{r_c^2}{r_0^2} \left(\frac{\omega}{v_m} \left(1 + \frac{\omega^2}{v_m^2} \right) \right) \right]^{-1} \tag{3.13}$$

With the current setup where $r_c = 0.0425$ m and $r_0 = 0.03$ and $v_m \sim 1 \times 10^7$ s^{-1}, the power transfer efficiency was calculated as 0.99. Although not entirely realistic, this is the ideal situation where all the power transfers from

the primary coil into the plasma during the discharge. The power transfer efficiency in a pure inductive discharge won't be this efficient due to imperfect geometry of the coil, coil resistance and small unavoidable contributions to capacitive coupling.

3.1.3 Radiation, Further Considerations and Shielding

One classical method to reduce capacitive coupling is the introduction of a Faraday shield between the coil and the dielectric tube. A Faraday shield works by acting as a conductor to short circuit a substantial portion of the electrostatic field. The spacing between each 'rung' of the shield is such that the electromagnetic field is weakly affected. The shield made for this ICP was constructed using aluminium adhesive tape (**Figure 3.5**).

FIGURE 3.5: A photograph of the experimental setup's conductive strip Faraday shield.

It should be noted that if a Faraday shield is too good at reducing capacitive coupling, the discharge will be difficult to initiate. The spacing of the tape strips was chosen to allow the alternating electromagnetic field to pass through unhindered whilst ensuring the electric field was suppressed. Narrower spacing would have also suppressed the electromagnetic field. In these electrically 'aggressive' environments, RF pickup on diagnostic equipment is a major concern and was been seen to prevent the operation

of the EQP. This was solved by installing a Faraday cage and two stainless steel tubes around the connectioning to the matching network, all connected to ground (**Figure 3.6**).
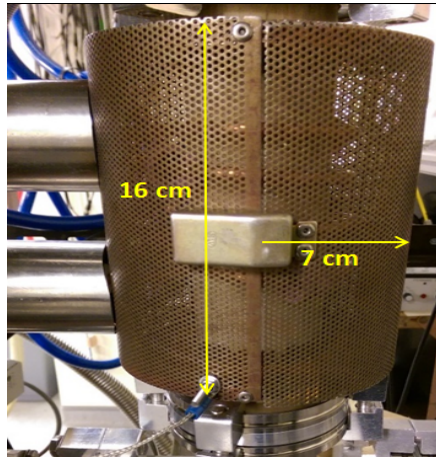
(A) Photograph of Faraday Cage used to shield users from RF radiation

(B) Photograph of teflon insulation used to prevent breakdown between the inductive coil and Faraday Cage

FIGURE 3.6: Photograph of Faraday Cage and teflon insulation to provide shielding and prevent breakdown respectively.

The shielding had the extra benefit of protecting the user from constant RF radiation and becoming in danger of touching the inductive coil. Further considerations were based on the issue of breakdown likely occur between the live inductive coil and the grounded Faraday cage. Installing teflon insulation solved this as the high dielectric constant ensured that there was no breakdown between the coil and the grounded Faraday cage. This again, minimized power losses.

3.2   Power Matching

A measure of power transfer was conducted on the setup using a 1 mTorr Ar plasma. The considerations discussed earlier relate to the transfer of power from the coil to the plasma, but does not include the power losses within the matching circuit even with there being perfect matching and zero reflection. Assuming ideal capacitors, the connecting wires would be the main source of power loss within the matching box. A 10 cm length, 2 mm diameter wire of two materials (Copper and Mild Steel welding wire) were compared, as was necessary to determine the best wire to use within the matching box. Steel wire was a consideration and used for a time due to its sturdiness and resistance to corrosion. For RF power, the current will only travel through a material's skin depth. So the RF resistance of copper wire was calculated based on a skin depth cross-section of wire:

$$R = \frac{\rho l}{A} = \frac{0.1}{6.59} = 0.015\,\Omega \tag{3.14}$$

The RF resistance of the same dimension of steel wire is 0.044 Ω. If power through the matching network is dissipated resistively as $I^2 R$ with a 10 A current, this gives power dissipated as 1.5 W and 4.4 W for copper and mild steel wires respectively. For short term discharges, this wouldn't be an issue as its not expected that the wires would heat up significantly. But for discharges numbering minutes, the mild steel wire becomes extremely hot as three times the power is dissipated and the increase in resistance due to temperature rise results in a greater resistive loss. Copper braid wire was therefore used where the braid made best use of the reduced skin depth.

A measure of power dissipation within the system was undertaken using a high impedance (1000x) voltage probe on the live coil and to ground and a Pearson current transformer (IV / A) to measure the RF current traveling through the coil. The voltage/current signals were recorded using a digital oscilloscope as shown in **Figure 3.7**.
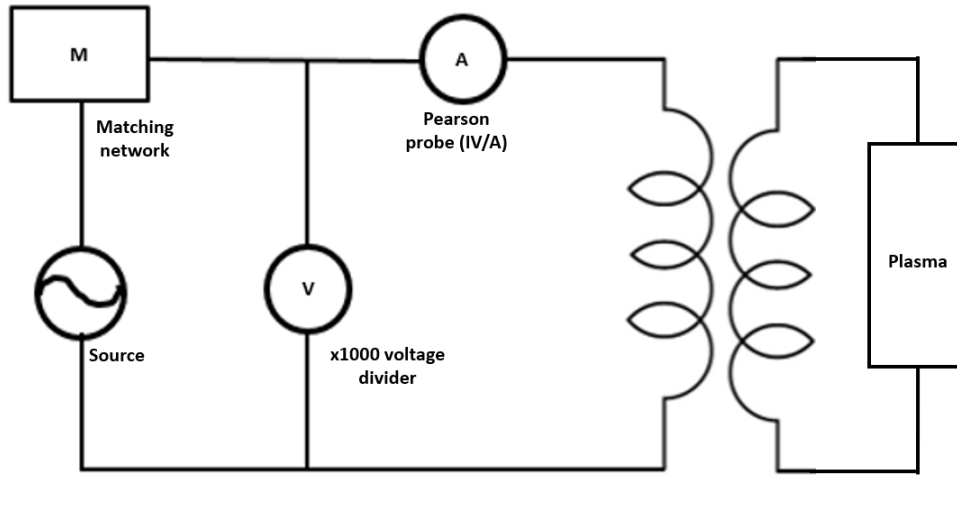
FIGURE 3.7: A schematic circuit of the experimental setup
with current (A) and voltage (V) sensors.

The voltage measured by the probe is substantially reactive (voltage and current not in phase). The forward power from the source was measured before the matching box using an Octiv RF sensor. However, reactive power $P = V_{rms}I_{rms}\sin\phi$ was not measured, therefore, the power absorbed into the plasma could not be determined. Only resistive losses along the matching network and coil were determined as a measure of power dissipation.

Thus, the calculated power losses are based on the current dissipation around the circuit. The voltage probe and Pearson probe are assumed to not dissipate power due to the high impedance and low impedance respectively. In practice, there will be some small dissipation and due to extra cables/geometry, there is some small effect on the matching. However, these are either very small or not possible to measure. The matching network losses are dominated by the connection wires (assuming ideal capacitors) and the RF resistances of these wires were calculated previously. The coil losses are the current dissipation at the inductive coil.
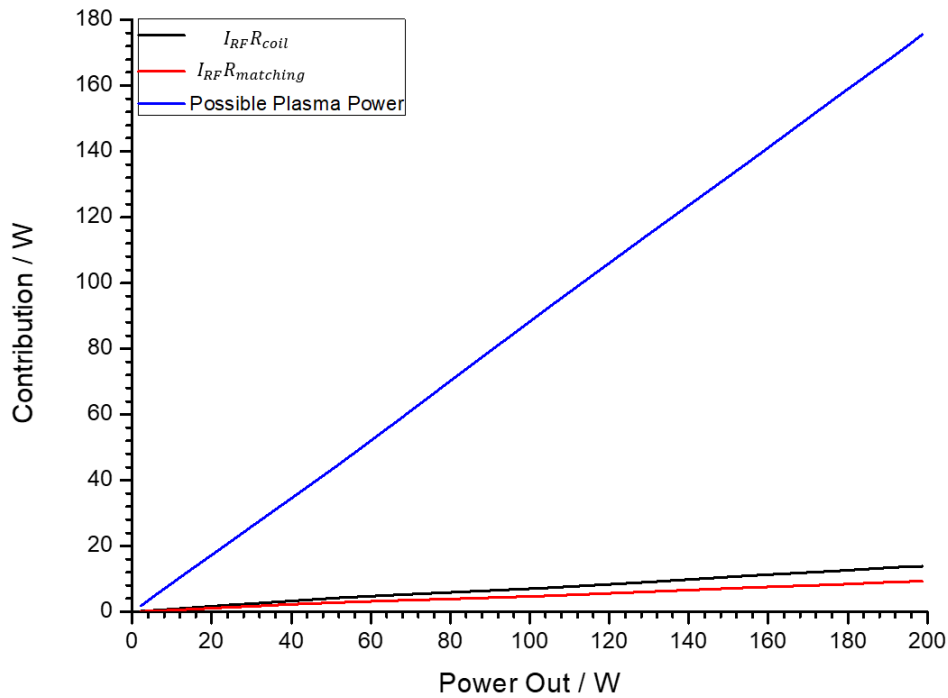
FIGURE 3.8: Total power from the source is illustrated on
the x-axis whilst this is divided into losses (coil and match-
ing circuit)/absorption (plasma) on the y-axis.

Figure 3.8 shows that as the power is varied, the losses are mostly within
the inductive coil itself and much of the power is dissipated at the plasma
itself. Water cooling prevented the heating of the copper coil and limited
thermal losses. After calculating resistive losses from the coil and wired
connections, the percentage losses versus input power are illustrated in **Fig-
ure 3.9**.
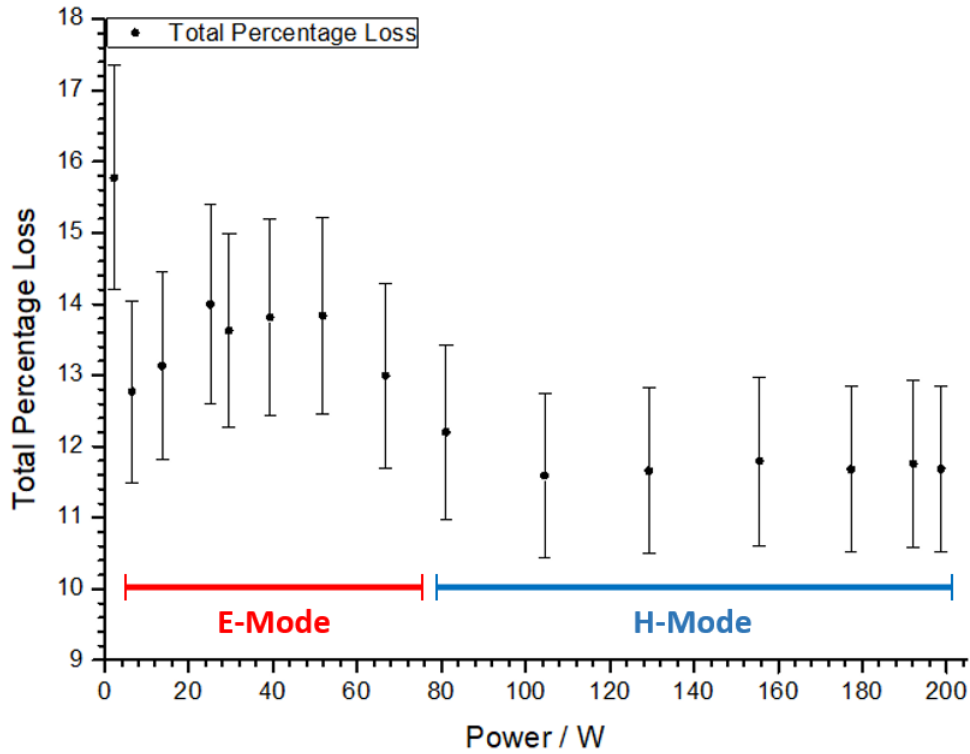
FIGURE 3.9: Percentage losses due to the coil and the matching circuit as a function of input power. It can be seen that a lower total percentage of loss of power due to resistive effects follows the transition into H-mode. H-mode is known for being a high power absorption, high density mode of operation.

A diffuse plasma was seen to be ignited as low as 2 W and this is accompanied with a higher percentage loss due to capacitive coupling. At low power, the percentage loss of power is greater. As the power is increased, the losses outside of the plasma increase (likely due to a combination of matching box heating and reflected power due to poor coupling). At the E-H transition (which is confirmed by diagnostics in **Chapter 4** to be around 70 W for an Ar plasma), it can be seen that the percentage losses are much smaller and total power losses settle at around 11% which is indicative of a high density, high power absorption ICP.

3.3   Development of a Neutralization Region

In order to generate energetic neutral particles, a scheme is needed that accelerates them as positive ions then neutralizes them. Designing conditions to achieve these processes is the focus of this section.

Ions entering a boundary sheath in which there is positive space charge will be accelerated. Accelerated ions will collide with neutral particles within the sheath volume if it extends beyond the collisional mean free path. Resonant charge-exchange interactions will occur if the ion and the neutral particle have the same mass and quantum mechanical structure. The plasma sheath could then be a source of directed, energetic neutrals if the ions have enough room to be accelerated before undergoing a charge-exchange collision. Furthermore, to maintain the integrity of the beam, any interaction with a surface must be within a further mean-free path. In practice, this is not possible unless the mean free path is of order a few Debye lengths (characteristic size of sheath) or the sheath is expanded by the application of a large bias. The probability of an ion beam being transformed into a neutral beam whilst traveling through a region of thickness x_s is:

$$P_N = 1 - e^{-\sigma_{cx} n_g x_s} \tag{3.15}$$

Where σ_{cx} is the charge-exchange cross-section and n_g is the gas density. In a 5 mTorr Ar plasma, the mean free path for charge-exchange collisions (λ_{cx}) is approximately 3 cm. Using equations **1.11 & 1.20**, the sheath scale length is of order $n\lambda_D \sim n10^{-4}$ m (n is an integer). If the plasma density $\sim 10^{17}$ m^{-3}, and sheath potential $\sim 5 - 50$V, the size of the sheath $x_s \sim (2 - 7)\lambda_D$. This means for a 5 mTorr plasma:

$$\frac{x_s}{\lambda_{cx}} \sim \frac{(2 - 7) \times 10^{-4}}{3 \times 10^{-2}} = (1 - 2) \times 10^{-2} \tag{3.16}$$

Most ions will pass through the sheath without having a collision, so the plasma sheath cannot be used to both accelerate ions and neutralize them.

Since $\lambda_{cx} \propto P^{-1}$ (mean free path depends on pressure), it would require the gas pressure be approximately 500 mTorr for the mean free path to be comparable to the sheath size. There are many consequences associated with going to such a high pressure; severe flattening of the IEDF, lower effect volume also flattens the EEDF (higher pressure plasmas are cooler) and the plasma uniformity suffers as a result. As will be seen in **Chapter 4**, high pressure plasmas have steep gradients in density sustained over a few mean free paths, which make them unsuitable for processing. Plasma uniformity is the result of the mean free paths being comparable to the system size. Therefore, the pressure is limited to 10 mTorr and below.

The very low neutralization fractions (**Figure 3.10**) at the system pressures suggest that pressure cannot be used as a parameter to affect the collisionality in the sheath.
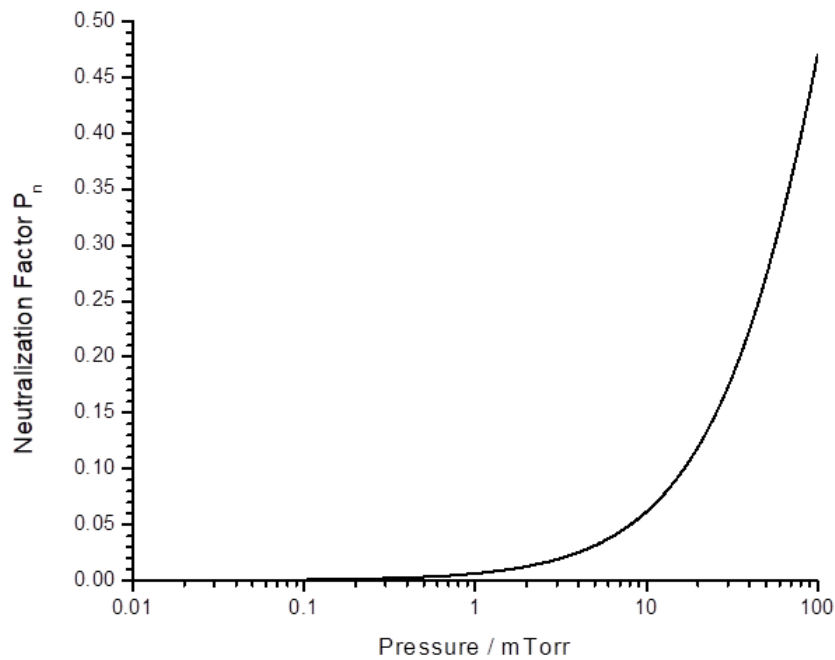
FIGURE 3.10: Fraction of ions neutralized as a function of plasma pressure.

Sheath size scales not only with λ_D but also with potential as discussed in **Chapter 1**. Therefore, rather than attempting to reduce mean free path, the sheath might instead be enlarged. In an ICP, this is achieved using DC

biasing. A simple ion-matrix sheath model (rather than Child-Langmuir) is applied here to estimate the required sheath bias. Poisson's equation with constant ion density and zero electron density in the sheath gives the sheath distance scaling as:

$$\frac{V}{x_s^2} = \frac{n_i e}{2\epsilon_0} \tag{3.17}$$

Dividing both sides by $k_B T_e / e$ and substituting for λ_D:

$$\frac{x_s}{\lambda_D} = \sqrt{\frac{2eV}{k_B T_e}} \tag{3.18}$$

It can be seen in **Figure 3.11** that in order to extend the sheath so that it is comparable to the mean free path, bias voltages become impractically large:
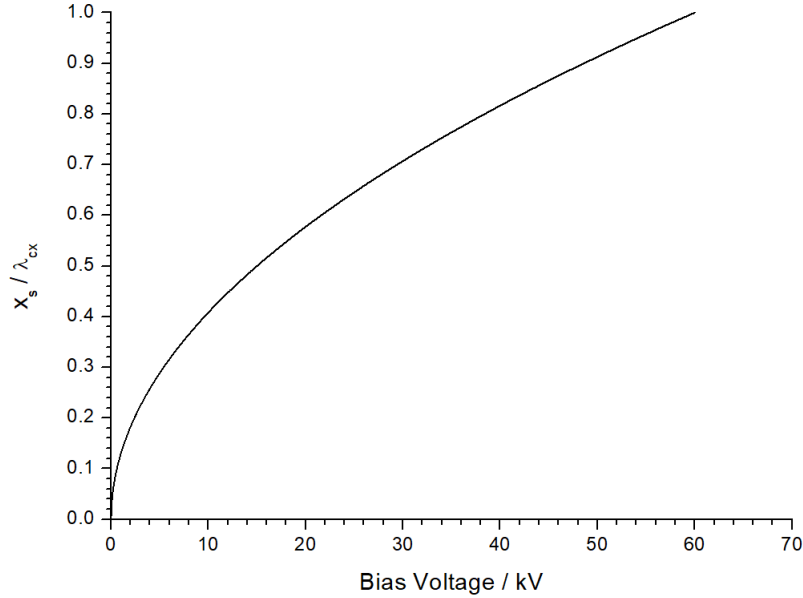
FIGURE 3.11: Ratio of sheath size to charge-exchange cross-section as a function of bias voltage.

At bias voltages more than 100 V, the ion energy becomes high enough to sputter and damages the substrate. For the 5 mTorr Ar plasma mentioned, the bias voltage needed would be 60 kV if the sheath x_s is to be comparable to λ_{cx}. Pressure variation and plasma bias variation are therefore unsuitable to control collisionality. For gas phase charge-exchange interaction, a region has to be separated and extended beyond the space charge

sheath. To realize this, an electrically grounded mesh was inserted to separate the space charge sheath from a volume of neutral gas; enabling both ion acceleration (in the sheath) in and charge-exchange neutralization (in a new external volume) as shown in**Figure 3.12**:
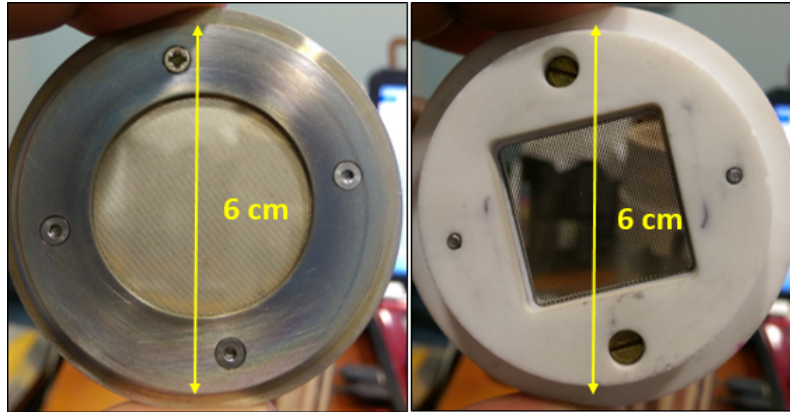
FIGURE 3.12: Photograph of steel mesh component (**left**) and ceramic double mesh component (**right**).

The grounded mesh component was installed on top of the ceramic tube to separate the plasma from a neutral volume. The distance between the mesh and the EQP was set to be in the region of the average mean free path for charge exchange between 0.1 – 10 mTorr (15 cm – 1.5 cm). The mesh hole diameter was small enough ($\sim \lambda_D$) to ensure that it did not mold the plasma potential and scatter exiting ions.
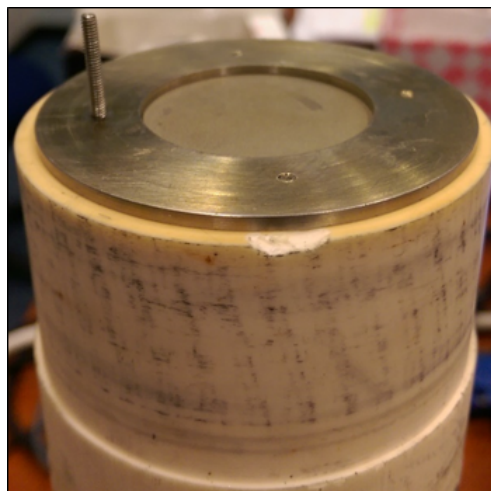
FIGURE 3.13: Photograph of steel mesh component settled on discharge alumina tube.

3.4   Summary

This chapter has introduced the construction of a bespoke ICP, created to address the research questions outlined in **Chapter 2**. The design considerations of the setup were discussed and it was found that following some power dissipation results, the setup performs as one that is well matched and dissipates most of its power into the plasma itself - the ICP has a high structural integrity. Other considerations were discussed which involve the suppression of capacitive coupling (accomplished with the physical design of a 4 turn coil and a Faraday cage), reduction of RF radiation to the user (and nearby electronic, diagnostic equipment) and the modification of the setup to perform as a source of energetic neutral beams which are crucial to this research. **Chapter 4** will now characterize the setup from the plasma perspective.

Chapter 4

Characterization of the ICP

This chapter discusses the characterization of the ICP using a variety of diagnostic techniques. A treatment of the ICP and the response of the electron temperature, plasma density and uniformity are necessary to address the the research questions outlined in the previous chapter. Variation of the plasma parameters are expected to reflect behaviours in the plasma that are well understood and replicated in other ICP discharges, such that the setup is qualified for this research. Previous thorough characterization of an ICP has been reported by Godyak *et al.* [56] (amongst many others) and the application of a variety of diagnostics to describe the plasma is presented in this chapter.

- **Hairpin Resonator Probe** - *electron number density*

- **Floating Double Probe** - *ion number density and electron temperature*

- **B-dot Probe** - *electromagnetic structure of the plasma and inference of plasma density*

- **Optical Emission Spectrometry** - *plasma composition and electron dynamics*

- **iCCD Plasma Imaging** - *visible emission structure*

4.1 The Hairpin Probe

The hairpin probe is a type of EM resonator probe used to determine electron density in its local environment. It was first introduced by Stenzel [57] and was revisited by Hebner *et al.* [58] in 2001 and further used by Piejak *et al.* [59] in 2005 and subsequently by several others. The hairpin probe measures the local dielectric properties of the plasma by creating electric standing waves of potential and current on a U-shaped wire (acting as a quarter wave resonator - see **Figure 4.1**). This has its characteristic resonant frequency dependent on the local permittivity:

$$f_0 = \frac{c}{4L\sqrt{\epsilon_r}} \tag{4.1}$$

In vacuum, the relative permittivity $\epsilon_r = 1$. In a plasma discharge, $\epsilon_r = 1 - f_p^2/f_r^2$ and the local permittivity being smaller than in vacuum, the hairpin probe resonates at a higher frequency $f = f_r$. f_r is the new resonant frequency of the probe in the presence of a plasma whilst f_p is the plasma frequency. The electron density of the plasma is related to the shift of the resonant frequency as:

$$n_e/10^{16}\text{m}^{-3} = \frac{(f_r/\text{GHz})^2 - (f_0/\text{GHz})^2}{0.81} \tag{4.2}$$

The presence of a plasma changes the permittivity of the local medium causing the probe to resonate at higher frequencies. The type of hairpin probe used was a reflection type probe:
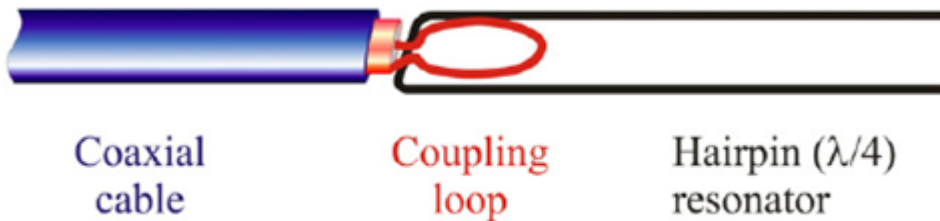
FIGURE 4.1: A schematic of a Hairpin Resonator probe.

A typical signal from the hairpin probe is given in **Figure 4.2**. The resonance peak is shifted to higher frequencies in the presence of a plasma due

to the probe attempting to radiate into its local surroundings:
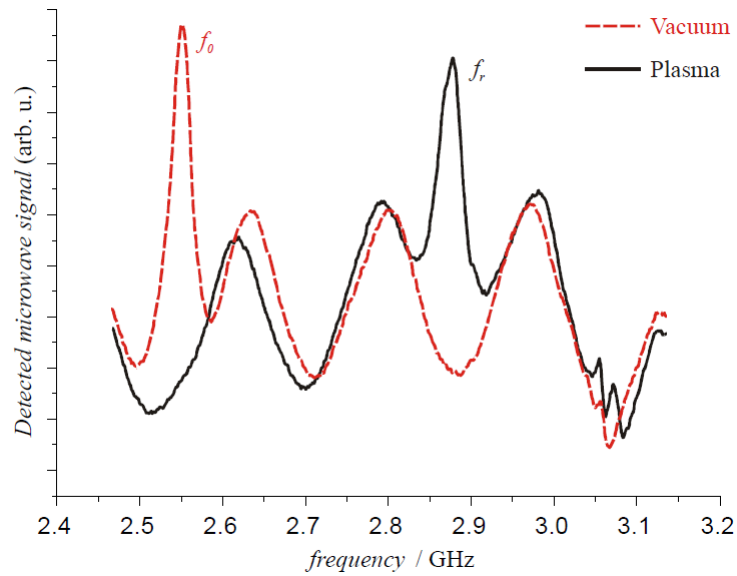
FIGURE 4.2: An adapted oscilloscope signal from the Hairpin Probe. The probe vacuum resonance frequency is shifted when immersed in a plasma. *Credit: Otell, 2013*

As electron density changes in response to changing ICP power, the permittivity of the plasma will shift the resonance and the positions of the peak can be mapped to give an account of n_e. The length of the quarter turn wave resonator was 3.21 cm which gave a vacuum resonance of $f_0 = 2.334$ GHz. This wire formed the U shape and was electromagnetically coupled to a loop of wire embedded in epoxy on the end of a coaxial cable carrying microwave signals. This loop was grounded to the outer sheath of a 50 Ω coaxial cable and connected to a circulator in a duplexer style arrangement (**Figure 4.3**) where the microwave from the source was isolated from the receiver (oscilloscope) and went to the antenna (hairpin probe). The return signal was then picked up by the oscilloscope:
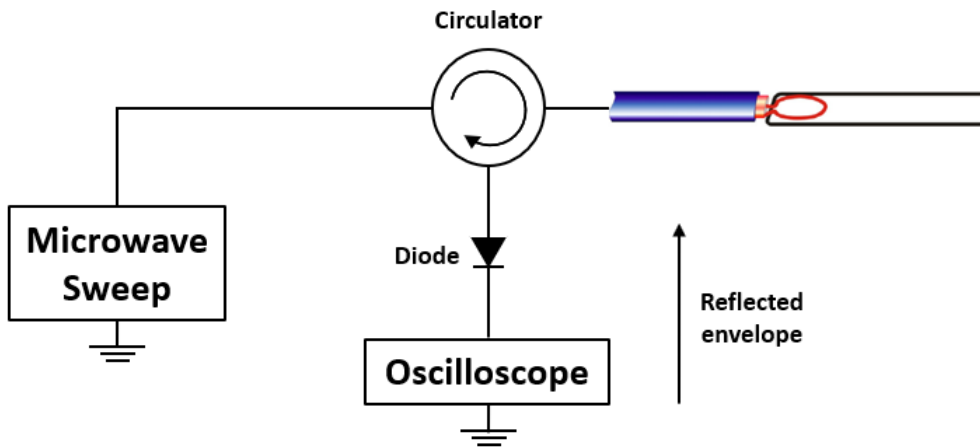
FIGURE 4.3: Circulator diagram of the Hairpin Probe

The design of the hairpin probe made it difficult to measure past 150 W in the Ar discharge due to heating of the epoxy by plasma species. Furthermore, the size of the system meant that standing waves from nearby surfaces contributed to the resonance of the probe and became inseparable at higher powers such that it was difficult to determine n_e. This was alleviated by placing the probe 10 mm below the bottom coil (this position is referred to as region "p" and is also where the double probe was stationed and where some B-dot probe measurements were extrapolated for comparison) where the plasma density was lower and interference was mitigated due to a slightly larger volume. The compromise was that the probe response in Ar did not accurately reflect the electron increase as the probe was not situated in the midplane of the coils. Past 150 W, it became difficult to resolve the resonance peak from the background.

Figure 4.4 shows the electron densities of an Ar plasma at different pressures with variable power:
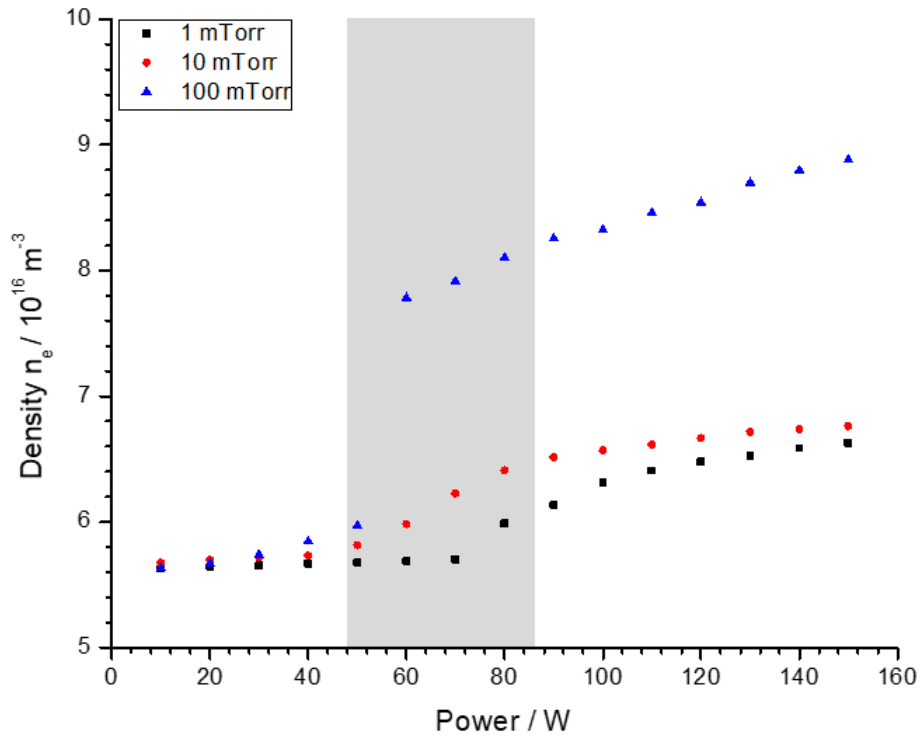
FIGURE 4.4: Electron density in Ar varied with power. The region of transition into H-mode is highlighted in grey.

The low power, low density (capacitive) regime is shown in more detail in **Figure 4.5**:
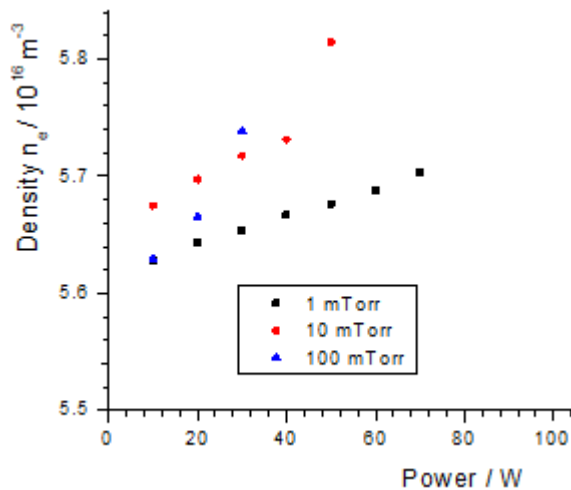
FIGURE 4.5: Low linear variation of electron density with power at low power.

The capacitive mode occurs when the electric field between the ground

and live coils dominates the power absorption into the plasma, this is re-
flected in **Figure 4.4 & 4.5** by lower density below 60 W. During the ini-
tial phase of breakdown where the axial field (of order of the coil voltage
and live to ground coil separation) transfers enough energy to electrons
for breakdown. Due to ionizations taking place along the axial direction,
this results in the development of diffuse discharges that are defined by
low density and low power absorption. The high density mode (H-Mode)
follows the development of an azimuthally induced electric field which
serves to localize the plasma within the coils themselves. The E-H tran-
sition (shown in **Figure 4.4** by the step into higher density) describes the
power range at which the magnetic field begins to dominate over the ca-
pacitive electric field.

Figure 4.6 shows an O_2 discharge at varying pressure and power.
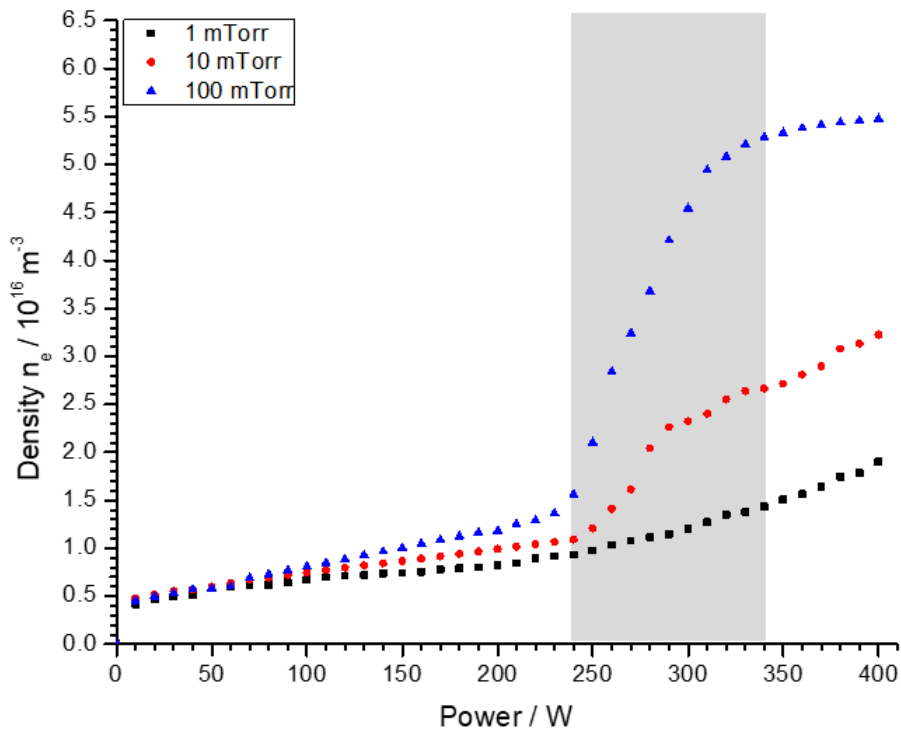
FIGURE 4.6: Electron density in O_2 varied with power. The
region of transition into H-mode is highlighted in grey.

The power was extended to 400 W when no obvious E-H transition

was noticed < 150 W. The lower electron density is a result of the quasi-neutrality condition not only having an electron contribution but a negative ion contribution such that $n_{i+} = n_{i-} + n_e$ although the ion density was not measured. It is also more difficult to have a high density molecular discharge due to recombination effects (particularly in the region "p" where there is lower power absorption), multistep processes and molecular excitations that allow energy losses. Compared to Ar however, the O_2 discharge shows a greater separation of pressure and does not overestimate the density at very low power. The density at 100 mTorr is almost an order of magnitude higher than that at 1 mTorr at 400 W of power. There is no marked transition in the 1 mTorr case although upon closer inspection, there is a small transition around 250 W. It is likely that placing the probe at the centre of the discharge would record a higher high density at 100 mTorr.

The results of both Ar and O_2 showcase average electron densities $0.5 \times 10^{16} \, \text{m}^{-3} \leq n_e \leq 10 \times 10^{16} \, \text{m}^{-3}$ which are comparable to other work reported by Corr *et al.* [60] who recorded densities of O_2 using a Langmuir probe in a 13.56 MHz inductively coupled GEC (flat spiral coil). Electron densities of $10^{16} - 10^{17} \, \text{m}^{-3}$ were reported in the high density regime and $10^{14} \, \text{m}^{-3}$ in the lower density regime. It is noted that the use of Langmuir probes typically underestimate the plasma density and the accuracy of the I-V curve is dependent on a number of factors which include plasma uniformity. The use of a Langmuir probe allowed Wang *et al.* [61] reported Ar electron densities of up to 2 x 10^{16} m^{-3} (at E-H transition) at pressures between 1 and 10 mTorr using microwave interferometry 3 cm above the inductive coil. This was only achieved however with powers approaching 700 W suggesting a very low gas flow rate or low power density (estimated as 15 x 10^3 W m^{-3} as opposed to 950 x 10^3 W m^{-3} at the same power for the setup used in this thesis) as a result of a larger system size. Higher pressures (> 100 mTorr) achieved H-mode at 200 W, with electron densities surpassing 10^{17} m^{-3} whilst also exhibiting hysteresis as the power was decreased. Hysteresis effects are only noticeable at higher pressures where multistep

ionization becomes more prominent and allows sustaining of the discharge by recycling excitation energy into ionization. At very low pressures/low gas density [62], E-H transition is not seen and instead the electron density varies linearly with power as observed in the very low pressure regime of the Ar and O_2 discharges.

Issues with this measurement technique may result from the fact that a sheath x_s of a few λ_D will have formed on the wires. However, this can be ignored when the radius of the sheaths around the wires are much less than the separation of the individual wires. The radius of the wire was 0.1 mm and a floating sheath would have formed around it. The distance between the wires was 1.5 cm. The probe recorded average densities approaching 10^{17} m^{-3} where any sheath formed was not comparable to the distance between the wires (1.5 cm $\gg x_s$). Therefore, the application of a sheath correction (Piejak, 2005) was not necessary. The exception is at low power where the capacitive mode was speculated to have overestimated the electron density and a large sheath would have formed on the probe tips particularly in the Ar discharge. As such, even though a discharge is seen at power as low as 2.8 W, the densities recorded at that power are likely lower by a factor of 100 based on [61]. A distance profile of the electron density in the axial direction of the plasma was not possible due to degradation of the probe. It can however be accurately inferred that had the probe been situated in the mid-plane of the ICP, electron densities more than 1 x 10^{17} m^{-3} at comparatively high power would have been recorded. Other diagnostic measurements have been able to record an axial profile instead.

4.2 The Floating Double Probe

Standard single electrode Langmuir probes measure plasma characteristics based upon the most positive electrode that the plasma can contact. However, without a reference electrode, these sorts of measurements can be misleading. Johnson & Malter [63] discussed the development of a floating double probe in place of a single Langmuir probe within a decaying plasma and in situations where a large single probe area draws so much electron current that it perturbs the plasma. For the purposes of this thesis, a double probe was primarily employed due to physical constraints preventing the use of a sufficiently larger reference electrode within the ceramic tube of the ICP. The double probe overcomes the need for a large reference area by employing two collection surfaces within the same region of plasma.

The double probe features two electrodes which are biased relative to each other and without bias, remain not very far above floating potential V_f (they will be negative with respect to the plasma). There is no net current drawn by the probe. Except for extremely low pressure discharges (which are not useful for processing), $T_i < T_e$ and the probe characteristics look similar to that of a single langmuir probe. The net current through the probe is expressed as:

$$I = I_1 + I_2 = 0 \tag{4.3}$$

Where I_1 and I_2 are the two respective probe tips drawing electron and ion current current. If the probes are biased, I_1 and I_2 are expressed as:

$$I_{i0} + I_{e0}\left(-\frac{eV_1}{k_b T_e}\right) + I_{i0} + I_{e0}\left(-\frac{eV_2}{k_b T_e}\right) = 0 \tag{4.4}$$

Again, no net current is drawn by the probe, this means that $I_{i0} = -I_{e0}$. The expression is reduced to:

$$I = I_{i0}\tanh\left(-\frac{eV_b}{2k_b T_e}\right) \tag{4.5}$$

Where V_b is the bias voltage $(V_2 - V_1)$ and the actual electron energy is found from:

$$\frac{k_b T_e}{e} = \frac{I_{sat}}{2\frac{dI}{dV}|_{V=0}} \tag{4.6}$$

A full evaluation of the probe theory is found in [5, 6] which are Pascal & Braithwaite and Liberman & Litchenberg respectively.

A double probe was inserted in the region "p" of the ICP in the inductive mode of a 150 W Ar plasma with pressure varied between $1 - 100$ mTorr. This position was chosen to avoid overheating and oversaturation of the probe. Electrostatic probe diagnostics can often be difficult to employ in RF environments. RF pickup along the probe was reduced with a coaxial sheath along the length of the probe wires. Further suppression of RF pickup and capacitive coupling was achieved by wrapping the probe wires around a soft solenoid (RF choke) just before the measuring instrument. The total cylindrical collection area per probe tip was 4.25 x 10^{-6} m^2. For the purposes of a neutral beam source, the double probe is a very suitable technique. Due to it being inserted at region "p" (far from the bulk), the floating double probe ends up giving an account of the electron energy closer to the tail of the distribution where they are likely to have energy close to ionization potential.

As a note, the Debye length of the plasma in the 1 mTorr case was ~ 0.15 x 10^{-3} m. The radii r_p of the tungsten probe tips were 0.25 x 10^{-3} m and as $r_p \sim \lambda_D$, a thick sheath hypothesis is considered [64]. The ion collection is therefore considered with cylindrical geometry (Allen-Boyd-Reynolds) and ions are drawn radially inwards to the probe surface - which ends up underestimating the ion saturation current. Consideration of the ion orbital motion within the sheath of the probe tip would correct this, but increases the complexity of the result.

Figure 4.7 illustrates the double probe characteristic of the ICP at three different pressures at constant power:
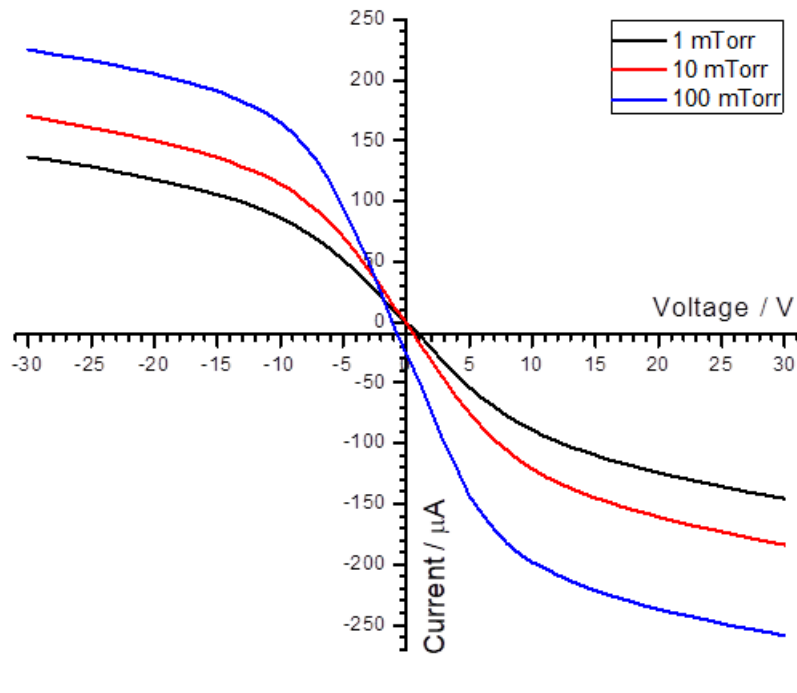
FIGURE 4.7: Double probe I-V curve as a function of pressure.

Differentiating the result (for example at 10 mTorr) indicates that the current to the probe doesn't accelerate past 20 V, suggesting that the plasma potential V_p is around that value. More accurate determinations of V_p are found in **Chapter 6** however with the use of the EQP. The saturation current was determined from the intersection of the two slopes (one from the plateau and the other from $\frac{dI}{dV}|_{V=0}$) shown in **Figure 4.8**:

The intercept method where the saturation current is determined close to the knee by the intercept of the two linear contributions
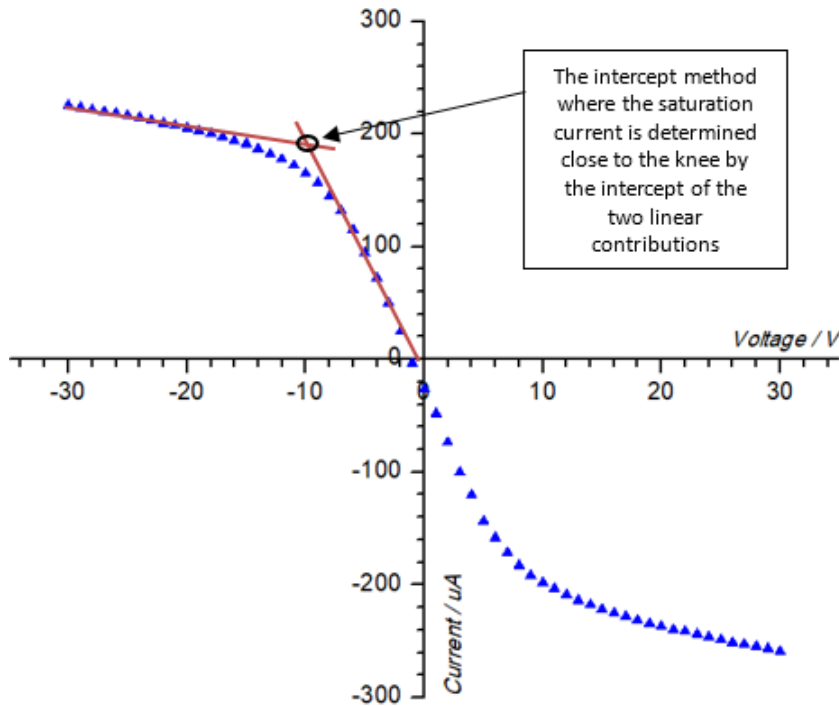
FIGURE 4.8: Intercept method used to determine the saturation current (Ar 100 mTorr)

Increasing the gas pressure results in a decrease of the mean free path for collisions. Although the plasma inevitably becomes cooler, the increased collision frequency encourages the generation of more ions from volume ionization assuming the power density remains high enough to sustain a discharge. At higher pressure (100 mTorr), λ_D is far less than r_p radius of the probe and the sheath looks thin. The transition from a thick sheath to a thin sheath with increased pressure is worth considering. In the thick sheath case ($\lambda_D \sim r_p$ at 1 mTorr) ions enter the sheath with a Bohm velocity and the ion flux to the probe gives a measurment of the plasma density. At higher pressure, the thin sheath ($\lambda_D \ll r_p$) gives the impression that the probe is in the bulk of the plasma and might encourage a collection of ion current such that the plasma is perturbed - this is generally mitigated by the inherent design of the double probe. Ions will no longer be collected with a large Bohm velocity as the scale length of λ_D is much lower and represents a lower bulk temperature. Otherwise, the steep density gradient at higher pressure implies that the density in region "p" will not be much greater than that in the lower pressure case. The ions will appear colder and the ion flux

to the probe is therefore not significantly higher. This means that a factor of 10 - 100 difference between pressure only nets a factor of 2 difference in the ion saturation current as seen in **Figure 4.7**.

	1 mTorr	10 mTorr	100 mTorr
Tail Electron Energy / eV	9.02	8.35	7.41
Saturation Current / μA	95.98	125.67	180.9
Edge Plasma Density / m^{-3}	3.03 x 10^{16}	4.13 x 10^{16}	6.31 x 10^{16}
Hairpin Probe Plasma Density / m^{-3}	6.63 x 10^{16}	6.67 x 10^{16}	8.88 x 10^{16}

TABLE 4.1: Comparison of Hairpin and Double Probe Values at different pressures. Taking the square root of the electron energy suggests average T_e 2 - 3 eV.

The plasma density at the edge of the sheath was then calculated using:

$$I_{sat} = e n_s c_s A \tag{4.7}$$

Table 4.1 shows the determined values of electron energy in the tail of the distribution, the density at the edge of the plasma and the comparison with Hairpin probe results at 150 W. Because the density determined is actually that at the plasma boundary, at low pressure, the density is approximately doubled in the bulk if the edge-to-centre ratio is taken as 0.5 [5]. The results were then modeled after a hyperbolic tangent.

$$f(x) = -\left[I_{sat} \times \tanh\left(\frac{V_b}{k_b T_e}\right)\right] - \alpha V_b \tag{4.8}$$

Where α is a fitting constant. In the case of 100 mTorr (**Figure 4.9**), because interference had shifted the original distribution from 0, the model had to also be shifted by a 20 μA in the y direction. This was due to a combination of RF interference and asymmetrical probe tips. The models show that there is small asymmetry in the current values and this can be attributed to the fact that the probe tips are not perfectly symmetrical. This asymmetry is less pronounced at 100 mTorr where large currents to the probe tips are expected.
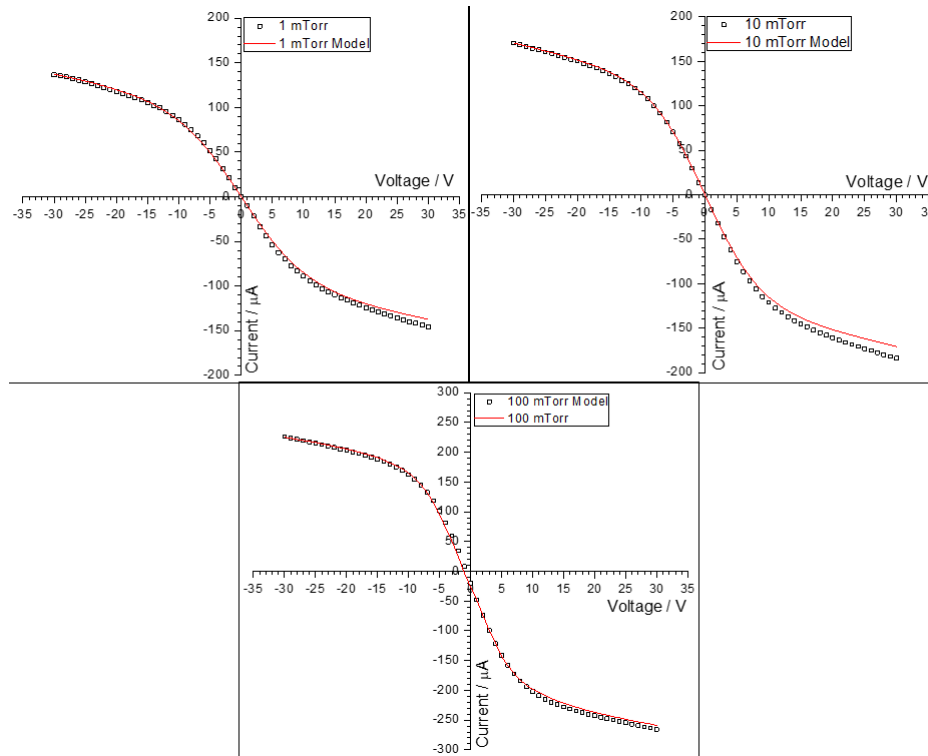
FIGURE 4.9: Double probe characteristics with hyperbolic
tangent fitting

Aside from slight asymmetry in the probe geometry, the results showed good agreement with the Hairpin density results to within a factor of 2 - 3. Due to the position of the probe away from the central discharge, the electron temperature T_e measured are actually closer to the tail of the electron energy distribution. Taking the square root of these energies suggest average T_e between 2 eV and 3 eV.

Various factors can affect the fidelity of the probe characteristic [65], such as probe size, circuit resistance and plasma/RF phenomena although many of these were accounted for. Comparison with previous hairpin results in the PL-80 (O'Tell, 2014) were in good agreement.

4.3 The B-dot Probe

The B-dot probe is an electrical diagnostic technique used to measure time varying magnetic fields. Its use in an ICP allows one to see the influence of plasma current. A B-dot probe features one or more loops which couple to the time varying total magnetic field to induce a voltage in proportion to $\frac{dB}{dt}$. The probe is very useful for characterizing highly symmetrical systems such as ICPs and examples of such application are found in the literature Piejak *et al.* [66, 67]. Results include a mapping of the electromagnetic fields radially and axially, and a determination of the plasma current from the outer edge of the discharge towards the centre. The plasma current was then used to infer plasma density values which were compared with other measuring techniques such as the resonant hairpin probe and floating double probe. Other plasma parameters such as skin depth and plasma conductivity were also calculated.
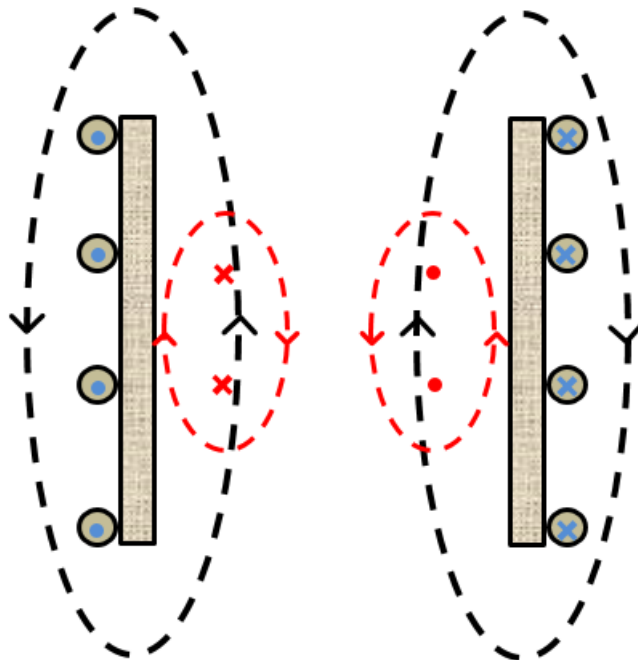
FIGURE 4.10: Schematic of induced current and field in an ICP. Induced current in red travels in the opposite direction to the coil current in black.

An ICP running in H-mode produces an axial time varying B-field which in turn induces an azimuthal (θ direction) electric field which drives plasma

current in that same direction (J_θ). Referring to Amperes Law, the current passing through a closed loop is related to the total integrated magnetic field around that loop. The plasma current will induce B-field in the z direction to oppose the coil's field (**Figure 4.10**). Because the plasma is formed as a result of induction, its existence should serve to oppose the change of that which induced it - that is, the plasma current flows in the direction opposite to the coil current. An expression of this plasma B-field is:

$$\oint \tilde{\underline{B}}_p \cdot \underline{dl} = \mu_0 \tilde{I}_p \tag{4.9}$$

Where the subscript p represents the plasma and the path encloses the current between $r = 0$ and $r = r_c$ for axial slices of Z. The net field along the axial path is given by:

$$\oint \tilde{\underline{B}} \cdot \underline{l}_0 = \mu_0(\tilde{I}_c - \tilde{I}_p) \tag{4.10}$$
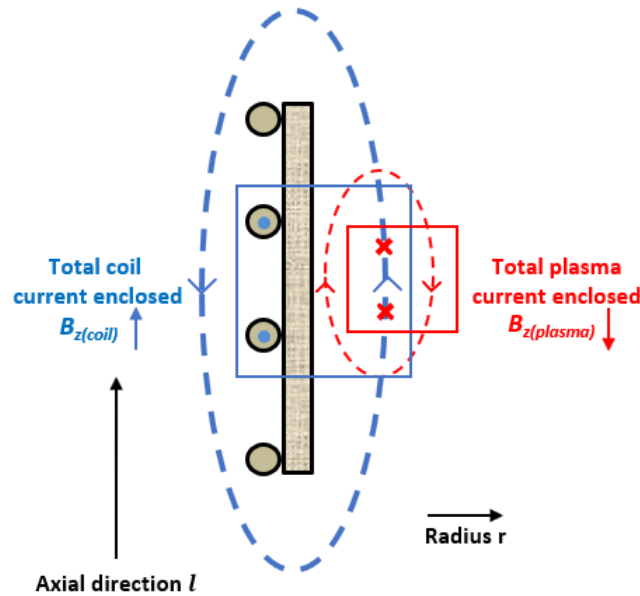
FIGURE 4.11: Illustration of the B-dot response as the total sum of the external coil current field and plasma current field.

The B-dot probe picks up the resultant B-field and would only be able to provide a value of the plasma B-field if the coil field was known prior in vacuum. This required a method in several steps:

1. The vacuum field was measured along z (*l* in **Figure 4.11**) and r with the B-dot probe. Experimental results confirmed that the vacuum field does not attenuate within the geometry of the ICP tube and is in fact constant along r.

2. Measurements were calibrated using a DC power supply and a Hall probe. A DC current of 10 A was passed through the coil and the resulting B-field (in the central coil region) was measured as 0.432 mT with the Hall probe. The B-field of a 10 A RF current in the coil was also measured as 0.432 mT. This is consistent with Pearson current probe measurements where at 200 W, the measured coil current was 14 A and the external B field in vacuum measured with the B-dot probe as approximately 0.6 mT.

3. The change in the B-field was recorded when the plasma was ignited. The plasma current was then derived from the difference and this enabled a measurement of the plasma density resolved along both Z and r.

In the vacuum case, the B-field from the coil in the central axial zone is constant across r when measuring within the coil. When taking measurements close to the top and bottom of the ICP, contributions of $\frac{dB_z}{dr}$ and $\frac{dB_r}{dz}$ which arise due to field curvature become more significant. In a low pressure plasma medium, the B-field decays exponentially within a collisionless skin-depth δ:

$$\delta = \frac{c}{\omega_p} \tag{4.11}$$

Manipulation of electron particle momentum equation gives the electron drift velocity v_d as:

$$v_d = \frac{e}{m} \frac{1}{\left(-i\omega + \nu_m\right)} E \tag{4.12}$$

Where ν_m is the collisionality. If $\nu_m \gg \omega$, then the result is similar to the treatment of RF in metals. If $\nu_m \ll \omega$, the skin depth simplifies to a collisionless case used in low pressure plasmas $\leq$ a few 10s of mTorr.

The B-dot response (in volts) is related to the axial B-field via Faraday's law:

$$|V| = |NA\frac{\partial B}{\partial t}| = \omega NA|B_z| \qquad (4.13)$$

Where N is the number of loops on the B-dot probe and ω is the RF frequency. For this experimental setup, V = 7274.88 $\times B_z$. 3 turns in the loop (radius 0.003 m) were chosen for a large enough signal to be recorded on the oscilloscope without greatly perturbing the plasma region. B_z is chosen as the system is axially symmetric and the structure of the probe is only sensitive along the axis. It was physically not possible to measure B_r due to the geometry of the ICP. However because the probe was constructed to be off centre but parallel to the z axis, it could be rotated along an arc to give a B_z response that varies as r which happens to be equivalent to the angle of rotation as:

$$d = 2r\sin(\frac{\alpha}{2}) \qquad (4.14)$$

Where d is taken to be the distance along the radius, α is the angle of rotation and r is below half the nominal radius (0.0125 m) due to design constraints. A schematic of the 3 turn loop B-dot probe arrangement is given in **Figure 4.12**:
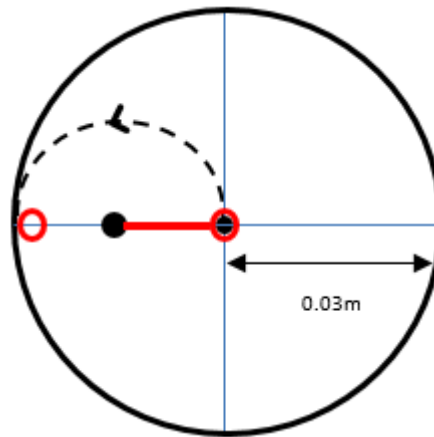
FIGURE 4.12: Schematic of the B-dot probe being rotated within the discharge. As the probe is rotated perpendicular to the z-direction, the loops sweep through r from the middle of the discharge to the edge.

The probe was rotated about its position and the angle of rotation was

translated into a radius. The probe was used to obtain instantaneous magnetic field values (B$_z$) that translated into a measurement of electric field, plasma current, density and a measure of the plasma conductivity and skin depth.

A 200 W, 1 mTorr Ar plasma was ignited and the B-dot probe was translated along z and rotated parallel to z to produce B_z values as a function of r and z as shown in **Figure 4.13**:
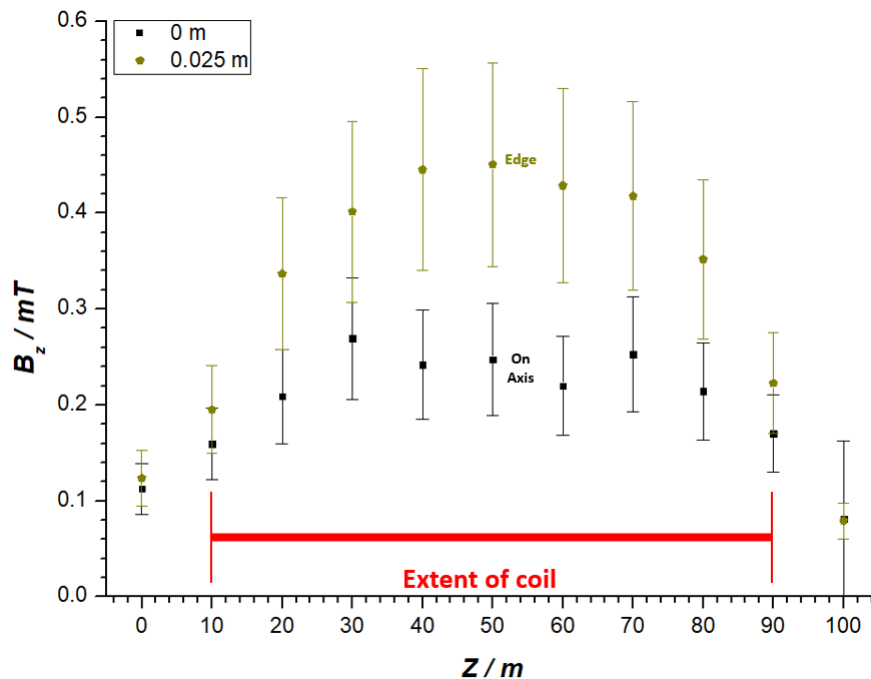
FIGURE 4.13: B-dot response obtained for the edge and centre of the discharge as the height z is varied.

Due to the solenoidal shape of the B-field produced by the RF excitation of the coil, the axial component is strongest towards the middle of z (0.04 – 0.06 m) and weakest at the ends – this is more pronounced at the larger radius of 0.025 m. The B_z component at 0.025 m rises strongly inside the coil and remains fairly steady ($\pm$ 5%) within it. The structure is symmetrical about the axial mid-plane. Piejak *et al.* [68] note that in an axially symmetric system, curvature at the ends (where $B_r \neq 0$) does not invalidate analysis based on the measured B_z values. The assumption that $\frac{dB_r}{dz} \sim 0$, is valid only in the axial mid-plane. Elsewhere, the field is solenoidal. Apparent

structure seen in the mid-plane near the axis of the discharge is attributed to possible misalignment of the B-dot probe at larger z and imperfect coil geometry.
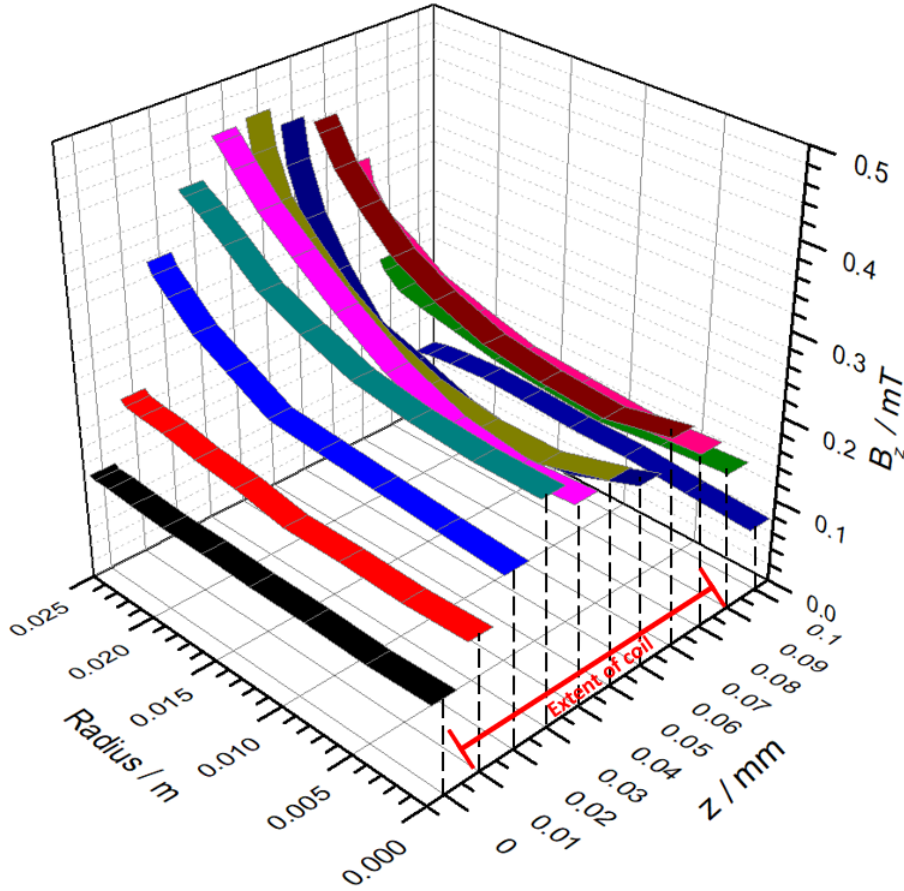
FIGURE 4.14: 3D ribbon of B_z in the discharge with varying radius at different height z.

Figure 4.14 shows the measured B_z component over a range of r and z. It can be seen that B_z is greatest towards the middle of the coil nearest to the wall. At axis, B_z is low. Note that for z = 0.1 m the probe was fully extended into the ICP tube and the larger uncertainty in r at that height may be the origin of apparent structure in the B_z symmetry that B_z increases on moving radially inwards from the wall (unphysical).

Due the B-dot probe being unable to fully rotate to 0.03 m (inner radius of the chamber), the above results were modelled using a third order polynomial and the boundary condition set to have B_z at the wall equal to the

vacuum field. There is little to no plasma at the wall (within a sheath x_s). By using the Child-Langmuir relation (**Equation 1.20**) one can approximate the sheath at the dielectric tube. Assuming a standard plasma potential of 25 V and a Debye length calculated for an $n_e \sim 10^{17} \mathrm{m}^{-3}$ as $\sim 0.5 \times 10^{-4}$ m, a suitable scale for the sheath at the wall gives a value for the sheath as $\sim 2 \times 10^{-4}$ m. Within 0.001 m (or half that) of the wall, the external field should remain approximately constant before being affected by any induced plasma currents.
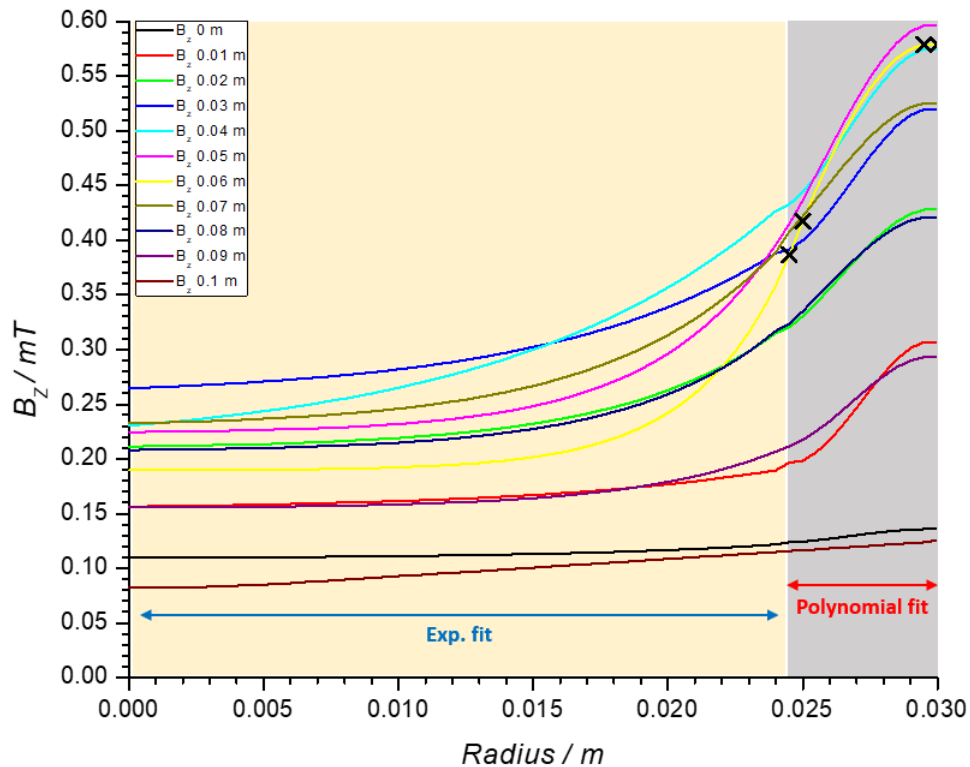
FIGURE 4.15: Modelled B-dot probe responses at varying z and r. X's refer to 4 points used for 3rd order polynomial fitting due to the wall of the discharge. The response rises to vacuum field as the wall is reached whilst the exponential behaviour within the discharge showcases the attenution of the vacuum field.

In **Figure 4.15** the grey region signifies the polynomial model and the rest of the response is the data fitted to an exponential decay. At Z = 0.1 mm the fitting fails due to an aberration in the field measured near the wall and at the extremity of the axial direction. However, the field must rise to the measured vacuum field, so instead a linear relationship was used for

completion.

A case can be made for the validity of these models so long as they are within acceptable error boundaries. The uncertainty in B_z was determined from uncertainty in the radius of the probe loop (Δb) and the measured oscilloscope voltage (ΔV):

$$\Delta B = B_z \sqrt{2\left(\frac{\Delta b}{b}\right)^2 + \left(\frac{\Delta V}{V}\right)^2} \tag{4.15}$$

The error in radial position was both a function of the size of the probe loop and the uncertainty in rotation angle:

$$\Delta r = b + r \sqrt{\left(\frac{\Delta l}{l}\right)^2 + \left(\cos\frac{\alpha}{2} \cdot \frac{\Delta \alpha}{\alpha}\right)^2} \tag{4.16}$$

Where $\Delta \alpha$ is found from the Taylor expansion of the rotation angle and b is the radius of the probe loop. It was seen that the error in the radial position of the probe is dominated by the radius of the B-dot probe loop. This however was a compromise as although a smaller B-dot loop area would reduce the uncertainty in radial position, the response of the probe would have been lessened and a much larger scanning range would have been required.

The response of the B-dot probe with uncertainties and arranged in symmetry is shown in **Figure 4.16 - 4.21**:
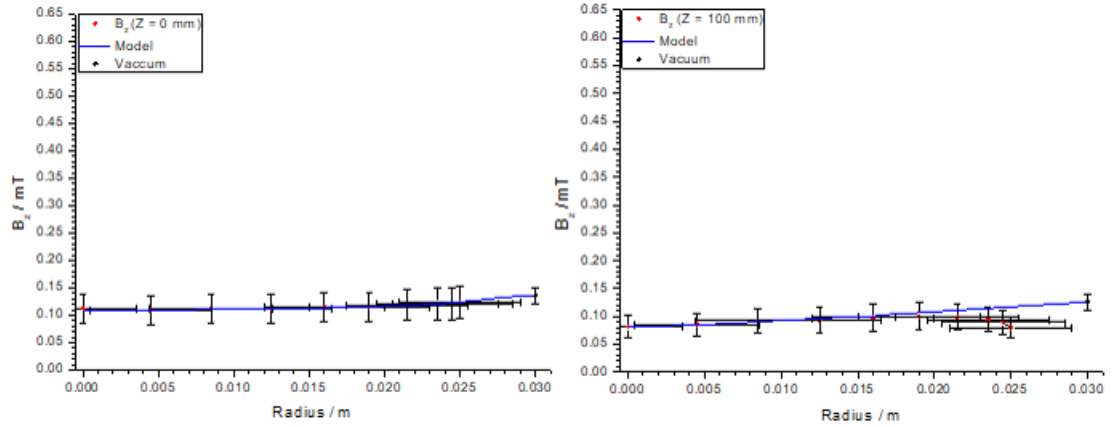
FIGURE 4.16: Z = 0 & 0.1 m
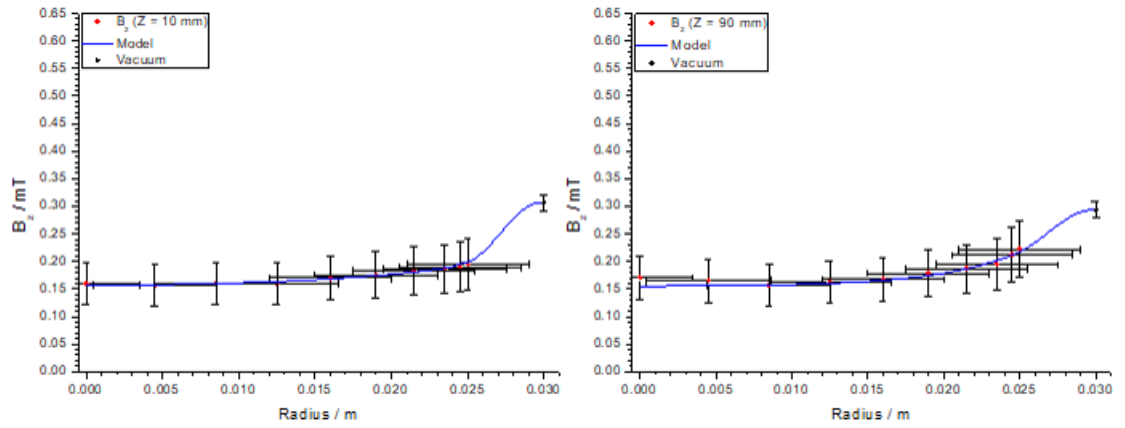
FIGURE 4.17: Z = 0.01 & 0.09 m
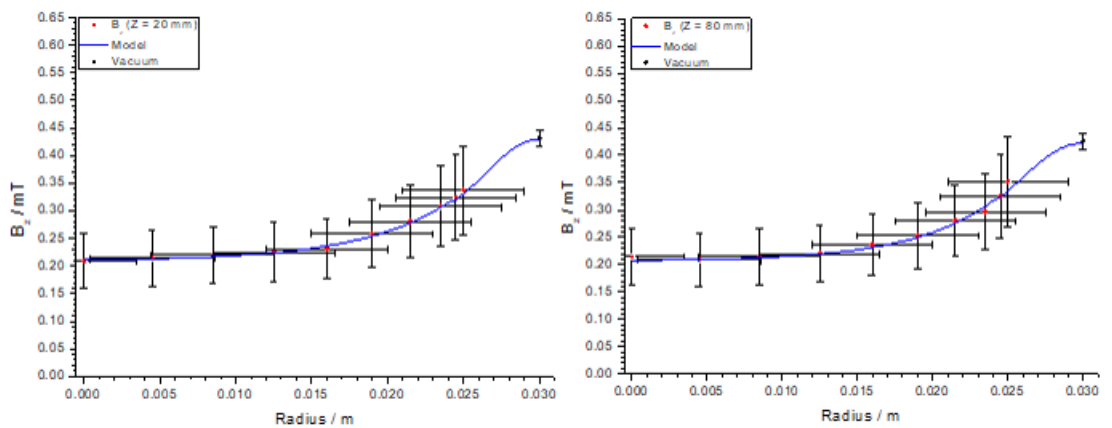
FIGURE 4.18: Z = 0.02 & 0.08 m
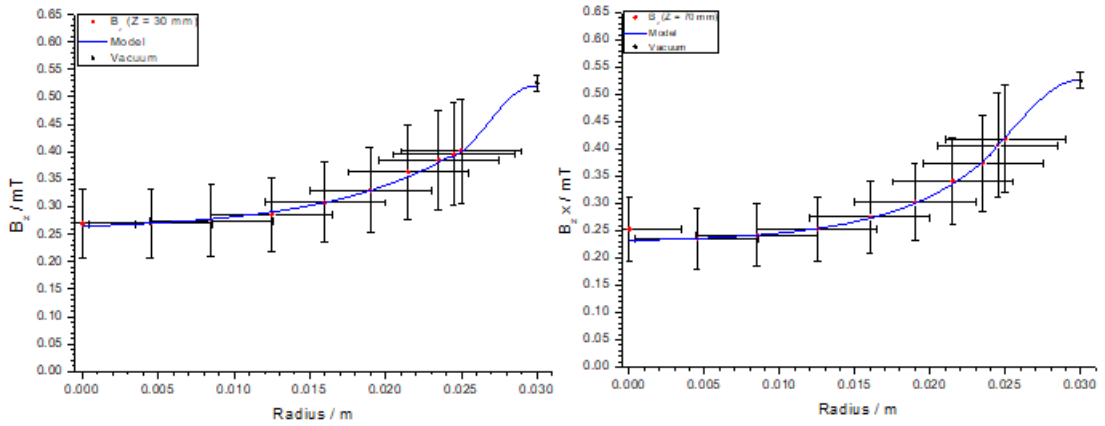
FIGURE 4.19: Z = 0.03 & 0.07 m
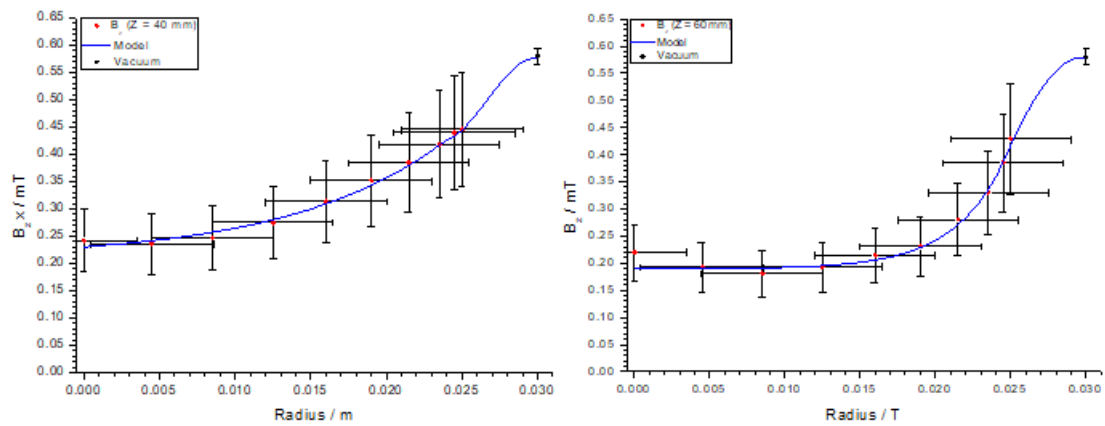
FIGURE 4.20: Z = 0.04 & 0.06 m
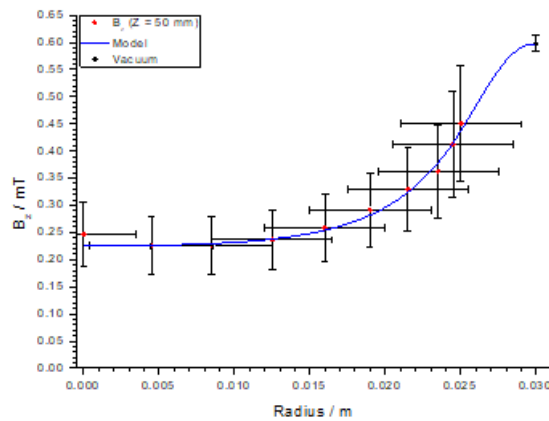
FIGURE 4.21: Z = 0.05 m

At the extremities of the coil, there is asymmetry where the probe responses at opposite axis of the coil are not identical. This suggests a coil that is either slightly misshapen or not perfectly equidistant around the ceramic

tube. However, as the probe sweeps through the middle of the discharge, this asymmetry is less apparent.

The induced plasma current at each step along the axis was deduced from Ampére's law using an integration path from the wall to the axis, up a small increment z, back out radially to the wall, down the wall and back to the start. This has been illustrated in **Figure 4.11**. The plasma current thereby enclosed is shown in **Figure 4.22**:

(A) Plasma current varying as Z.

(B) Schematic of incremental current calculation.
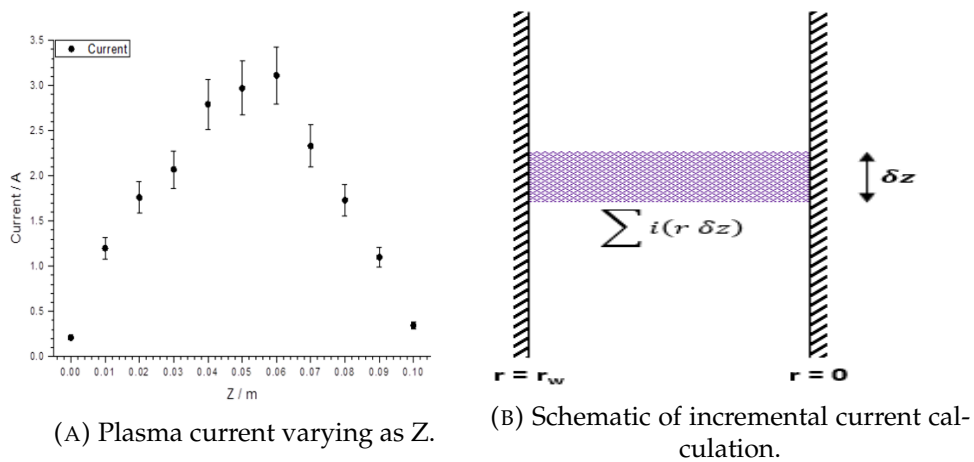
FIGURE 4.22: Plasma current calculated from the B-dot response varying as z and schematic of current increment

The coil current at 200 W was measured as 14 A. It can be seen that at every point along the axial direction, the total plasma current is less than the coil current. The total current enclosed by an Ampére's law pataroundt the 4 turn coil is therefore 64 A. The total plasma current enclosed along z for an Ampére's law path in the presence of the plasma and enclosing on the plasma current (but not the coil) was calculated to be 19.62 A. This corresponds to approximately a third of the Ampére turns of coil current and is consistent with the observation that the mean axial field within the coil is about a third of the vacuum.

A measure of the plasma skin depth was obtained by inferring the electric field in the plasma. Faraday's Law can be re-written in terms of the

azimuthal (θ) electric field and expanded as:

$$E_\theta(r_0) = \frac{\omega}{r_0} \int_0^{r_0} B_z r \, dr \qquad (4.17)$$

This enables a determination of the response of the azimuthal eletric field decaying from the edge of the ICP tube to the centre:
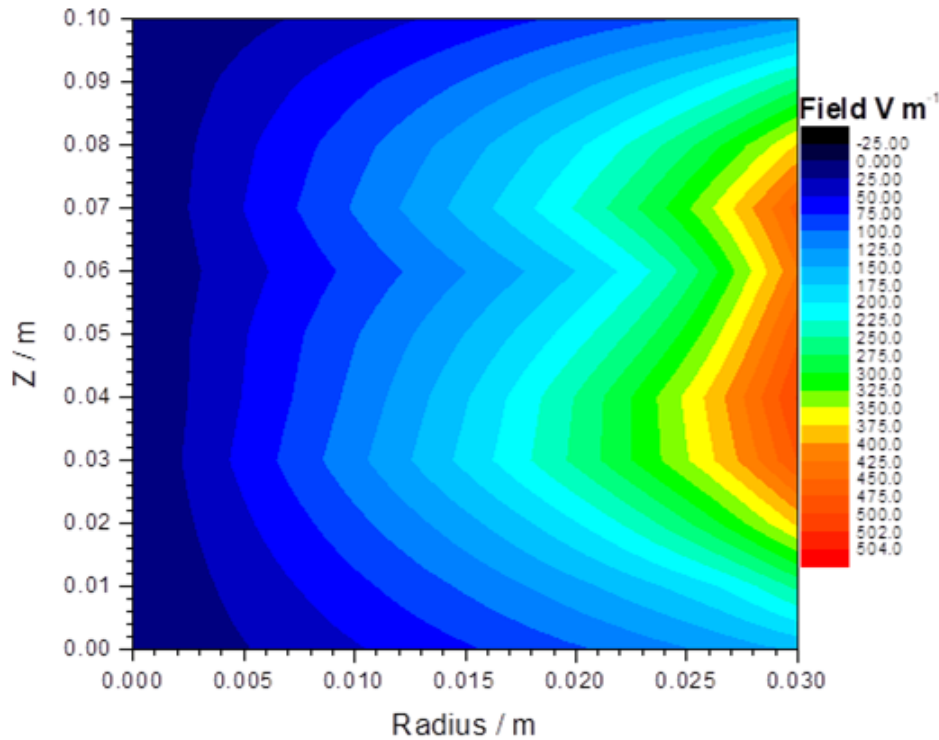
FIGURE 4.23: Contour map of electric field. The azimuthal (induced) electric field is greatest nearest to the coils and decays within a skin depth towards the centre of the discharge.

Figure 4.23 was based upon 60 x 11 data points evenly distributed in radial and axial positions. The apparent distortion of the field towards the mid-point can be attributed to a combination of measurement uncertainty at that particular height Z and imperfect coil geometry. Closer towards the centre of the plasma, this imperfection is smoothed out.

Figure 4.24 agrees with that found in the literature [5]. At very low densities and approaching vacuum, the electric field decays linearly as this is seen at the extremes 0 m and 0.1 m (and to a slightly lesser degree at 0.01 m
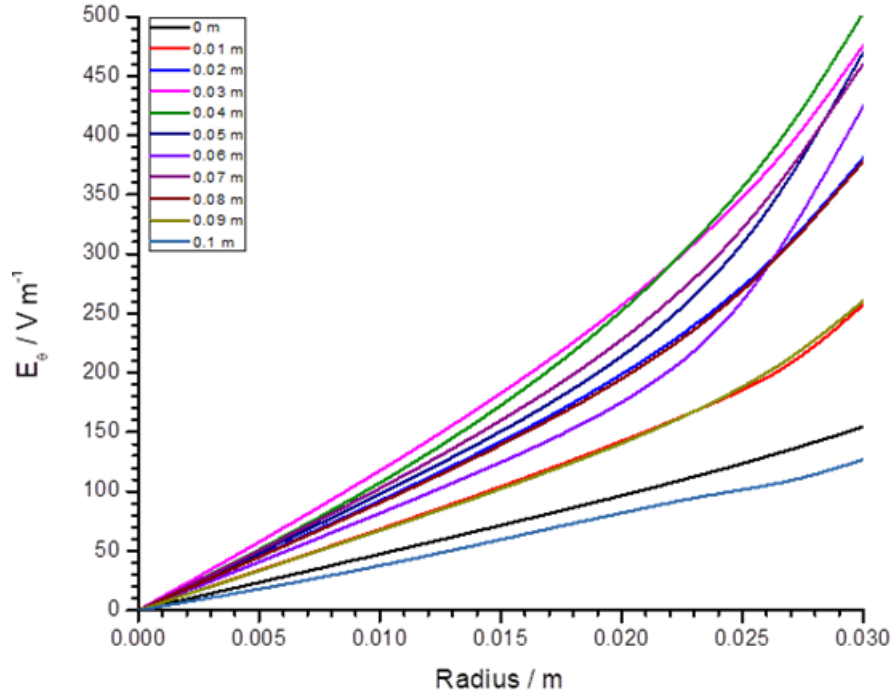
FIGURE 4.24: Electric field varying as r and z. Curvature of
the field decay is more exponential towards the axial centre.

and 0.09 m) where the calculated plasma density in those regions are very
low. The axial magnetic field component B_z in these regions is very small
and only a small azimuthal field would be induced by its RF fluctuations.
At the edge of the plasma in the mid-plane of the coil, there is a large az-
imuthal field induced which exhibits an exponential decay (especially at
0.06 m) radially inwards.

The skin depth in one cartesian dimension is related to the electric field
E [68] as:

$$\delta = \frac{1}{\partial(\ln(E/E_0))/\partial x} \tag{4.18}$$

However, the experimental geometry is cylindrical, so the skin depth can-
not be found completely this way owing to in-homogeneities at the wall
and close to the centre. To overcome these aberrations, the electric fields
were normalized using the electric field at the wall (E_0) and the skin depth
was estimated from the linear region away from the axis as evident in **Fig-
ure 4.25**:
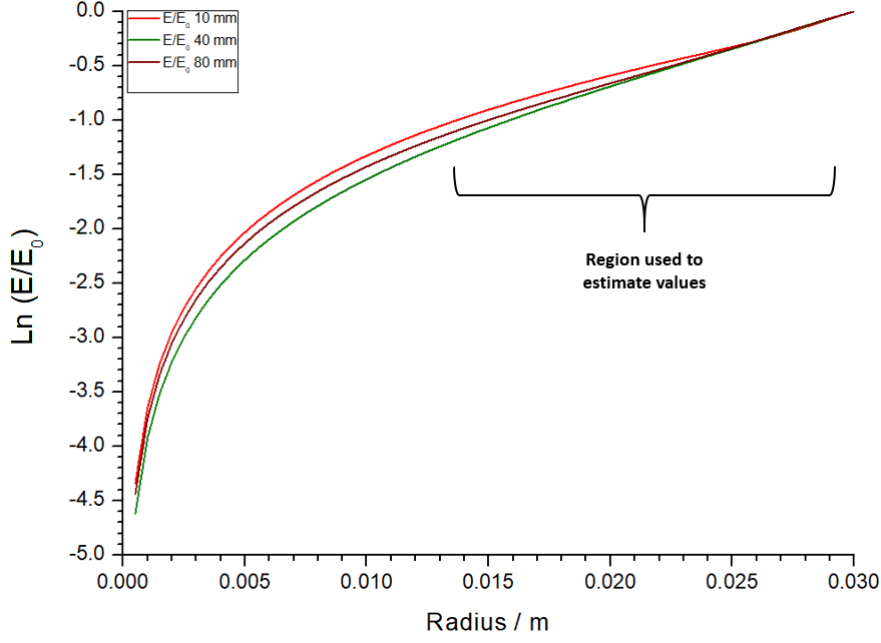
FIGURE 4.25: The skin depth is determined from the most
linear region of the response which is just before the edge
of the discharge.

z / m	0	0.01	0.02	0.03	0.04	0.05	0.06	0.07	0.08	0.09	0.1
δ / m	0.019	0.018	0.016	0.016	0.014	0.014	0.014	0.015	0.015	0.017	0.02

TABLE 4.2: Determined Values of Skin Depth from the nor-
malized E-Field

Table 4.2 implies that within the mid-plane of the coil (where most of
the power absorption occurs), the external field attenuates within 0.014 m
of the wall. The result is representative of a collision-less skin depth where
in the low pressure case, $v_m \ll \omega$ and the plasma is considered collisionless.
At 1 mTorr, n_e is expected to be $\sim 1 \times 10^{17}$ m^{-3} in the central discharge, this
would be a skin depth of [5]:

$$\delta = \frac{c}{\omega_p} \sim \frac{3 \times 10^8}{1.78 \times 10^{10}} \sim 0.017\,\mathrm{m} \tag{4.19}$$

This value is in good agreement to experiment. One way to directly infer
the plasma density involves using $I = n_e e v_d A$ where v_d is the collision-less
drift speed calculated using the average electric field at the edge of the skin
depth:

$$v_d = \mu E = \frac{qE}{i\omega m} \tag{4.20}$$

Where μ is the electron mobility. The cross-sectional area A was taken as $\delta r \cdot \Delta z$. This averaging method shows an axial profile of the plasma (**Figure 4.26**) density nearest to the coil with a smaller marked localized region of high density. This averaged method however removes information about the structure of the plasma towards the centre of the discharge, although the density gradient implies that most of the plasma is contained in a 'shell' nearest to the coils whilst the centre of the discharge is of lower density.

By having imagined concentric rings of plasma stacked along r, the individual plasma currents at each radius r were calculated by considering the B-dot probe response and $\frac{dB_z}{dr}$, for there to be a change in B_z along r, there must be a ring of plasma current causing this change. This has made it possible to resolve the plasma density at different radii and Z as a set of contours. The results roughly display the annular 'doughnut' shape of the plasma; where most of the net induced plasma current exists near the periphery of the plasma (nearest to the coils) and with slight asymmetry at the midplane.
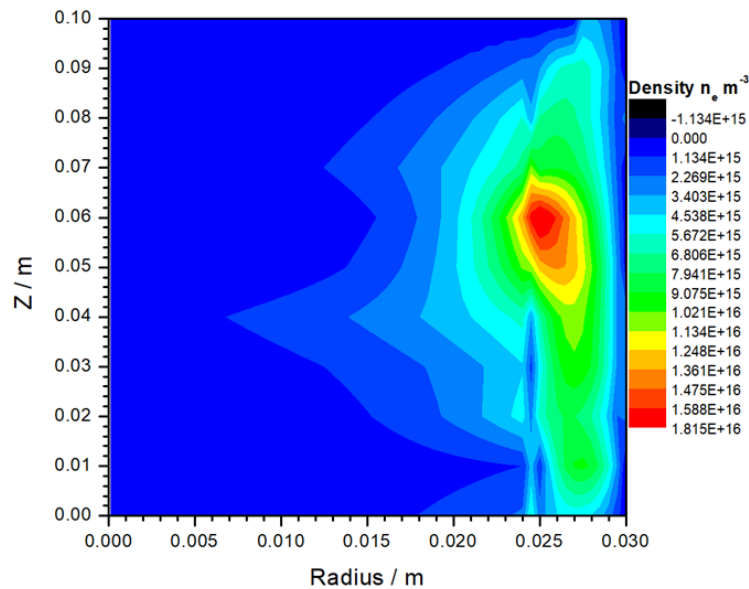
FIGURE 4.26: Contour map of the averaged electron density.
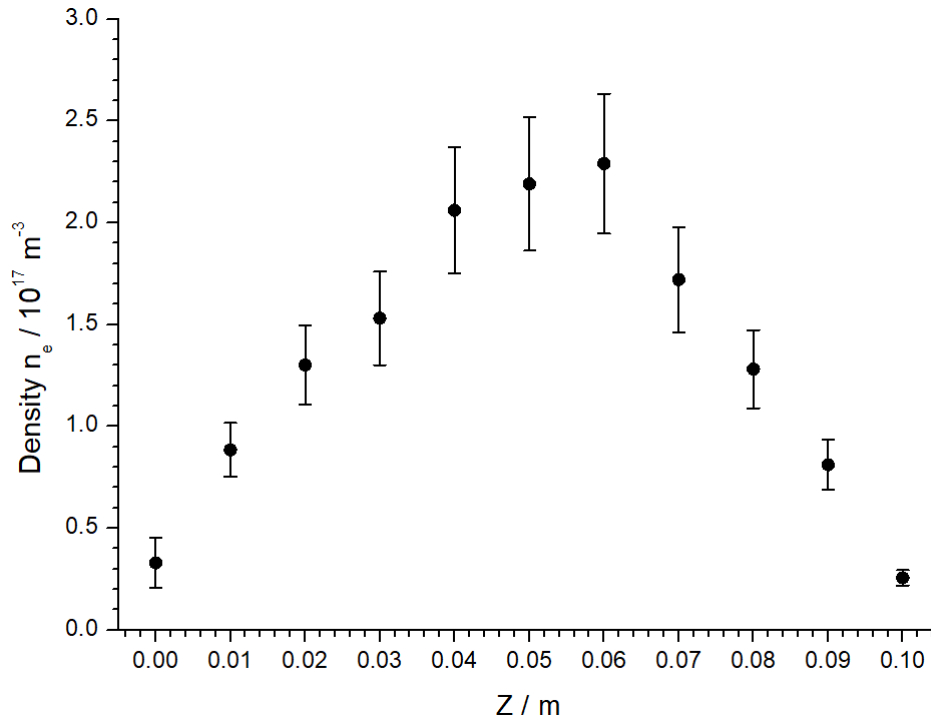
FIGURE 4.27: Summed electron density varying as z.

As seen in **Figure 4.26**, there is not enough information to accurately model the centre of the discharge due to the diminishing E-field and the subsequent lack of drift velocity. Yet in order to sustain the discharge, there must be a flow of species towards the centre. Both factors cause the electrons to be transparent to probe techniques and gives rise to artifacts. Much of the plasma current and therefore plasma density is seen to be located where the external field drops more markedly i.e within the skin depth at the axial centre. This 'shell' of current is the result of electrons lying in the tail of the Maxwellian electron energy distribution. However, the transport of these electrons and slower electrons towards the centre of the plasma is unaccounted for. There is however a density gradient which illustrates transport towards the centre of the plasma, though the lack of information about the electrons which constitute this transport make assumptions about the central structure of the plasma to be tenuous.

Modelling of the plasma structure has been previously attempted. Shiozawa *et al.* [69] modelled the electromagnetic fields and particle densities

in an ICP Cl$_2$ plasma using a Monte Carlo method. The geometry was a chamber with a many turn coil spanning a 385 mm long tube and radius 100 mm. The diffusion chamber was 250 mm long with a 174 mm radius. Contour plots show the E_θ distribution (**Figure 4.28**) as greatest nearest to the coils and decaying to zero towards the centre, essentially similar to what has been reported here.
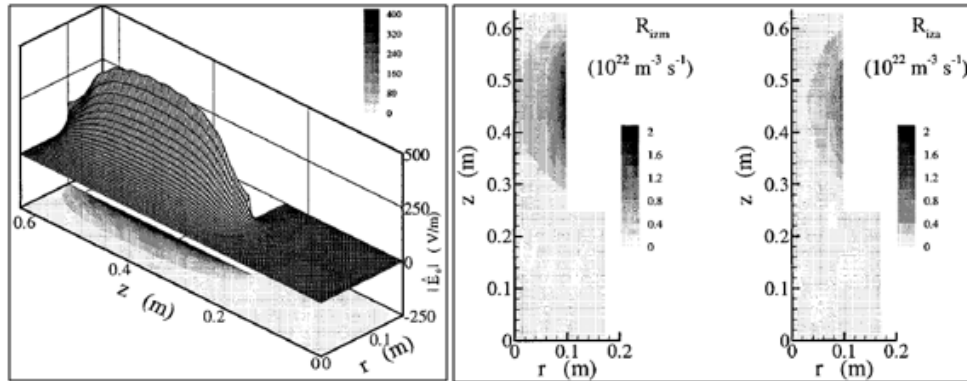
FIGURE 4.28: **Left to right**, electric field, Cl$_2^+$ ionization and Cl$^+$ ionization. *Credit:* [69]

This corresponds with densities of Cl$_2^+$ and Cl$^+$ being greatest in that region due to much of the power deposition taking place there. The electron density has been mapped to be greatest in the centre of the discharge and decaying radially outwards and the authors state that this decrease is due to the high electron temperatures which drive ionization collisions:
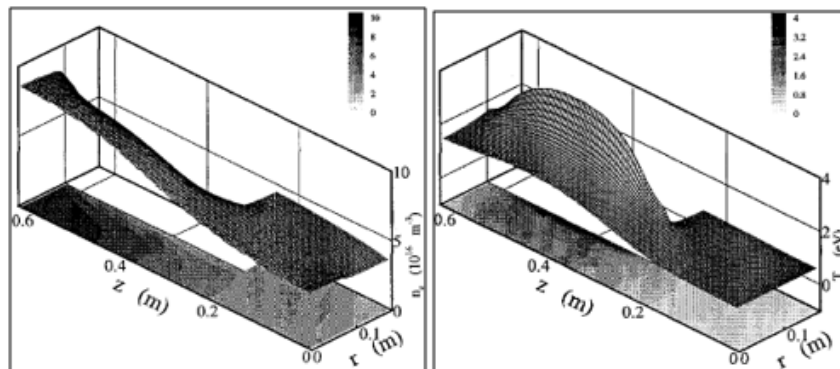
FIGURE 4.29: **Left to right**, electron density and temperature *Credit:* [69]

The electron density (**Figure 4.29**) is relatively uniform in the lower region of the discharge and in the diffusion chamber. It can be seen that immediately beyond the edge of the discharge, the electron temperature is markedly lower and constant throughout the discharge. Combined with a decaying azimuthal electric field, electrons will drift and collect towards the centre of the discharge. In another investigation by Takao *et al.* [70] using a pancake coil, in a collisional and collision-less model, the electron "temperature" was greatest nearest to the coils where much of the power deposition took place. The electron "temperature" was then observed to cool towards the midplane and outwards from the coils (**Figure 4.30**):
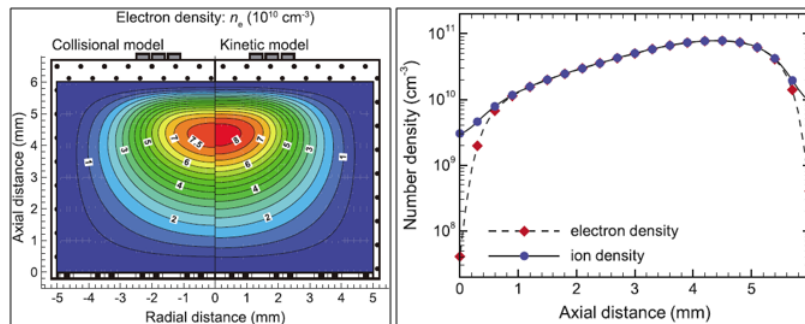
FIGURE 4.30: **Left to right**, electron density with kinetic and collisional models, charge density variation along the axial distance of the discharge

The hollowing out of the plasma in the experiment relates back to Faradays law of induction and the attenuation of the external B-field within a distance δ. Closer to the centre of the plasma, there will be less induced current due to the external B-field being at a minimum and the path for the current to flow becoming vanishingly small. To investigate how the structure of the plasma varies with pressure, a 1 mTorr and 10 mTorr Ar plasma were both ignited at 200 W and the B-dot probe was stationed permanently at Z = 0.04 m whilst rotated to give a variation along r. The vacuum field was also re-measured when there was no plasma. Again applying the boundary condition that the B-dot field response equates to the external field at the edge and does not decay noticeably until beyond the Debye sheath, this

yielded a model of the resultant B-field which physically represented the plasmas as shown in (**Figure 4.31**).
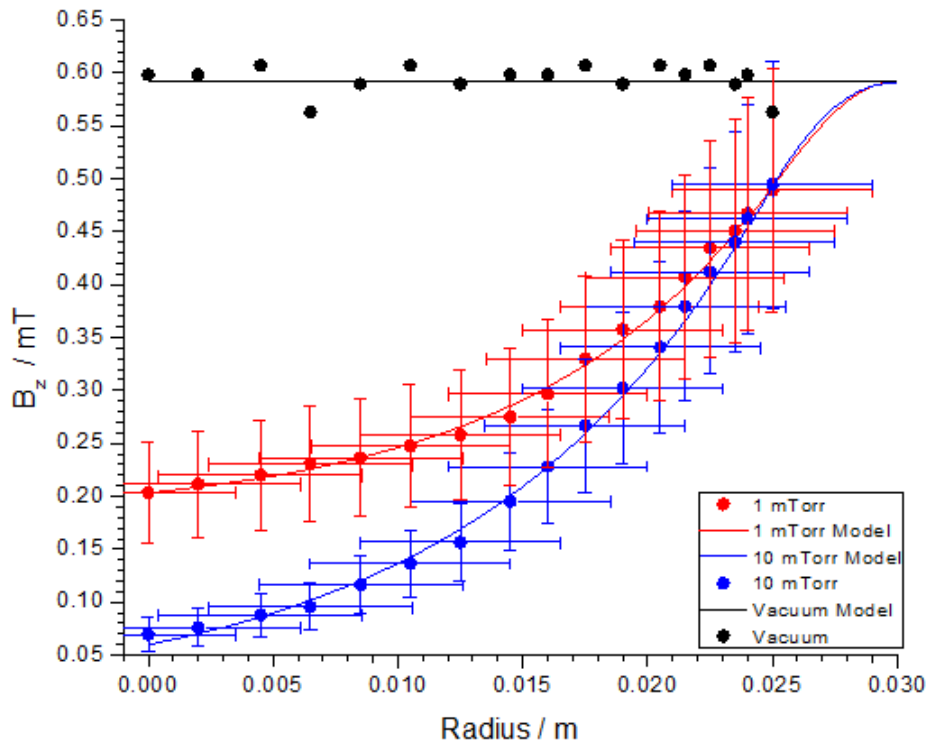
FIGURE 4.31: B-dot probe response at z = 0.04 m at 1 and 10 mTorr.

	1 mTorr	**10 mTorr**
Skin Depth / m	0.0126	0.009
Mean Plasma Density / m^{-3}	3.38×10^{17}	7.83×10^{17}

TABLE 4.3: Determined Values of Skin Depth and Plasma Density for 1 mTorr and 10 mTorr Ar Plasma at z = 0.04 m.

These results are in close agreement to previously determined Hairpin Probe and Double probe results. Specifically at z = 0.00 m (the beginning of the axial direction when moving the B-dot probe and also known as region "p"), the plasma densities at 1 mTorr and 150 W have been determined as:

- Hairpin Probe - 6.63×10^{16} m^{-3}

- Floating Double Probe - 3.03×10^{16} m^{-3}

- B-dot Probe - 3.29×10^{16} m^{-3}

It should be noted that the use of the B-dot probe and measurement of the induced electric fields has enabled a determination of the electron temperature T_e. Using **equation 4.20** and the value of E_θ where the power deposition is greatest ($\sim 500 \text{ V m}^{-1}$), the drift speed ν_d can be plugged into the kinetic energy equation:

$$\text{K.E.(eV)} = \frac{\frac{1}{2}mv_d^2}{q} = \frac{\frac{1}{2}\text{x}(9.31\text{x}10^{-31})\text{x}(1\text{x}10^6)^2}{1.6\text{x}10^{-19}} \sim 3\text{eV} \qquad (4.21)$$

This value is the expected value of the average T_e in a 1 mTorr ICP operating in H-mode. Furthermore, there is a close agreement with the square root of the electron temperature values measured with the floating double probe **Table 4.1**.

In other literature [67, 66], their discharge symmetries and probe constructions meant that $\frac{dB_r}{dz}$ and therefore J_z was measurable. The current experimental geometry did not allow this measurement. In particular, the use of planar coil ICP's and the construction of 3 looped two dimensional probes meant that the determination of $\frac{dB_r}{dz}$ was used to calculate an azimuthal current density as:

$$J = \mu_0^{-1}\left(\frac{dB_r}{dz} - \frac{dB_z}{dr}\right) \qquad (4.22)$$

The B-dot probe has provided an electromagnetic profile of the plasma and the results were used to spatially resolve the electron density. In comparison to earlier electrostatic/magnetic hairpin probe and double probe results, measurements of absolute density are in reasonable agreement.

4.4 Plasma Spectrometry and Imaging

4.4.1 i-CCD Plasma Imaging

Charge-coupled device (CCD) imaging has also been used as a method to spatially resolve plasmas. Anderson *et al.* [71] used a CCD camera in the optical region to spatially monitor the thermal properties of a cylindrical plasma. An externally triggered Andor i-Dus (Andor - Oxford Instruments) CCD camera was used to measure the light intensity and plasma structure across the entire volume of the ICP. Because at low power, the light emission was weak, the triggering enabled imaging in low intensity conditions combined with ultrafast shuttering. This application was not spectrally resolved and captured all wavelengths in the visible spectrum. The ceramic tube was replaced with Boron Silicate glass. Monitoring of a 1 mTorr Ar plasma in the approximate mid-point (pixel x:525, y:525) of the tube showed the increase in plasma activity when the RF power was raised. It can also be seen that there is an E-H transition beginning at 60 W (**Figure 4.32**):
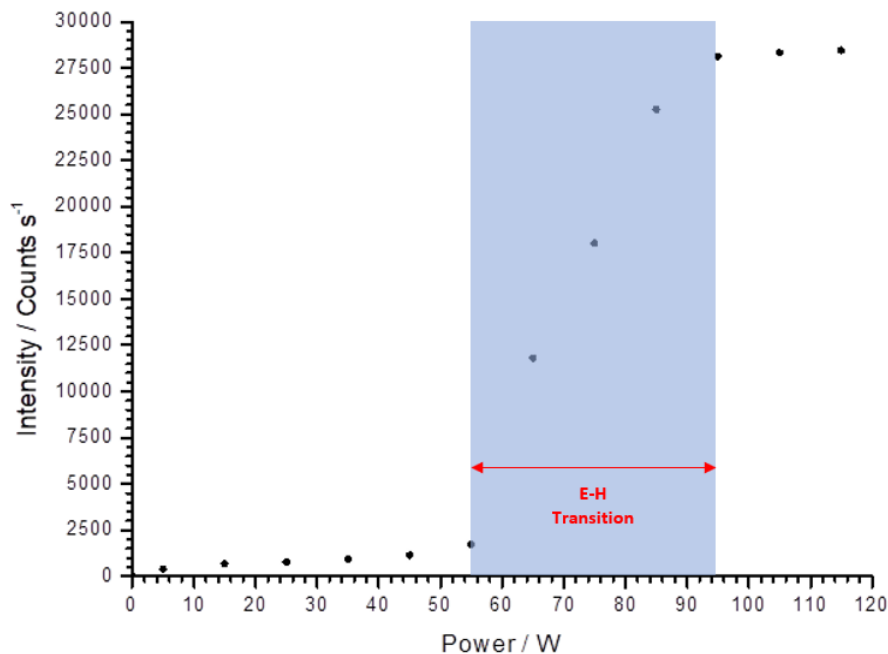
FIGURE 4.32: Light emission variation of a 1 mTorr Ar plasma as a function of power. A sudden increase in light emission follows a transition into H-mode.

The result is consistent with previous hairpin probe measurements where a low density was recorded in a low power capacitive mode. An E-H transition was then reached at approximately 70 W and the density rose sharply as the plasma entered a high density inductive mode. The increase in density then diminished as plateau was reached. The result taken by the CCD camera is an illustration of this plateau but is limited by saturation of the camera.

The shape of the plasma through the E-H transition was observed as in **Figure 4.33**:
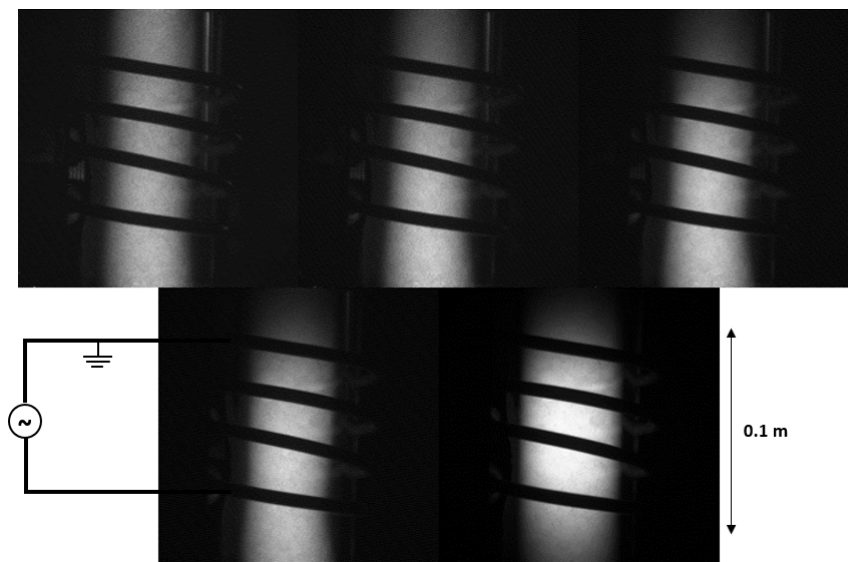
FIGURE 4.33: **Top** 2.8 W, 10 W and 30 W. **Bottom** 50 W and 70 W. Photographed light intensity variation of Ar plasma as a function of power.

Earlier chapters reported on the efficiency of power transfer into the discharge at powers low as 3 W and this is shown here in a diffuse and low density plasma. Powers 2.8 W - 30 W show a narrow, localized plasma characterized by low light emission (typical of E-mode). There is a slightly increased density building up around the bottom electrode due to the greater electrostatic potential between there and nearby grounded surfaces. From 50 W onwards, the shape of the plasma gradually expands becomes less localized by spreading outwards towards the surfaces and nearest to the coils.

This suggests the building up of an electromagnetic skin depth nearest to the coils where a current 'shell' forms as part of a greater power absorption in that region. The power is increased until E-H mode transition arises and a central, bright discharge is maintained. There is also a dissipation of the previously noted high density region appearing near the bottom electrode. As noted in the figure, the plasma appears 'squashed' into a doughnut which is indicative of very low electrostatic field coupling and instead a coupling with that of the B-field.

FIGURE 4.34: **Top** 100 W, 150 W and 200 W. **Bottom** 250 W, 300 W and 350 W. Photographed light intensity variation of Ar H-mode plasma as a function of power.

As more power is absorbed (**Figure 4.34**), the plasma must fill more of the reactor and this can be seen by higher light emission at the axial extremes. This also coincides with the external coil current increasing, therefore the applied B-field is more likely to reach and induce plasma current in those areas. Furthermore, in the steady state there is an axial flow of ions out of the plasma whilst more are created in the central discharge. As the power is increased, the plasma grows in size in the axial direction.

The CCD imaging suggests a symmetrical plasma with the light emission that is greatest at the axial centre. In order to further confirm previous

B-dot probe measurements, the signal intensities of the CCD imaging and the B-dot probe were compared axially. For reference, the original CCD data contains blind regions where the body of the coil blocks the emission. These regions were deducted and the response modelled by a parabola. The intensities were normalized and plotted side by side. **Figure 4.35** shows the comparison of CCD data with B-dot probe measurements using localized and averaged density values for a 1 mTorr 200 W Ar plasma:
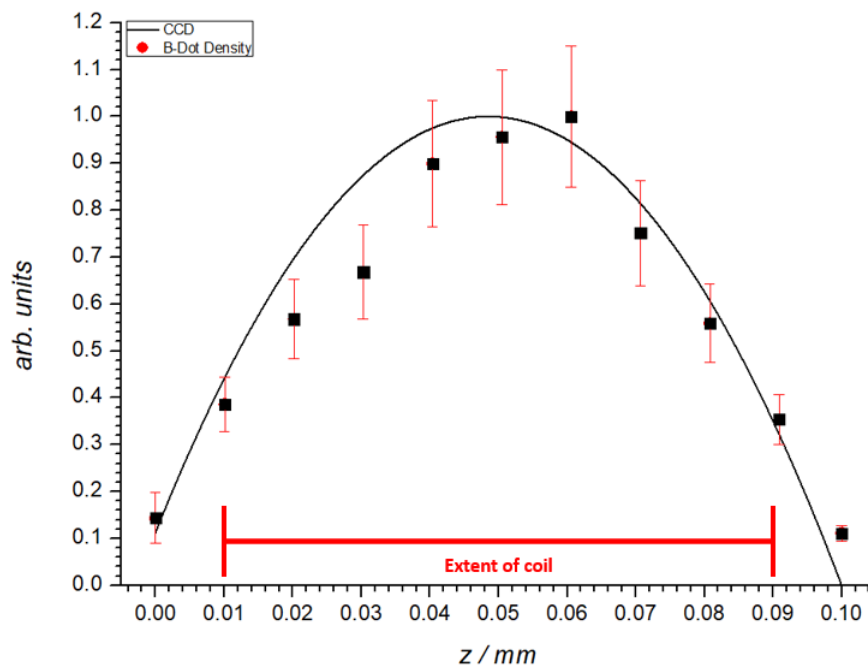
FIGURE 4.35: Comparision of axial intensity of the CCD compared with the axial B-dot response.

It can be seen from the imaging that the light intensity has a maximum on the axial centre and then falls in intensity at the axial extremes where there is not much plasma induced. This is represented in the lower count rates. The B-dot probe results suggests an almost identical behavior with the region of highest intensity being localized at the axial centre ($Z \sim 0.05$ m). Although the distributions are broad along Z, the introduction of a parabolic modelling to the CCD data underestimates the count rates at the axial extremes and slightly overestimates the count rates either side of the centre. The results agree reasonably and it is suggested that the outer edge of the plasma is not evenly distributed along axis, but is in fact localized on

the axial centre. A top-down picture taken of the plasma through an optical window strongly suggests lower density in the centre as the window at the bottom of the experiment can be seen. It is difficult to resolve a clear image near the wall due to the plasma being thicker (**Figure 4.36**):
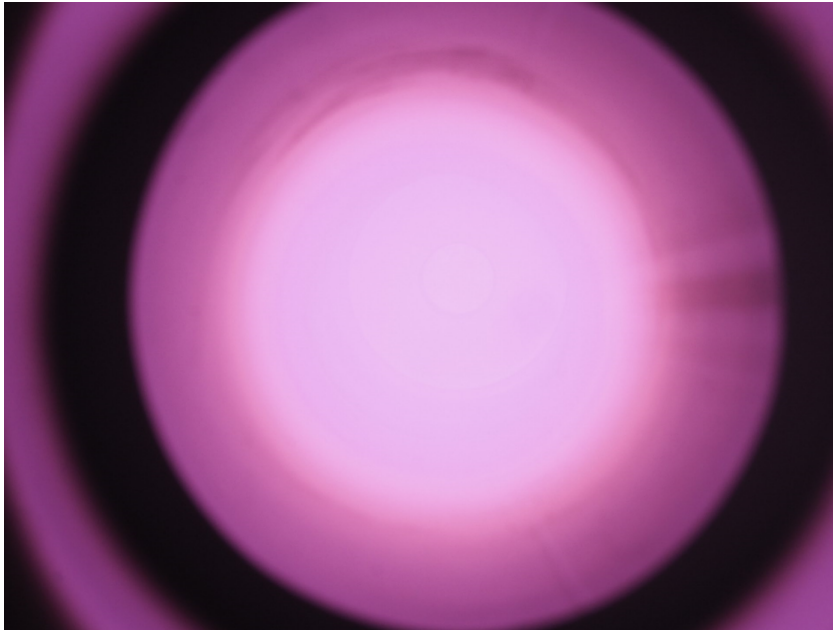
FIGURE 4.36: Picture of the plasma (250 W, 1 mTorr) taken above from an optical window.

4.4.2 Optical Spectrometry

It is possible to resolve the discharge by mapping the light emission at particular wavelengths using optical emission spectroscopy (OES). OES provides a non-intrusive method of plasma characterization. The spectral properties are primarily the result of atomic and molecular transitions (from excitation, ionization and dissociation events) whose photons give detailed information about the chemistry and species densities within the plasma. OES can also measure electron and gas temperatures of discharges as demonstrated by Schabel *et al.* [72] although it was not used for this purpose within this thesis. Within this work (**Table 4.4**) OES (within the visible range of 300 nm - 900 nm) was used to monitor plasma species as power, pressure and flow rate were varied in an O_2 plasma. O_2 was used due to it being a molecular discharge. Compounding issues of signal to noise and

the ambiguity of excited states mean that OES was used more as a complement to other more resolved forms of diagnostics. The use of global modeling code at the end of this chapter helps to conclude some of the results measured here.

Species	Wavelength / nm	State	Reference
O	844.6	$3p^3P$	[73]
O	777	$3p^5P$	[73]
O	615	$4d^5D^o$	[73]
O^+	538.3	$^4S^o$	[73]
O_2	765	$b^1\Sigma_g^+$	[74]
O_2^+	558.7	$b^4\Sigma_g^- \rightarrow a^4\Pi_u$	[75]

TABLE 4.4: Common O_2 Spectral Wavelengths

An optical spectrum was taken for a 1 mTorr 200 W O_2 discharge with a flow rate of 5 SCCM in **Figure 4.37**.
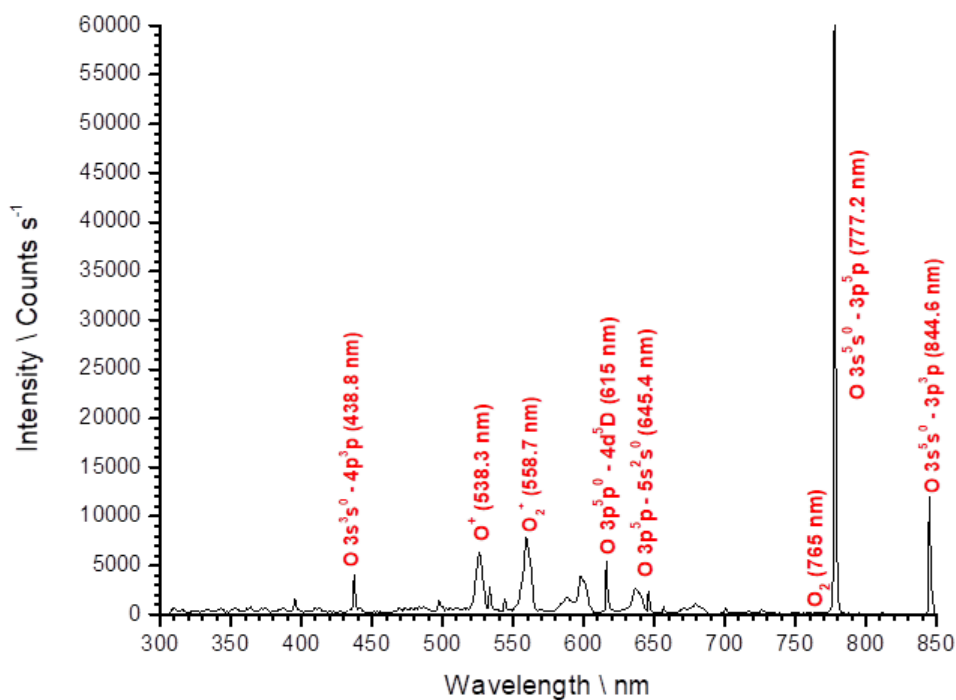
FIGURE 4.37: Emission Intensities of Oxygen species as wavelength.

Molecular transitions are characterized by broad peaks in the 500 nm and 650 nm regions. There is a noticeable peak at 558.7 nm which corresponds to the first ionization potential of molecular O_2. The absence of sharp transitions (OH - 308 nm or UV region of spectrum) suggests a lack

of water in the discharge. Atomic transitions (615 nm, 777.2 nm and 844.6 nm) are very narrow but form much of the intensity.
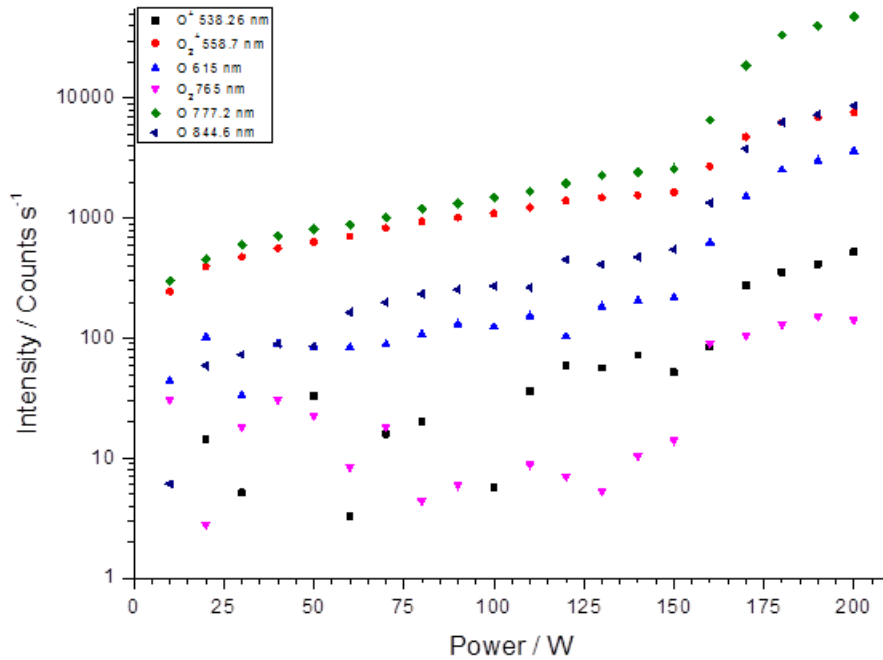
FIGURE 4.38: Variation of emission intensity with power.
Other plasma conditions are identical to **Figure 4.36**

Figure 4.38 shows that as the RF power is increased, there is a rise in emission from O_2 species due to the increase in power absorption by the electrons. Significant dissociative processes are seen around 150 W with the rise of atomic O lines such as 777.2 nm and 844 nm. An increased rate of ionization is indicated by the rise of O_2^+ (558.7 nm). At 150 W power, there appears to be transition from a lower density into a higher density as illustrated by a step. This corresponds with a greater absorption of power into the plasma, although in previous hairpin probe measurements, this transition was seen closer to 250 W in O_2. Because the plasma is dominated by the atomic O 777.2 nm spectral line, it is deduced that the discharge is still in a low power state and the E-H transition has not been reached yet. Furthermore, the low intensity of singly ionized atomic O (538.26 nm) indicate that not much energy is required to ionize neutral atomic O. Therefore, most of the transitions are excitation and dissociation events.

The pressure was then varied for a 250 W discharge in H-mode (**Figure 4.39**).
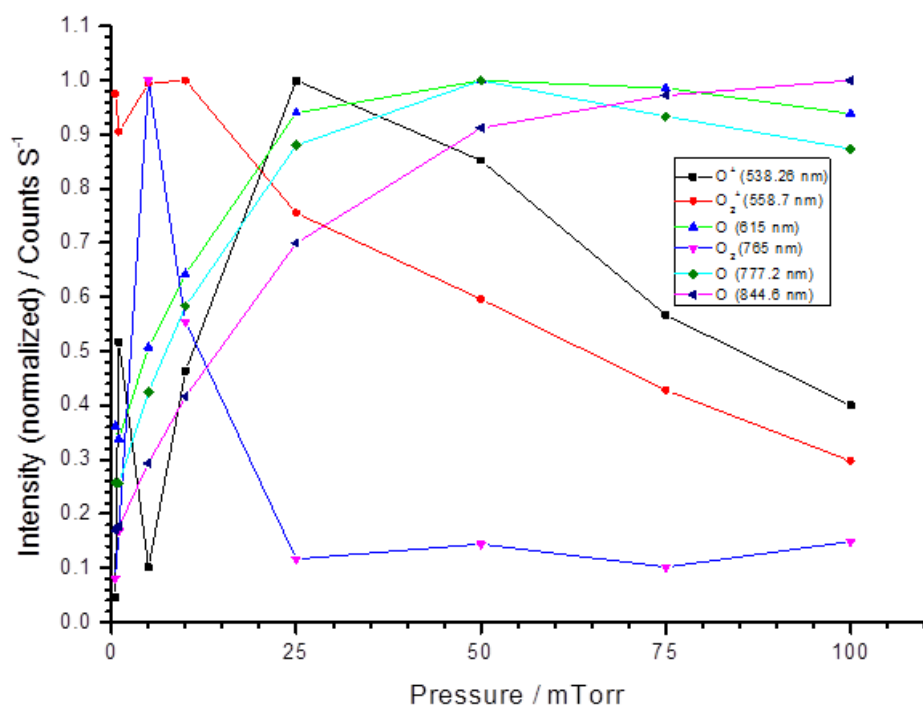
FIGURE 4.39: Variation of emission intensity with pressure.
Emission reaches a maximum for ion species then reduces
as the electron temperature decreases.

At low pressures the mean electron energy tends to be higher than at higher pressure, but due to the high mean free path, the cross-section for electron ionization collisions is reduced. This is seen by the lower intensities of atomic O (electrons too energetic for dissociative processes) and high intensity of O_2^+. As the pressure is increased, the mean free path is lowered such that dissociative processes can dominate. This is seen by the increase in atomic lines 615 nm, 777.2 nm and 844 nm. O^+ also rises due to there being a greater number of neutral atomic O to ionize. Recombination processes are also encouraged such that O_2^+ decreases as the pressure is increased. At even higher pressures (more than 100 mTorr), the discharge cannot be sustained at high density due to the electron temperature becoming lower. This is observed by atomic O peaking at 50 mTorr and then decreasing. Negative ion formation by electron attachment also contributes to a lowering of the electron density.

4.5 Global Modelling

Global modelling is utilized as a useful tool to benchmark processing plasmas. The code used was developed by Kokkoris *et al.* and was used to study the discharge kinetics of an SF_6 plasma [76] where a set of gas phase and surface reactions on the walls of an ICP reactor where used to balance particle production and loss in steady state. This particular model more closely resembles a fluid description of the plasma, aiming to reduce complexity by describing the plasma based on macroscopic quantities. Another 0D investigation by Lallement [77] saw the use of a Druyvestyn energy distribution function to map the density profiles of reacting species. 0D modelling is volume averaged, hence, the densities of species within the plasma are spatially uniform and interactions happen homogenously across the reactor space. The practicality of this method is that it gives an approximation of species densities whilst cutting down greatly on complexity and computation time. This is contrasted to 2D and 3D models such as HPEM (Hybrid Plasma Equipment Module) [78] where a multi-step deep etch of silicon was simulated using separate gas phase plasma chemistry and material profile evolution modules. Although the coupling of the surface physics to the gas phase reaction kinetics were in close agreement to experiment, this method of modelling is very complex and computational time is high such that global modelling is used to compromise complexity for short computational times and a focus on discharge chemistry.

A simple global model was used here to benchmark previous diagnostic results and to give an account of plasma parameters in Ar and O_2 discharges and mixtures. The global model considers ionization everywhere within the reaction space isotropically and so it is more accurate to consider the results from the modelling as taken from the center of a discharge. Moreover, although the fluid description can provide meaningful results on densities, average energies and chemistries, because the distribution function of the electrons/species are assumed means that some of the physics

may not be represented. Adapted from Kokkoris, 2009, Plasma-R modelling code was used with reaction schemes adapted from [76, 77, 60, 79].

The density variation with power for different pressures is shown for an Ar plasma in **Figure 4.40**.
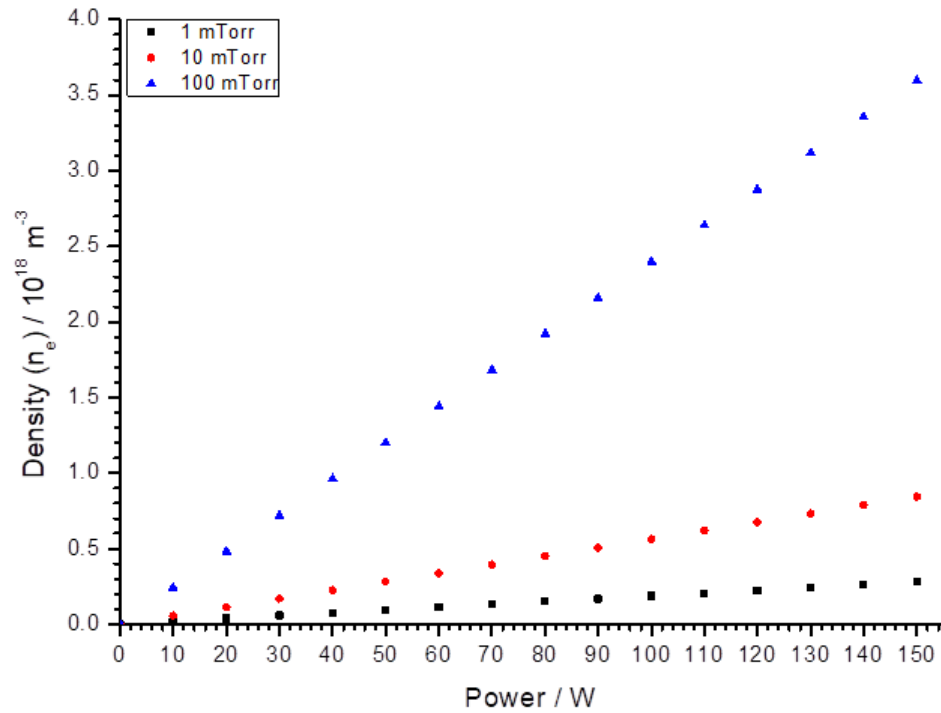
FIGURE 4.40: Variation of plasma density (n_e) in a modelled
Ar discharge as a function of power.

Figure 4.40 illustrates the lack of spatial resolution. The main input is power per unit volume such that no E-H transition is seen.

The density variation with power for different pressures is shown for an O_2 plasma in **Figure 4.41**:
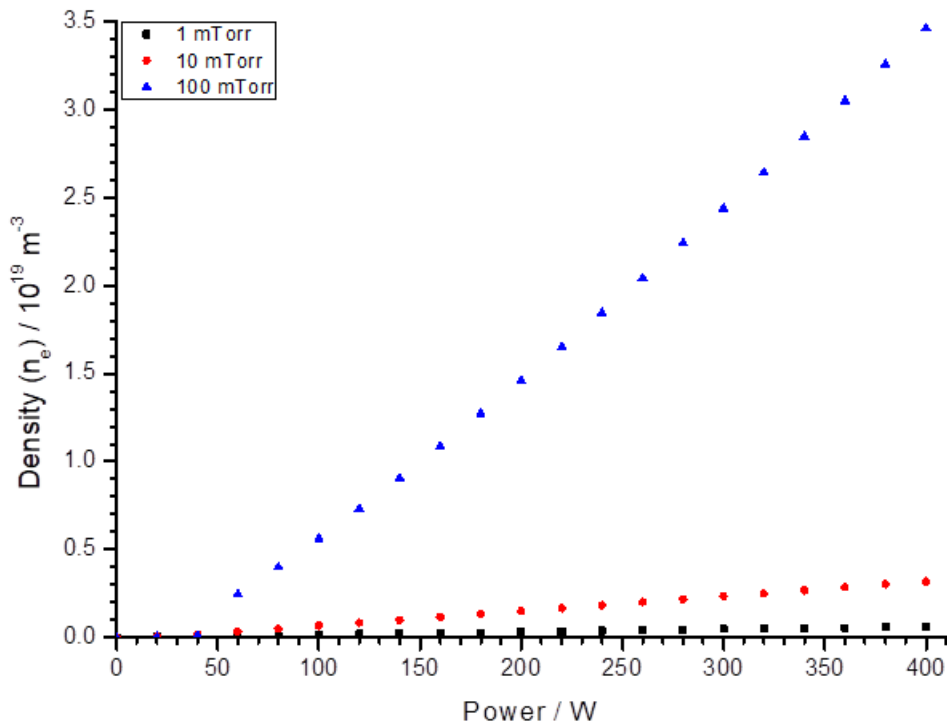
FIGURE 4.41: Variation of plasma density (n_e) in a modelled O_2 discharge as a function of power.

Because the model is volume averaged, recombination and other loss effects are not accounted for in regions of the plasma where there is little or no power absorption i.e. region 'p' where the hairpin probe was situated. Through the B-dot probe however, it can be confirmed that had the hairpin probe been situated in the central discharge, it would have been able to record plasma densities 10^{17} m^{-3} – 10^{18} m^{-3} at comparable pressures. The disparity between experiment and modelling is especially apparent in the O_2 discharge where recombination both in the central discharge and in low power absorption regions play a much larger part. The model agrees closely in the Ar case, but differs more notably for the O_2 case where densities of 1.5×10^{17} m^{-3} at 400 W were recorded for 1 mTorr when compared with 6×10^{17} m^{-3} for the model.

In order to directly compare with OES data, a 250 W, 5 SCCM O_2 plasma varied with pressure was modelled in comparison to **Figure 4.39**:
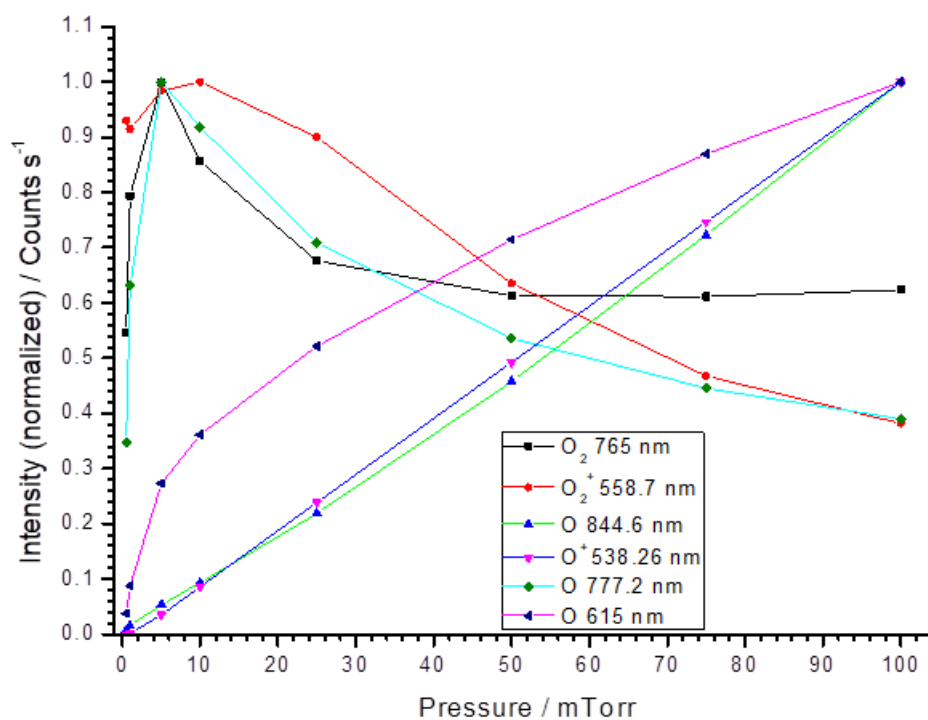
FIGURE 4.42: Modelling of O_2 density at different pressures.

As pressure is increased, densities of O_2 and O_2^+ decrease. There is a brief rise at lower pressures from 0.5 mTorr to 10 mTorr but this is known to be due to greater efficiency of ionization from the lowering of the mean free path. The short rise in O_2 is attributed to recombination events. As expected, O densities rises with pressure, although the rise in O^+ does not agree with experimental results. It is confirmed that higher pressures encourage dissociation events hence the rise of O_2. But the rise in O^+ suggests that there is not a facilitation of O_2 recombination. However, as seen experimentally, the ionic line is not very intense and at higher pressures the signal is swamped by other wavelengths.

A global model is not spatially resolved and does not take into account regions in the plasma where some mechanisms may occur more than others. For example, experimentally one may find that recombination effects of

O into O_2 occur more rapidly at the axial edges of the plasma. At first, O^+ is more likely to be created from electron impact dissociation nearest to the coils where power dissipation is greatest. At higher pressure, the overall power absorption by electrons is lower and more easily spread throughout the volume such that recurring attachment dissociation and recombination processes are more frequent – with recombination favored due to the mean free path. This is shown experimentally in **Figure 4.38** where there is a diminishing increase in O with pressure and the densities begin to fall. The global model cannot accurately portray this as power is absorbed everywhere within the reactor space. This means that it overstates the production of O by assuming that there is electron attachment occurring everywhere within the reaction vessel. **Figure 4.43** shows the comparison of O^+, O_2^+ and ground O:
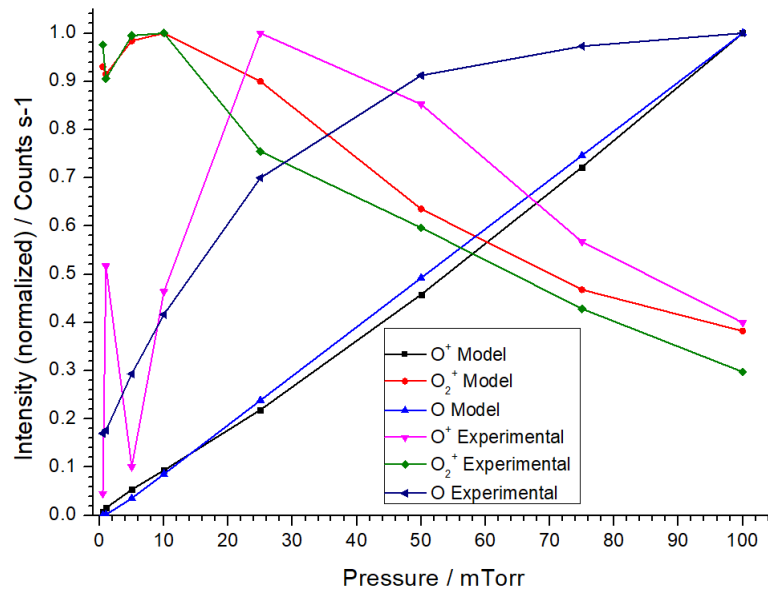
FIGURE 4.43: Comparison of the emission of O^+, O_2^+ and O (844.6 nm) between experiments and global modelling.

It can be seen that there is a reduction of heavy O_2^+ ions in the plasma as the pressure is increased in both experimental results and the modelling results. There is also an increase in ground state O, marginally energetic from energy transferred due to multiple collisions. However, the increase of O^+ in the model is not seen experimentally.

4.6 Summary

Chapter 4 has investigated the experimental setup from the plasma perpective. The bulk electron temperature was estimated to be between 2 - 3 eV and the tail of the electron energy was found to be between 7 - 9 eV (depending on pressure). The electron density was found to be $3 - 8 \times 10^{16}\,\mathrm{m}^{-3}$ at the axial extreme using a Hairpin Probe and a Floating Double Probe. A B-dot probe was then used to confirm the density at the axial extreme ($3.29 \times 10^{16}\,\mathrm{m}^{-3}$) and further used to map the electromagnetic structure of the plasma with both axial and radial resolution. A further measure of the mean electron density in a 1 mTorr and 10 mTorr plasma was found to be $3.38 \times 10^{17}\,\mathrm{m}^{-3}$ and $7.83 \times 10^{18}\,\mathrm{m}^{-3}$ respectively. This also enabled a measure of the ionization efficiency using values for 1 mTorr:

$$\eta = \frac{n_e}{n_0}\text{x}100\% = \frac{3.38\text{x}10^{17}}{3.2\text{x}10^{22}}\text{x}100\% \sim 0.001 \qquad (4.23)$$

Which was found to be reasonable as this gives an ionization ratio $\ll 0.1$. Furthermore, mapping of the electromagnetic fields showed that the plasma was relatively uniform. Attempts to measure the centre of discharge were found to be difficult due to the induced current not penetrating to the centre of the discharge. Optical diagnostics were used to complement these results with OES describing the chemistry of an oxygen plasma by measuring its spectral properties. H-mode was seen via the intensity of the oxygen species increasing at 150 W indicating the beginning of an inductive transition. An i-CCD camera used the total light emission from an argon plasma and confirmed the H-mode transition at 70 W. Lastly, global modeling was used to benchmark some of the earlier probe results and densities were found to be within the same order of magnitude. The results show that the experimental setup has the properties of a low pressure, high density ICP discharge with a good uniformity. This is consistent in its use for plasma processing and justifies the investigation of the setup as a neutral beam source.

Chapter 5

The Electrostatic Quadrupole (EQP) Mass Energy Analyzer

This chapter introduces the EQP as the major diagnostic instrument and discusses its primary mode of operation. The EQP is used for analyzing ionic species in secondary ion mass spectrometry mode (SIMS) and neutral species in residual gas analysis mode (RGA). The chapter will also discuss the use of the instrument for a novel measurement of energetic neutral species. The chapter will then explore these measurements and their validation which is continued in **Chapter 6**.

5.1   Conventional Use of an EQP

The EQP allows the resolution of plasma species via mass to charge ratio and by energy. Particles are sampled through an extraction orifice with a diameter of 100 μm. The choice of diameter was a compromise between the signal intensity which favours a large orifice, and the need to maintain a substantial pressure differential which favours a small orifice. The orifice is located 7 cm above a grounded steel mesh that provides a porous boundary to the plasma volume. At the working pressure, this distance is appropriately matched to the mean free path for one charge-exchange collision.
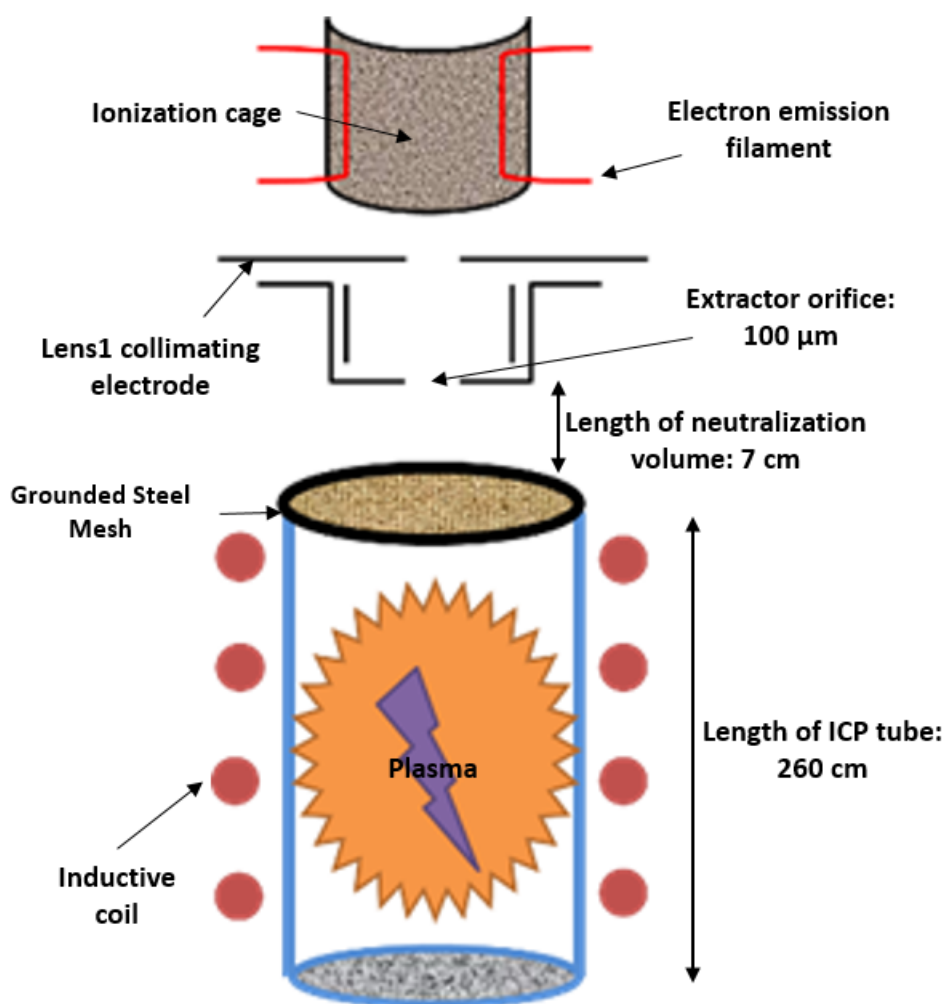
FIGURE 5.1: Schematic of the EQP setup (not to scale).

A more complete schematic of the EQP is found in **Appendix A, Figure A.1**. The EQP is similar to many mass/energy analyzers in that it is based

on RGA measurements. In this mode, cold thermalized gas, is sampled and then positively ionized by energetic electron impact within the instrument in order for them to be filtered by mass and detected. SIMS mode is used when the ions that are analyzed are created in a plasma outside of the instruments. These ions can also be filtered by mass and energy once inside the analyzer. Charged particles enter through the orifice either of their own accord or due to being drawn in by the extractor electrode which creates a 'bubble' field that collects ions into the EQP. Despite the collimating effect of the plasma sheath, many ions from the plasma will not be traveling exactly parallel to the axis especially slower moving species that were scattered. In the present work, the extractor electrode was generally set to 0 V during experimentation since it had been observed that high extraction voltages cause false artifacts in the energy spectra.

As can be seen in **Figure 5.1**, Lens1 is the first electrode beyond the extractor and it collimates the external ion beam to pass through the ionization cage in SIMS mode. The ionization cage is the region where in RGA mode, neutral particles are ionized by impact ionization by electrons emitted from the filament, typically set at energies between 40 – 70 eV by a negative voltage (called Electron Energy) (40 – 70 V) set on the iridium filaments. The combination of cage, emission filaments and electron energy value are referred to as the ionization source and are normally active only in RGA mode. The electrons are accelerated from the filaments towards the slightly positive (1 V – 3 V) cage which allows them to reach energies equal to and greater than ionization potential. Physically, the cage is a cylindrical mesh with transparency to allow the electrons through. The slight positive voltage on it is necessary to ensure all positive species have minimum energy to traverse through the transfer electrodes and into the field-free drift region.

The EQP volume must be evacuated to an operating pressure of at least

1 x 10^{-7} mTorr to eliminate collisions. The voltage on the cylindrical field-free drift tube is set by the Axis electrode **Figure A.1** and ensures that all charged species are centred on axis before being transferred into Lens2 where they are again collimated (in case of any divergence) to pass through to the energy filter (a 45° bend). The energy filter discriminates independent of mass by systematically adding or removing kinetic energy from the sampled species. The mass filter then discriminates based upon mass/charge ratio using the quadrupole. The quadrupole is a system of four parallel rods which are electrically connected and have opposing DC and AC radio-frequency voltages set between them. This creates a complex alternating field which only ions of a particular charge/mass ratio and energy can pass through without being swept onto the rods or surrounding surfaces. Ions that have the right mass to successfully traverse the quadrupole fields bombard the detection surface, creating secondary electrons (ie a secondary electron multiplier). The resulting showers are recorded as counts. Negative RGA and negative SIMS modes can also be used to measure negative plasma ions (in pulsed plasmas mainly) or molecular neutral species that have a large electron attachment cross-section. In the case of negative RGA, low energy electrons (1 eV – 10 eV) are used to ionize via attachment or dissociate to create negative ions. In both of these modes, most of the collimating and focusing electrodes are reversed in polarity. The circuit schematic of all electrode voltages are given in **Figure A.2 Figure 5.2 & 5.3** illustrate results in RGA mode without gas flow and in SIMS mode in an Ar plasma:
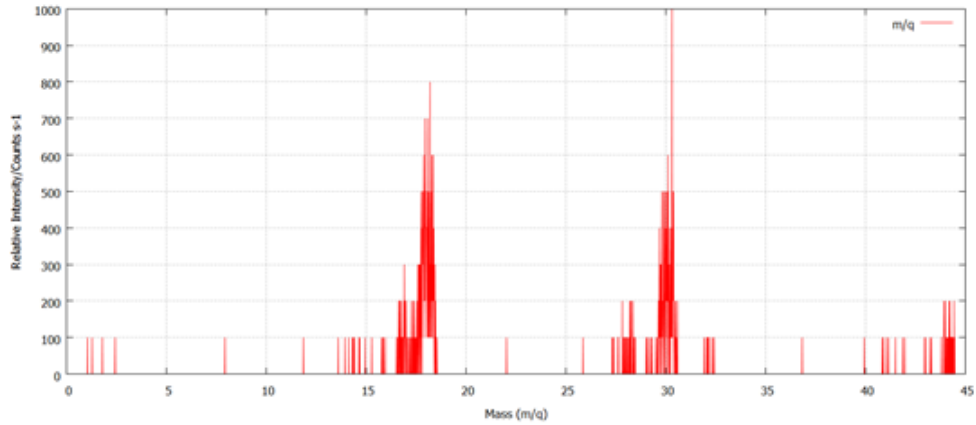
FIGURE 5.2: RGA mass scan (linear scale) of the evacuated chamber. Peaks at m/q = 18, 28 and 30 are known to be trace H_2O, CO and NO molecules respectively.
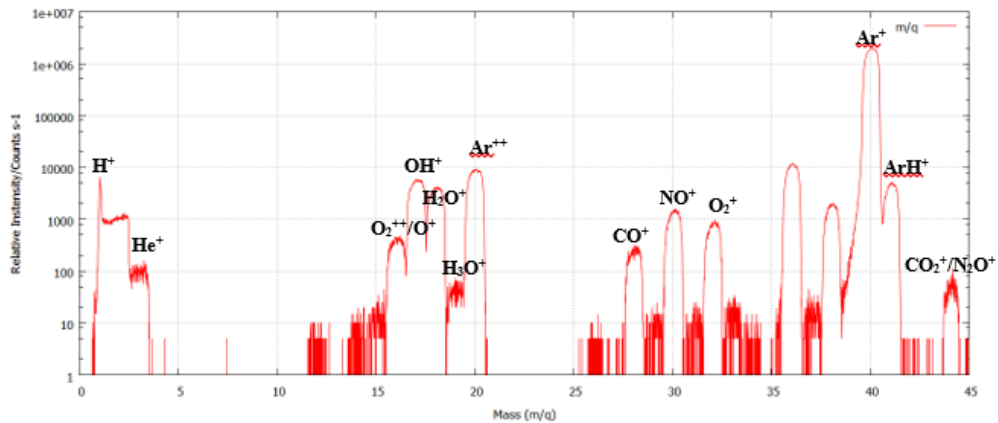
FIGURE 5.3: SIMS (plasma ion) mass (100 W, 10 mTorr) scan (logarithmic scale) of an Ar plasma. m/q = 40 (Ar^+) represents the most dominate ionic species.

As it can be seen in **Figure 5.2**, trace atmospheric gases are still measured. **Figure 5.3** shows that Ar^+ is the most dominant species and it is over two orders of magnitude more intense then the next peak. The presence of other species such as H_2O, H and other atmospheric gases are attributed to them being present in the line of the carrier gas.

The resolution of the EQP can be inferred from a measurment on cold neutral gas. In RGA scans without a discharge, it is not expected for neutral gas to surpass 0.025 eV:
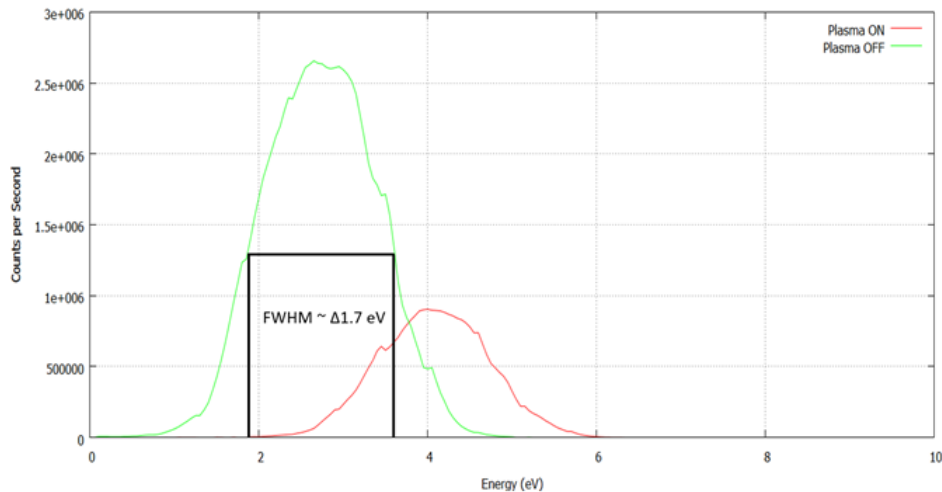
FIGURE 5.4: Resolution test of Hiden EQP by measuring the
energy of thermalized neutral particles in RGA mode.

The peak of the Maxwellian energy distribution of RGA mode ions is
shifted due to the potential of the cage (see **Figure 5.4**) – all charged parti-
cles must have minimum energy equal to the cage voltage (here, the cage
voltage is 3 V) before traversing into the field free drift region. The broad-
ening of the peak (and minor dips seen in the peak) is attributed to the
resolution of the instrument which in other works [50] has been agreed as
approximately 1.7 eV. When the plasma is switched on, the intensity of this
peak decreased due to interference from the ICP detuning the EQP. The
shifting of the peak of about 1 eV is attributed to the stray RF voltage on the
body of the EQP due to RF power. This was confirmed with a voltage probe
and oscilloscope. The combined effect of the cage potential and parasitic RF
causes all neutral energy to be slightly overestimated.

An EQP is an important and versatile tool in plasma diagnostics due to
its ability to gain internal information about the plasma such as chemical
composition and energies which is essential for characterization. The use
of mass spectrometers in low temperature etching plasmas is well docu-
mented by Olthof J *et al.* [80] where energy distributions of an Ar discharge
in a GEC reference cell were measured using a modified QMS. A review of
QMS for plasma research is given by Benedikt [81].

5.2 Modelling the EQP Using COMSOL Multiphysics

5.2.1 Motivations

Energy measurements made with an optimized EQP resulted in the consistent measurement of fast neutrals, via filament modulation, which mirrored the EDF of their parent ions (**Figure 5.5**). The protocol for fast neutral measurement involved measuring the energy of species in RGA mode with the filaments off (no emission of ionization electrons). It was expected that the distribution would mirror that taken in SIMS mode as only external plasma ions would be detected. Upon turning the filaments on, ionizing electrons are released. Any enhancement of the distribution would be due to the ionization of fast and background neutral species.
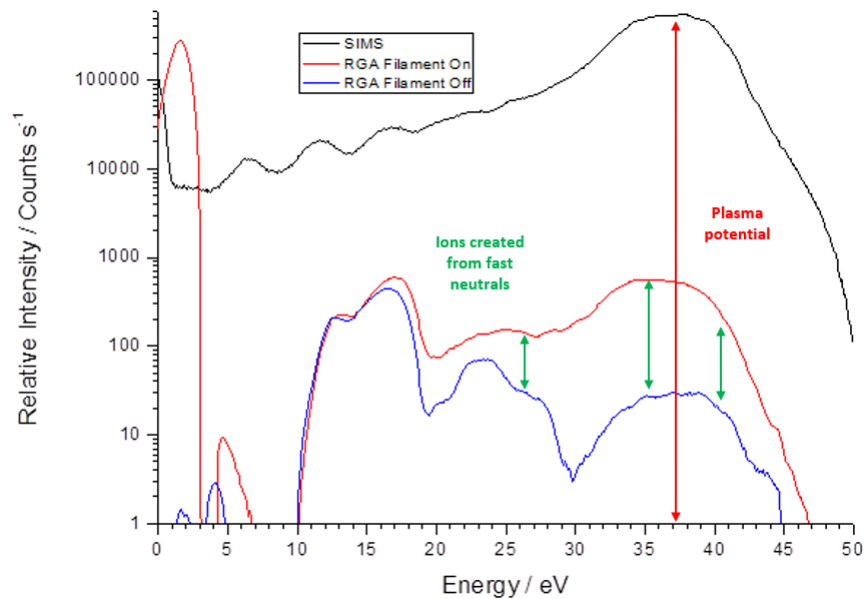
FIGURE 5.5: The energy distributions of Ar species measured in SIMS mode (plasma ions), RGA mode cold filaments (plasma ions) and RGA mode hot filaments (plasma ions and neutrals).

It was observed that starting in SIMS mode and simply biasing the filaments (while still cold) resulted in some ions no longer being detected and reduced ion intensity as can be seen from **Figure 5.5**. The signal is then enhanced once the filaments are switched to emissive where ionized neutrals join the signal. It is hypothesized that ions present in the conventional

SIMS mode had been deflected off axis due to the potentials from the filaments. This isn't an issue as any enhancement of the signal via filament modulation is taken as the presence of fast neutrals which should be unaffected by filament bias. However there was a concern that some deflected ions could be picked up again and falsely interpreted as energetic neutrals. There is an observed difference in the transmission of ions between SIMS mode and RGA mode – in normal RGA mode, cage electrodes and filaments are automatically switched on, whereas normal SIMS mode has these electrodes automatically switched off. This causes a separate optimization for ion transfer from the cage into the field-free drift region between RGA and SIMS modes which explains small shifts at low energy and appears to be the cause of the persistent blind region observed at around 10 eV.

To investigate ion trajectories further a multi-physics modelling code was developed. COMSOL has previously been used to model various plasma diagnostics such as Langmuir probes [82] and plasma characterization [83]. In contrast to those studies, COMSOL 3D modelling was applied not in the plasma volume, but inside the EQP diagnostic to recreate the geometry from the extractor to the field-free drift region. The electrostatic fields in this region are influenced by the potentials on various surfaces such as the extraction and transfer lenses, filaments, chamber walls and the cage itself. COMSOL was chosen as a simpler modelling tool when compared to more complex suites which were also considered such as Opera3D and SIMION.

5.2.2   Design of the COMSOL 3D Model

The static electrical properties of the ion flight path and the EQP's ionization cage region were modeled with a standard COMSOL package ("AC/DC" module). An electrostatics sub-module solved for the potentials and fields in the given geometry and a charged particle tracing sub-module traced the trajectory of charged particles (simulated argon ions at various energies and initial angles) in these fields. The model was thus comprised of 2 components:

1. A stationary electrostatic solution which computed the electric fields

2. A time dependent charge-particle tracing solution which computed the trajectories of injected charged particles based upon these electric fields.

A cylindrical infinite element domain provided the necessary boundary conditions to bring all fields to zero at distances far enough away from the surfaces. The geometry was reconstructed directly from official Hiden EQP schematics (**Appendix A, Figure A.2 & A.3**), confirmed to be appropriate to the project's systems dimensions and settings.

The geometrical space recreated the physical structure and electrical conditions within the cage region but was kept as simple as possible without losing any of the physics. For example, the ceramic spacers separating the live and grounded electrodes were replaced with a hollow surface that had the material properties of vacuum – that is, a dielectric with a permittivity of 1. These were then attached to the cylindrical infinite element domain which provided a boundary condition of the finite model, so that electrical field equations were automatically scaled. The full annotated schematic of the geometry is shown in **Figure 5.6**:
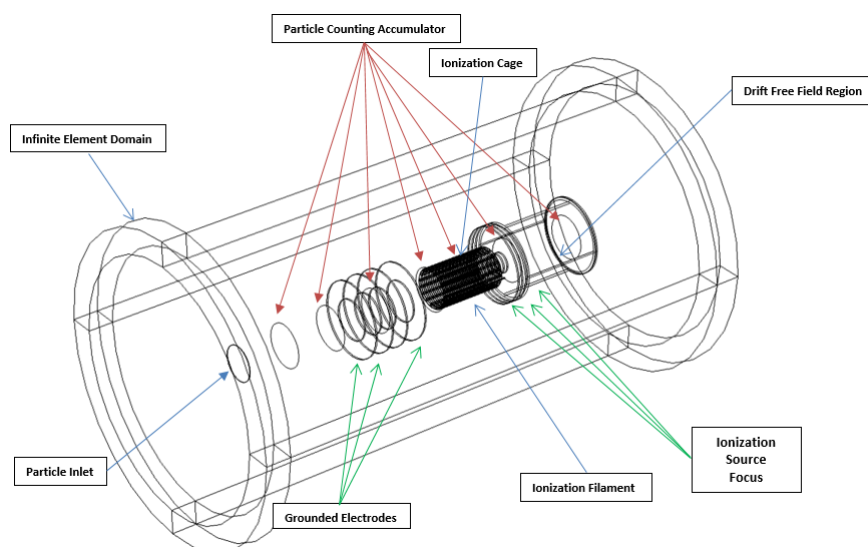
FIGURE 5.6: Annotated schematic of the EQP flight path.

The model was simplified using a number of factors. A single ionization filament was modeled as a thin straight cylinder of given length. The actual filaments are uniform iridium wires of 0.15 mm diameter. The cage was modelled as a surface with a 40% transparency to particles. The transparency relates to the total empty area divide by the solid materal of the mesh. The actual cage is formed from a woven mesh and is approximately 40% transparent to incoming electrons. There were no collisions along the ion flight path or within the cage (within the instrument $\lambda_{mfp} \sim$ several km) . The space charge of the beam itself was not included on the basis of the particle densities being sufficiently low. Therefore, ions will rarely be in close enough proximity to one another to self bias. Expanding upon this, at the background pressure the particle density is of order 10^{15} m^{-3}, so particles are on average 10 micrometres apart. The average electrical field of an ion from its centre can be estimated using Coulombs law:

$$E = \frac{q}{4\pi\epsilon_0 r^2} = \frac{1.6 \times 10^{-19}}{4\pi \times 8.85 \times 10^{-12} \times (10^{-5})^2} \sim 0.014 \, \mathrm{V \, mm^{-1}} \tag{5.1}$$

Ions at 10 eV - 30 eV would not experience any noticeable perturbation from space charge, especially within a region where external fields are set up with potentials of tens of volts. Slower ions (thermal energy ~ 0.025 eV) may however experience some space charge related perturbation. Note that electrons from filaments travel several orders faster than ions and do not collect within the cage in order to build up a significant charge density.

5.3 modelling Results

Electrostatic modelling was undertaken with three filament voltages:

- 0 V represented an environment with no filament bias and there should be no deviation off axis for the ions.

- -70 V is a typical filament voltage for RGA work since it is close to the maximum of the cross-section for the ionization of most gases.

- -150 V is an environment meant to force an extreme degradation of ion signal.

These scenarios were also used to quantify the transmission of particles and their energies into the EQP. Experimental results suggest that when the filaments are switched on (voltage applied), some charged species from the plasma are deflected off axis and fail to reach the quadrupole of the EQP. In conventional RGA, this is acceptable since the aim is to detect species ionized within the analyzer and not secondary ions.

Electrode	Voltage / V
Lens1	-190
Cage	3
Filament	0, -70 & -150
Ionization	3
Focus	-74
Axis	-40

TABLE 5.1: EQP Electrode Settings

At different filament voltages (**table 5.1**), the potential map and electrical field in XY plane (looking down onto the mid plane of the modeled region) are illustrated in **Figure 5.7, 5.8 & 5.9**.
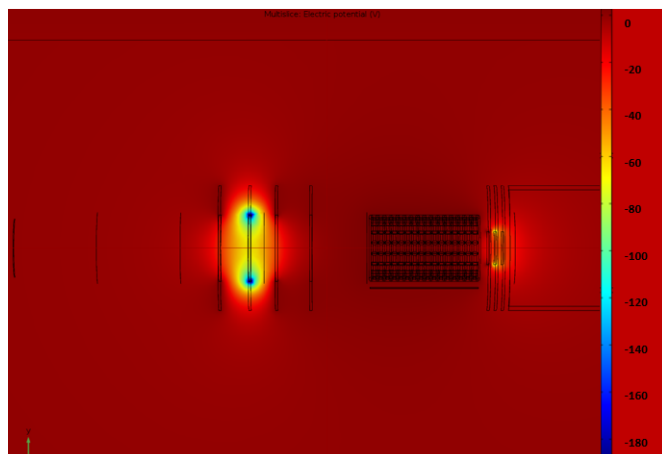
FIGURE 5.7: Potential with 0 V filament, in V.
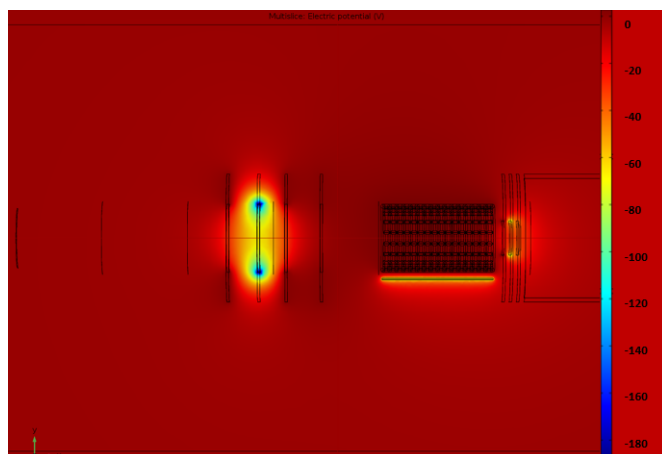
FIGURE 5.8: Potential with -70 V filament, in V.
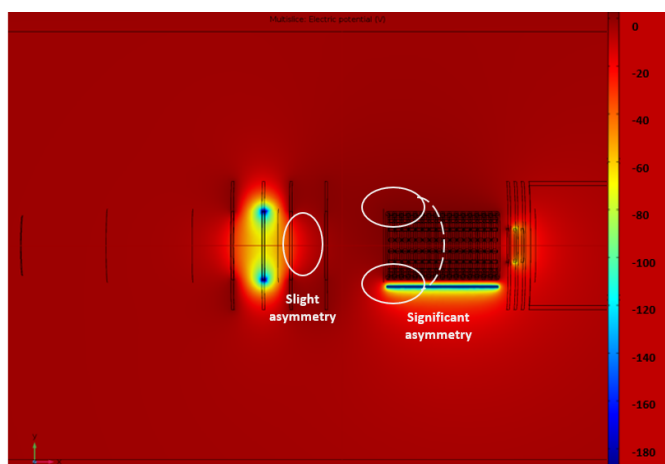
FIGURE 5.9: Potential with -150 V filament, in V.

For SIMS mode, the potential of Lens1 is shielded to prevent field induced distortions in the collimated ion beam as it approaches the cage. At 0 V filament voltage, there is no potential gradient and ions passing through the cage should do so without being deflected. At increasingly large potentials of the filament, gradients form between Lens1 and the side of the cage. The presence of an increasingly negative filament also encourages a slight decrease in potential between the grounded electrode and the region of cage (very edge of the cage interior) closest to the filament. This has been associated with a small electric field that deflected some ions off axis. Furthermore, a noticeable gradient forms between the filament and the first transfer electrodes after the cage. This serves to slow down ions and deflect them passing through that region.

The electric fields associated with the potentials were also plotted to monitor the influences of charged particles traveling through the cage and their directions. The colour shows intensity whilst the arrows show direction in **Figure 5.10, 5.11 & 5.12**:
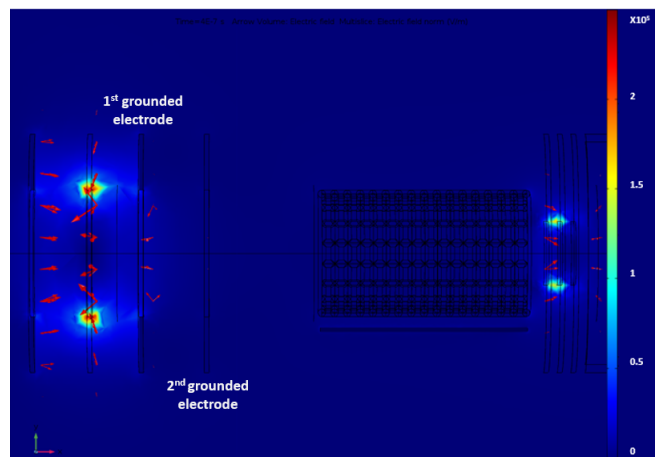
FIGURE 5.10: E-field with 0 V filament, in V mm^{-1}
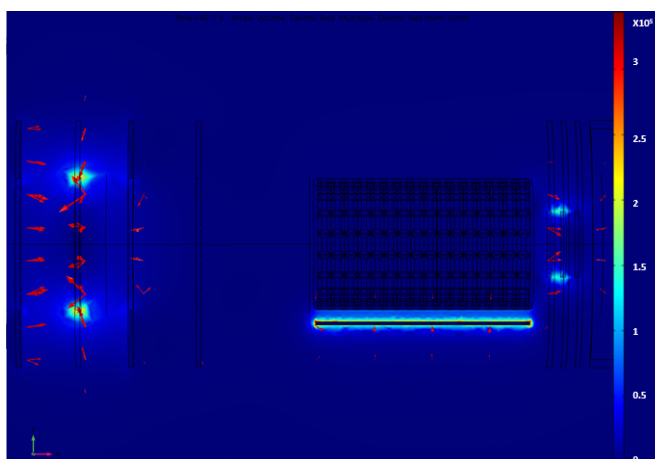
FIGURE 5.11: E-field with -70 V filament, in V mm^{-1}
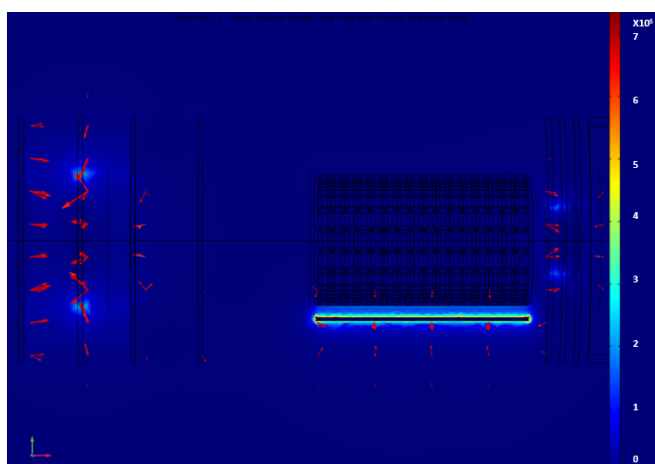
FIGURE 5.12: E-field with -150 V filament, in V mm^{-1}

As can be seen, there is no electric field within the bulk of cage. The cage at 3 V does its job of shielding the majority of the field from the filaments such that it penetrates only to the edge of the inside of the cage. The field experienced by ions is predominantly on the openings and at the very edges on the inside which corresponds with the asymmetry of the ion beam. The collimation effects for an ion beam can be seen via the direction of the electric field vectors towards Lens1. It can be see an electric field began to form at the grounded electrode at a filament voltage of -70 V due to the potential gradient between the filament and the grounded electrode. This grew larger and eventually fed to the second grounded electrode. This introduced some curvature effect on the trajectory of ions passing through that region – especially on slower moving ions. At the cage region, an electric field formed between the cage and filament and permeated slightly into the cage itself. Although this field is non-existent in the bulk of the cage, ions closest to edge of the cage experienced the field. This ended up causing an asymmetrical effect where part of the beam was displaced and collided into the side of the cage closest to the filament. This affected the transmission of ions from the inlet to the field-free drift region. Lastly, electric fields formed between the filament and the Focus transfer electrode. This was shown to contribute to the deflection of ions passing through the cage region.

The energy of the injected ions were varied as 10, 20 and 30 eV. Because damage free etching requires ions between 10 eV and 30 eV, ions lower than 10 eV and higher than 40 eV were not modelled.
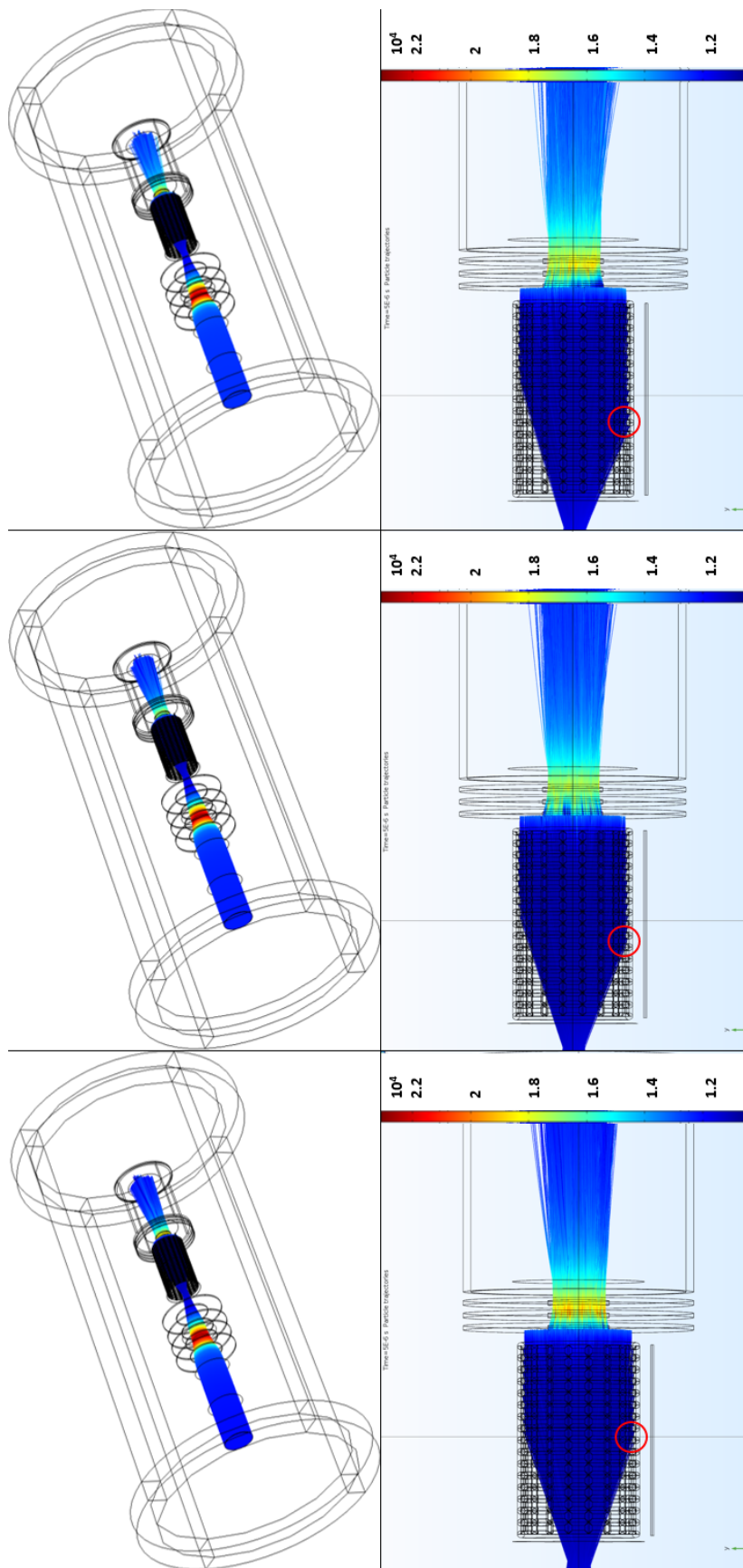
FIGURE 5.13: Trajectories of 30 eV ions along the EQP flight path, speeds measured in m s^{-1}.
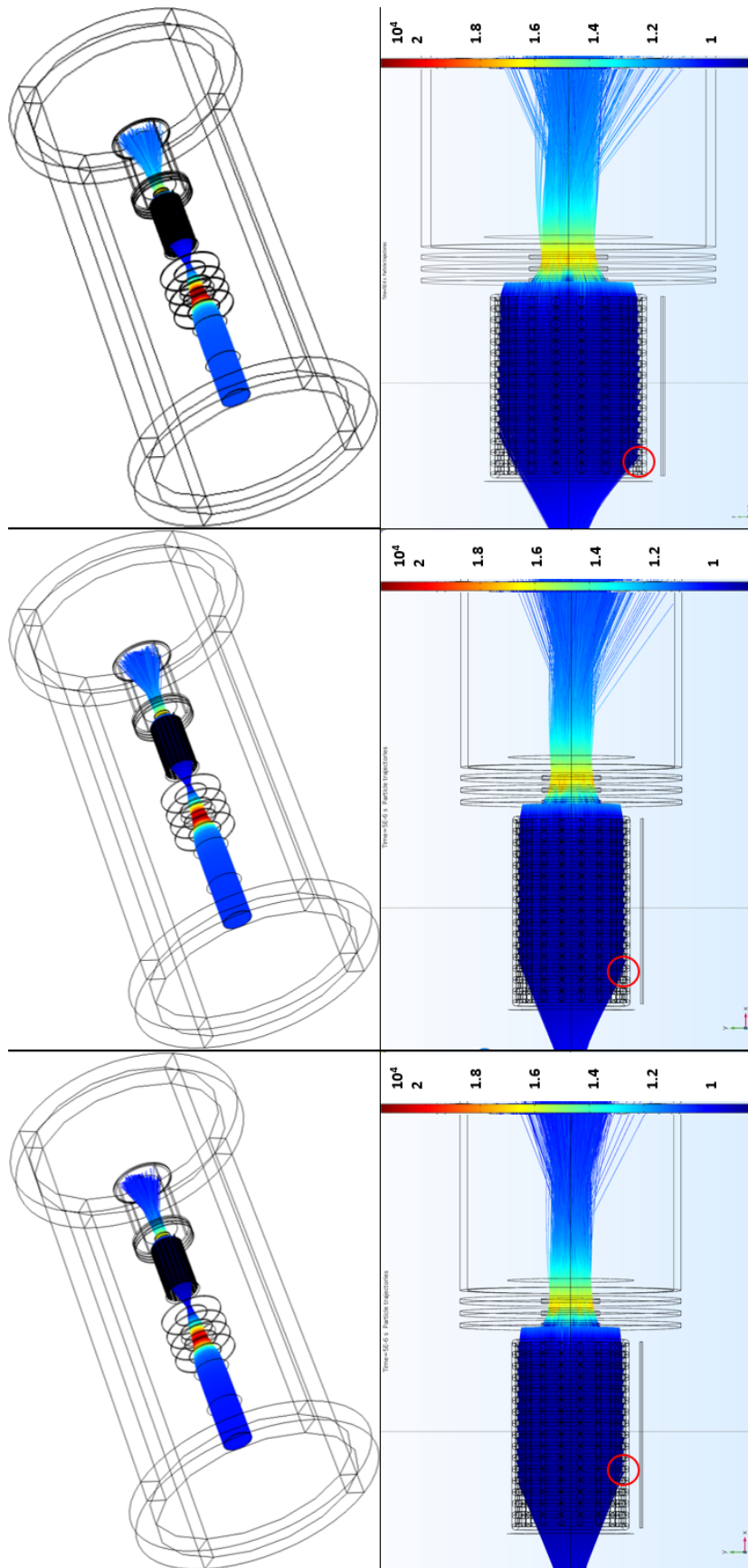
FIGURE 5.14: Trajectories of 20 eV ions along the EQP flight path, speeds measured in m s^{-1}.
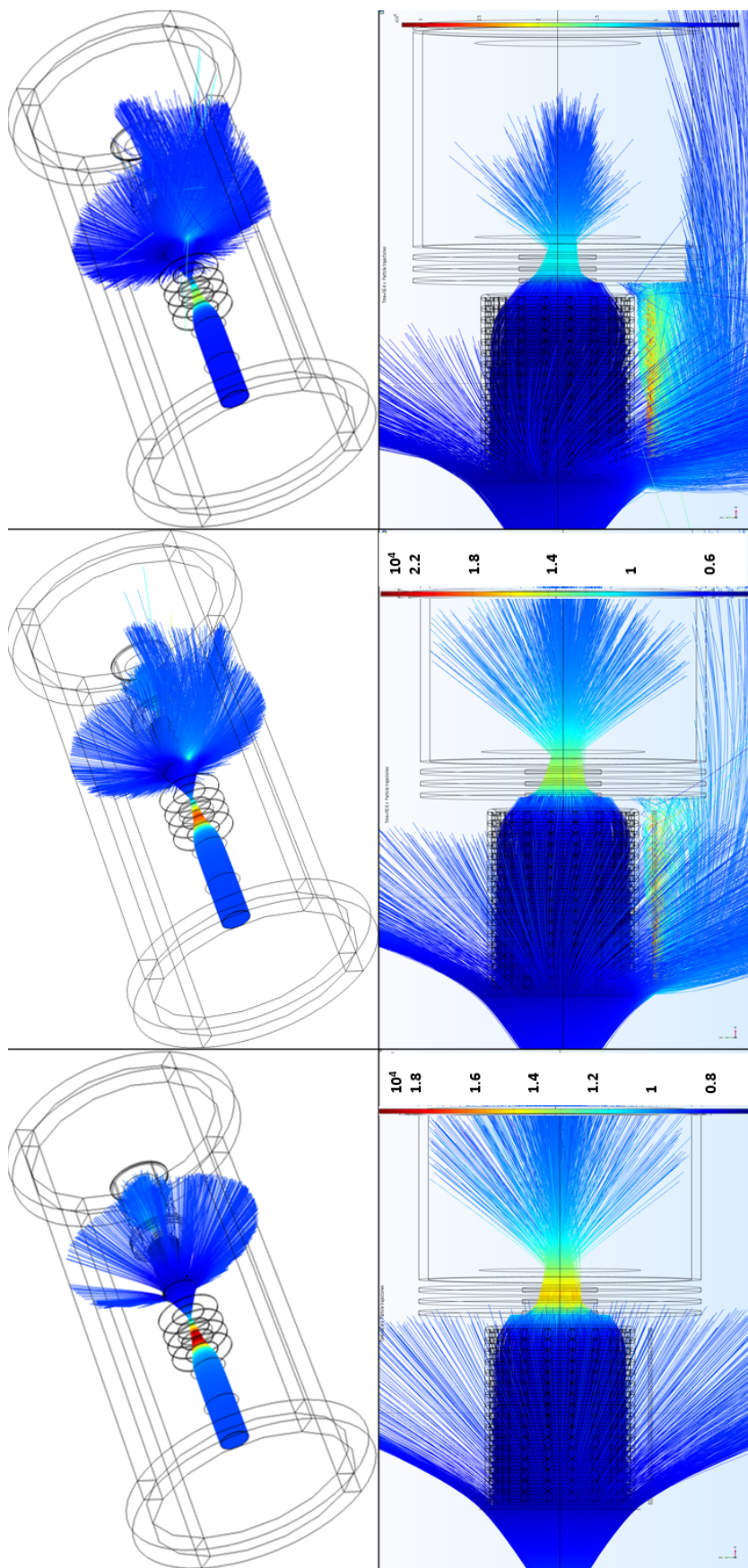
FIGURE 5.15: Trajectories of 10 eV ions along the EQP flight path, speeds measured in m s^{-1}.

Increasing the filament voltage drags ions towards the side of the cage where the filament is closest. This affects the number of ions traveling through the field-free drift region which decreases as the filament is made negative. The slower 20 eV ions (**Figure 5.14**) makes them more susceptible to the fields and this can be seen by a larger divergence of the ion beam within the entrance to the cage. Again, the ions closest to the filament are lost. A lot of the ions that do end up traversing to the field free drift tube, do so off axis. 10 eV ions (**Figure 5.15**) are slow enough to be greatly deflected by the cage field and are especially susceptible to the filament. When the filament is at 0 V, some of them traverse the cage and reach the field-free drift region but off-axis. It also appears that the geometry of the transfer electrodes contributes to the loss of ions between the cage and the field free drift region. This is magnified with increasingly negative filament voltage and slower energy ions. If the filament is made even more negative, 10 eV ions are lost completely and this appears to correspond with the consistent 'blind' regions often seen in RGA mode.

The number of particles passing through certain points of the flight path were measured using accumulator type objects. Symmetrical circles were created at certain distances along the ion flight path and given the wall condition 'pass through' and set to object 'accumulator'. This meant that they offered no interaction to the ions. The initial ions from the inlet were defined as a having a current of 10 μA with 10,000 particles (1000 particles for every 1 μA).
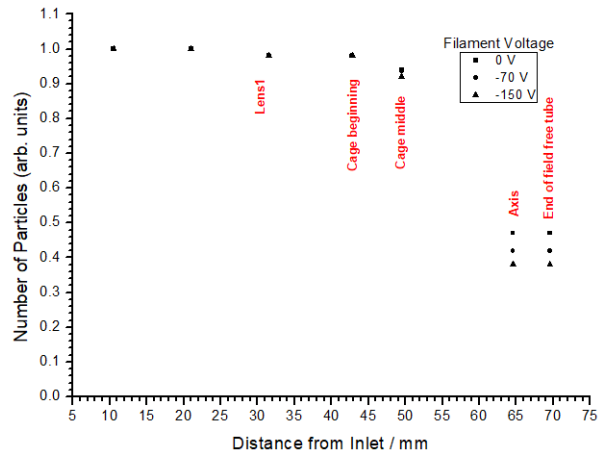
FIGURE 5.16: Number of 30 eV particles measured.
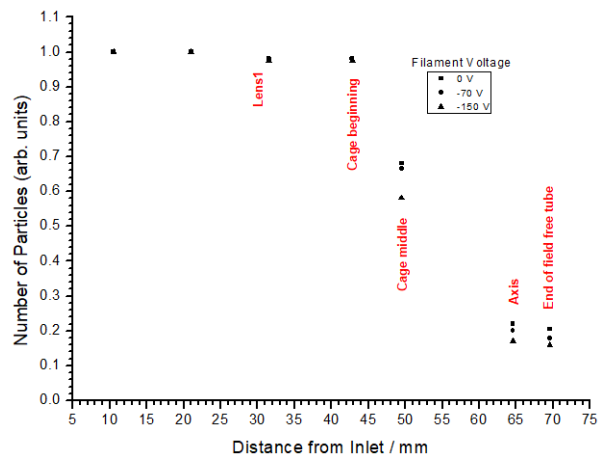
FIGURE 5.17: Number of 20 eV particles measured.
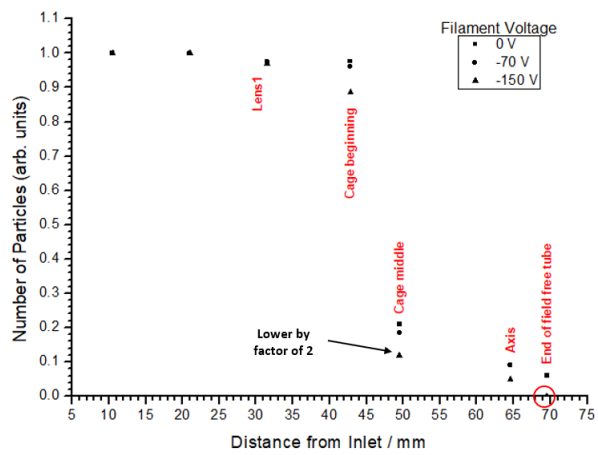
FIGURE 5.18: Number of 10 eV particles measured.

(**Figure 5.16, 5.17 & 5.18**) show that the largest losses appear to come

from just before the cage or within the cage, although there is a slight loss in particle population just before Lens1. Even without filament bias, ions appear to be colliding with the cage and transfer electrodes and are subsequently lost. This becomes more pronounced when the filament is biased and large numbers of ions are lost suggesting that a lot of the losses are geometrical in nature. It can be seen that for 10 eV ions, they are affected by electrostatic fields before they reach the cage and are subsequently deflected off axis to the extent that fewer than 10% of them are detected past the field free tube and none are detected when the filaments are biased. Increasing the energy of the ions makes them less susceptible to field effects, as can be seen with 20 eV and 30 eV demonstrating a large number of them passing into the cage. However, many are still lost within the cage regardless and only at 30 eV do about 50% of the original population still leave the cage. The energetic response of the EQP below 5 eV is dependent on the extraction field and optimization. However, for ion energies in the range 5 eV to 100 eV it is stated by Hiden Analytical to be approximately constant. The optimization of the EQP is done through tuning where the extraction and transmission electrodes are optimized for the highest count rates across all energies. This optimization method is also dependent on the geometry of the system. The experimental results and the modelling shown here appear to suggest that there is an energy dependence.

At increasing energies, it is less likely for there to be losses due to the geometry and field effects. But for neutral detection, increasing their energies appears to make them more difficult to capture. Combined with some ionized neutrals still being lost (if they were ionized at the beginning of the cage), this creates a balancing point where for neutral beam studies, the appropriate method is to measure the ion signal when the filaments are non-emissive and then to measure the signal again when the filaments are emissive. Any enhancement of the signal is taken to be energetic neutrals which not only replaced the ions lost but also added to the distribution.

In conclusion, it can be seen that fast neutral energy measurements can be made and the method of detection works because once plasma ions are lost from the axis, there is no mechanism which can restore them. The small sample size constrained the generalization of these results, however the sample size is representative of a majority of plasma conditions, the energies of the ions created and the relevance of these energies (10 – 30 eV) being used for damage free neutral beam etching. Although the quantification of the ion beam and its variation due to energy and system geometry has been showcased, quantifying them has challenges. Not only would plasma ions be lost on axis, but depending on where neutrals are ionized within the cage, it can be inferred that some of those neutrals would also be lost on axis. Neutrals ionized towards the beginning of the cage could possibly be at the same risk of being lost as an external ion. This would be less significant at plasma potential (represented by 30 eV modelled particles) where overall approximately 60% of the ions still make it through to be detected. 10 eV ions created from 10 eV neutrals still have a higher chance of being lost and this is consistently reflected in blind regions about 10 eV. Variation in the transmission of ions at different energies appears to be largely geometrical in nature as seen by marked drops in particle numbers within the cage and at the transfer electrodes.

5.4 Summary

The EQP was introduced as the main diagnostic instrument for the study of process plasmas in an ICP. Peculiarities within the EQP were highlighted and modelled using COMSOL 3D. It was shown that within the the energy range of 10 - 30 eV, there are potentially severe electrical interferences which prevent the transfer of ions into the detector. Some of the interference is geometrical in nature, with many ions being lost within the cage and at the transfer electrodes. It was shown that more energetic ions are likely to travel along the EQP flight path without being deflected. Ions deflected off axis were shown to have no mechanism by which they could come back on axis, therefore eliminating the ambiguity in neutral energy measurements via the modulation of ionization filaments. There is a greater understanding of the use of an EQP in conventional positive ion and RGA modes, and its potential use for fast neutral measurements. The case to use it in fast neutral detection mode has been presented and chapter 6 will display and discuss these results.

Chapter 6

Neutral Beam Energy Measurement

This chapter follows directly from **Chapter 5** and illustrates the measurement and characterization of energetic neutrals in Ar and O_2 discharges. O_2 was used because it represented a slightly more complex molecular discharge. Results are compared with earlier works [50, 84]. Detecting and measuring neutral particles is more difficult than measuring ions. Classically, electrostatic probes are used to provide detailed information about ionic species and electrons present in a plasma. Neutral species are not amenable to such methods of detection and remain a challenge. Diagnostics such as calorimetry, microparticles and gridded pressure sensors [85] have been used with limited success due to a combination of indirect measurement and low resolution. A neutral particle analyzer was developed by Vanblokland *et al.* [86] to measure neutral particles within the energy range of $10 - 90$ keV with mass discrimination. The analyzer used a carbon foil mechanism to strip the neutral particles and this mechanism was also adopted by Kusama *et al.* [87] for neutral particles in the MeV energy range. Although most fast neutral detection is applied for very high energy neutral beams in fusion plasmas, work has been done to characterize neutral beams < 100 eV which includes the use of calorimetry and microparticles by Trottenberg *et al.* [88] and Stahl *et al.* [89]. With respect to calorimetry, discrimination of ions from neutral species and the low resolution of

calorimetric probes make this method challenging. The most straightforward approach to measure < 100 eV neutral particles is the application of mass/energy analyzers such as in this work.

Challenges associated with neutral detection can be summarized in 3 points:

- Cross-sections for electron ionization variy depending on fast neutral energy (though not greatly). This is mitigated by firing ionizing electrons perpendicular to the neutral flight path such that they appear at rest to the much faster electrons. This is within the design of the EQP.

- The fluxes of fast energetic neutrals are not very high (much less than cool neutral gas and no more than ions). This is a product of the source of energetic neutral species and the average particle density within the EQP itself. Any neutral beam source must be able to provide a significant quantity of neutral species. Being able to detect them is encouraged by measuring with high dwell times.

- Neutral species may not always be traveling completely on axis, cannot be pre-collimated and may not be collectible in the standard ion optics of the EQP.

This chapter nevertheless demonstrates the successful detection of energetic neutral particles from the experimental ICP setup using an EQP. Ions extracted from the ICP through a mesh and passing through a 7 cm neutralization zone will be discussed first. Afterwards, the ion signal when a carbon neutralizer is placed after the mesh will be compared. Lastly, the neutral component itself will be discussed.

6.1   Plasma Characterization in SIMS Mode

6.1.1   Overview of an Ar / O_2 Discharge

Ions were sampled by the EQP beyond a mesh from an Ar/O_2 plasma ig-
nited at 300 W and 1 mTorr pressure (10 SCCM flow rate each), the mass
spectrum of the most intensive ions have their main peaks at m/q = 16
(O^+), m/q = 32 (O_2^+) and m/q = 40 (Ar^+):
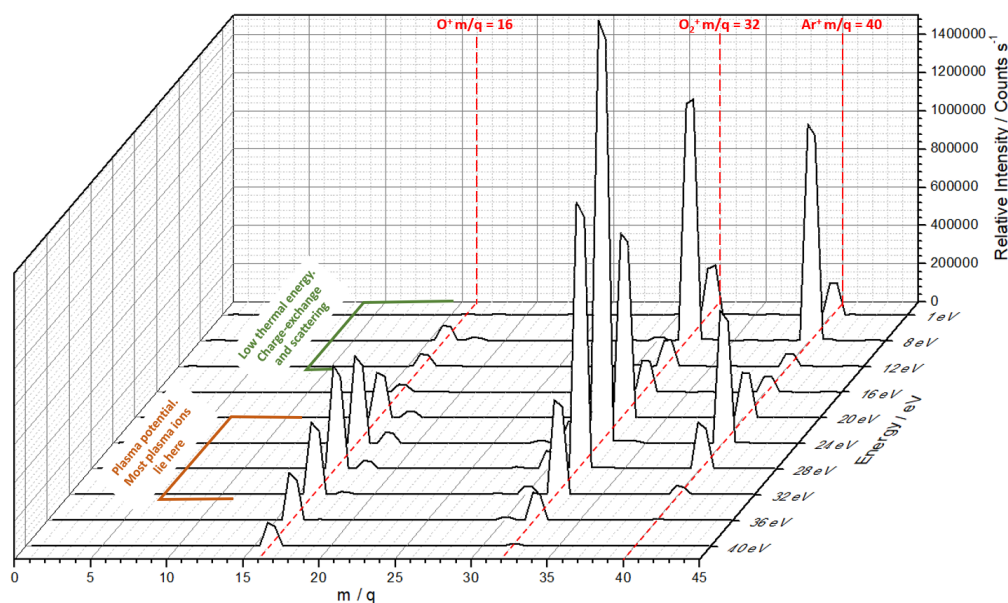
FIGURE 6.1: 3D SIMS scan of Ar/O_2 ions. Distributions of
O^+, O_2^+ and Ar^+ are seen at m/q = 16, 32 and 40 respec-
tively.

The pressure in the neutralization region was measured to be compa-
rable to the plasma pressure at 1 mTorr. In **Figure 6.1**, small H_2O peaks
(mass 18 and 17) of comparatively low intensity but high energies were de-
tected. The energy distribution of Ar^+ begins with a low energy peak at
1 eV – 8 eV. Because it is quite intense but falls off rapidly approaching
10 eV, this is interpreted as the result of resonant charge-exchange colli-
sions with neutral species within the neutralization volume leading to low
energy ions close to the analyzer entrance. The mean free path for charge-
exchange at this pressure is approximated to be 15 cm so that with the 7

cm neutralization region, a large number of ions should pass through without having a collision. However, there still appears to be sufficient charge-exchange and scattering to produce low energy ionic species that mirrors the low energy distribution. The steady rise of intensity up to 24 eV is indicative of ions gaining energy approximately equal to plasma potential as they travel from the bulk plasma and fall through the sheath. Multiple secondary peaks suggests collisions within the sheath. Past the plasma potential are higher energy ions which gained energy from the bulk, passed through the sheath and reached the detector without collisions. These are fewer in number as represented by their lower intensities. The IED of **Figure 6.1** is dominated by mass 32, O_2^+. This suggests that there is more O_2^+ within the plasma even though O_2 and Ar were both introduced into the chamber at the same flow rates. Again, there are large low energy peaks which mirror that of mass 40, suggesting the charge-exchange occurring with neutral O_2. The IED's mirror each other closely which is representative of the comparable masses of O_2 and Ar. The IED of mass 16 (O^+) has very low intensity low energy peaks, suggesting reduced opportunity for charge-exchange and there being not as much neutral O as there is O_2. Also, its peak energy appears to be at 28 eV which is indicative of lighter masses being more responsive to the RF field and having a wider energy spread. The general presence of large peaks at lower energies for both Ar^+ and O_2^+ does suggest charge-exchange collisions rather than the result of secondary plasmas formed within the neutralization volume. If there was secondary plasma being formed on the grounded mesh grid, this would have been seen via optical observation. Also, there was very little effect on the energy of these peaks when the plasma was biased.

It is notable that the low energy peaks of O_2^+ and Ar^+ are almost identical suggesting comparable charge-exchange mechanisms both with themselves and each other, whilst the mechanism for O^+ is non-resonant and of a lower reaction rate with heavier species – as seen by extremely low intensity low-energy peaks. The rate constants for resonant and near-resonant

charge-exchange between the heavy and light species are considered:

$$Ar^+ + Ar_{slow} \rightarrow Ar^+ + Ar_{fast}; \; K_{Ar,\,Ar} = 4.67 \times 10^{-16}\,\mathrm{m^3\,s^{-1}} \qquad (6.1)$$

$$O_2^+ + O_{2\,slow} \rightarrow O_2^+ + O_{2\,fast}; \; K_{O_2,\,O_2} = 5.17 \times 10^{-16}\,\mathrm{m^3\,s^{-1}} \qquad (6.2)$$

$$O^+ + O_{slow} \rightarrow O^+ + O_{fast}; \; K_{O,\,O} = 5.22 \times 10^{-16}\,\mathrm{m^3\,s^{-1}} \qquad (6.3)$$
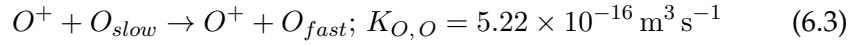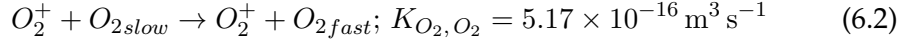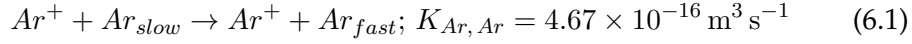
The above rate constants for resonant charge-exchange were calculated from the capture cross-section [6]:

$$\sigma_L = \left(\frac{\pi \alpha_p q^2}{\epsilon_0 m} \right)^{\frac{1}{2}} \frac{1}{v_0} \qquad (6.4)$$

Where α_p is the polarizability and v_0 is the relative speed. The rate constants are approximately equal. The net production of each slow ion species depends on the gas density and ion density as $K[n_{fast}^+][n_{slow}^0] = \mathrm{products\,m^3\,s^{-1}}$. Non-resonant charge-exchange between Ar, O_2 and O and near-resonant charge-exchange between Ar and O_2 were considered:

$$Ar^+ + O_{slow} \rightarrow O^+ + Ar_{fast}; \; K_{Ar,\,O} = 1.2 \times 10^{-17}\,\mathrm{m^3\,s^{-1}} \qquad (6.5)$$

$$O_2^+ + O_{slow} \rightarrow O^+ + O_{2\,fast}; \; K_{O_2,\,O} = 1.55 \times 10^{-17}\,\mathrm{m^3\,s^{-1}} \qquad (6.6)$$

$$Ar^+ + O_{2\,slow} \rightarrow O_2^+ + Ar_{fast}; \; K_{Ar,\,O_2} = 5.1 \times 10^{-17}\,\mathrm{m^3\,s^{-1}} \qquad (6.7)$$
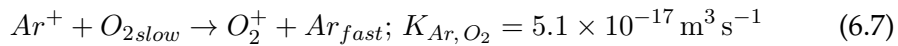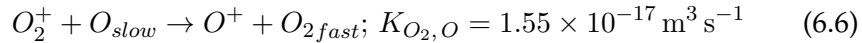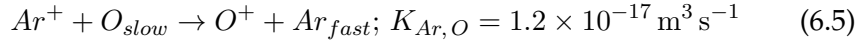
Reaction rates were adapted from Tinck *et al.* [90]. Resonant charge-exchange has up to 40 times the rate of non-resonant charge-exchange. Furthermore, within the neutralization region there is no absorption of power and neutral atomic species are likely to recombine rather than be created - thus, the densities of O and O^+ are much lower compared to heavier species. This is consistent with the observation of low counts of low energy O^+ in **Figure 6.1**.

6.1.2 Porous Mesh Studies

The IED of Ar^+ is shown in **Figure 6.2**:
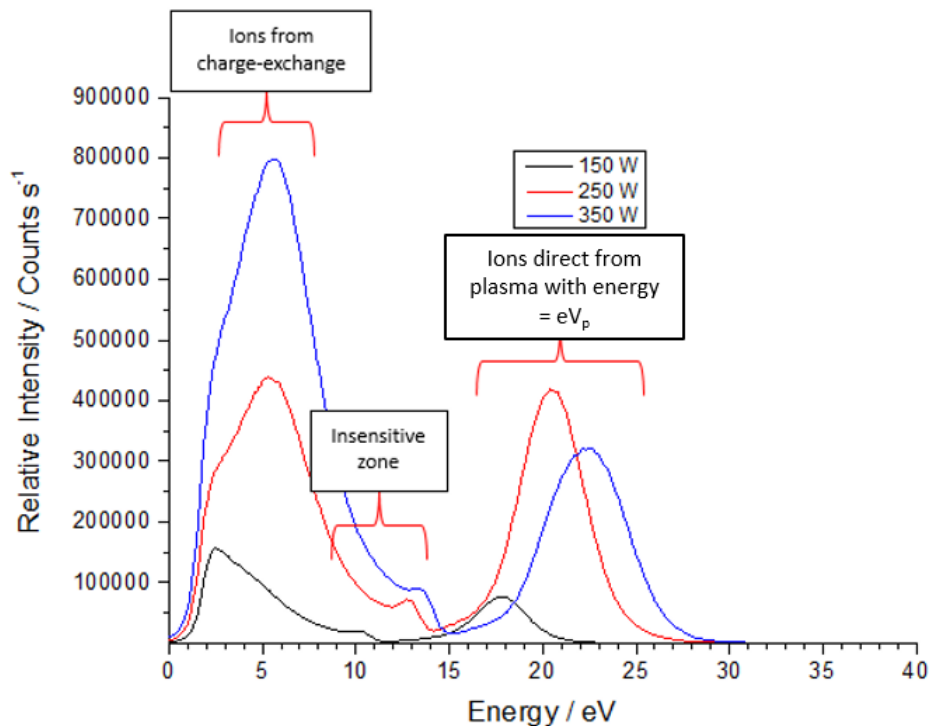
FIGURE 6.2: SIMS scan of Ar^+ 1 mTorr with changing power.

It can be seen that the plasma potential V_p (high energy peak) varies within 5 eV as the power is increased. Due to contributions from capacitive coupling in an ICP, small increases of plasma potential with RF power are expected. At 150 W, a large low energy peak was recorded at around 2.5 eV which grows with power until it peaks at 5 eV at 350 W. Visual inspection through an optical window of the neutralization region and the mesh grid, showed no secondary discharge. This low energy group of ions must have therefore originated from the main plasma, losing their energy in charge-exchange collisions in the neutralization volume and scattering collisions. **Figure 6.2** also illustrates the effect of the extractor electrode on the EQP which drags ionic species in from different directions in order to sample all energies and may produce artifacts. To avoid this, it was later set to ground potential. Due to the nature of the setup and the fact that there is no potential gradient between the mesh and the EQP orifice, there should be no

mechanism to gain energy within the neutralization region.

At 150 W, the power absorption is lower which reduces the ionization efficiency and therefore the plasma density. This is illustrated in **Figure 6.2** by a lower intensity energy distribution and a plasma potential peak at about 17 eV. When the plasma power is raised, there is an increase in plasma energy density illustrated by the shifting of the plasma potential to 20 eV at 250 W and then 23 eV at 350 W indicating increased power absorption. The increase in signal intensity of the ions is because electron density varies approximately linearly to plasma power and this translates into a higher plasma density. It is also seen that the tail of the distribution steadily increases.

In further studies, the plasma was biased with a stainless steel perforated bias plate (10 cm from bottom electrode of the ICP coil) at several voltages. The potential structure of the plasma with plasma bias is shown in **Figure 6.3** whilst the full electrical circuit of the EQP setup is shown i **Figure 6.4**.
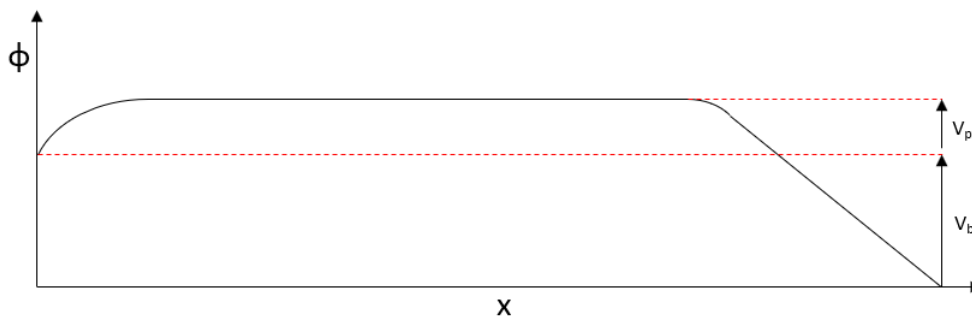
FIGURE 6.3: Schematic of biased plasma potential structure. x axis is distance. V_p and V_b represent the plasma potential and plasma bias respectively
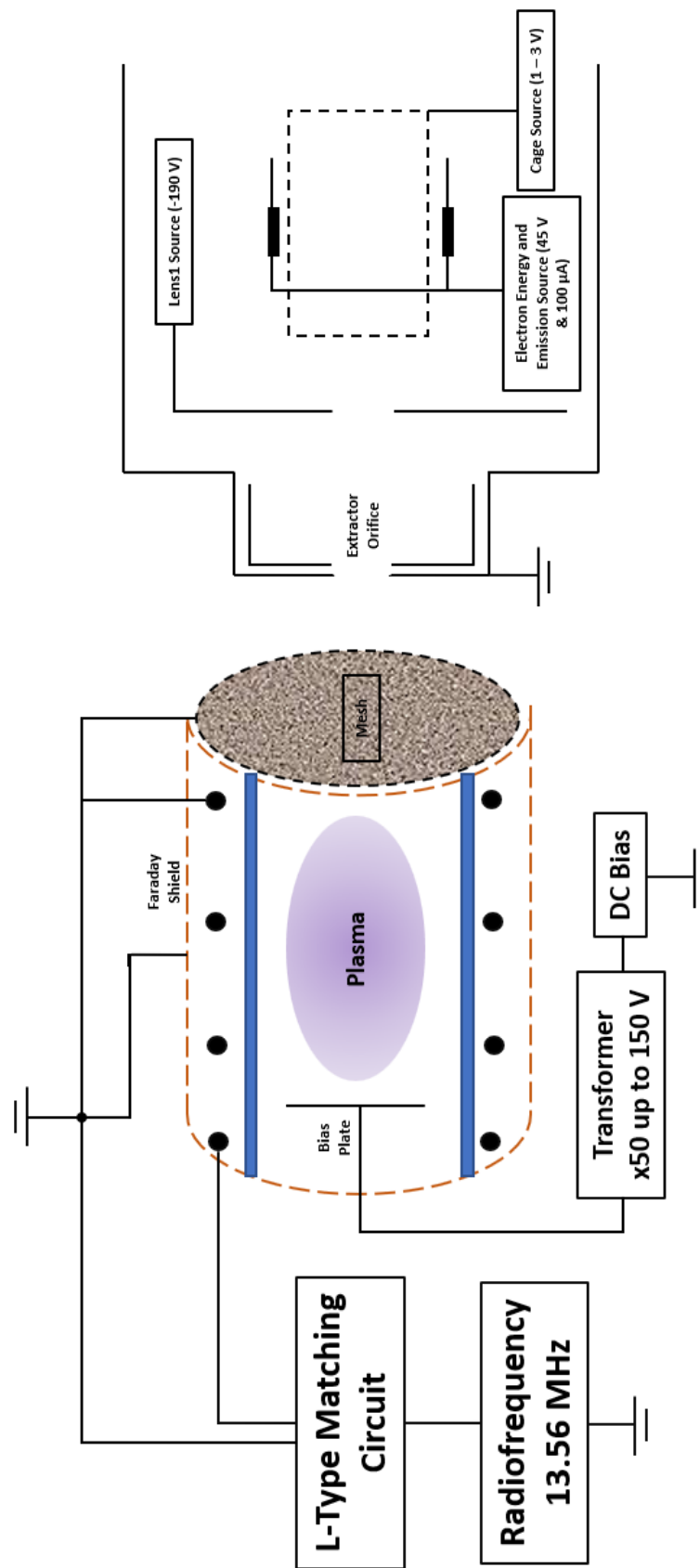
FIGURE 6.4: Schematic of the experiment with plasma biasing.

As mentioned in **Chapter 1**, the plasma sits above a known ground (in this case the reactor vessel) at plasma potential. In order to prevent a total loss of negative charge density onto the plate and maintain equilibrium, the plasma must therefore sit more positively above this plate bias. V_b is increased to raise V_p further above ground, this results in the extraction of increasingly energetic ion species. **Figure 6.5** illustrates the 1 mTorr, 250 W Ar discharge when it is biased in 10 V increments:
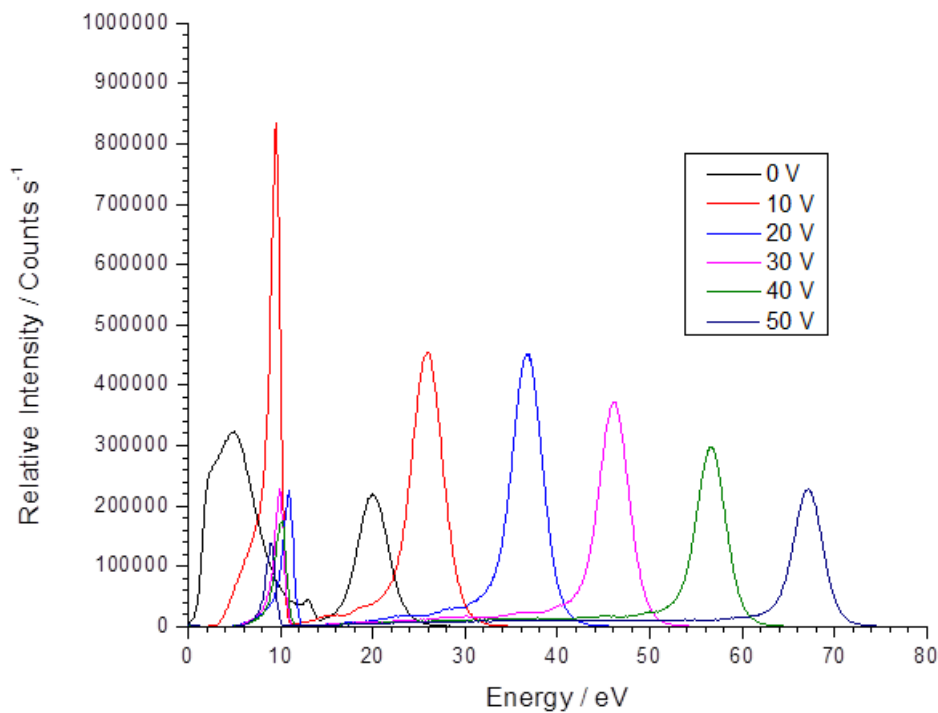
FIGURE 6.5: SIMS scan of Ar$^+$ with plasma bias.

10 V increment bias steps translate into shifts of approximately 10 eV on the IED's. 0 V bias represents the trace at 250 W seen in **Figure 6.2** with an intensive low energy peak centered at 2.5 eV. When 10 V bias is applied to the stainless steel electrode, it can be seen that the plasma will sit at a higher potential and this is seen as an approximately 6 eV shift in the peak to 25 eV plasma potential which suggests an absorption of the potential elsewhere in the system other than the plasma. Subsequent IED's are however 10 eV apart. The low energy tail of each distribution persists until around 10 eV which is a known insensitive region before becoming intensive again at the high energy plasma potential peak.

At 10 V, this low energy peak shifts to approximately 9 eV and becomes very intense. The intensity drops markedly at increasing bias voltages and regresses in energy between 40 V and 50 V bias. This is considered an artifact. With the exception of 10 V bias, plasma biasing does not appear to markedly shift this low energy peak, only becoming a lower intensity at higher plasma biases. It could be argued that not all the energy is being lost in charge-exchange collisions (near-resonant collisions between Ar and O_2) and within the neutralization region there may be a degree of 2nd and 3rd collisions. But due to the calculated mean free path at the working pressure, multiple collisions are unlikely as well as resonant charge-exchange having a higher rate coeffcient. These artifacts must therefore be a consequence of the extractor.

Some further conclusions can also be made from the above results in **Figure 6.5**; the directionality of the incoming ions can be increased or decreased with biasing the plasma hence the increase in signal intensity from 0 V to 20 V. This intensity reduces between 30 V and 50 V biases. This can be explained with regards to the geometry of the EQP as the extraction and transfer electrodes of the EQP are sensitive and tuned to the energies of incoming particles and it is likely that for certain plasma biases, some energies are more likely to be traveling on axis. There is also the question of response of the detector to higher energy particles. The EQP SIMS signal maintains the distinction between biases but gradually decreases in intensity which suggests that at higher biases, energetic particles are either not completely traveling on axis or the EQP is less responsive to those energies. These observations are summarized in **Figure 6.6**:

(A) Intensity plotted against V_p.

(B) V_p plotted against V_b
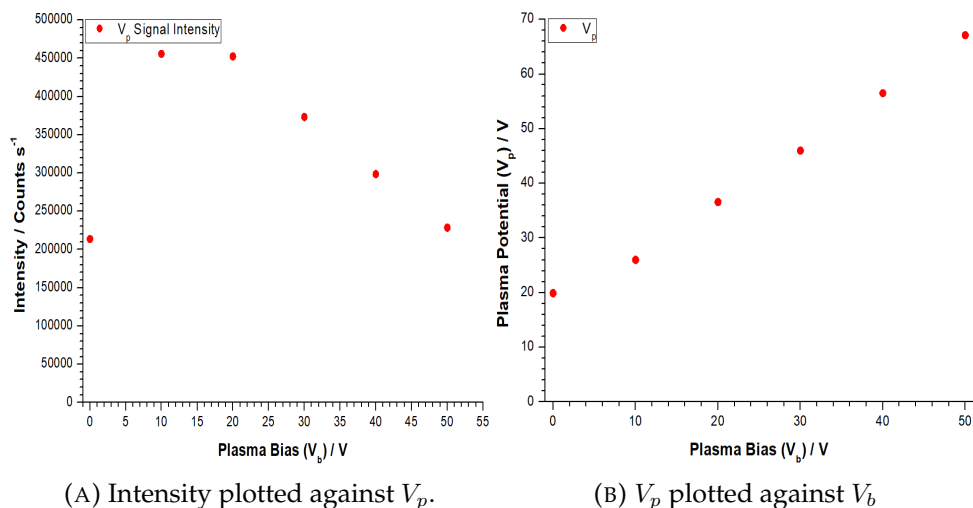
FIGURE 6.6: Combined graphs of intensity and V_p varying with V_b.

It is seen that although the intensity increases at the first increment of bias (**Subfigure A**), it decreases linearly at subsequent bias voltages V_b - contradictory to the idea that plasma biasing increases the flux of ions. **Subfigure B** however confirms that V_p is directly related to V_b and increases linearly as V_b is raised.
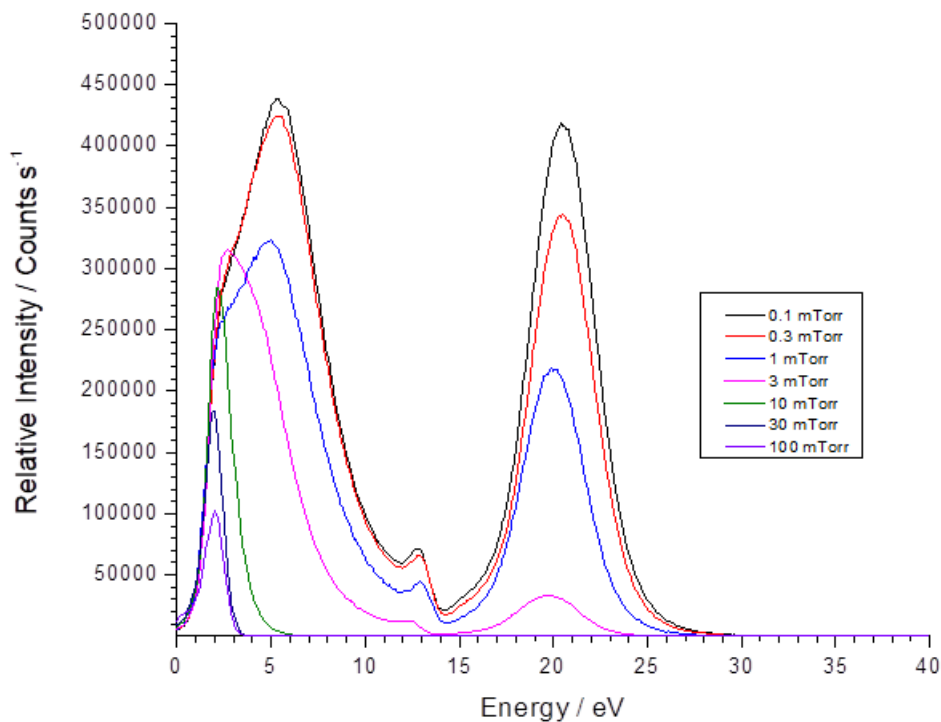
FIGURE 6.7: SIMS scan of Ar^+ 250 W with pressure. The increase of the pressure results in the suppression of the energy distribution function.

Figure 6.7 illustrates the effect of increasing the gas pressure on the intensity of ions detected and their energies. An increase in pressure lowers the mean free path which not only reduces the distance that electrons can accelerate to gain energy for ionization (ionization becomes less efficient), but also reduces distance between collisions such that energetic particles become scattered very quickly and thermalized. At 0.1 mTorr, the mean free path for scattering collisions is approximately 84 cm. Although the charge-exchange mechanism depends on pressure (mean free path approximately 1.5 m), it does not appear to be suppressed at low pressure due to the intensive low energy peak. Also at 0.1 mTorr, there should not be a very dense plasma and this is seen optically with lower light intensity and a diffuse plasma. This however not translated into counts with the EQP as at 0.1 mTorr, the distribution is the most intense with 0.3 mTorr gas pressure similar in intensity. This makes it difficult to perform absolute quantification of species population using the EQP at certain plasma parameters.

Increasing the pressure gradually suppresses both high and low energy peaks. This is due to more collisions at higher pressures and the added difficulty for ionization collisions to occur between electrons and neutral gas. The low count rates at 100 mTorr are a cause for discussion as despite an average plasma density of at least 10^{17} m^{-3}, the EQP has quantified this as fewer particles leaving the plasma therefore less particles existing within the plasma itself. It is however viable that consecutive charge-exchange and scattering collisions have made it so that very few ions manage to get to the EQP as ions and rather the neutral distribution is what becomes representative of the plasma density. This is actually illustrated in later results.

6.1.3   Carbon Neutralizer Studies

Although in this thesis gas phase charge-exchange is the main source of fast neutrals, many investigations in the field have used surface neutralization mechanisms (Auger process) based on grazing incidence. Due to the geometry of the experimental setup and the axis of the EQP flight path, it was

not possible to install a forward angle reflector. A carbon neutralizer (used extensively further on in this research and illustrated in **Figure 7.1**), also used previously in the PL-80 system [52], was located immediately after the mesh grid that separated the plasma. The carbon neutralizer had high aspect ratio holes of 1 cm length and 1 mm diameter and was grounded to the mesh grid. Ions extracted from the plasma would charge-exchange on the surface of the neutralizer and exit the structure as energetic neutral particles. Beyond the carbon neutralizer was the gas phase neutralization region used in **section 6.1.2**. **Figure 6.8** shows that the presence of the carbon neutralizer produces a lower Ar^+ signal when compared to **Figure 6.2**:
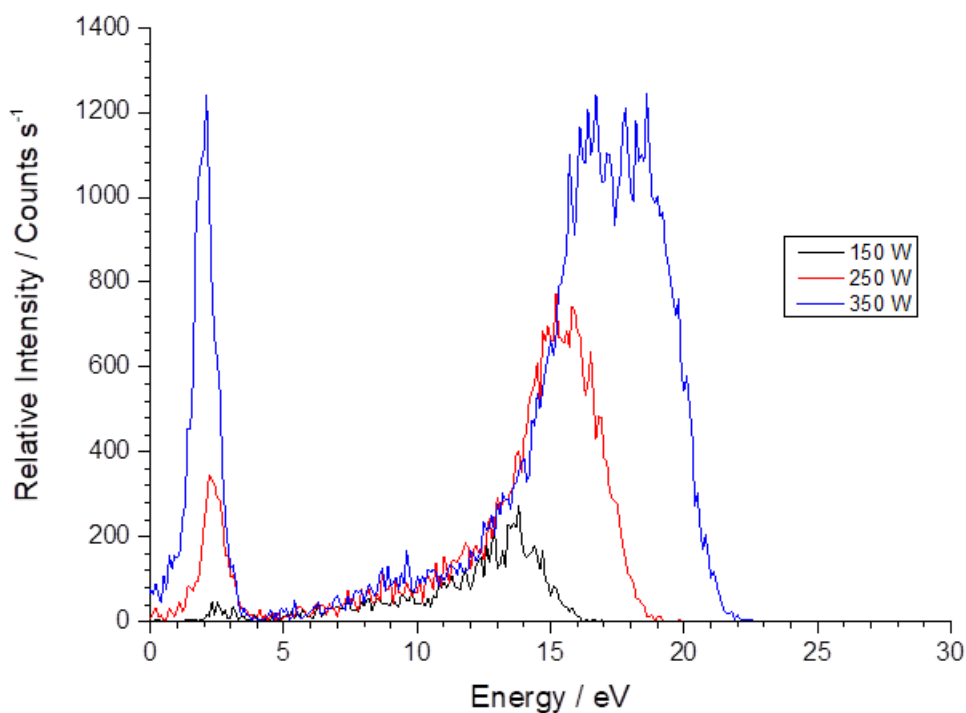
FIGURE 6.8: SIMS scan of Ar^+ 1 mTorr with changing power and a carbon neutralizer.

The presence of the carbon neutralizer appears to suppress the ion signal and this is thought to be due to ions being scattered off axis due to multiple collisions within the carbon neutralizer. The large extended low energy peaks are now absent, the low energy peak is markedly smaller at 150 W. It is noted that there is a -5 eV shift to the plasma potential peak at all powers. This is attributed to energy losses of colliding with the carbon

neutralizer (whose surface is not very smooth) and also suggests that the presence of the carbon neutralizer changes the geometry of the setup.

An increase in plasma power increases the intensity of the signal and and the average plasma ion is more energetic as the peak signal shifts to the right and corresponds with higher power absorption by the plasma. At 350 W, the intensity of the low energy peak is comparable with that of the plasma potential peak. It suggests an increase in charge-exchange.
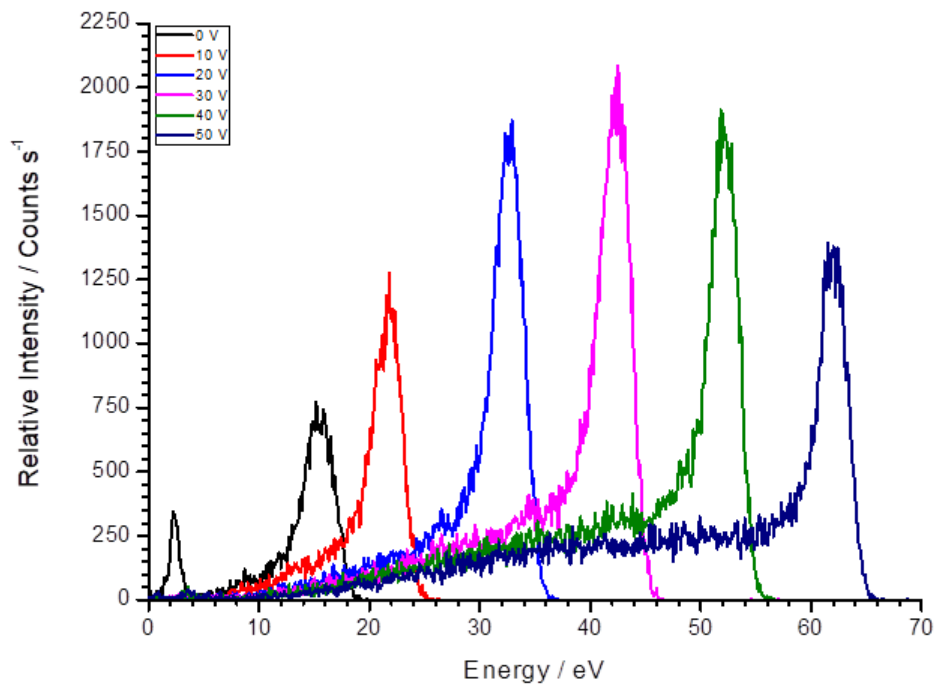
FIGURE 6.9: SIMS scan of Ar^+ 1 mTorr, 250 W with plasma bias and a carbon neutralizer.

Figure 6.9 shows that the peaks grow in intensity as the plasma is biased then falls slightly beyond 40 V. Similar to **Figure 6.5**, this suggests the variation in the directionality of ions and their collimation by the EQP transfer electrodes. However, whilst the maximum signal was seen at 20 V bias in **Figure 6.5**, the peak signal is seen at 30 V bias in **Figure 6.9**. This is also attributed to more ions passing through the carbon neutralizer without having a collision and being deflected off-axis. The low energy tail (very noticeable at 50 V bias) suggests a lot of collisionality. This could be a combination of surface collisions on the carbon neutralizer and charge-exchange

and/or scattering collisions within the volume of the neutralizer apertures. It is notable that as the bias increases, the ion spectrum becomes narrower with an eventual FWHM of ~ 1.3 eV. This is inline with the desirable effect of having a more monoenergetic stream of species following plasma biasing.
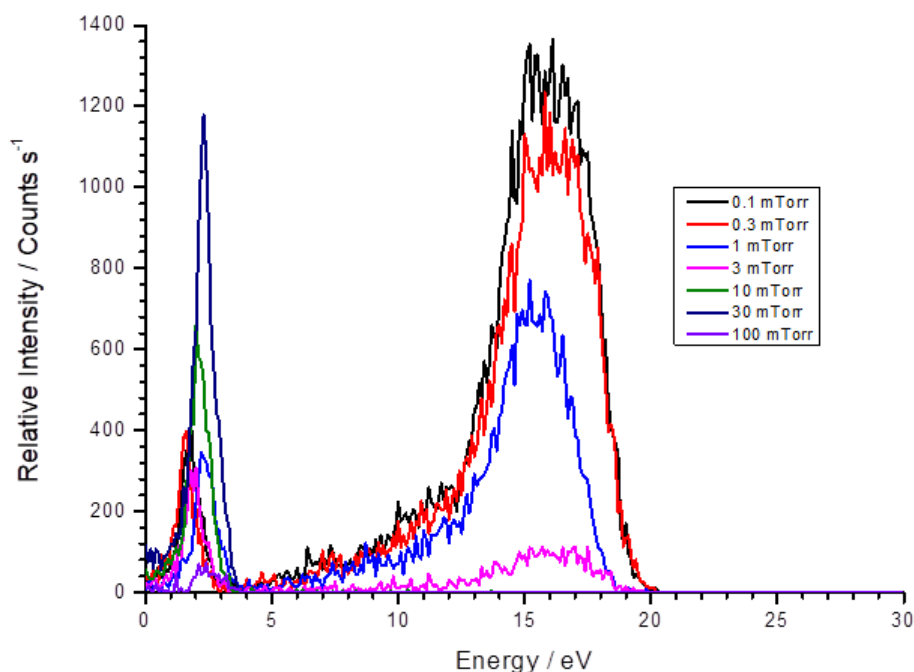
FIGURE 6.10: SIMS scan of Ar^+ 250 W with pressure and a carbon neutralizer.

Figure 6.10 shows that at very low pressures, the peak ion energy distribution is most intense. Increasing the pressure lowers the mean free path and prevents most ions from obtaining energy equal to plasma potential as they scatter continuously between the bulk and the sheath. It becomes more apparent that aside from the effect of the transmission area, gas phase collisions occur within the volume of the neutralizer aperture itself at higher pressure which diminishes the signal at all energies. This suggests scattering and total thermalization of all particles such that most ions are traveling off axis. The gradual spread of energy (peak broadening) is indicative of thermalization as the signal intensity decreases.

The lack of separate pressure control between the plasma volume and

the neutralization region made it difficult to avoid multiple instances of scattering within the aperture volume of the neutralizer at higher presure. At 100 mTorr, the ions are almost exclusively thermalized and scattered, so most will not be traveling on axis to the EQP and so there is very little signal. This is also reflected in the low energy distribution as that too is greatly suppressed, showing that at increasing pressure, no particles are traveling directionally on axis to the EQP.

Turning now to results from pure O_2 plasmas, the O_2^+ energy distributions are very similar to that of Ar^+ since they have similar masses but with greater intensity suggesting a greater population within the plasma.
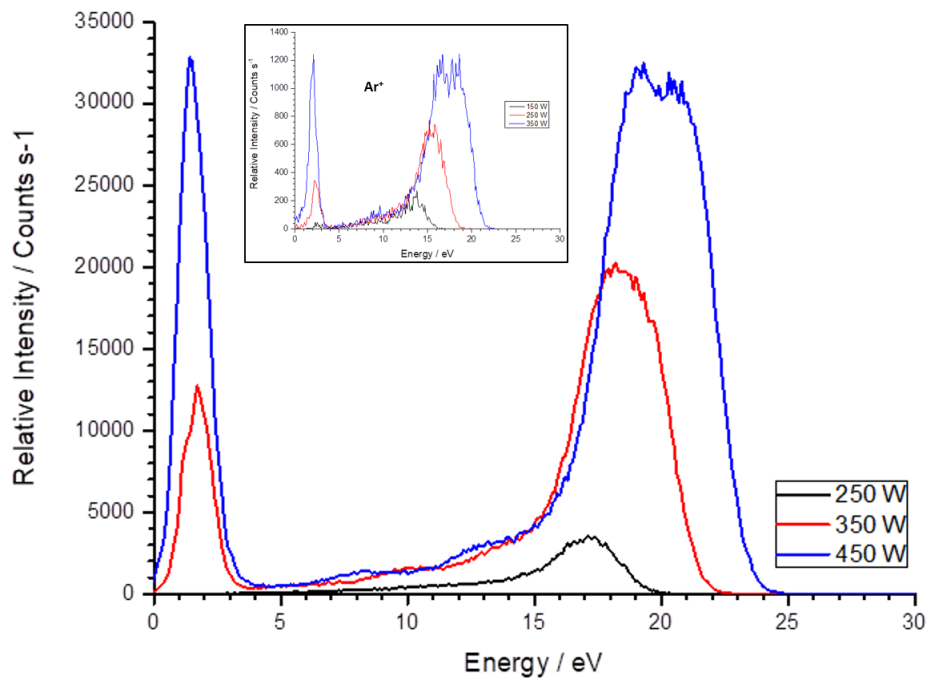
FIGURE 6.11: SIMS scan of O_2^+ 1 mTorr with power and a carbon neutralizer. **Figure 6.2** inset.

Figure 6.11 shows the effect of varying plasma power on the molecular oxygen ion density. In comparison to previous diagnostic results discussed in **Chapter 4**, it can be confirmed that the high density mode in oxygen is reached at about 250 W as there is a large jump in intensity between 250 W and 350 W. Power absorption is more complex in a molecular discharge. Again, the increasing effect of charge-exchange is seen by the gradually

increasing low energy peak against power and mirroring the low energy thermal peak of cold neutral gas. It should be noted that the feature that illustrates the charge-exchange mechanism is the presence of two very distinct peaks, one near what is assumed to be thermal energy and the second at plasma potential to highlight the momentum transfer of the charge exchange mechanism without energy loss. The range in between them in the distribution, is populated by collisions within the sheath.

The plasma peak (corresponding with potential) rests slightly higher in oxygen than that of argon. This is because O_2 being slightly lighter than Ar couples slightly more to the RF field. This is further represented by the slightly twin peak distributions for O^+. The ion energy distribution of O^+ is shown in **Figure 6.12**:
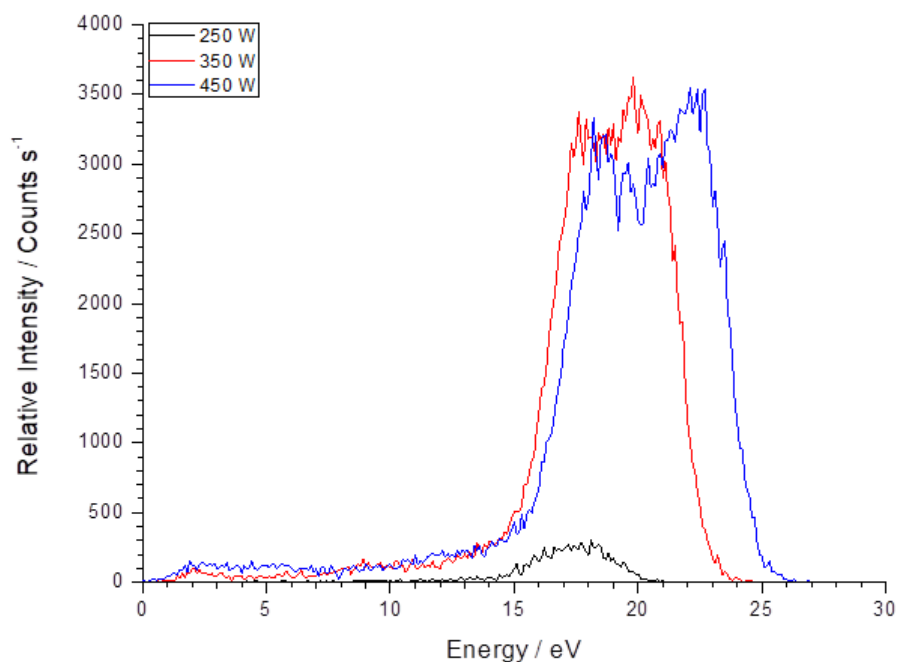
FIGURE 6.12: SIMS Scan of O^+ 1 mTorr with power and a carbon neutralizer. Widened plasma potential is attributed to greater RF response.

The small saddle structure and broad (twin) peak (FWHM   10 eV) is indicative of lighter ions following plasma potential fluctuations. The absence of ions in the thermal energy region suggests a lack of resonant and

near-resonant charge-exchange.

In summary, the ion energy distributions of Ar and O_2 discharges have been recorded with the EQP mass/energy analyzer. Immediate observations are that the intensity of ions getting through to the EQP is markedly less when the carbon neutralizer is installed. This appears to indicate a significant degree of collisional processes (not just charge-exchange) within the carbon neutralizer apertures which was difficult to separate out without pressure control. Most of the ions are further scattered and therefore lost from the axial flux entering the analyzer.

6.2   Neutral Energy Measurements in a Hybrid Analyzer Mode

The previous section demonstrated that evidence of charge-exchange can be observed in the extracted ion flux. This section now describes the adaptation of the system to directly measure fast energetic neutrals in a hybrid of SIMS and RGA modes. It is expected that charge-exchange leads to energetic neutral species that have EDFs that are identical with those of their parent ions. Conversion of these ions into fast neutrals should therefore introduce additions to the distribution that are 'ghosts' of the SIMS signals.

Fast energetic neutrals were detected via a filament modulation method. 1. with the filaments turned off , all plasma species passing the extractor mesh and neutralization volume pass into the analyzer and on to the ionization cage region. 2. with bias applied to the cold filament, some ions deflected off axis due to the filament voltage. 3. when the filaments are turned on, neutral species were ionized, enhancing the distribution seen in stage 2. Subtracting the previous plasma ion distribution from the enhanced distribution gives just the neutral component.

6.2.1   Filament Modulation and Ionization Probabilities

The initial stage is to select an optimal filament bias. The effect of the electron filament bias on Ar^+ is shown in **Figure 6.13**. Here, the energy filter was set to a single ion energy (5 - 35 eV) and the mass filter set to m/q = 40 (Ar^+). Note that the filaments are biased but not heated so that there is no electron emission:
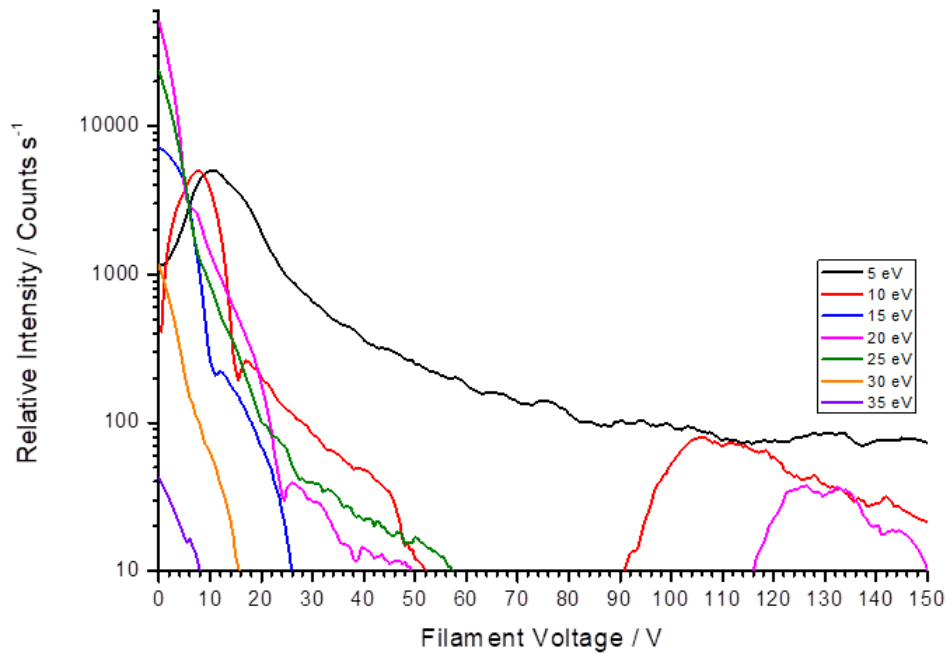
FIGURE 6.13: Ar^+ (1 mTorr, 250 W) signal at specific pass
energies when the filament voltage is varied.

At different ion energies, the filament voltage (also known as *Electron
Energy*) was varied. It can be seen that for ions with 10 eV or more, a dead
zone opens up over a range of filament biases. At 90 V and 120 V, there is
a sharp increase again for 10 eV and 20 eV ions, but this falls off again and
is thought to be the result of specific paths within the electrostatic fields of
the EQP and is taken as an artifact.

Although it is expected that 5 eV ions would be even more heavily sup-
pressed (their numbers fall about 2 orders of magnitude by 150 V of fila-
ment voltage), the intensity persists to around 100 counts at 150 V. This is
further established by the response of the EQP known to not be very good
for particles 5 eV and below, yet the intensity remains measurable. This
is explained by large fluxes of low energy ions entering the EQP. The 10
eV trace persists to 52 V, the 20 eV persists to 50 V whilst the 30 eV trace
is suppressed by 16 V. This is at odds with the earlier COMSOL modeling
which suggested that greater particle energy makes them less susceptible
to deflection whilst traveling on axis - although the modeling results do not

consider the number of these ions entering into the EQP. There is a suggestion that geometry and optimization of the transfer lenses has a substantial effect on these ions. As seen in the COMSOL modeling results, lower energy ions, although lost before and during transit in the cage, appeared more responsive to the fields of the transfer electrodes.

When the electron filaments are heated (emissive), the neutrals become ionized by electron impact and are then detected as an enhancements to the ion energy distribution. **Figure 6.14** shows the net effect (after subtraction of bias related signal) of ionization arising from electron impact on neutrals:
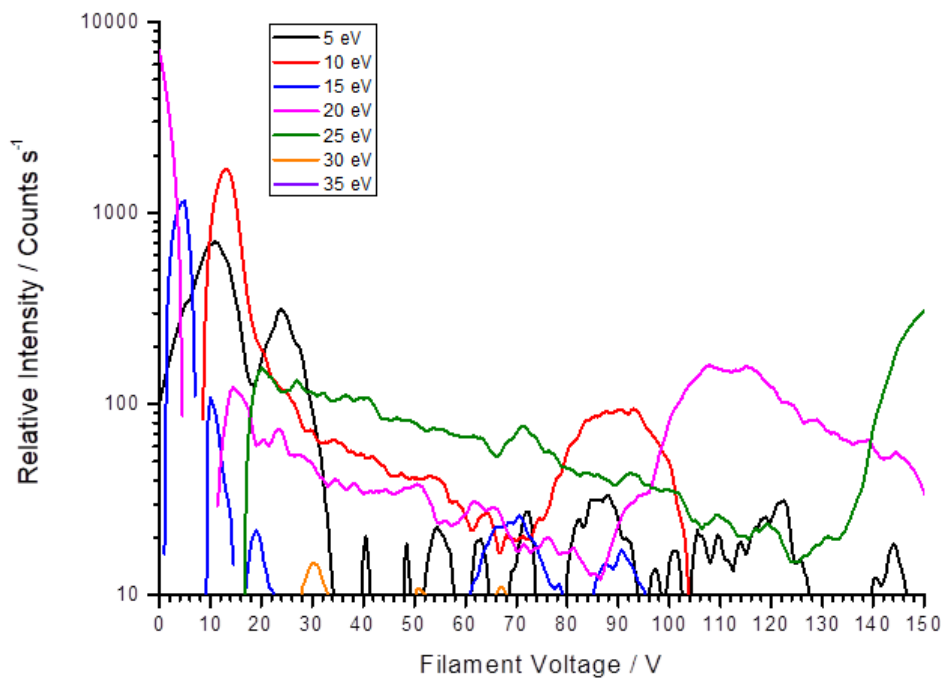
FIGURE 6.14: Ionized neutral component signal (Ar, 1 mTorr, 250 W) at specific pass energies.

When the filaments emit electrons there is an enhancement of the ion signal showing that ionized neutrals have joined the distribution and have been detected. There are peculiar regions where the ion signal is unexpected. For example, with 20 eV neutrals, it appears that ionization of Ar neutrals begins with electron energies as low as 0 eV which is not possible. 5 eV and 10 eV neutrals are also seen to be ionized by electrons with energies < 10 eV. With the exception of metastable or excited states, ionization

of neutrals is not expected for electron energies < 15.6 eV. According to **Figure 6.14**, only the 25 eV signal looks normal. The 5 eV drops to noise levels at 35 V and this suggests that 5 eV neutrals are being deflected by filament bias post ionization. The 10, 20 and 25 eV signals appears more continuous whilst across the electron energy range. There are peaks in the signal intensities at 90 V (a known maximum for the ionization cross-section), 110 V and > 150 V. 15 eV represents the insensitive region of the EQP and this is characterized by a signal in the noise level. 20 eV to 25 eV represents the normal peak of the ion energy, so most fast neutrals detected here have energy identical to their parent plasma ions. The ionization potential of Ar is 15.6 eV and it can be seen that the signal of 20 eV neutrals begins at 11.5 eV electron energy whilst the 25 eV neutral signal begins at 16.5 eV electron energy. Neutrals appearing with 30 eV have intensities comparable to noise and 35 eV neutrals are not seen at all. There were very few ions detected at this energy in previous SIMS scans. Moreover, **Figure 6.13** indicates the severe deflection of 30 eV and 35 eV ions within 20 V of filament voltage.

Figure 6.13 & 6.14 illustrate the very complex electrostatic environment within the EQP as alluded to by COMSOL modeling in **Chapter 5**. Fast neutrals are able to be detected but this is conditional with respect to the filament voltage adding fields either within or outside the ionization cage. Although possibly artifacts, the rising signals by electrons with energy of < 90 eV suggest complex potential gradients that enhance collection of ionized neutrals on the detector. The electrons themselves may not be ionizing only within the cage. At 70 eV, electrons have an average speed of 3 $\times 10^6 \, \mathrm{m \, s^{-1}}$. A neutral Ar atom at 30 eV would be traveling at 8000 $\mathrm{m \, s^{-1}}$. The ionization filaments and the cage itself were designed such that electrons are emitted perpendicular to the flight path of the neutrals such that they appear to ionize stationary particles. In practice, this is not the case and electrons appear to be emitted with an angular distribution that, with their speed, makes them likely to ionize neutrals before they reach the cage or after – making them immediately susceptible to fields when ionized.

The ionization of cold Ar neutrals in RGA mode is shown in **Figure 6.15** where the electron energy was varied:
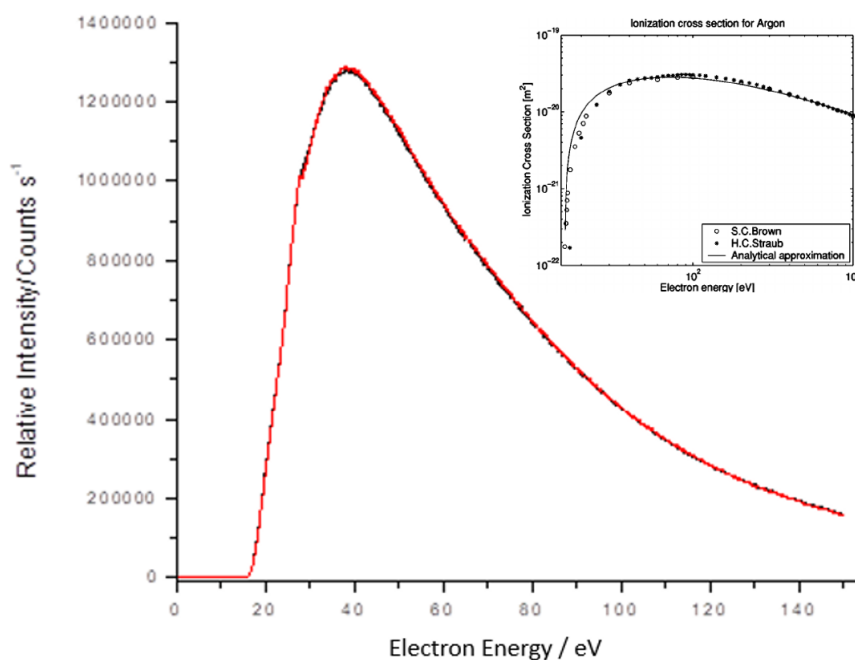
FIGURE 6.15: Cold neutral Ar atoms ionized in pure RGA mode with increasingly energetic electrons. Udiljak, 2004 determination of Ar ionization cross-section [91] inset.

Within the EQP, ionization probability appears to be dependent on system geometry as the ionization signal peaks at around 40 eV, contrary to the result reported by Udiljak *et al*. Ar has an ionization potential of 15.6 eV as seen from the sudden steep rise in intensity at that electron energy. At very low energies, the electrons cannot transfer enough energy into the neutral Ar to cause ionization although this can be overcome if the neutral atom itself is a metastable. The ionization probability peaks at 40 eV and then falls off as seen by the tail of the signal. This fall off appears at around half the electron energy compared to that reported by Udiljak, 2004 where the cross-section peaks at ~ 80 eV. The filament voltage and therefore electron energy chosen for further neutral detection was set at 45 eV due to the signals of 10 eV - 25 eV neutrals being reasonably high with electrons at this energy. As illustrated in **Figure 6.12**, most of the incoming plasma ions are deflected off axis which aids the discrimination of neutral energy from plasma ion energy.

Although **Figure 6.14** illustrated the inability to measure energetic neutrals of energies 30 eV and beyond, electron ionization signal measurements were attempted at this energy as it represented the tail of the parent ion energy distribution. They are also difficult to see. Because of the non-existent signal in **Figure 6.13**, the dwell time was raised to 500 ms and averaged over 10 scans:
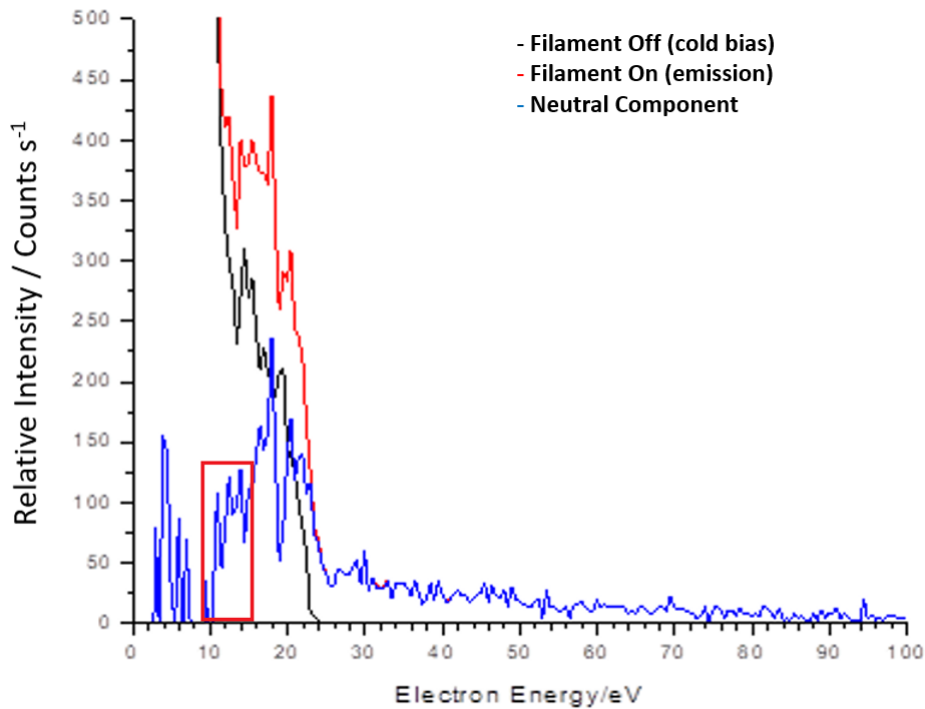
FIGURE 6.16: 30 eV neutral Ar (1 mTorr, 250 W) atoms ionized with increasingly energetic electrons.

Figure 6.16 is another example of what is observed in a hybrid mode for energetic ions and ionized neutrals. Some ions are derived directly from the plasma (filament off) and others will be fast neutrals that were re-ionized via electron impact ionization within the cage and enhance the previous ion distribution (filament on). The difference is then just the neutral contribution (neutral component). The boxed region in **Figure 6.15** highlights the ionization of neutral Ar with $\sim$ 10 eV electrons. This is due to the ionization of metastable Ar atoms which have emerged from charge-exchange. Referencing the peculiar dependence on system geometry, the ionization probability was observed to peak at 20 eV instead of 40 eV suggesting that

it is more efficient to attempt to ionize fast neutral Ar atoms with 20 eV electrons rather than 45 eV electrons. Increasing the electron energy above 20 eV causes the instrument to become less efficient at detecting these species, suggesting a deflection off axis due to the potential of the filament. Regardless, an electron energy of 45 eV was used for all fast neutral energy detection.

6.2.2 Neutral Beam Characterization

The evidence of increasingly energetic neutrals as a consequence of biasing to raise the plasma potential is illustrated in **Figure 6.17**:
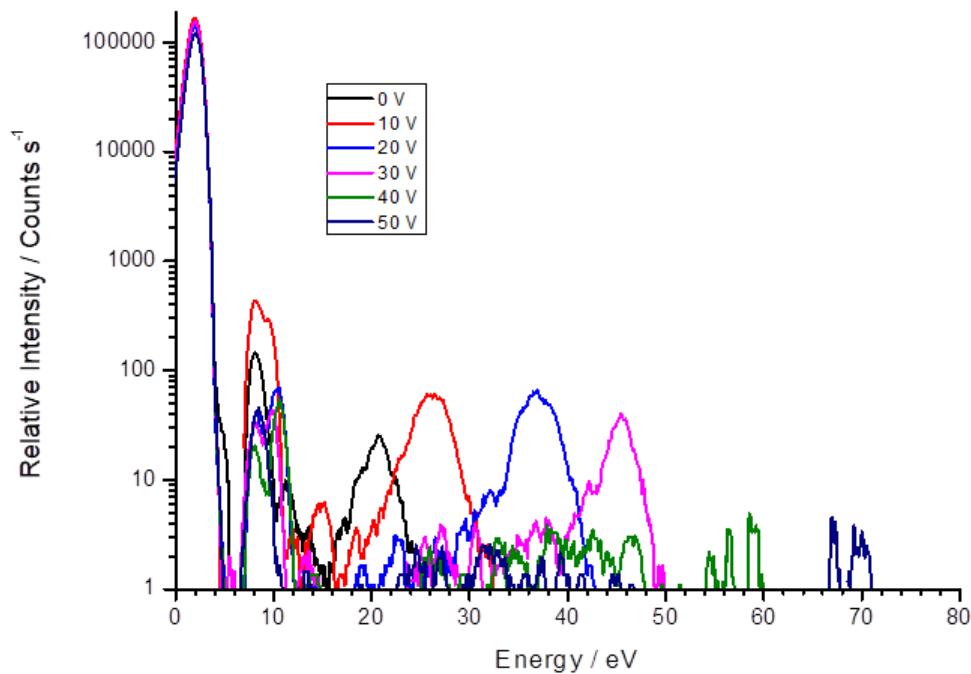
FIGURE 6.17: Hybrid energy scan of neutral Ar (1 mTorr, 250 W) with changing V_b.

The results show that biasing the plasma can provide a source of very *energetic* and *directional* neutral particles with most of them having identical energy to their parent ions (**Figure 6.5**). There is a noticeable increase in signal between 0 and 30 V of plasma bias, suggesting that more fast neutrals are traveling on axis and are more easily detected by the EQP. However this falls off by about an order of magnitude at 40 and 50 V bias, suggesting

that most of the fast neutrals are now traveling off axis and won't be detected post ionization. The issue of geometry and optimization of the EQP extraction and transfer electrodes compared with incident species energy is documented in **Chapter 5** and in **Section 6.2.1**. It is also shown later on in this chapter that the re-tuning of transfer electrodes enables the detection of products of dissociative electron attachment which were not traveling on axis post ionization. Re-tuning amounts to adjusting the set of preferred trajectories through the cage region.

Figure 6.17 shows that low energy neutral distribution persists as bias is applied to the plasma and it is expected that this is from cold thermal gas. The peak at 10 eV slightly shifts when bias is applied. Increasing the bias to 10 V causes the intensity to rise. Other plasma bias voltages cause the intensity of this peak to fall. **Figure 6.17** illustrates that the intensity of this peak can be manipulated when the plasma power is varied:
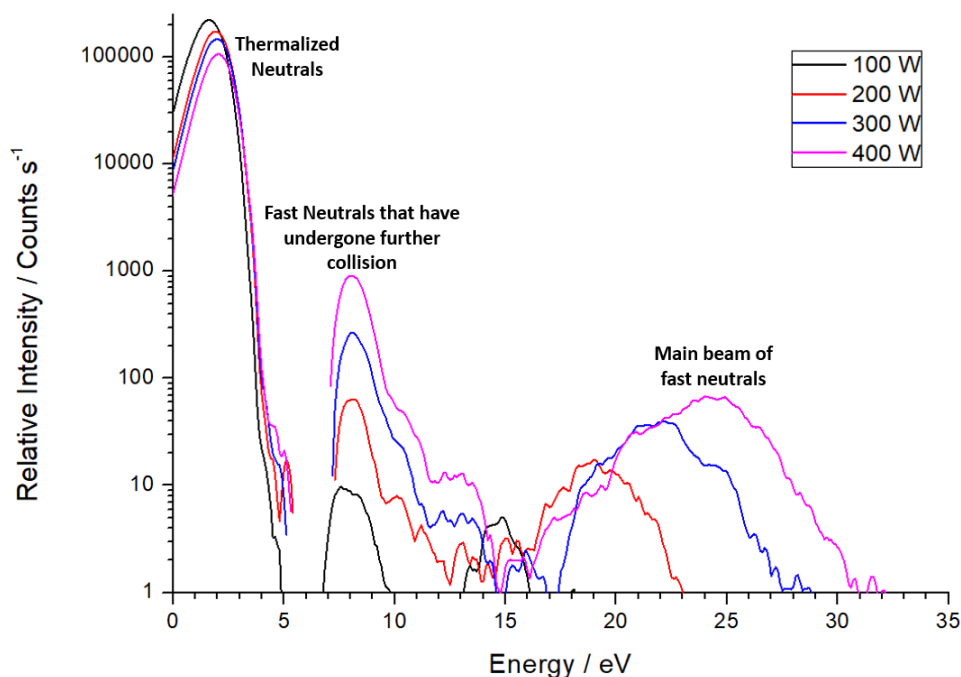
FIGURE 6.18: Hybrid energy scan of neutral Ar (1 mTorr) with changing power.

There is a clear indication that the amount of energetic neutrals and

their peak energies (effectively V_p) is related to the plasma power. **Figure 6.18** shows that increasing the plasma power results in the detection of larger numbers of energetic neutrals as the ion density in the plasma is increased (the rate of charge-exchange therefore increases). The blind spots at 5 eV and 15 eV appear to persist, but gradually, counts are recorded in that region especially with higher dwell times. Because the peak around 10 eV rises in intensity as the plasma power is increased, this suggests that it is probably not an artifact but the result of non-resonant charge-exchange which was was discussed in **Section 6.1.1**. As the power absorption increases, the peak energy of the re-ionized neutrals increases and more of them are detected. On the other hand, the effect of gas pressure on the population and energy of the re-ionized neutrals is illustrated in **Figure 6.19**.
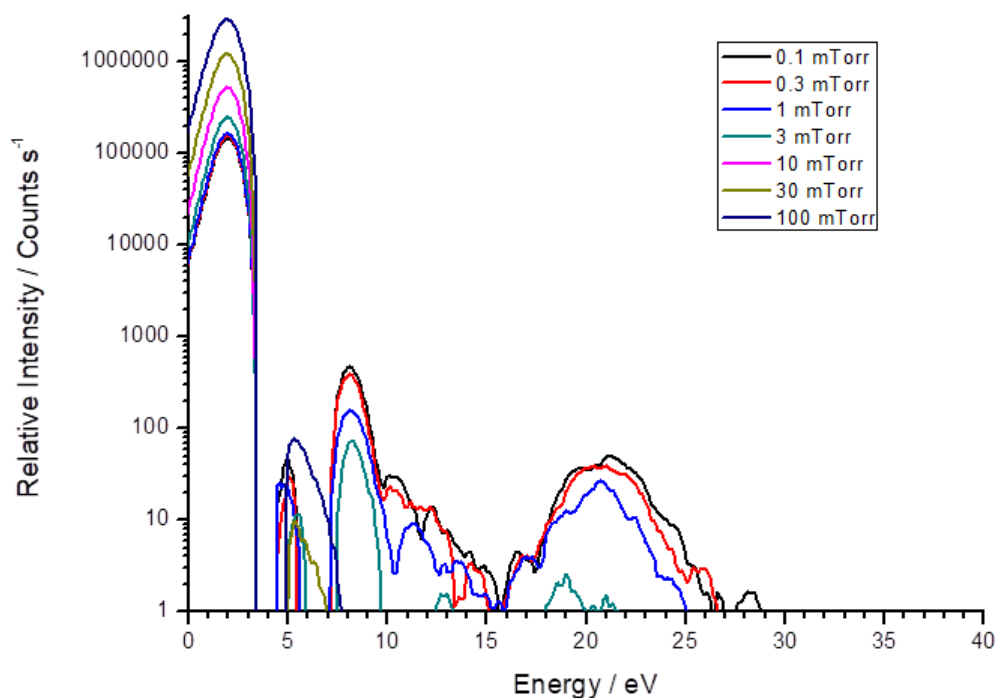
FIGURE 6.19: Hybrid energy scan of Neutral Ar (250 W)
with changing pressure.

Increasing the gas pressure suppresses the high energy signal as the plasma energy density decreases and fewer charge-exchange interactions will produce very energetic neutrals. Thermalization can be seen as the low energy peak (0 - 3 eV) increases with pressure. The production of a beam of energetic neutrals depends on one charge-exchange collisions within the

neutralization volume. Increasing the gas pressure lowers the mean free path and charge-exchanged neutrals will scatter and thermalize due to multiple collisions. At 100 mTorr, the plasma potential peak is non-existent as it is not possible to see species falling out of the plasma with directed energy and neutrals entering into the EQP resemble a thermalized gas.

The charge-exchange mechanism is pressure dependent. The ideal situation should be should only be one collision between ions and neutrals within the neutralization volume in order to have a directional and energetic beam of neutral particles. It was seen that at plasma pressures approaching 10 mTorr and higher, the pressure in the neutralization region could not be adequately controlled. To correct this, extra pumping was installed such that there was separate pressure control of the plasma chamber and the neutralization region. This pressure control is illustrated in **Figure 6.20**.
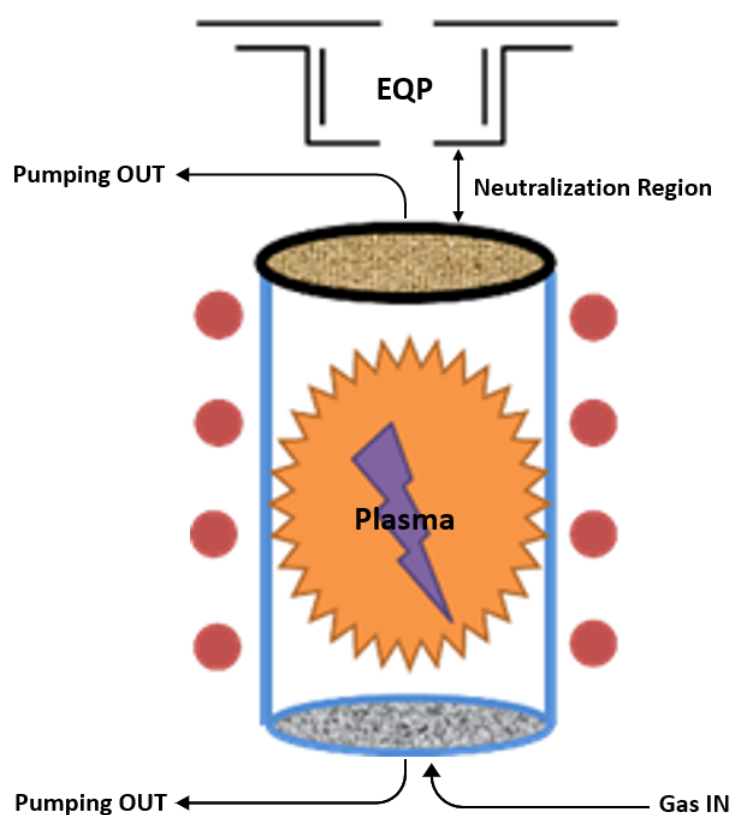
FIGURE 6.20: Schematic of differntial pumping. Separate pressure control was maintained with two butterfly valves.

In a 350 W O_2 and Ar discharge, the gas pressure in the plasma cham-
ber was maintained at 10 mTorr and the flowrate 10 SCCM for each gas.
The neutral energy distributions were measured for four neutralization re-
gion pressures and **Figure 6.21** illustrates how the variation of this pressure
affects the EDF of the re-ionized neutrals.

(A) 0.5 mTorr Neutralization Pressure   (B) 1 mTorr Neutralization Pressure

(C) 5 mTorr Neutralization Pressure   (D) 10 mTorr Neutralization Pressure
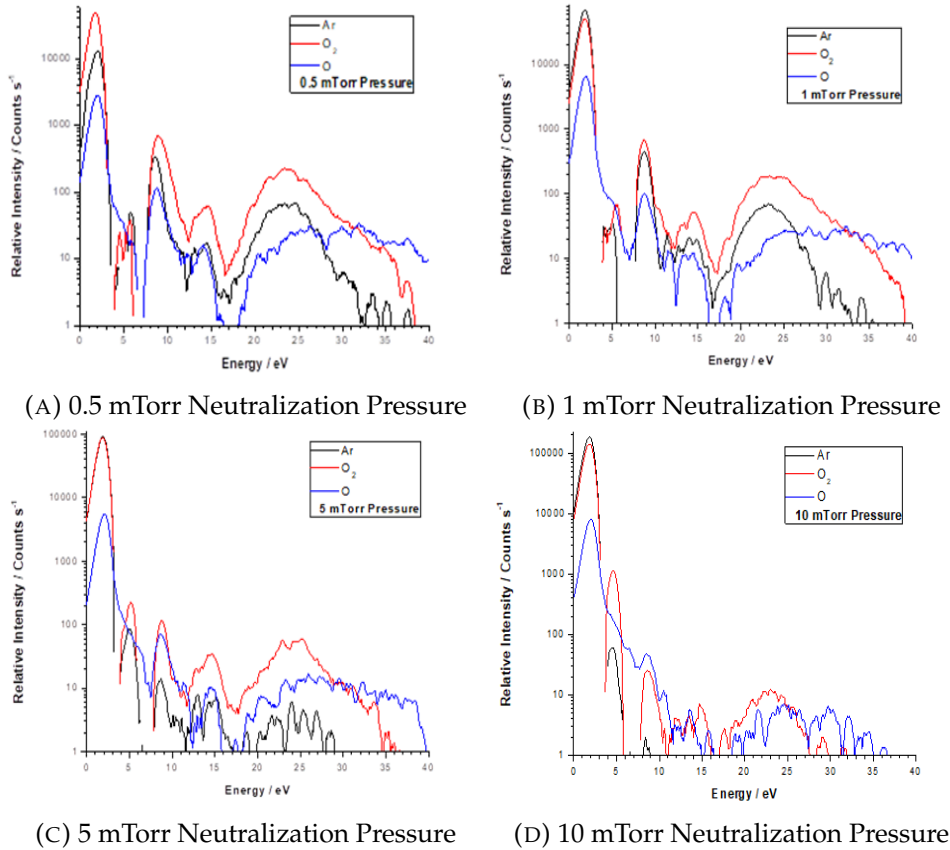
FIGURE 6.21: Hybrid energy scans of Ar, O_2 and O with
changing pressure in the neutralization region.

At low gas neutralizer pressures (less than 0.5 mTorr), the mean free
path is long enough (10's of centimetres) such that many ions should pass
through without collision. At these low pressures however, the limit of
the pressure (Pfieffer capacitance manometre) gauge was reached. For the
given neutralization length, a pressure of ~ 2 mTorr would just match the
mean free path for charge-exchange. **Figure 6.21**, shows that the differences
in intensity between 0.5 mTorr and 1 mTorr are very small even though the
mean free paths are 30 cm and 15 cm respectively. The signal for Ar at
peak energy ~ 23 eV is constant in the range 0.5 - 1 mTorr, indicating no
response to the neutralization pressure. The difference in the signal of O_2

at ~ 23 eV is more noticeable. With 0.5 mTorr pressure, ~ 250 counts s^{-1} were measured. Increasing the pressure to 1 mTorr decreases this signal to just below 200 counts s^{-1}. At 5 mTorr the high energy neutral signal is markedly lower whilst the low energy thermal peak increases. This suggests thermalization. The results show that neutralization pressures of < 2 mTorr are more suitable for directed, charge-exchanged neutrals.

The effect of this pressure variation in the neutralization region is also seen in pure SIMS mode where the intensity of high energy O_2^+ ions was observed to be suppressed by higher pressures:
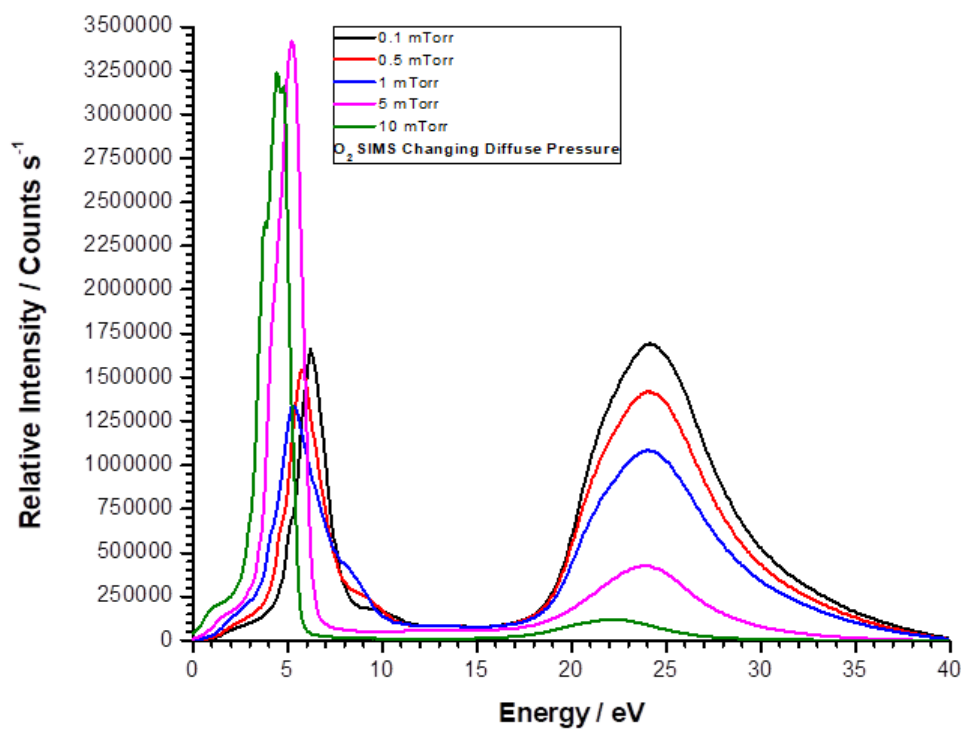
FIGURE 6.22: O_2^+ (350 W) energy distribution with changing neutralization pressure in pure SIMS mode.

Figure 6.22 shows that there is a large jump in signal intensity between 1 mTorr and 5 mTorr where the thermal peak increases suddenly by a factor of 2. This suggests a 'sweet' spot (1 - 5 mTorr) of pressure where many ions are lost to collisions. This is thought to be charge-exchange, but there is the possibility that some of them are simply scattered.

6.3   Validation of Neutral Energy Measurement

If neutral beams are being detected, they must be reproducible and responsive to parameter changes. In previous works by Yunogami, 1995 and Hara, 2008/2014 ([41, 50, 84]), direct neutral beam energy measurement was attempted but not validated. This section attempts to remove ambiguity from the previous results via the following validation methods.

6.3.1   Filament Current Modulation

The method used to determine fast neutrals was to modulate the ionization filaments (electron emission) in a hybrid RGA mode and any enhanced signal of the ion energy is taken as being due to the presence of energetic neutrals. If the enhancement is from ionization of neutrals, then it should show a dependence on the electron emission current. Increasing the emission current would increase the number of electrons into the cage which should therefore encourage more ionization of neutral species. **Figure 6.23** illustrates the change in neutral energy signal when the filament current is varied:
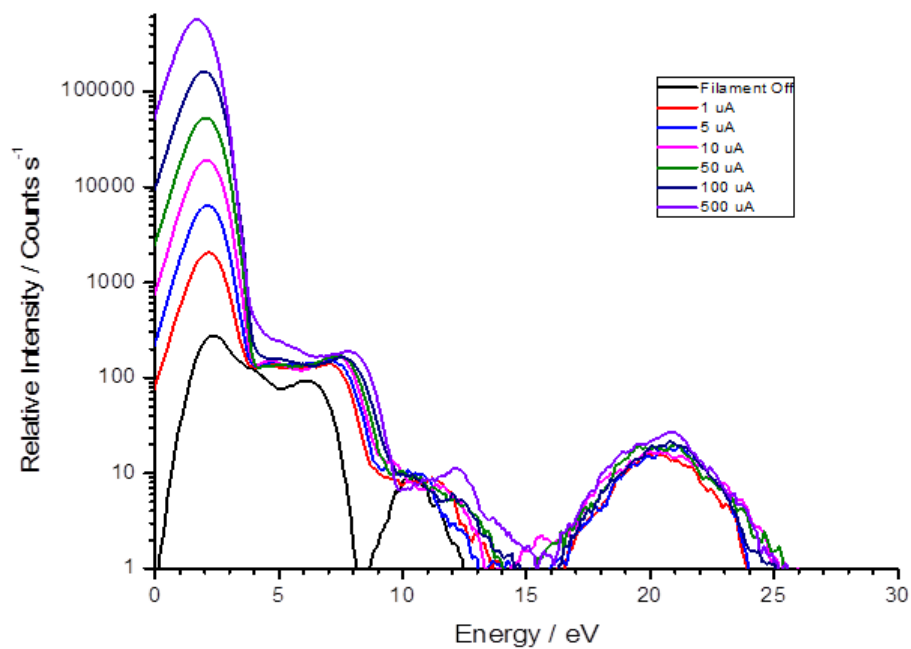
FIGURE 6.23: Hybrid energy scan of Ar varying with emission filament current. **Black** represents just plasma ions.

The lower energy thermal peak of the neutral distribution is more responsive than the higher energy plasma potential peak. There is a noticeable dependence of the neutral intensity on the electron emission current although this diminishes at higher energies and higher currents indicating a saturation – depending on plasma conditions, there is a minimum electron current where most of the energetic neutrals are ionized. The black trace represents just plasma ions, the cold filament was still biased and the absence of signal > 12 eV indicates that plasma ions were deflected off axis.

Between 0 and 10 eV, there is an overall increase in the number of neutrals being detected. At higher energies, this dependence on filament current was smaller suggesting that there are either not a lot of highly energetic fast neutrals entering the EQP on axis, or the detection of them saturated after a given emission current. Most of the energetic neutrals appear to be picked up at 0.2 μA. The limit for increase of the signal appears to be reached at 100 μA whereby an uncharacteristically high filament current (500 μA) only appears to increase the signal by an extra 10 counts. This observation is summarized in **Figure 6.24**:
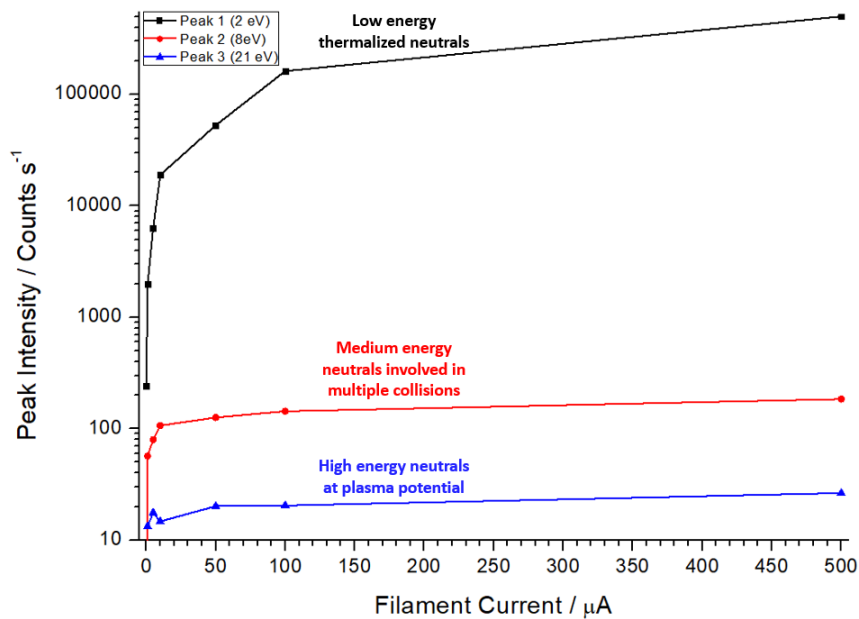
FIGURE 6.24: Variation of peak intensities with filament current.

6.3.2   Negative Ion RGA

Ionizing energetic neutrals to create positive ions internally within the EQP in a hybrid RGA mode has been demonstrated. To validate measurements further, the EQP was configured to detect neutral energy via the dissociative electron attachment (DEA) mechanism on molecular species in the negative RGA mode. In this mode, the transfer electrodes are polarized to positive, such that positive ions can never traverse through the transfer electrodes and discrimination of ions from neutrals is undisputed. The mechanism for attachment considered was:

$$O_2 + e \rightarrow O^- + O \tag{6.8}$$

The attachment of an electron onto neutral O was not considered as it is extremely rare due to the challenge of conserving energy and momentum in 1 product particle. In the DEA mechanism, because both products are the same mass, both the neutral O and the O^- should each carry away half of the energy of the parent molecule. The mass and the momentum of the attaching electron are very small in comparison so it was neglected. This means, that the temporary resonant molecular anion will split into two parts which equally conserve the kinetic energy and momentum of the parent molecule. For the purposes of illustrating the energy distribution of the detected O^-, a low power (200 W, 1 mTorr) O_2 plasma in capacitive mode was generated:
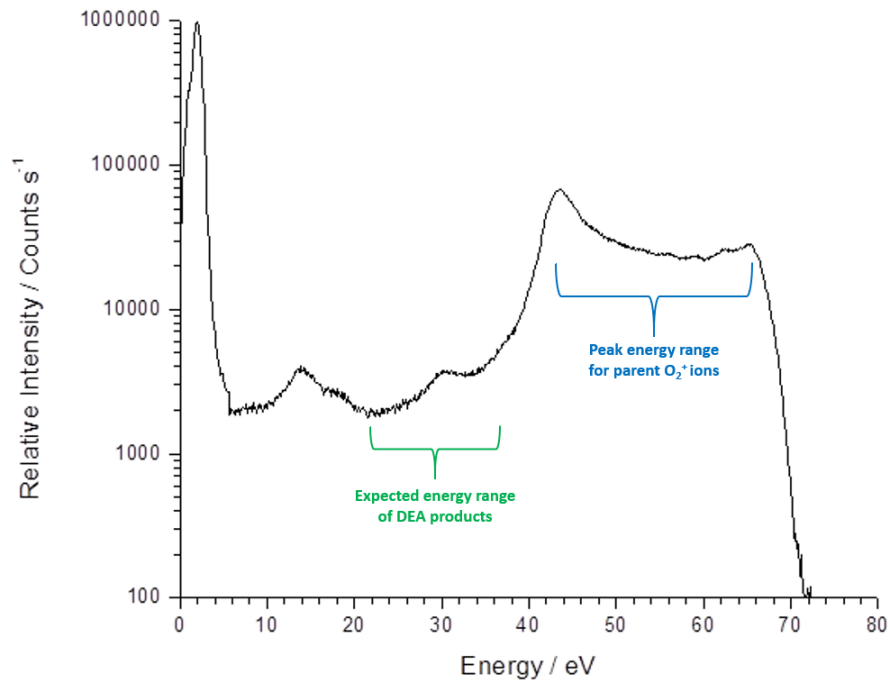
FIGURE 6.25: Extended IED of O_2^+ is representative of capacitive mode.

Figure 6.25 shows the ion energy distribution of O_2^+ to have a large saddle structure and energy range which is indicative of capacitive mode discharges. The RF fluctuation of the plasma is such that there are twin peaks at 40 eV and 65 eV. Between 5 eV and 40 eV, the presence of smaller, secondary peaks suggests collisions within a large sheath whilst a large intensive low energy peak suggests ions that have been scattered to low energies via the charge-exchange mechanism.

Figure 6.26 visualizes the detection of fast neutral energy using the DEA mechanism.

FIGURE 6.26: DEA protocol

A signal (**Figure 6.27**) represented the probability for electron attachment on thermalized O_2:
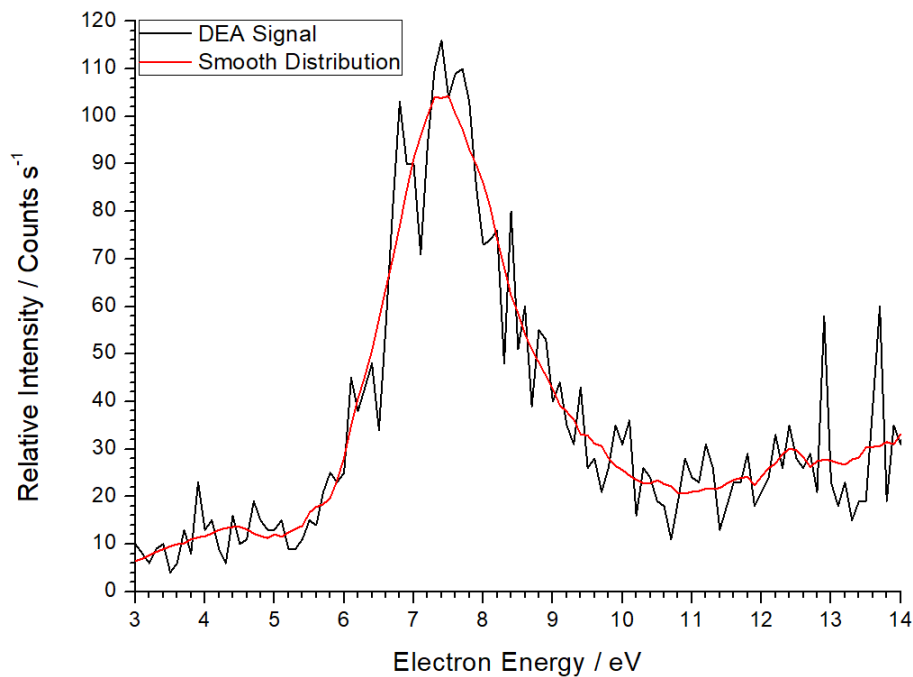
FIGURE 6.27: DEA signal representing the attachment (O^-
ions) probability of cold O_2. Energy filter = 2 eV.

The EQP mass filter was set to mass 16 as the interest was in O^- as the
product from DEA of O_2. It can be seen that the detected O^- signal peaks
at approximately 7.5 eV and is comparable to work reported by Laporta *et
al.* [92] to within 1 eV of the peak of the sum of the measured DEA cross-
section:
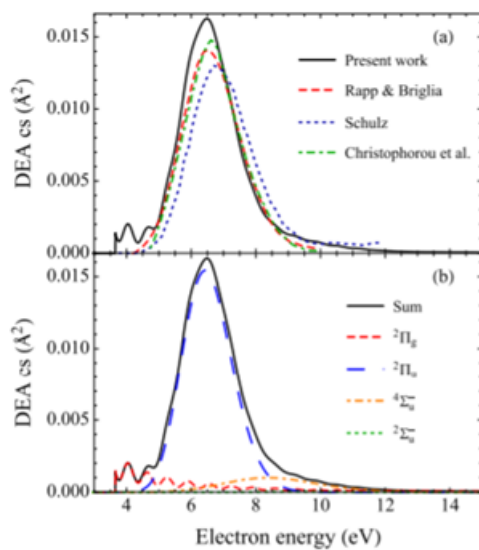
FIGURE 6.28: DEA Cross-section of O_2. *Credit: [92].*

The distribution then falls as higher electron energies create rarer res-
onant states. It was shown (**Figure 6.29**) that for pass energies of 20 eV
and above (the discharge had been switched on), the peak of the ionization
probability had shifted (this phenomena had also been observed in **Section
6.2.1**).
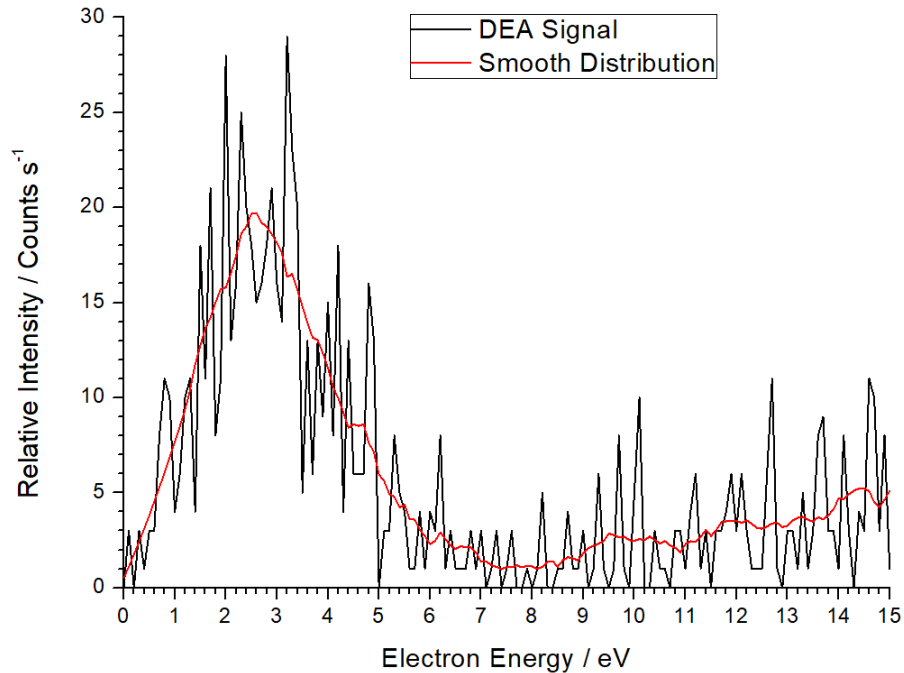
FIGURE 6.29: DEA signal representing the attachment (O^-
ions) probability of fast O_2. Energy filter = 25 eV.

The distribution suggests that the electron attachment mechanism on
energetic O_2 is maximum at 2.5 eV. There was a challenge associated with
capturing these species due to their trajectories post DEA. **Figure 6.30** illus-
trates some possible trajectory of O^- products from DEA:
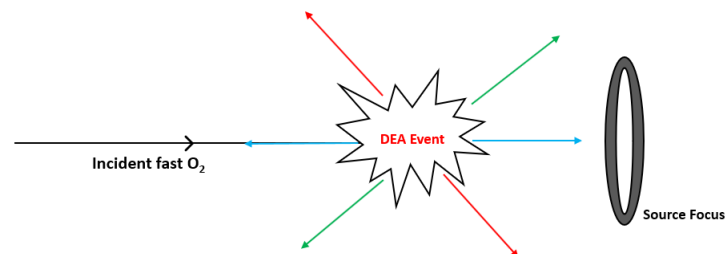
FIGURE 6.30: Schematic of possible DEA product trajecto-
ries within the ionization cage. Not to scale.

Only a small fraction of the incoming neutrals give rise to negative anions ions ions moving out of the ionization region along the main axial path. Several voltages were explored (**Figure 6.31**).
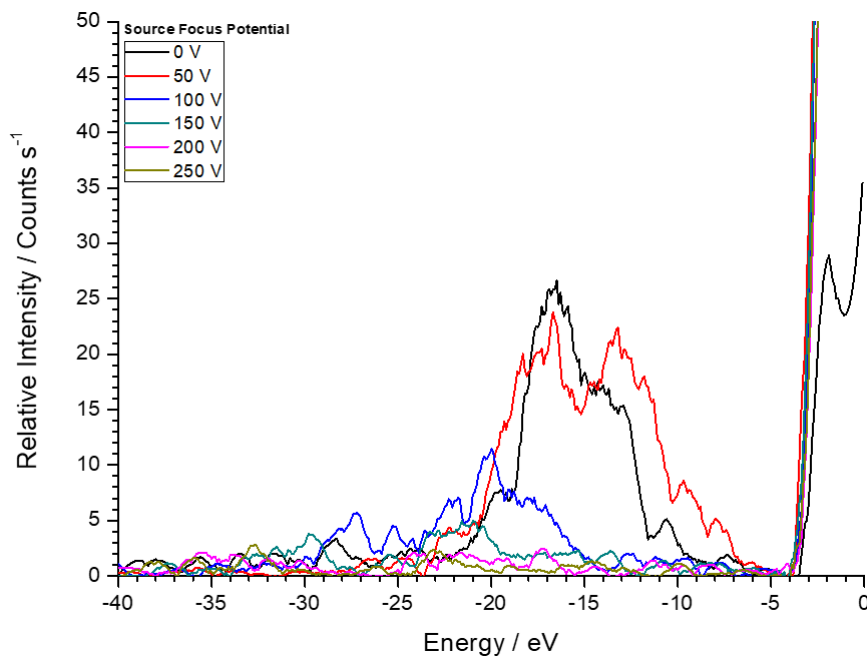
FIGURE 6.31: Variation of DEA energy signal of O^- with source focus voltage.

At standard source focus voltages of 200 V and 250 V, the signal is flat and only the low energy anions are detected suggesting that the more energetic anions are likely traveling off axis. At 100 V, the shape expected for about half the energy of the SIMS saddle structure appears with twin peaks at -27 eV and -20 eV respectively. Continual decreasing of the electrode voltage diminishes the twin peak shape of the distribution and instead forms a broader, single peak centering around 15 V. Anions at this energy must be easier to detect at this Source Focus voltage. 100 V Source Focus was chosen as a compromise on a lower count rate but a distribution that more accurately described the energy of the parent ions.

To improve the signal, the filament current was set to 150 μA, the dwell time of the instrument was set to 500 ms and the distribution averaged over 10 scans.
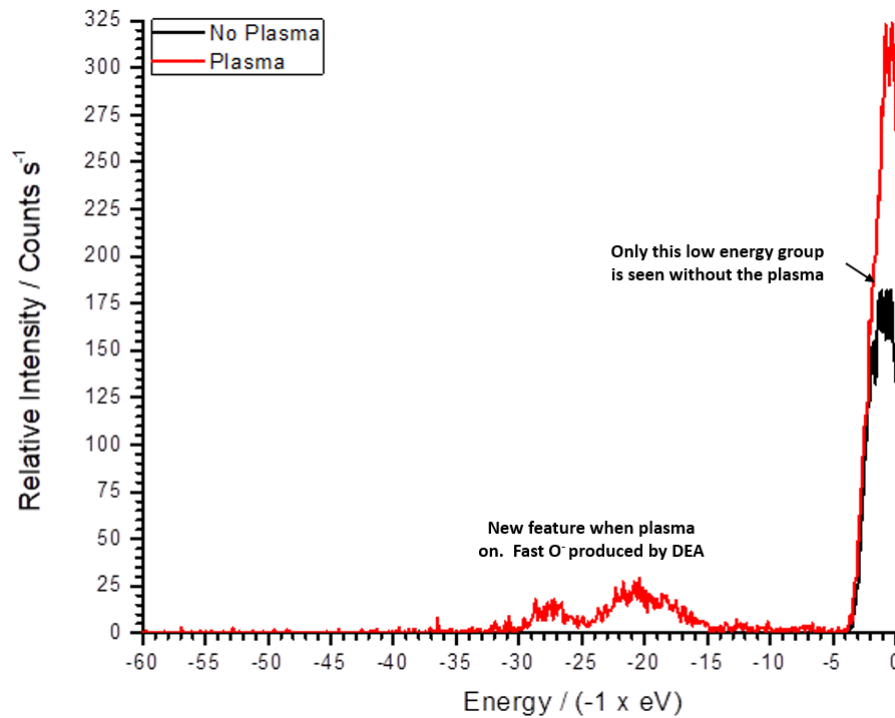
FIGURE 6.32: DEA Energy signal of energetic O^- ions (200 W O_2, 2.5 eV electron energy) in negative hybrid mode.

In **Figure 6.32**, two peaks are seen between $20 - 30$ eV which correspond approximately to half the energy variation of the saddle structure on the O_2^+ IEDF, confirming that the anion carries half the energy away from the point of dissociation. From the parent IED, most of the energetic species are located around 40 eV, this is reflected in the negative hybrid distribution where the most intensive high energy peak is at 20 eV. The lesser peak in the DEA signal from fast neutrals between $25 - 30$ eV corresponds to the extent of the saddle structure towards 60 eV in the original O_2^+ ion distribution (**Figure 6.25**). It can be seen that very little energy was detected beyond 35 eV and this corresponds with the equivalent sharp cut off in the parent IED. The high energy signal is low compared to the thermal signal. Again this suggests the challenge of their detection.
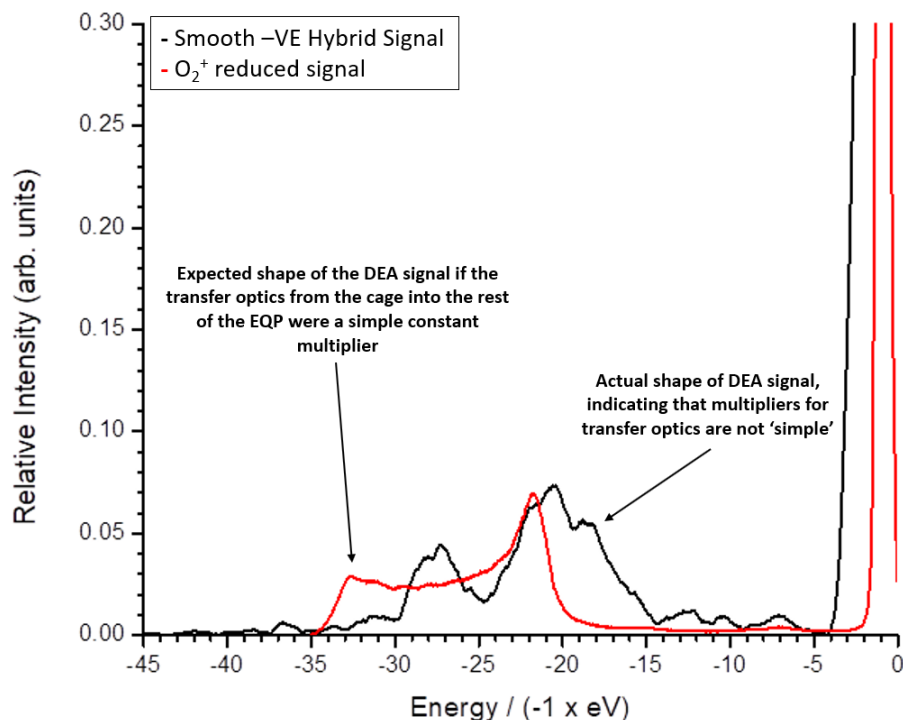
FIGURE 6.33: DEA signal superimposed on to the Energy
of parent ions with reduced horizontal and vertical scale.

Taking a more qualitative approach, the horizontal scale of the parent
IED was compressed by a factor of 2 whilst the vertical scale was normal-
ized in **Figure 6.33**. This signal was then mapped onto the DEA energy
scale so that $\mathrm{IED}_{O_2^+}(E/2) = \mathrm{IED}_{\mathrm{DEA}}(E)$. The broadening of the negative hy-
brid peaks and the fact that they are closer together correspond to a number
of things. The saddle structure of O_2^+ is very broad, the possible energies of
the resulting anion are not restricted to the peaks of the parent ion. Extra
eV's of energy are gained via the transfer of energy in the molecular oxygen
bond into kinetic energy, split between the two O fragments. This spread
is typically $1 - 3$ eV to account for the bond potential and is given by the
expression:

$$E_{\mathrm{Threshold}} = \mathrm{Bond\,Dissociation\,Energy} - \mathrm{Electron\,Affinity} \qquad (6.9)$$

For the DEA of Cl_2, this is about 1.1 eV that is transferred as kinetic energy
within the anionic fragment. Gope *et al.* [93] discusses the DEA mechanism
for a similar molecule (Cl_2) and its momentum distributions although much

of the work is beyond the scope of this thesis. Given that Cl_2 is similar in electron affinity to O_2, it is assumed that this numerical value of energy is not far from what would be reality in O_2 dissociation. The peak broadening is further increased via the resolution of the instrument which has been noted to vary between $1.5 - 2$ eV. Furthermore, the angular distribution of the parent molecule translates into a distribution for the DEA products. The result is that the dissociation of the O_2 molecule will not be perfectly symmetrical and result in energy spread.

6.3.3 Detection of ArH$^+$

There is no known stable neutral of argon hydride (ArH, $m/q = 41$), but the ionized molecule ArH$^+$ does exist. The ArH$^+$ can be used to further determine the validity of energetic neutral measurements by having no meaningful dependence on filament modulation. Theoretically, ArH$^+$ cannot be involved in resonant charge exchange since there is no neutral ground state.

Figure 6.34 shows that IED takes on a similar shape to that of Ar with considerably lower intensity. Protonation mechanisms on cold neutrals enable a thermal peak to form with thermal neutrals which eventually find their way into the analyzer. Further mechanisms to produce this unexpected low energy peak may include penning-type ionization. Neutral argon and hydrogen atoms repel each other at normal intermolecular distances, this is why ArH is unstable in its ground state.
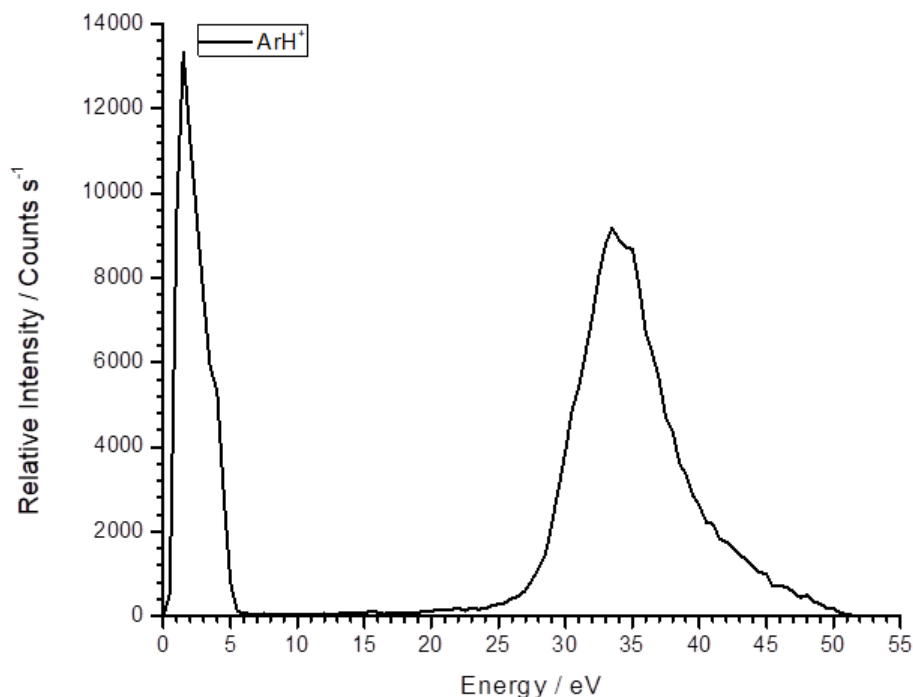
FIGURE 6.34: SIMS Scan of ArH^+ (250 W, 1 mTorr, 20 V bias).

ArH^+ was then detected in hybrid mode (**Figure 6.35**) with the expectation that although turning on the filaments (no emission) would deflect some of the ions, turning on the emission and varying the emission current should not lead to any enhancement of the energy distribution.
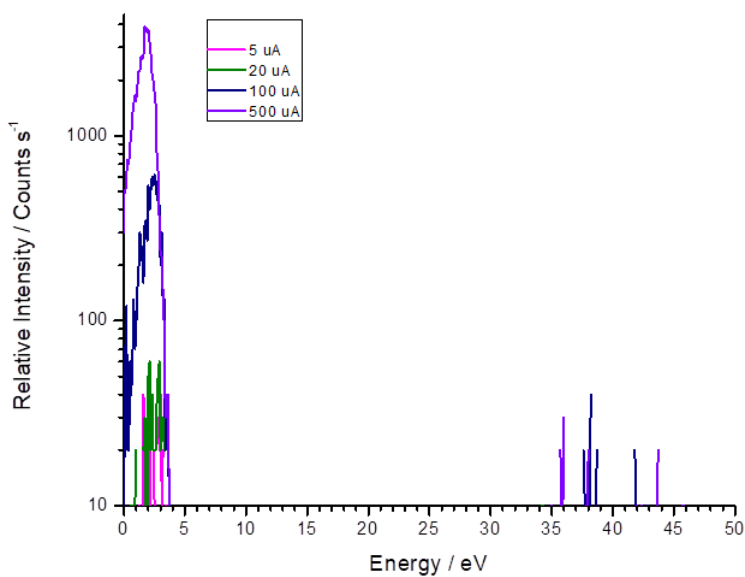
FIGURE 6.35: Hybrid scan of ArH^+ with changing filament emission current.

When the filament current is turned on, there is at first no additional ArH$^+$ signal , so the difference in signal is zero. Structure appears after 5 μA but only at low energy and of a relatively low intensity. The low energy peak sharply increases at 100 μA indicating that a significant protonation or penning-type mechanism on thermalized neutral Ar is now a viable reaction pathway within the EQP. A noise signal where the original ArH$^+$ peak is observed arises from the differencing of of the previous signal.

Section 6.1 has demonstrated the determination of ion energy in SIMS mode using an EQP when Ar and O$_2$ plasmas are discharged. Several parameters were explored such as power, pressure and plasma bias and their effects were reflected in the energy distributions. It was discussed that a gas phase charge-exchange mechanism could produce directed, energetic neutrals which carry the same energy and direction of their parent ions. **Section 6.2** introduced the use of the EQP RGA in a hybrid analyzer mode, where the determination of these energetic neutrals from their parent plasma ions (post charge-exchange) was achieved via the modulation of electron emission filaments. It was shown that although filament emission enabled energetic electrons to ionize fast neutrals, their presence also deflected plasma ions and ionized neutrals off axis such that their measurement was not straightforward. Peculiarities in the ionization probabilities of fast neutrals were also illustrated and discussed. Variation of the plasma parameters and subsequent measurement in hybrid mode showed that fast neutrals had the same EDF's as their parent ions. **Section 6.3** attempted to validate these measurements and included an elegant application of the DEA mechanism on neutral O$_2$ to show that the DEA products should carry away half the energy of the fast parent molecule.

6.4   Quantification of Neutral Beam Using a Planar Ion Flux Probe

This work is compared closely to Hara, 2008 [50] where neutral beams were created in a neutral volume beyond a surface wave discharge and detected using a QMS. The method of neutral beam detection was similar to this thesis, where electron emission was modulated in a hybrid mode to detect energetic neutral particles. Although the authors do not mention independent pressure control, they state a set pressure of 0.25 Pa (1.87 mTorr) in the process chamber and 9.25 Pa (69 mTorr) in the discharge which is similar to the pressures used in this thesis (0.5 - 10 mTorr and 10 mTorr for the neutralization/process region and discharge respectively). Hara, 2008 reported neutral Ar beam counts similar to that of the ion beam.

The residual ion beam was measured using a planar ion collection probe and the neutralization region pressure varied. At a fixed distance of 7 cm from the mesh, the ion current was recorded for several pressures in the neutralization volume (**Figure 6.36**):
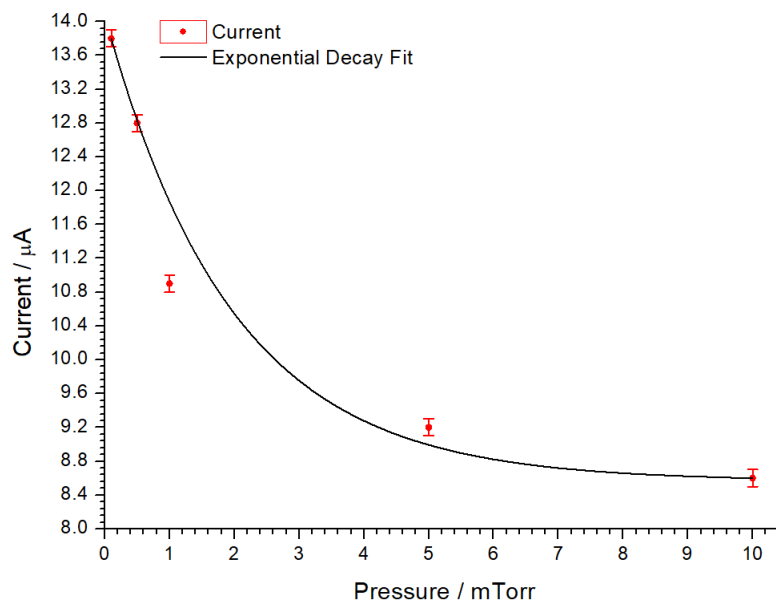
FIGURE 6.36: Ion (Ar 250 W, 10 mTorr plasma discharge) current measured in the neutralization region.

The results reflect the decrease in ion intensities seen in argon and oxygen plasmas when the pressure is varied up to 10 mTorr and by extension, the energetic neutral beam. At 1 mTorr neutralization pressure, the mean free path for charge exchange collisions between Ar^+ ions and Ar is approximately 15 cm whilst the mean free path for momentum transfer between Ar^+ and Ar is estimated as 8.4 cm. An ion beam traveling to the EQP will pass through 7 cm of neutralization region. The ion beam would therefore decrease as $e^{-\frac{0.07}{0.084}} \times e^{-\frac{0.07}{0.15}} = 0.272$, due to a combination of charge exchange on neutral species and scattering with neutral species. The flux ratio of an energetic neutral beam is estimated with the condition that the neutral beam appears with the same properties of an ion beam but charge-less. At 7 cm, the neutral beam is estimated as $e^{-\frac{0.07}{2.78}} \times (1 - e^{-\frac{0.07}{0.15}}) = 0.363$, which is now comparable to the ion beam as they are able to survive longer downstream due to the Ar neutral-neutral cross section being about 20 times smaller than that of the ion-neutral cross section. The flux of the neutral beam can therefore be estimated from the ion flux taken with the planar ion flux probe (r = 1.7 cm, A = 9.08 x $10^{-4}\,\mathrm{m}^2$). At 1 mTorr and 7 cm, the current density was therefore 0.12 A m^{-2}. This suggests that the ion beam exiting the plasma was $2.75 \times 10^{18}\,\mathrm{ions\,m}^{-2}\,\mathrm{s}^{-1}$. The neutral beam flux density 7 cm into the neutralization region is therefore estimated as $1 \times 10^{18}\,\mathrm{atoms\,m}^{-2}\,\mathrm{s}^{-1}$. This value is six times less than that calculated by Hara, 2008 based upon the same principle.

Hara, 2008 estimated fluxes using cross-sections from Phelps *et al.* [94]. Hara, 2008 state the mean free path for scattering at 0.25 Pa (1.88 mTorr) as 19 mm whilst for charge exchange it was stated as 37.6 mm. This is false. This was in fact a misreading of the cross-section by Hara, 2008. For this thesis, the neutralization path was based upon the mean free path for charge-exchange reactions as it was known that the cross section for neutral scattering was at least an order of magnitude less. The ion beam was modelled to scatter and charge-exchange with neutral species. The neutral beam however was modelled to scatter only with neutral species and the

cross-sections reflect this. **Figure 6.37** illustrates the mean free paths for scattering and charge exchange and shows that the cross-sections for ion-neutral charge exchange and scattering are comparable.
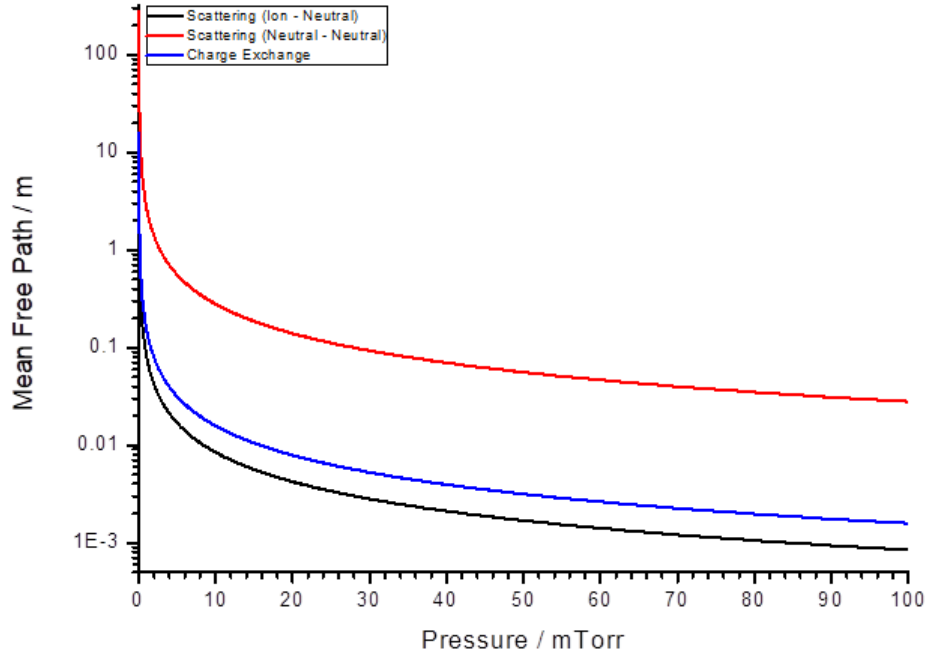
FIGURE 6.37: Mean free paths of scattering and charge-exchange with pressure [95, 94].

The scattering cross-section between strictly neutral species is taken as $1.3 \times 10^{-20}\,\mathrm{m^2}$ and the charge-exchange cross section between ions and neutrals is taken as $20 \times 10^{-20}\,\mathrm{m^2}$ as referenced from Robinson[96] and Brown [95]. The scattering cross section between ions and neutrals is comparable to that of charge exchange at $43 \times 10^{-20}\,\mathrm{m^2}$ as referenced from [94] and this implies that the ion beam will deplete more than the neutral beam along the same path length.

The above analysis is not expected to provide an exact numerical quantification of the fluxes from the plasma based on EQP data. It is however possible to obtain a relative ratio of ions to fast neutrals if only energetic particles > 10 eV are considered. The data is measured in "counts per second" in the energy interval "eV". In fact, it is the result of the dwell time (amount of time spent measuring a particular energy value) combined with

the energy interval (typically 0.1 eV) that give the result. This is expressed as $\frac{d\dot{N}}{dE}\Delta E$ where $\dot{N}$ represents a time derivative in flux of particles per second, E is the energy they appear at and ΔE is the energy interval. To obtain the total flux of ions and neutrals, the summation is expressed as:

$$\frac{1}{\Delta E}\int_0^\infty \left(\frac{d\dot{N}}{dE}\times\Delta E\right) = \dot{N} \tag{6.10}$$

The time derivative is essentially the dwell time which was typically set at 200 ms in the hybrid mode. ΔE was 0.1 eV. Referring directly to the data, the flux of particles becomes:

$$\Gamma_{i/n} = \frac{1}{A}\sum_{i=0}^\infty \mathrm{cps_i}\cdot\Delta\mathrm{E} \tag{6.11}$$

At 1 mTorr, the total number of ions per second was measured to be 101×10^6. If the ion beam is approximated as coming through an area equal to that of the extraction orifice (A = $7.85\times10^{-9}\,\mathrm{m^2}$), then this gives a flux density of ions = $1.3\times10^{16}\,\mathrm{m^{-2}\,s^{-1}}$. The EQP data differs by 3 orders of magnitude due to a combination of optimization and divergence/losses of the ion beam during its transit through the EQP flight path. Moreover, there is over 3 order magnitude difference in count rates for ions detected in SIMS mode and ions detected in hybrid mode if only energetic species are considered (**Figure 5.5**). The Ar neutral count was measured to be 17,350 which therefore gives a flux density of neutrals equal to $2.12\times10^{12}\,\mathrm{m^{-2}\,s^{-1}}$. Although the EQP collects over a much smaller (orifice) area, the flux density measured with the EQP should be closer to that measured by the ion flux probe. The large differences are attributed to most species entering the EQP not being detected due to off-axis transit.

6.5   Summary

Chapter 6 has discussed the creation of energetic, directed neutrals with the ICP and their characterization using an EQP. Determination of ion energy distributions of Ar and O_2 plasmas was achieved in SIMS mode. The measurment of energetic neutrals following the resonant charge-exchange mechanism in a fixed length neutralization volume was achieved in a hybrid RGA mode. It was shown that the neutral beams follow the energy distribution of their parent ions and continue to do so along a range of plasma parameters. Hence, the simple electrostatic tailoring of an energetic neutral beam between 10 eV - 60 eV is feasible. Furthermore, these measurements were indirectly validated via electron emission studies, negative ion hybrid mode detection on energetic O_2 and the use of ArH^+ to eliminate some of the questions raised by peculiarities of the system seen shown in **Chapter 5** and **Chapter 6**. In particular, the dissociation of energetic O_2 was consistent with the anion carrying away half the energy of the parent molecule in a DEA interaction. Lastly, an attempt to quantify the neutral beam flux was made using an ion flux probe and fluxes were comparable to previous investigations. Due to optimization between SIMS mode, hybrid mode and various challenges of capturing ions traveling through the EQP, the adequate quantification of neutral beams using an EQP remains a task that should attempted using a simpler source (no E-H transition, monoenergetic species, ceramic walls and neutralization volume).

Chapter 7

Neutral Beam Processing

Chapter 7 investigates the etching of dielectric materials using directed, energetic neutral beams within an Oxford Instruments PL-80 plasma etcher. The chapter begins with an investigation of the etching of hydrocarbon (HCP), fluorocarbon (FCP) and silicon dioxide (SiO_2) substrates using both O_2 and SF_6 gases. It was found that charge-free etching with directed neutral beams does occur. The chapter then investigates the contribution of UV photons within the neutral beam etching process using He, Ar and O_2 discharges. Ellipsometry, Atomic Force Microscopy (AFM) and X-ray photoelectron spectroscopy (XPS) were used to provide an insight into the physical and chemical characteristics of the substrates post-etch.

7.1   Initial Etching Trials

Charge free etching of coated polymer surfaces was attempted by the extraction of positive plasma ions which were neutralized by a charge-exchange mechanism. The mechanisms considered were surface charge exchange and gas phase charge-exchange in the process chamber volume. Previous investigations on this setup [52] used pulse modulation of a reactive SF_6 plasma. The motivation for pulsing was based on forming neutrals from stripped negative ions which were accelerated out of an ICP in afterglow. The investigations discussed in this chapter were conducted in continuous wave and primarily with Ar and O_2 mixtures. In the case of SiO_2, SF_6 was used because fluorine is required to volatilize silicon.

7.1.1   Methodology

The two surface neutralizers were a carbon neutralizer with high aspect ratio holes and a low grazing forward angle reflector with polished gallium arsenide wafers:
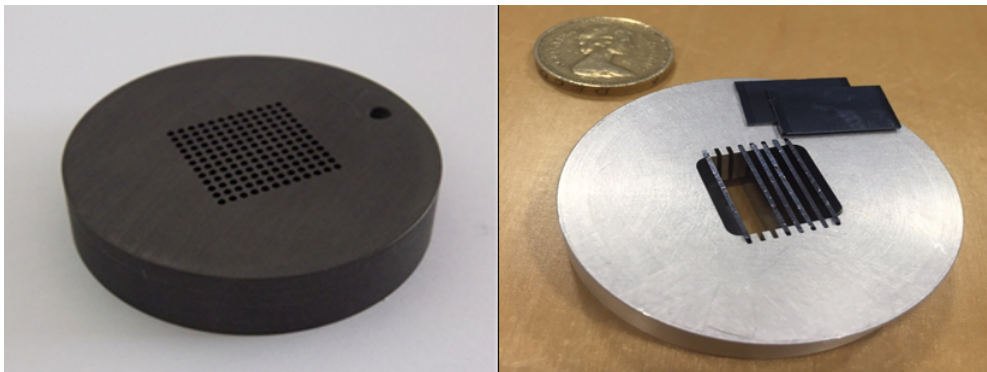
FIGURE 7.1: **Left** Carbon Neutralizer with high aspect ratio apertures. **Right** Wafer Neutralizer with low forward angle reflectors.

1. Carbon neutralizer with high aspect ratio apertures of 1 mm diameter and 10 mm in length. High aspect ratio holes provide a high neutralization efficiency and line of sight with the plasma enables the exposure of the substrate with neutrals.

2. Polished and cleaved gallium arsenide wafers arranged in a venetian blind array. The wafers were held at 6° with 10 mm depth designed to obstruct line of sight for the purposes of producing a flux of directed neutrals with a high neutralization efficiency, while observing direct hv illumination for the plasma.

3. A single mesh extractor for gas phase neutralization was also used.

A schematic of the PL-80 system in the arrangement used is shown in **Figure 7.2**.
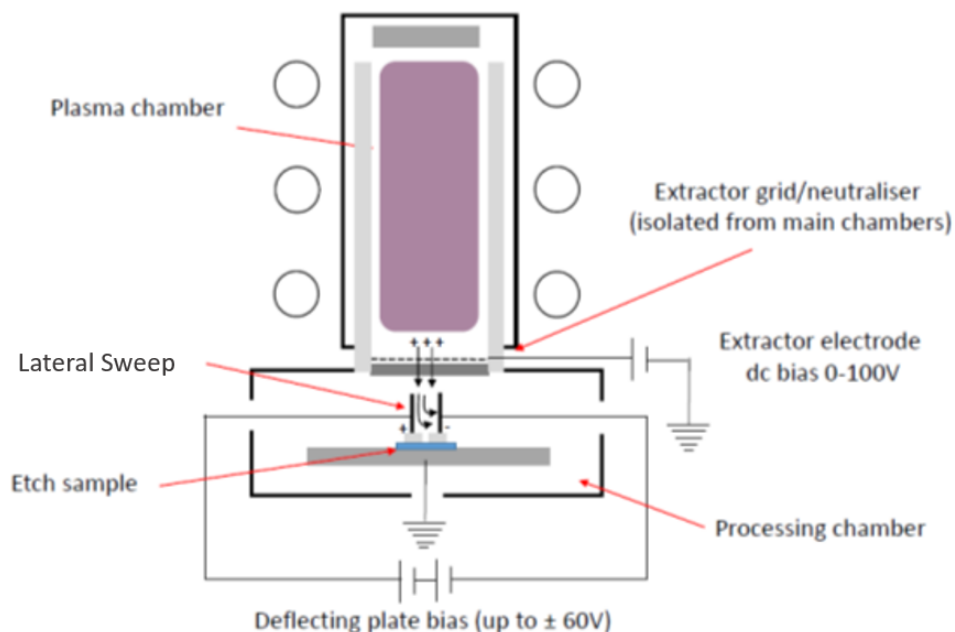
FIGURE 7.2: Schematic of PL-80 arrangement

The only diagnostic available in this instrument is a simple retarding field analyzer (SEMION RFA). This was used to check the effectiveness of a lateral sweep field that was used to remove ions from the particle flux reaching the substrate (**Figure 7.3**). The SEMION works by using a series of parallel, electrostatic grids to discriminate incoming plasma ions in order to determine the ion energy distribution. The arrangement is typically 3 grids (some analyzers have 4) where the first grid is held at floating/ground potential in order to shield the SEMION from plasma perturbations. The second grid is held at a negative potential in order to sweep out electrons. The third grid has a positive sweep (retarding) voltage applied that allows the

SEMION to discriminate ions of different energies. At low voltage, most ions are let through. The voltage where the signal falls completely is considered the maximum ion energy of the distribution.
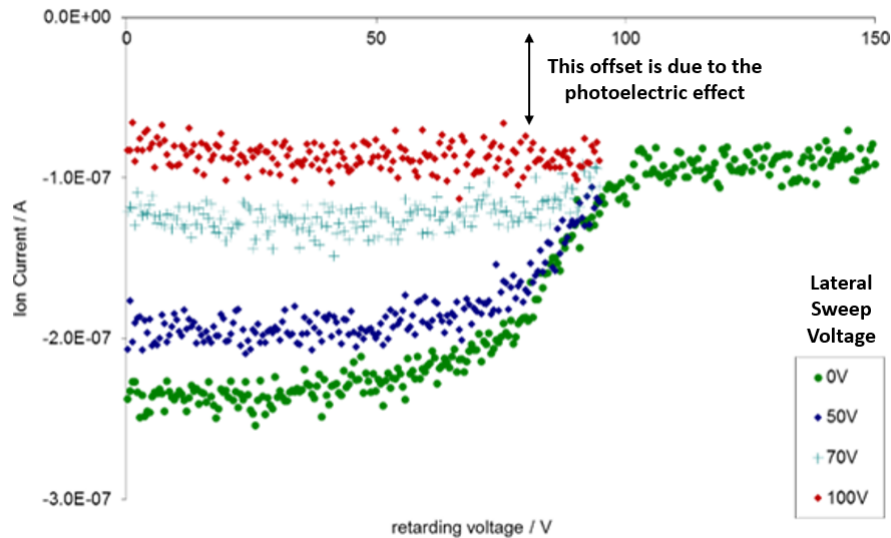
FIGURE 7.3: Ion current variation in a 250 W 5 mTorr Ar discharge. The retarding voltage signifies the SEMIONs scanning range.

As the lateral sweep voltage is increased, the residual ion current reading in the sample plane is reduced to the background level.

The extractor was a photo-etched mesh with 360 μm diameter holes equally spaced in a honeycomb pattern with a 120 μm spacing between each hole. This gave a 50% transmission between the plasma to the processing chamber. The extractor (as well as the top plate electrode) was biased in this arrangement which set the plasma potential positive with respect to a grounded processing chamber. The neutralizer component sat after the extractor and vertical deflecting plates eliminated ions that were not neutralized in their passage through the neutralizer.

The polymer samples were prepared by Oxford Instruments. These were hydrocarbon polymer (HCP, hydrogenated amorphous carbon a-C:H).

The HCP was deposited onto a silicon substrate from a CH_4 plasma. Fluro-carbon polymer (FCP a poly-tetra-fluoride structure $(CF, CF_2, CF_3)_x$), deposited onto silicon a substrate from a CHF_3 plasma. Silica glass (SiO_2) deposited onto a silicon substrate. **Figure 7.4** illustrates the chemical makeup of the surfaces whilst **Table 7.1** lists some numerical details.
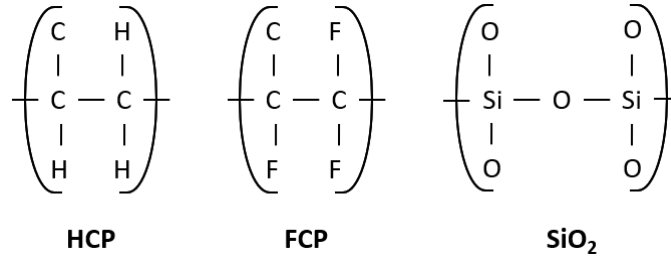
FIGURE 7.4: Chemical schematics of etched materials

Details	Thickness / nm	Refractive Index / n	Gas
Fluorocarbon Polymer, FCP	148.4 ± 0.20	1.385	O_2
Hydrocarbon Polymer, HCP	96.2 ± 0.25	2.021	O_2
Silicon Dioxide, SiO_2	133 ± 0.77	1.459	SF_6

TABLE 7.1: Coating surfaces and gases used for etching

HCP was used because of the interest in HCP films and their mechanical and tribiological properties. Specifically, HCP has a density, chemical inertness and transparency that make it ideal for optical coatings - which include applications in integrated circuitry [97]. FCP having a structure similar to polytretrafluoroethylene has dielectric properties that make it an excellent insulator for printed circuit boards. Its high melting point also makes it a choice for high performance computing applications. The silica glass has applications in photolithography due to its strength, UV transparency and thermal stability. Silica can only be etched with a chemical discharge and presented an opportunity to discharge SF_6 in an NBE process.

The wafers were cut into 20 mm x 20 mm size coupons. The coupons were coupled to a larger wafer piece using a small drop of Fomblin oil in order to maintain a low wafer temperature. The wafer was placed in the processing chamber of the etcher and centered with the vertical bias plates

either side of the sample. The etching process consisted of a 30 s stabilization period after starting the gas flow, followed by a switch on of the discharge and an etch period of up to 10 min. After etching, the thickness of the coatings on the samples were measured using an *ex situ* ellipsometer (at the London Centre for Nanotechnology). The main etch area was centered on the sample and the ellipsometer was configured to perform a line scan in 1 mm increments.

7.1.2 Results with Varying Ion Current

Figure 7.5 illustrates the etch rates of HCP, FCP and SiO_2 when undergoing plasma processing in a single extractor (only gas phase charge-exchange) arrangement. The horizontal axis is based on a separate SEMION measurement in the same position as that of the sample, where the ion current at different lateral bias sweeps was measured. With the single extractor, the etch rates for all samples decrease with the ion current. This ion contribution is approximately linear and directly proportional to the flux of ions allowed through to the substrate. Some plasma ions are converted into energetic neutrals via the gas phase charge-exchange mechanism without energy loss. The other contribution stems from diffuse thermal neutrals which etch the substrate in chemical reactions. Alongside neutral and ion species, there is also a contribution from UV photons although this is not quantified presently.
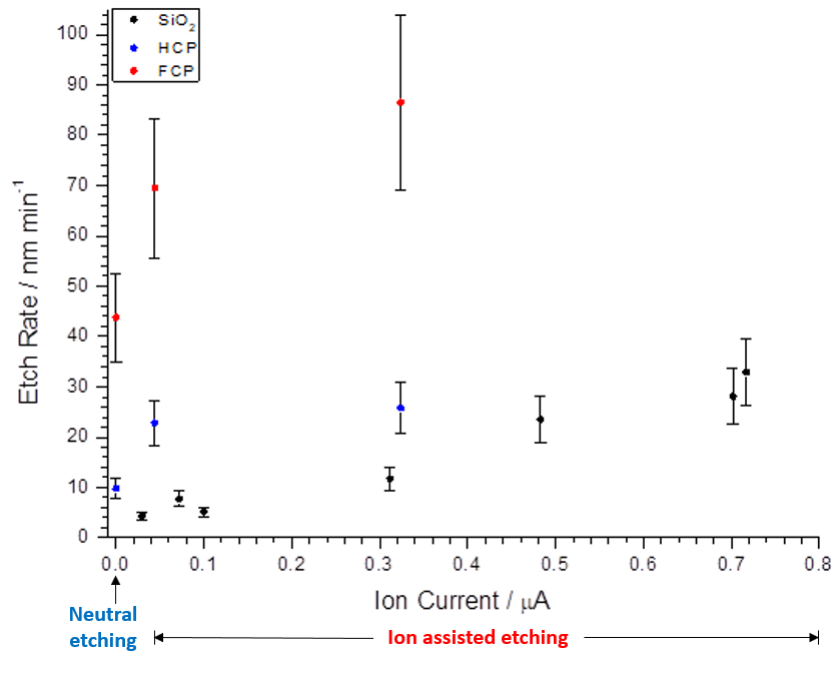
FIGURE 7.5: Etch rate varying with ion current in a single extractor arrangement (gas phase) with a 250 W & 5 mTorr plasma. The gas mixture was 10 SCCM O_2 + 1 SCCM SF_6.

The UV contribution appears reduced with the introduction of the wafer neutralizer (**Figure 7.6**) where it is noted that GaAs has a high extinction and absorption coefficient at the relevant energies as studied by Akinlami *et al.* [98]. In this case, surface neutralization provides the generation of directed neutrals. The neutral etch rates in the wafer neutralizer appear up to 4 times lower than that measured in **Figure 7.5**. HCP appears insensitive to ion current and maintains an etch rate ~ 3 nm min^{-1}. The etch rate of FCP increases up to an ion current of 0.026 μA then stays the same. The etch increase for SiO_2 is very small although it appears to rise at some critical ion current between 0.022 μA and 0.03 μA. At 0 μA ion current, the etch rate is about three times smaller for FCP between a single extractor and wafer neutralizer whilst it is about two times less for HCP. The lower ion currents between the single extractor and wafer neutralizer arrangements indicate a high neutralization efficiency of plasma ions on the wafer neutralizer surface, yet the resulting 'energetic' neutrals seem ineffective for etching. Either they have lost their energy or direction.
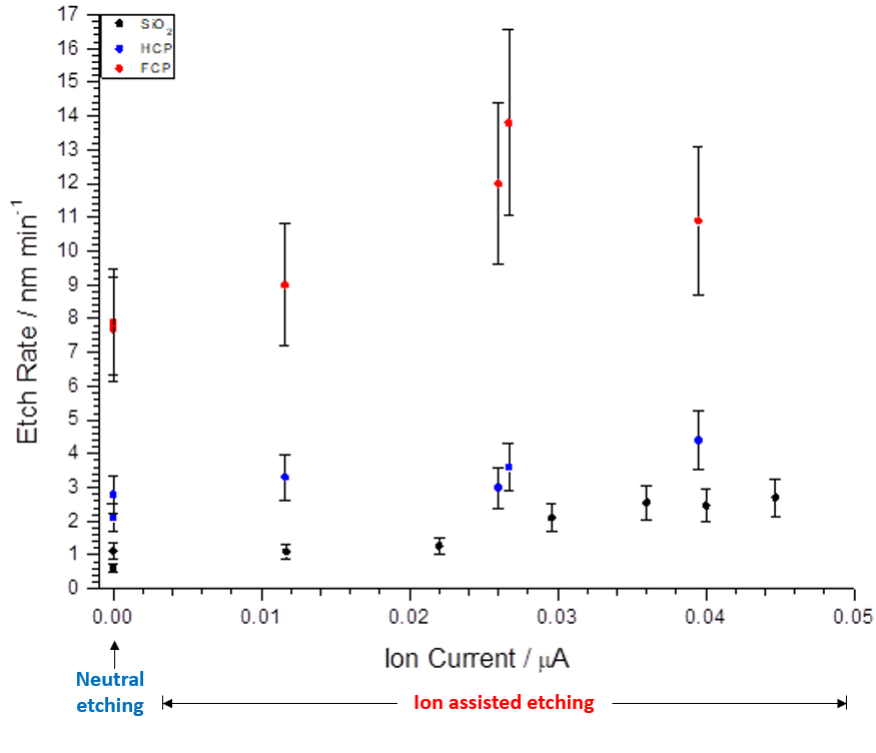
FIGURE 7.6: Etch rate varying with ion current in a wafer neutralizer arrangement (surface phase) with a 250 W & 5 mTorr plasma. The gas mixture was 10 SCCM O_2 + 1 SCCM SF_6.

A summary of the normalized etch rates for the substrates, with and without lateral sweep is given in **Table 7.2**:

	FCP		HCP		SiO_2	
	N_+ & N_0	N_0	N_+ & N_0	N_0	N_+ & N_0	N_0
Single Extractor	57.6	29.2	17.2	6.5	21.9	2.9
Wafer Neutralizer	13.8	7.9	4.4	2.8	2.7	1.1

TABLE 7.2: Etch rates for single extractor and wafer neutralizer.

The etch rates were corrected due to the reduced transmission area of the wafer neutralizer. N_0 is equal to $\pm$ 60 V for lateral sweep and only neutral particles reached the substrate. N_+ & N_0 is equal to 0 V lateral sweep and there is an ion contribution to the particle flux.

The etch rates of FCP and HCP were higher than SiO_2 and reflects the resilience of this substrate even when etched with SF_6. There are also marked

differences in etch rates between the two extractor methods. As previously mentioned, with lateral sweep the etch rate for the single extractor is up to four times greater than the wafer neutralizer. If the neutralization is 100% efficient and it is assumed that both sources create a directed stream of neutral particles, then the two rates should be comparable. This difference can be explained, in part, by the reduced transmission area for the wafer neutralizer. Accounting for the wafer edges and the geometry of the holder, the transmission of the wafer neutralizer was around 66% of the single extractor. The other contributions, refers to UV photons of which the single extractor mesh has full transmittance and the seeming lack of thermalized neutrals when the wafer neutralizer is installed. To determine the contribution from thermal neutral etching, part of the ceramic aperture was covered with a glass slide leaving a gap for non-directional neutral particle etching. Thickness measurements made at a reference point, in the etch region and at the covered region showed no significant etching on the covered region relative to the reference measurement. This indicates the contribution from thermal neutrals was greatly reduced when the wafer neutralizer was fitted. **Table 7.3** details contributions during common etching processes:

Source	Single Extractor	Wafer Neutralizer
Fast Ions / Neutrals	✓	✓
Photons	✓	X
Thermal Ions / Neutrals	✓	X

TABLE 7.3: Etching contributions for the two neutralizers

7.1.3 Results with Varying Top Electrode Bias

In a wafer neutralizer arrangement, the plasma was biased via the top electrode in order to monitor the effect of neutral beam energy on the etch rate.

(A) FCP

(B) HCP

(C) SiO_2
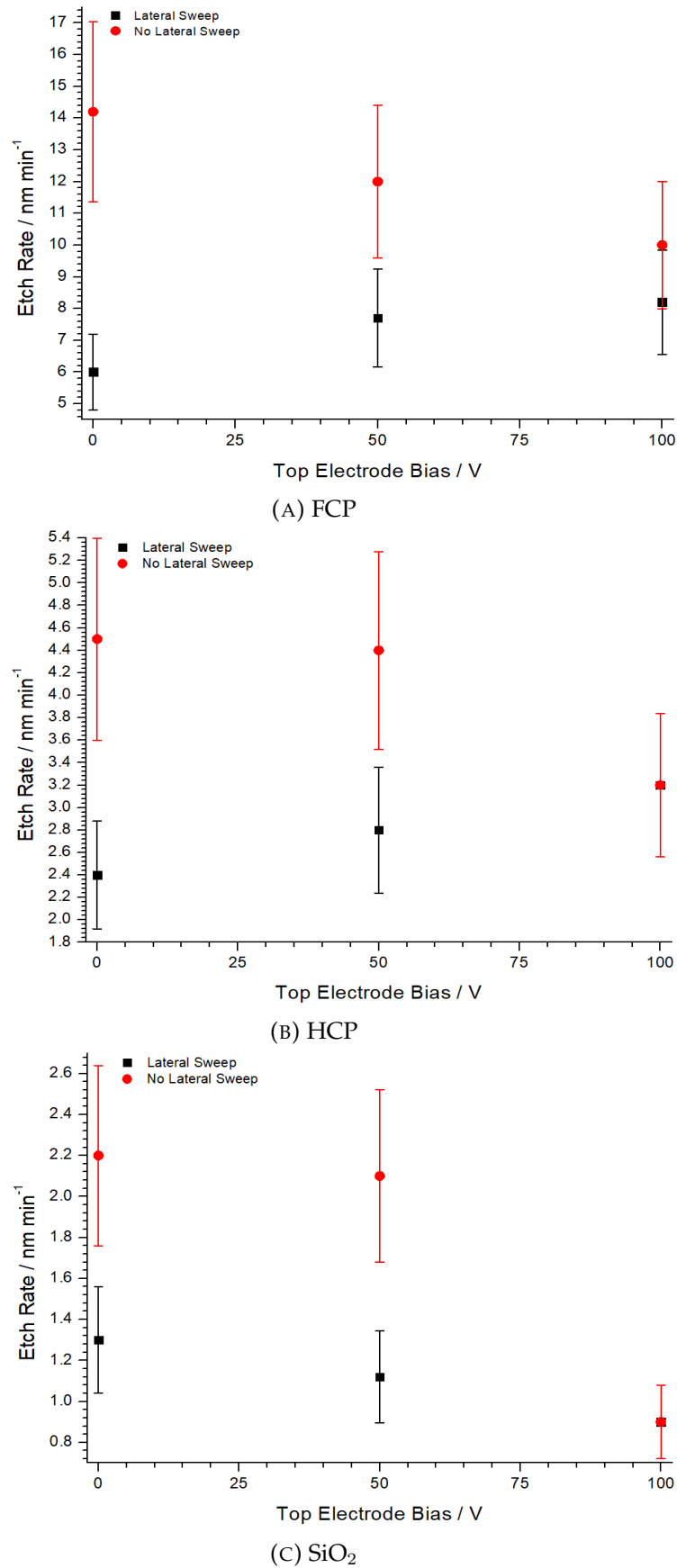
FIGURE 7.7: Plasma conditions are identical to **Figure 7.6**.
The decreasing etch rate (**red trace**) is the result of charge
build-up due to increasing flux of ions to the surface.

In **Figure 7.7**, etch rate does not vary significantly with electrode bias. For FCP (A), the neutral beam etch rate (lateral sweep) increases with increasing eelectrode bias but with less than $0.04 \, \text{nm} \, \text{min}^{-1} \, \text{V}^{-1}$. For HCP (B), the increase in etch rate is comparable with the diameter of carbon atom and cannot be taken as an indication of increased substrate removal. For SiO_2 (C), there is an unexplained decrease in the neutral beam etch rate although given the low etch rates could be statistical. For HCP and FCP, it is believed that the etch rate responds very weakly to plasma biasing because the contribution of diffuse reactive neutrals (and UV photons) has been removed. As discussed in **Chapter 2**, the use of forward angle reflectors had already been investigated by Lee, 2001 and Chung, 2002 [45, 46]. Etch rates were recorded to have a low variation with plasma bias with up to 700 V of bias ($0.014 \, \text{nm} \, \text{min}^{-1} \, \text{V}^{-1}$) with directed O_2 neutral beams. Other investigations (Panda, 2001) used high aspect ratio holes which did not suppress the diffuse neutral contribution [44] and reported etch rates up to $400 \, \text{nm} \, \text{min}^{-1}$ with directed O_2 neutral beams onto silicon polymers at plasma biases up to 130 V ($2.08 \, \text{nm} \, \text{min}^{-1} \, \text{V}^{-1}$). White *et al.* [99] reported rates of at least 200 nm min^{-1} whilst the etching of HCP films with a neutral atomic O_2 beam showed a markedly higher response to plasma bias, Bourdon, 1993 [100]. Without a reactive contribution, the mechanism of neutral-surface interaction seems unfavorable for high etch rates. This may be related to sticking coefficients of neutrals onto surfaces and the transfer of their energies.

The results suggest that without the contribution of ions or diffuse reactive neutrals, neutral beam etching has a low etch rate and the energy gained from biasing does not translate into a greater removal of substrate material. It was proposed that charge is not necessary when trying to etch. However neutral particles are not known for high sticking coefficients and energy transfer during elastic collisions with the surface is poor. The subject of increasing neutral beam etch rates suggests the contribution of UV photons to the etch rate as discussed in the next section.

7.2   Investigation of UV Photon Contribution in NBE

Initial trials strongly confirmed the charge-less neutral beam etching process. The etch rate is low and the energy dependence is very low. This work considers the contribution of UV photons and their effects on the surface of the substrate as a possible additional means of enhancing etch rates.

7.2.1   Motivation and Literature

It is understood that plasmas are sources of UV radiation depending on the discharge chemistry and the power input. This UV radiation has been reported to have deleterious effects on the substrate quality through the formation of defects within the etched features. However in a charge-free etching environment where surface charging and excessive ion damage has been eliminated, it may be possible to tailor the plasma's characteristics such that it can contribute an amount of UV that has a noticeable, positive effect on the low etch rates currently reported. Moreover, these UV photons can contribute to surface reformation which maintains smooth etch features during the etching process.

Chan *et al.* [101] reviewed the use of reactive plasmas and UV photons on polymer surfaces. While conventional plasma treatments are limited to the surface, UV photon mechanisms can take place deep within the bulk (at least 20 nm) of the material. These mechanisms will result in cross-linking, oxidation and dissociation. Other exotic photo-chemical reactions may also occur depending on the substrate. Fukasawa *et al.* reported the increase in etch rate of silicon nitride substrates when exposed with a combination of UV and plasma species by UV [102]. The penetration depth of UV and the extension of photo-chemistry were studied and found to be strongly dependent on the incident wavelength and the optical properties of the material [103]. Both vacuum UV (> 10 eV) and UV (< 10 eV) radiation were used alongside a fluorocarbon plasma in a capacitively coupled setup. Several optical window setups were used to differentiate the UV radiation and it

was found that the action of UV radiation on the silicon nitride caused de-hydrogenation which enabled an increase of the etch rate.

The enhancement of the etch rate via UV photon mechanisms was also investigated by Samukawa *et al.* [104] using an ICP and a chlorine discharge. Neutral beams of up to 100 eV were created via the extraction of a Cl_2 ion beam onto a carbon neutralizer with high aspect ratio apertures. UV photons of wavelengths 200 nm - 600 nm were created using a Xe flash lamp and used to irradiate a silicon substrate sample. It was found that the etch rate of a silicon substrate tripled when the illumination power was raised to almost 40 mW cm^{-2}. The etch depth was measured using atomic force microscopy for etching times of 20 minutes. It was speculated that the presence of UV radiation created crystal defects on the Si surface which increased the surface energy for reactions with Cl_2 radicals and allowed directed neutrals to embed deeper into the surface.

The surface modification of polypropylene was investigated by Grobe-Kruel *et al.* [105] using an ECR plasma and directed Ar ions. It was shown that the exposure to the plasma ion source reduced an initially high etch rate due to the transformation of the polymer into an inter-connected surface. UV action on polymers can cause hardening via crosslinking and the formation of double bonds which impedes etching. Yoshimura *et al.* used a CF_3 ICP where UV photons created by an Ar power source were emitted through a MgF_2 window [106]. It was found that the etching yield of SiO_2 via CF_3 and UV exposure was lower than that of ions. This went against the hypothesis that UV radiation would result in the temporary weakening of atomic bonds to increase the etch rate. The surface modification and subsequent hardening of the substrate was suggested to have lowered the etch rate. Irradiation of just UV photons onto substrate through a MgF_2 window yielded no detectable etching suggesting that photons alone could not remove material from the surface. Conversely, the etch rate can be markedly improved with the addition of UV to conventional etching methods. This

suggests a possible overlap of surface modification and material removal.

7.2.2   Methodology

The Oxford Instruments PL-80 plasma etcher was used to form an ICP discharging He, Ar and O_2 in order to direct energetic neutrals, diffuse neutrals and photons onto HCP and FCP polymer samples. The physical and chemical properties of the samples post-etch were measured. These gases were chosen as they represented atomic (bombardment) and molecular (reactive) discharges that have relatively straightforward chemistries and even when mixed, the fluxes of species do not vary significantly if the plasma power and pressure are kept constant. This was also confirmed using global modelling. Helium was chosen as a VUV/UV photon source due to a wide range of transmissions that encourage modification both on the surface and deep within the bulk. He has a very low mass such that momentum transfer of He species to the substrate surface is insignificant [107].

Common lines of helium are adapted from NIST [108] and are considered representative of a typical helium discharge in **Table 7.4**.

Species	Wavelength / nm	Energy / eV	Intensity / arb
He I	668	1.85	200
He I	588	2.11	120 - 500
He I	502	2.47	100
He I	447	2.77	200
He I	389	3.18	200 - 300
He II	164	7.56	120 - 180
He I	58.4	21.23	1000
He I	53.7	23.08	400
He I	52.2	23.7	100

TABLE 7.4: Strong lines of He

Where He II represents emission from He^+. Since Argon was also used, its common lines are shown in **Table 7.5**:

Species	Wavelength / nm	Energy / eV	Intensity / arb
Ar II	661	1.87	150
Ar II	670	1.85	300
Ar II	671	1.84	1000
Ar II	723	1.71	1000
Ar II	725	1.71	150
Ar I	806	1.53	100

TABLE 7.5: Strong lines of Ar

It is not expected for Argon to provide enough energetic UV photons at the plasma power to instigate noticable photochemistry on the surface. The gas pressure was set at either 30 mTorr or 15 mTorr (**Figure 7.8**). A pressure of 30 mTorr ensured that the average particle energy was approximately 20 eV and comparable with the photon energy without compromising the pressure of the process chamber. 15 mTorr was used to produce more energetic and directed particles as no plasma bias was used. In the case of He mixtures, the He species took a wider range of energies and this also translated into a higher average particle energy. The photon flux could directly be controlled by the plasma power and so the discharge was varied between 100 W and 400 W. In most scenarios, the plasma power was fixed at 200 W to avoid further complexity.

(A) Ar + O_2

(B) He + O_2
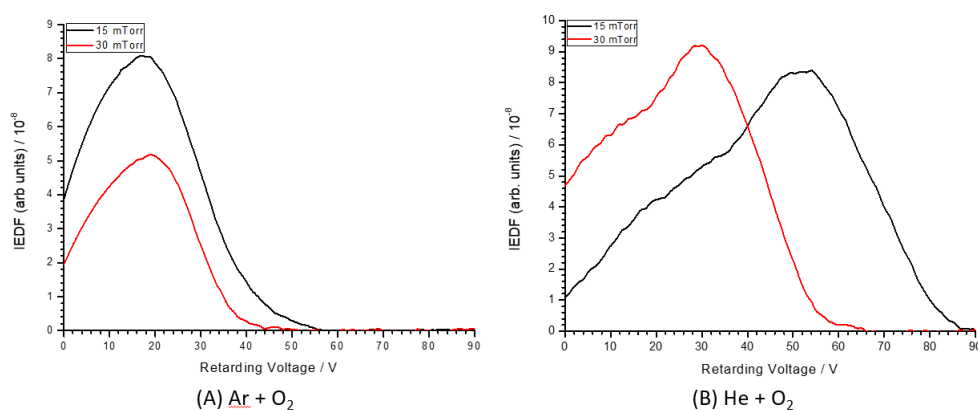
FIGURE 7.8: IEDF's measured with the SEMION. Gases are in 50% ratios. The shift in IEDF (B) is a combination of electron photoemission which overestimates the current and the discharge kinetics varying rapidly at reduced pressure in a He + O_2 mixture.

Polymer samples were cleaved into strip coupons of approximately 1 cm x 1.5 cm. The samples were then placed underneath the open area of

a lateral sweep bias to remove plasma ions from the particle flux reaching the substrate surface. The gas flow was allowed to settle at pressure for 30 s before the plasma was ignited. Mixtures of He, Ar, O_2, He + O_2 and Ar + O_2 were used in 50% admixtures to investigate the effects of changing photon content, chemical reactivity and physical bombardment across a range of substrates. Aside from an open mesh setup, a wafer neutralizer and carbon neutralizer were also used to assess different methods of neutralization and their effects on the substrate. The charge-free etching environment was again monitored by the SEMION as shown in **Figure 7.9**.
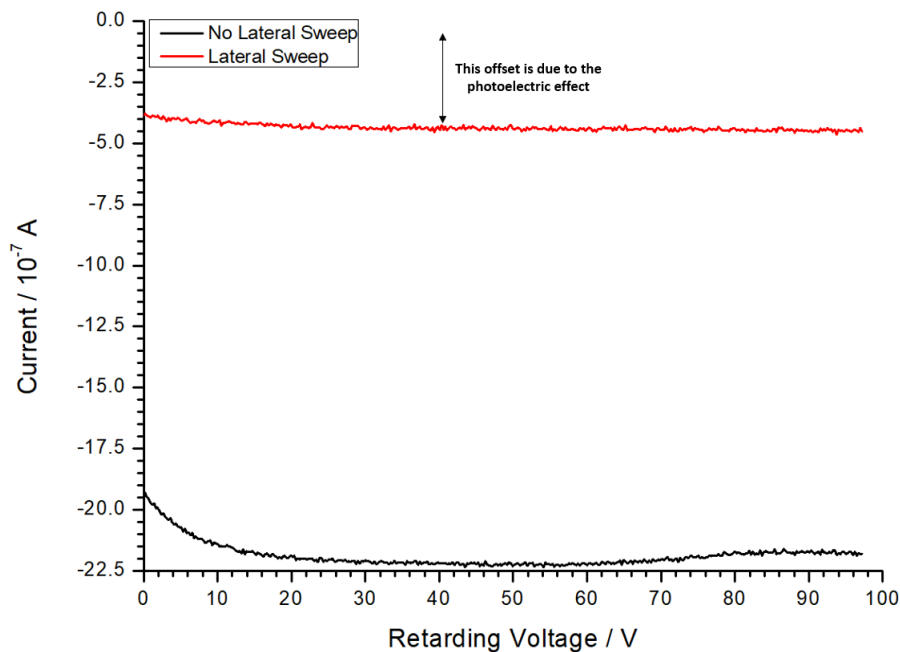
FIGURE 7.9: SEMION IEDF of He plasma with lateral sweep. Applying lateral sweep reduces the ion current to a background signal.

The polymer samples were analyzed post-etch using the following diagnostics:

- Ellipsometry; sample thickness and etch depth

  The thickness of polymer films were measured using a UVISEL ellipsometer at Birmingham University over the wavelength range 250 – 800 nm and at an angle of incidence of 70°. Calculation of the film thickness was performed for each measurement, based on a four-phase ambient Air/Film/SiO$_2$/Si model and each layer was assumed to be isotropic.

- Atomic Force Microscopy (AFM); surface roughness and uniformity

  Surface topographies were acquired using a MFP-3D atomic force micro-scope at the Open University (Asylum Research, UK) operating in intermittent contact mode, employing pyramidal tipped Si cantilevers (PPP-NCL, Windsor Scientific, UK). The cantilever tip presented a hemisphere with radius of curvature 10 nm. A scanning velocity in the range 2 - 6 $\mu m\ s^{-1}$ was employed over a 1 μm x 1 μm region in scans of 5 along the central area of interest. Statistical descriptors of the surface roughness were calculated using Scanning Probe Image Processor (Image Metrology, Denmark).

As a baseline, the surface characteristics of polished GaAs and Si were measured with AFM whilst Air was measured for noise floor:

Material	Average Roughness (S_a)	Error	Peak to Valley (S_z)	Error
GaAs	0.228	0.02	7.111	7.523
Si	0.058	0.005	0.647	0.121
Air	0.0009	n/a	0.102	n/a

TABLE 7.6: AFM Results of GaAs, Si and Air

Table 7.6 shows that the roughness characteristics of polished GaAs is comparable to the characteristics of the pristine polymer substrates. This was rougher than expected, considering the mirror-like quality of the surface to the naked eye. This has consequences for the repeated use of GaAs as a neutralizing surface within the wafer neutralizer. The measurement of Si represents the resolution of the AFM. The Air measurement represents the noise floor of the instrument where the cantilever motion was recorded above the surface (cantilever was not in contact or adjacent to any surface) and the cantilever was allowed to move 1 nm from side to side. Resulting measurements were attributed to mechanical vibrations emanating through the floor of the laboratory or from thermal noise. For practical surface measurements where the cantilever is in contact with surface, the silicon measurement should be taken as the resolution of the system.

7.2.3 HCP Etching Results

Etch Rate and Profile Measurements with Process Time

The effect of UV radiation on HCP was investigated by monitoring the etch depth and the resultant surface roughness characteristics. It was speculated that prolonged exposure to a UV source would result in a hardening of the substrate which would reduce an initially high etch rate.
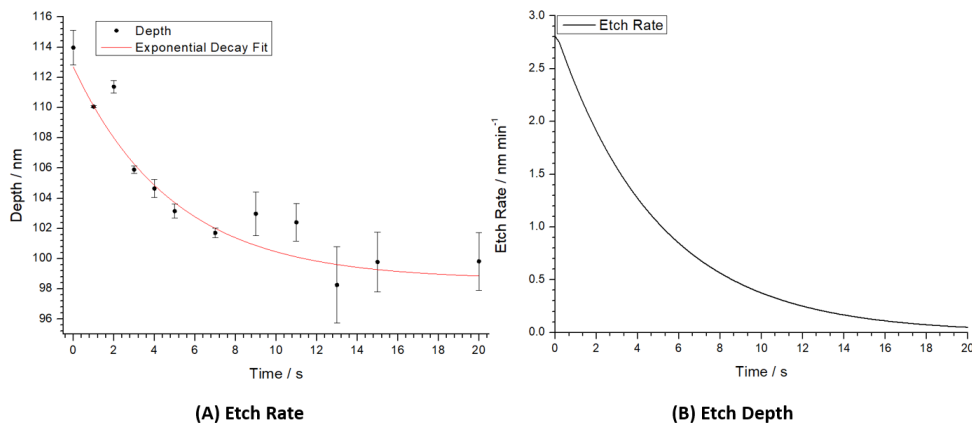
FIGURE 7.10: Evolution of HCP etch depth and etch rate with time in a He + O_2 30 mTorr 200 W plasma. Exposure was with just UV photons, diffuse neutrals and energetic neutrals from gas phase charge-exchange.

Figure 7.10 (B) shows that the etch rate (the time derivative of the exponential decay fit) decreases with time which suggests a modification that makes the surface more resistant to mass reduction. Initially, simultaneous mechanisms of photon absorption and action of plasma particles mean that the etch rate is about 2.8 nm min^{-1}. However, after standard etch times of 10 – 20 mins, the etch rate diminishes to below 0.5 nm min^{-1}. The experiment was later repeated in an oxygen discharge (no He) and no diminishing etch rate was recorded. It appears that continued exposure to UV radiation results in the hardening of the HCP substrate and this is attributed to a combination of dehydrogenation and the formation of cross-linking/double bonds driven by photo-chemistry. An example of this mechanism is given in **Figure 7.11**:
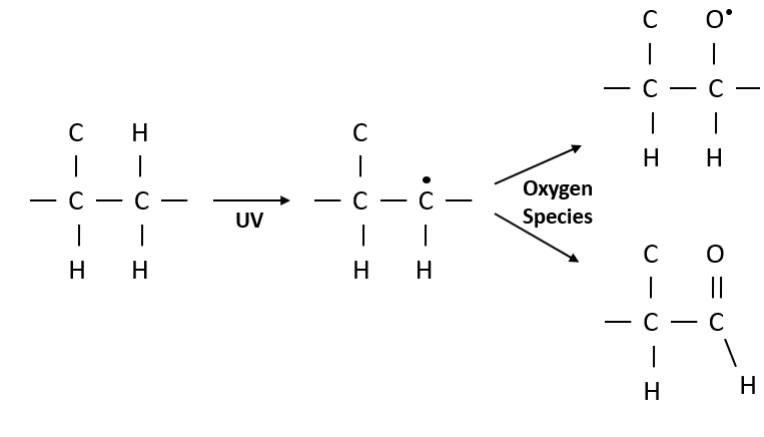
FIGURE 7.11: Illustration of UV causing photochemistry on a HCP polymer. UV photons cause dehydrogenation which are then occupied by oxygen species in single cross-link and double bonds for surface hardening.

Similarly, the effect of UV radiation on the FCP polymer will dissociate C-F bonds, producing F radicals which are chemically active and may go on to dissociate more bonds whilst the alkyl radical becomes filled with oxygen diffusing from the surrounding bulk or process region.

The effect of time on the surface roughness is shown in **Figure 7.12**. Measurements of surface roughness under just UV exposure behind an MgF$_2$ glass ($hv \lesssim 10$ eV) showed a decrease in average roughness, suggesting that the absorption of medium range UV photons transfers energy enough to restructure the surface but not enough to remove mass. This is partly replicated in **Figure 7.12** (no MgF$_2$ glass) at 1 minute where it is not expected to have major mass removal but surface restructuring instead since photon driven mechanisms happen at much shorter time scales than particle mechanisms.
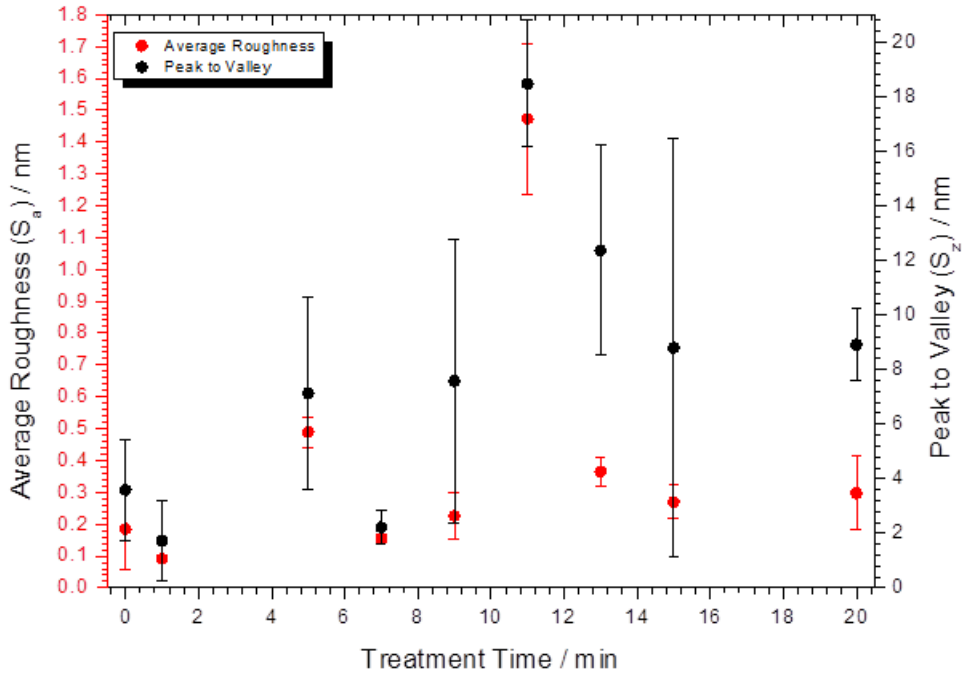
FIGURE 7.12: AFM roughness characteristics of HCP with time.

The arithmetic average of the surface profile given by:

$$R_a = \frac{1}{n} \sum_{i=1}^{n} |z_i| \tag{7.1}$$

It therefore describes the height variations of the surface where a low value suggests very little height variation. Peak to valley however only considers two pixels on the surface between the highest peak and lowest trough and has more direct physical meaning:

$$R_{pv} = \frac{1}{s} \sum_{i=1}^{s} (R_p - R_v) \tag{7.2}$$

Where R_p is the maximum peak height, R_v is the maximum valley depth and s is the number of sampling lengths. It should be noted, large peak to valleys will contribute to a higher average roughness.

Between the pristine sample, there is an absolute change of 14.88 nm between the highest and lowest points on the surface. This increase coincides with the greatest change in etch rate (**Figure 7.10** 0 − 8 mins) where there

is a higher rate of mass removal. At 10 mins, the etch rate begins to level, indicating that the surface is no longer changing rapidly and this appears to coincide with large changes in peak-to-valley in **Figure 7.11**. It was found that the large variations in peak-to-valley (between 9 - 15 mins) were related to impurities and nucleated sites embedded within the substrate that became exposed during the etching process as shown in **Figure 7.13 & 7.14**. Δz refers to the height range of the sample.
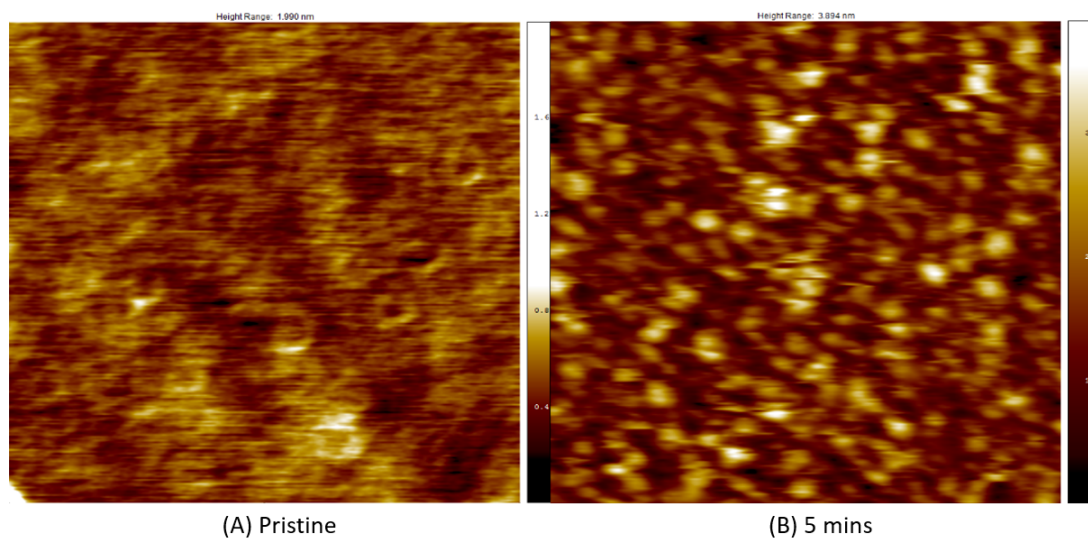
(A) Pristine   (B) 5 mins

FIGURE 7.13: AFM image of the HCP surface at (A) pristine: $\Delta z = 1.99$ nm and (B) 5 minute: $\Delta z = 3.89$ nm treatment.

(A) 11 mins   (B) 20 mins
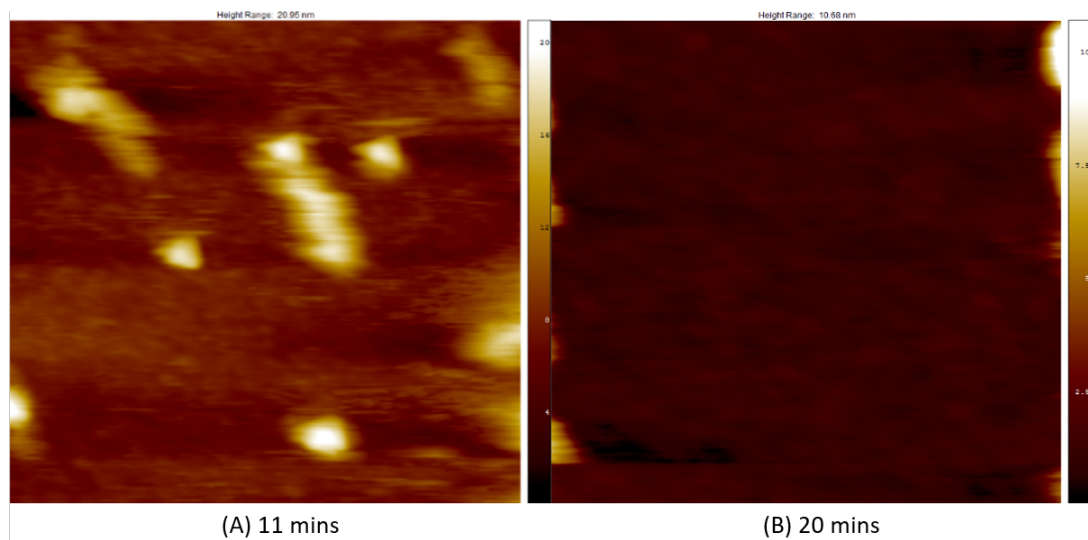
FIGURE 7.14: AFM image of the HCP surface at (A) 11 minute: $\Delta z = 20.95$ nm and (B) 20 minute: $\Delta z = 10.58$ nm treatment.

Phase imaging of nucleated sites did not show any contrast or energy difference to the rest of the surface. These regions must therefore be the same material as the rest of the substrate and are higher density sites. The etch depth of the substrate was greater than the height range of sites, so they cannot have occurred due to micro masking. At 20 mins, it is assumed that most nucleated sites are degraded when under plasma exposure whilst the rest of the surface remains un-etched as the height range became smaller. The regions took longer to modify and etch due to their higher densities. Eventually, the surface became smooth.

The average surface smoothness was low throughout the etching process (average ~ 0.39 nm). The average diameter of a carbon atom is 0.17 nm suggesting that the neutral beam etching process is uniform, where atomic layers are removed. The contribution from UV exposure is that a hardened surface is more likely to maintain this smoothness as there is an absence of preferential material removal on surface. Conversely, the surface roughness of a HCP surface treated by ions was recorded as 0.47 ± 0.3 nm with a peak to valley of 20.6 ± 21.4 nm. This suggests that ion assisted etching would produce rougher features of which NBE would produce comparatively smooth features.

A UV photon contribution to both the etch rate and surface profile of a HCP substrate has been measured. The etch rate diminished over a 20 minute process time and this was attributed to the dehydrogenation and subsequent hardening of the HCP surface. The surface became immediatly smoother by a factor of 2 (**Figure 7.11**) and this was attributed to photon absorption that occurs much faster than physical surface interactions. The high peak to valley values stem from competing mechanisms of UV hardening and reactive mass removal.

Etch Rates and Profile Measurements with Gas Phase Neutralization

In an extractor mesh setup, the discharge pressure was maintained at 30 mTorr whilst the processing chamber pressure was less than 10 mTorr. The power was set at 200 W and the treatment time at 20 mins. Ions were laterally swept.
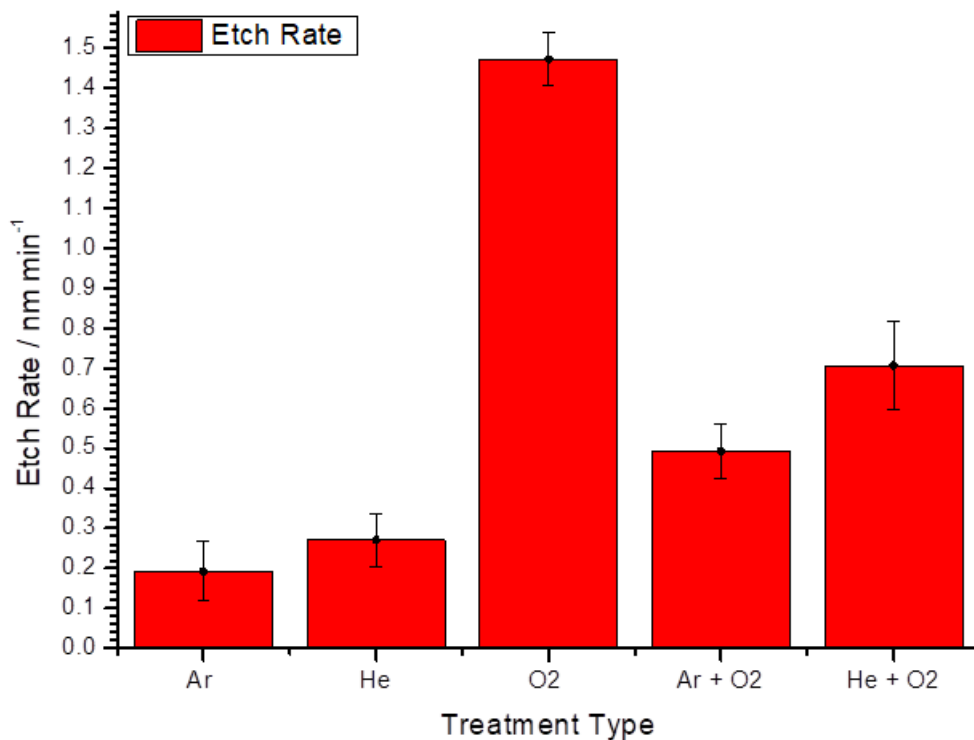
FIGURE 7.15: Etch rates of HCP in the gas phase.

The low etch rates measured in **Figure 7.15** are a combination of low plasma energy density and gas phase neutralization where only 30 - 40% of potential bombarding species are actually directed neutrals. Although He cannot efficiently etch via particle bombardment due to its low mass, an etch rate of 0.27 nm min^{-1} suggests that there is a process which dominates any physical surface interaction such as embedding of metastables [107] and encourages some mass reduction or surface reformation. The etch rate of Ar (a particle known for heavy bombardment of substrates in conventional plasma etching) is even lower. If Ar cannot etch faster than He, it is inferred that neutral bombardment is not a process that encourages etching

on the HCP polymer and therefore the etch rate measured on He is not related to mass reduction. An Ar etch rate of 0.19 nm min^{-1} suggests that every minute, only 1 layer of atoms are removed. This could be related to UV photon mechanisms in the bulk. There is no physical chemistry at the surface of HCP when exposed to a noble gas discharge and this was confirmed via XPS analysis. In the presence of a pure O_2 discharge, surface reactions are expected due energetic oxygen depositing energy in 'hotspots' which enable the adsorption of O radicals on the surface to remove material. This is seen in a greater 1.47 nm min^{-1} etch rate which is approximately 7 layers of atoms removed a minute.

O_2 discharges do not have high intensities of energetic UV. So the etch rate appears to be mainly the result of neutral beam assisted chemical reactions on the surface of HCP. The addition of He or Ar to the O_2 discharge reduces its etch rate by at least half. In the Ar + O_2, it would have been expected that there would be no change to the etch rate as determined in global modelling results, 50% Ar did not noticably lower the main reactive species. Any addition of Ar in theory would have benefited the neutral beam assisted etching via surface bombardment. Instead, the decreased etch rates of He + Ar addition to O_2 indicates simultaneous processes of VUV absorption which causes surface hardening and chemical reactions which attempt to etch the surface. Furthermore, although neutral flux was unable to be measured in this setup, global modelling results indicated that there was a negligible difference in the population of specific plasma species even up to 50% admixtures. Therefore, it is argued that as the plasma power and pressure are kept constant, the fluxes of neutrals to the surface in each case are comparable.
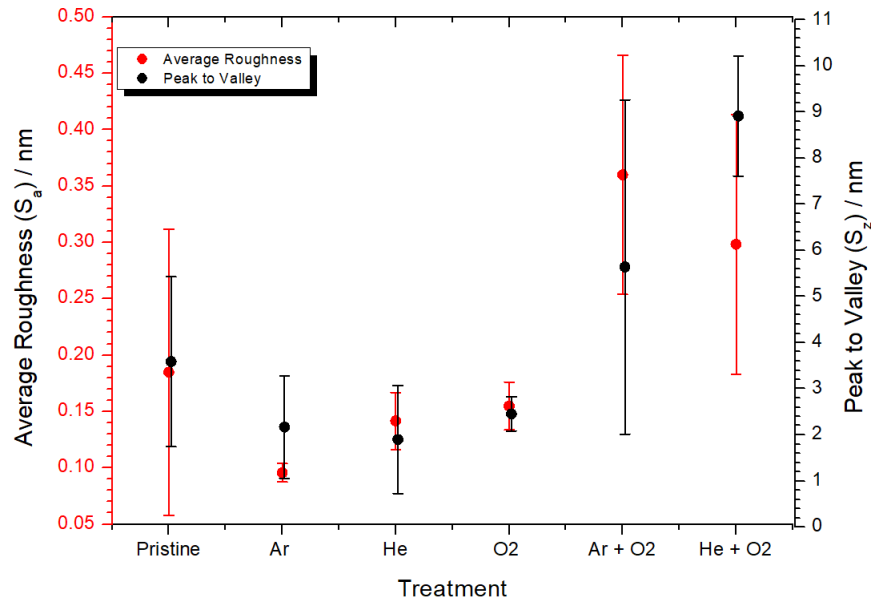
FIGURE 7.16: AFM roughness characteristics of HCP in the
gas phase.

The roughness characteristics of pristine and post-etch HCP are shown
in **Figure 7.16**. In the case of Ar and He, the very low etch rates suggest
that the surface has reformed and smoothened due to photon absorption
processes. It would have been expected that in the case of Ar, if it had
been transferring a lot of energy via physical bombardment, the surface
post process would be rougher. Instead, the roughness characteristic mir-
rors that of medium UV exposure behind MgF_2 glass. This suggests that in
the low energy (< 100 eV) regime, some energy is transferred to the surface
to create 'hotspots' [41]. This energy then dissipates locally and encourages
surface reformation. In the case of O_2, the smoothness of the surface sug-
gests that the etching mechanism was uniform and that energy deposition
by bombarding heavy species, assisted chemical reactions. Gas mixtures
of He + O_2 or Ar + O_2 appear to have increased the roughness and this is
due to competing mechanisms of surface reformation/hardening and mass
reduction via chemical reactions. The consequences for smoothness in the
He and Ar cases are that the directed neutral beams are not transferring
enough energy into the material bulk in order to break bonds.

Etch Rates and Profile Measurements with Carbon Neutralizer

The mixture of the discharge was He/O$_2$ whilst the power and pressure were varied. The treatment time was set at 20 minutes with lateral sweep.
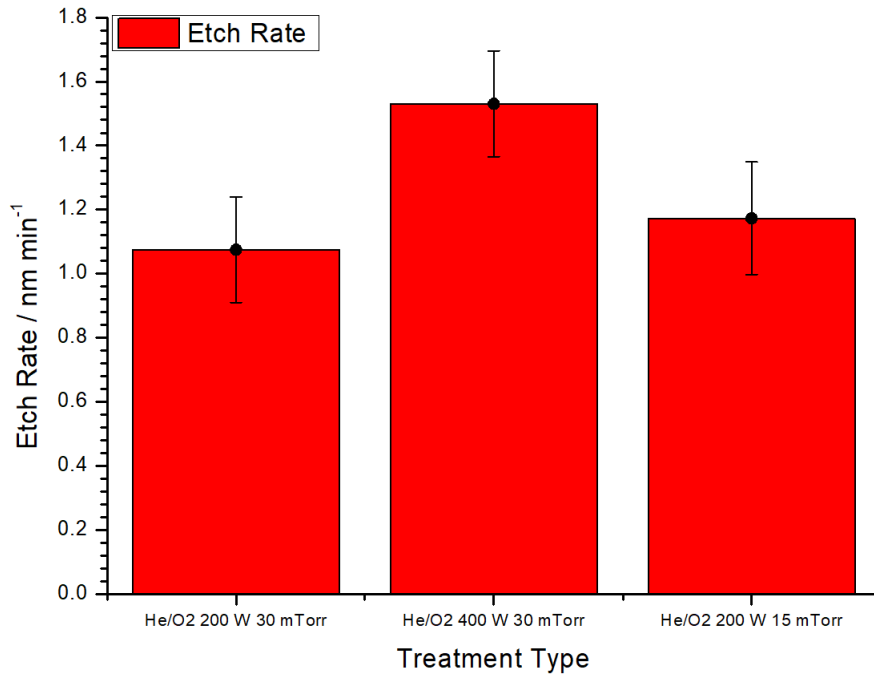
FIGURE 7.17: Etch rates of HCP with carbon neutralizer.

FIGURE 7.18: AFM roughness characteristics of HCP with carbon neutralizer.

In **Figure 7.17**, the etch rate was corrected for the reduced transmission of the carbon neutralizer as the etching area was not defined by the size of aperture. In **Chapter 6**, it was not evident that a carbon neutralizer could produce a directed flux of energetic neutrals due to multiple collisions and scattering within the apertures. This was however due to the very tight geometric constraints that required particles to be traveling on axis with the EQP flight path for detection. In previous work by Marinov *et al.* [52], the carbon neutralizer was reported to have up to 95% neutralization efficiency such that most of the particles exiting the neutralizer were neutralized. The reduced transmission and high aspect ratio aperture also means that the UV emission is reduced and this can be seen by the increase in etch rate of the He + O_2 mixture when compared to **Figure 7.15**. Since it is known that He suppresses the O_2 etch rate by at least 50%, the reduced photon transmission due to the carbon neutralizer has increased the etch rate to 1.07 nm min^{-1}. Doubling the power produced more reactive O and the etch rate increased to 1.53 nm min^{-1}. Lowering the pressure had no noticeable effect on the etch rate, suggesting very little energy dependence.

The etch rate responds weakly to large changes in plasma parameters such as power (greater O content) and pressure (higher energy range of bombarding species). In the latter case, this seems to suggest that much of the energy of bombarding species is lost within the carbon neutralizer and this was observed by Marinov, 2015. The roughness characteristics (**Figure 7.18**) indicate that changing the pressure had no effect on the etching process with HCP in the carbon neutralizer setup. Although some larger height ranges were seen, increasing the power only slightly made the surface less smooth. The etching of HCP with a carbon neutralizer was therefore predominantly chemical in nature due to the reduction of UV photons and low energy transfer via bombarding species. This infers that fast neutrals were supplementary in the final etching process.

Etch Rates and Profile Measurements with a Wafer Neutralizer

The power of the discharge was set to 200 W, pressure to 30 mTorr treatment

time was set at 20 minutes with lateral sweep.
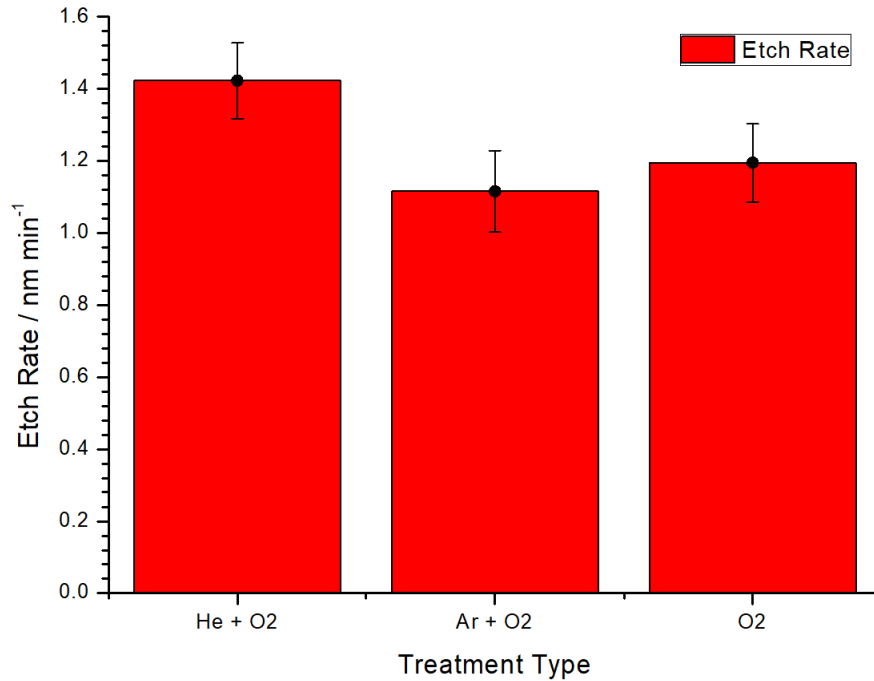
FIGURE 7.19: Etch rates of HCP with wafer neutralizer.

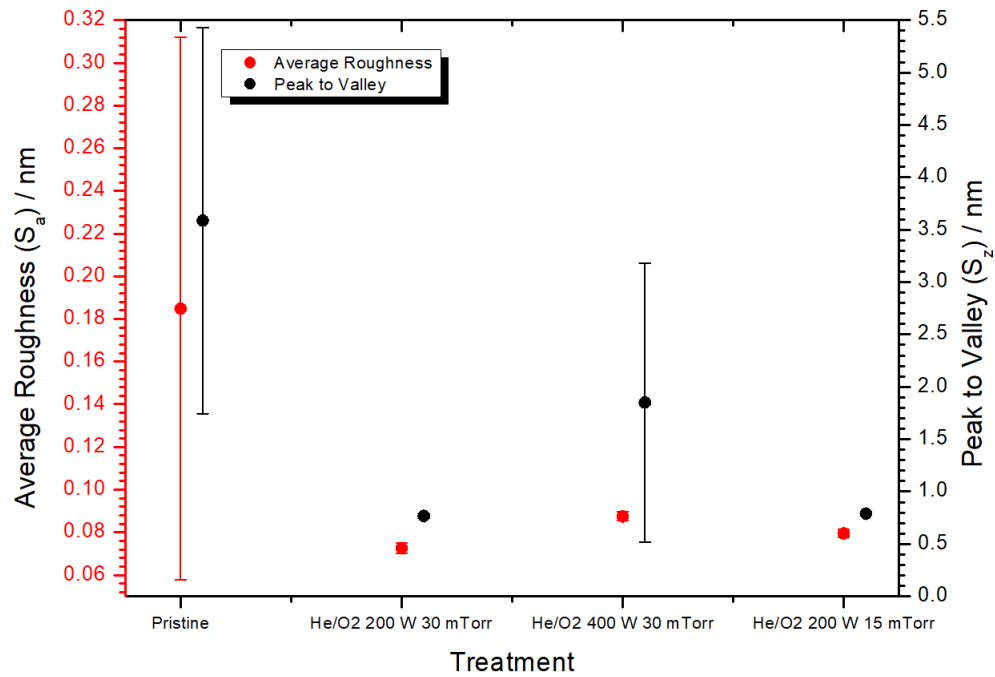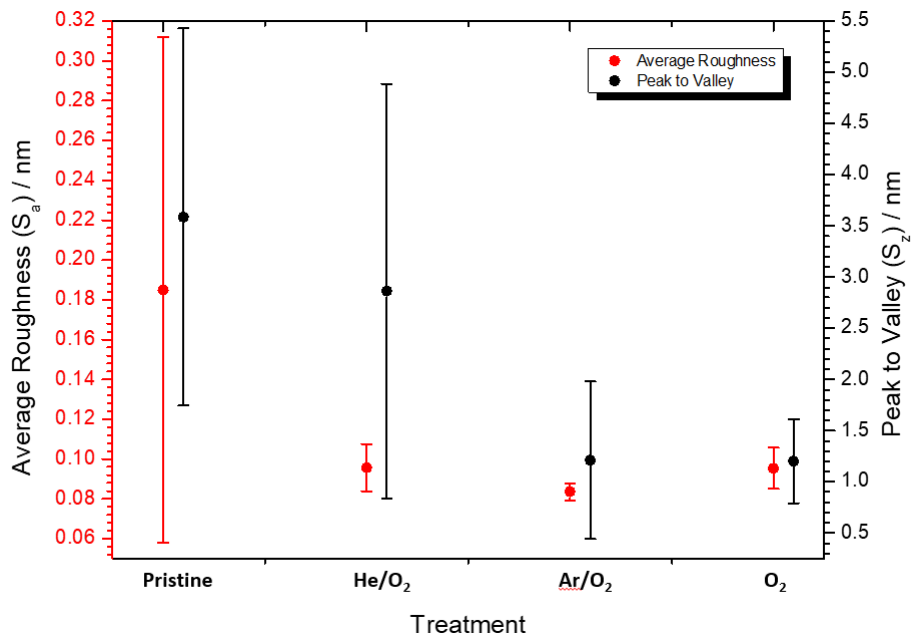FIGURE 7.20: AFM roughness characteristics of HCP with
wafer neutralizer.

There was no line of sight through the wafer neutralizer so that the arrival of UV photons to the substrate was not expected. **Figure 7.20** shows that an increased etch rate of the He + O_2 (compared to **Figure 7.15 & 7.17**) suggests that the removal of UV photons has prevented surface hardening. The etch rate is comparable to that of O_2 in a gas phase neutralization mechanism (**Figure 7.15**). Because there is no marked difference between He + O_2, Ar + O_2 and O_2 It is reasoned therefore, that the etch rates of all cases are mainly the result of neutral radicals rather than directed neutrals. This again suggests that neutral beams deposit very little of their energy on the surface to lower the activation of neutral reactions. The slightly higher etch rate of He + O_2 can be attributed to process within the plasma discharge itself where absorption of of UV encourages the dissociation of O_2 into O.

The roughness characteristics (**Figure 7.20**) indicate that the surface of HCP became smoother with average surface roughness comparable to using a carbon neutralizer. The decrease in average roughness in these molecular discharges is explained by considering the interaction of diffuse reactive neutrals which uniformly cover the surface.

Summary

HCP has an etch rate of 1.5 nm min^{-1} when etched with an O_2 ICP at 200 W for 20 mins. This is larger than that achieved with He, Ar, He/O_2 and Ar/O_2. The generally low etch rates indicates that HCP is a resilient material and actively hardens during plasma exposure. This is noticeable in Ar and He mixtures where there was a high flux of UV photons to the surface. It is thought that the surface hardening occurs due to dehydrogenation and cross-linking which is driven by photo-chemistry. It is also seen that noble gas neutral beams do not have a significant effect on the surface and cause no damage, instead, depositing a fraction of their energy in a local area to allow the greater absorption of thermalized neutrals. This corresponded with noticeable smoothening in the presence of noble gas discharges with or without UV.

7.2.4 FCP Etching Results

Etch Rates and Profile Measurements with Gas Phase Neutralization

Compared to HCP, the treated surface of FCP is shown to be generally rougher and less uniform. This is attributed to the higher density of states present on the surface and within the bulk. For example, there are the usual C-H and C-C groups. But there are also C-F, $C-F_2$ and $C-F_3$ in various configurations that increase the electron density of the material and contribute to its roughness. The physical surface properties were measured as the treatment time was varied. The average surface roughness visibly decreased for the first 10 mins of treatment time in **Figure 7.21**. The roughness then rose by a factor of 3 at the end of 20 mins.
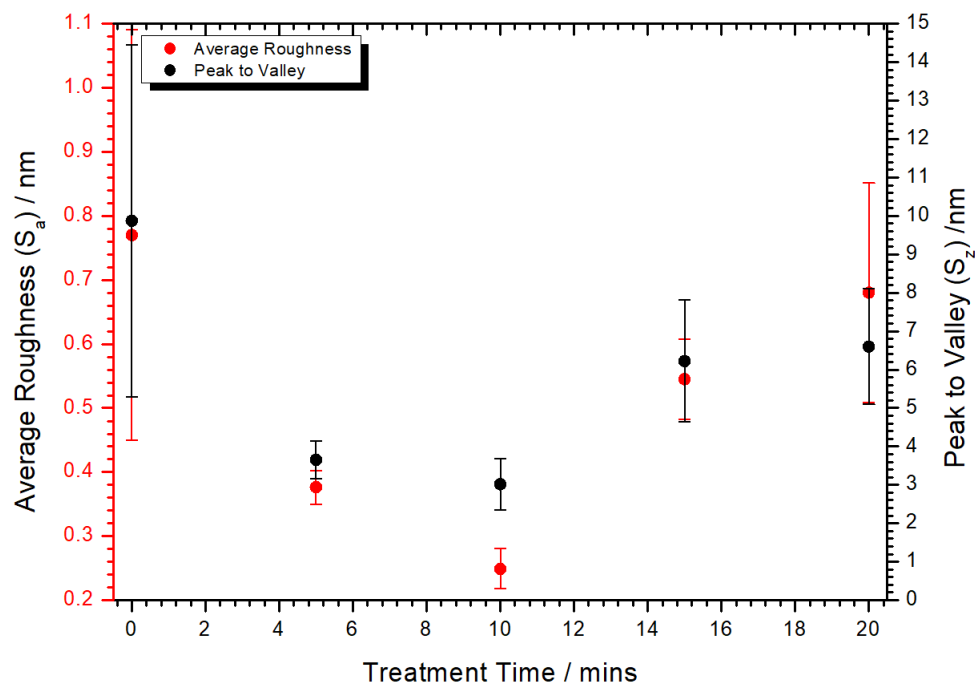
FIGURE 7.21: Evolution of FCP roughness characteristics. The substrate was exposed to a 200 W He/O_2 plasma.

Consecutive imaging of the substrate at the treatment times are shown in **Figure 7.22 & 7.23**.
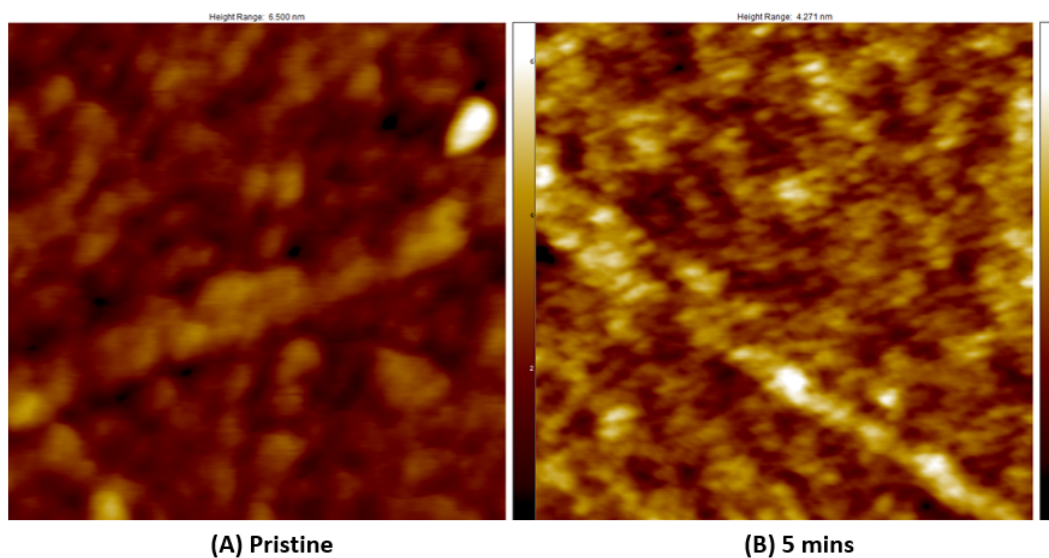
FIGURE 7.22: AFM image of the FCP surface at pristine: (A) $\Delta z = 6.5$ nm and (B) 5 minute: $\Delta z = 4.27$ nm.
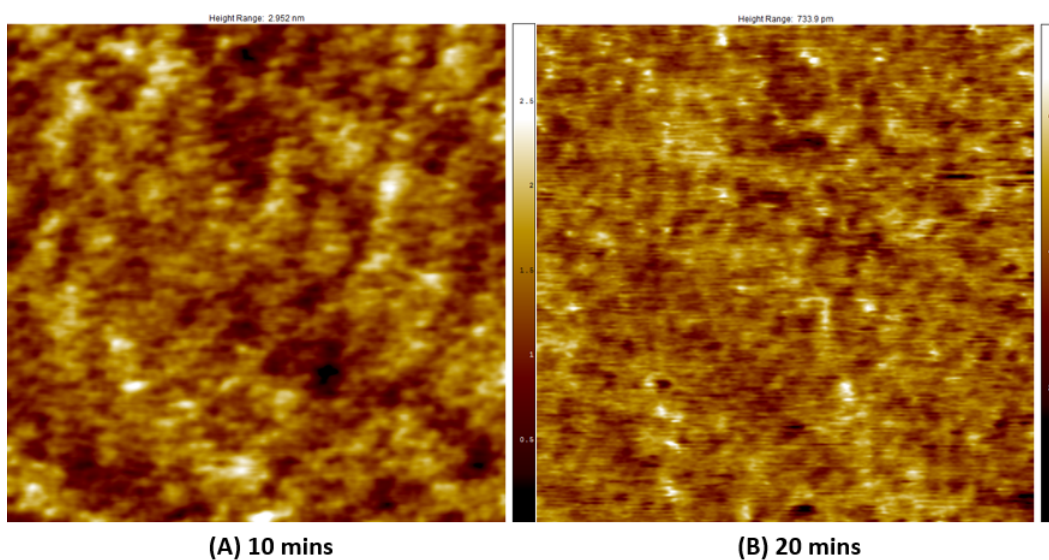
FIGURE 7.23: AFM image of the FCP surface at (A) 10 minute: $\Delta z = 2.95$ nm and (B) 20 minute: $\Delta z = 0.73$ nm.

Reducing height range and color homogenization over time suggests a smoothed surface. The surface is seen to visibly smoothen and become uniform over time. This is contrasted to HCP which showed some form of roughening (with the uncovering of nucleated sites) before becoming smooth once again.

The power of the discharge was set to 200 W, pressure to 30 mTorr and the treatment time set at 20 minutes with lateral sweep.
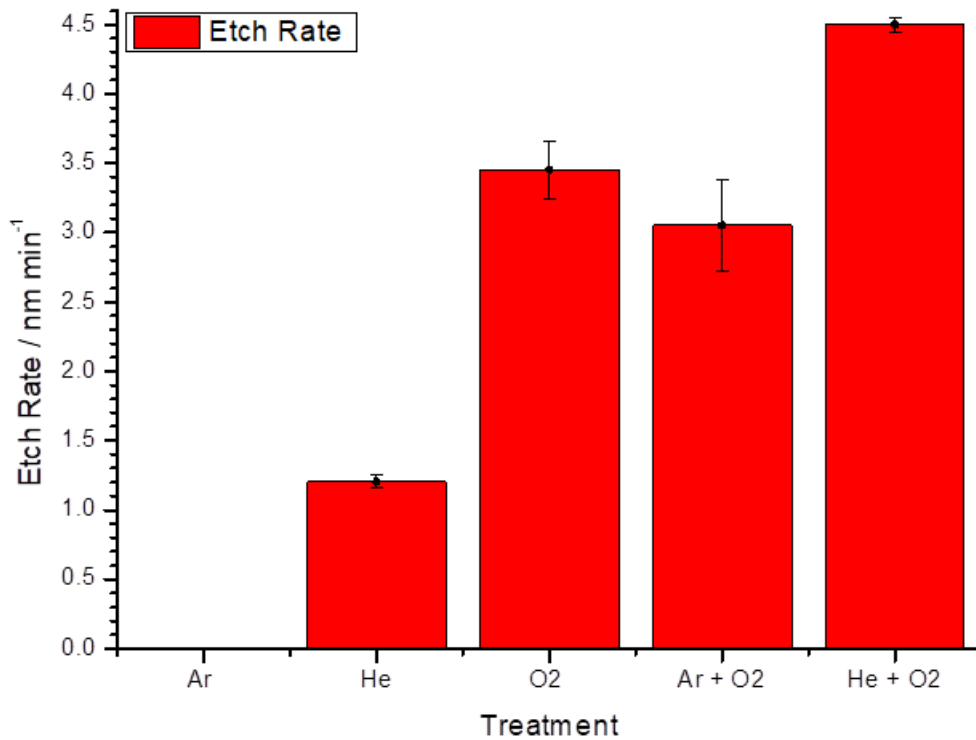
FIGURE 7.24: Etch rates of FCP in gas phase.

In **Figure 7.24**, the addition of He not only establishes a contribution to the etch rate from UV photons, there also appears to be a large smoothing of the surface both in terms of average roughness and peak to valley (**Figure 7.25**). Exposure to a He plasma by itself reduces the average surface roughness by about 50% (0.77 nm to 0.4 nm). Because He is not expected to sputter the surface, this must be due to dissociation of bonds on the surface and within the bulk of the FCP substrate. There are many C-F polar bonds that can be broken by VUV and especially appear less stable to radicals present in an O_2 plasma as the etch rate in O_2 is 4 times that of HCP. Adding He and O_2 together improves the etch rate almost 4 times that of He alone. Specifically with He + O_2, the etch rate rises to 4.5 nm min^{-1} from O_2 (3.45 nm min^{-1}) alone, the difference of which is comparable to the etch rate when exposed to a He plasma (1.2 nm min^{-1}). This difference suggests that while

O_2 contributes a chemical reaction mechanism to mass reduction, He provides energetic UV photons which photo-dissociate C-F bonds and increase the surface energy for neutral reactions to take place.
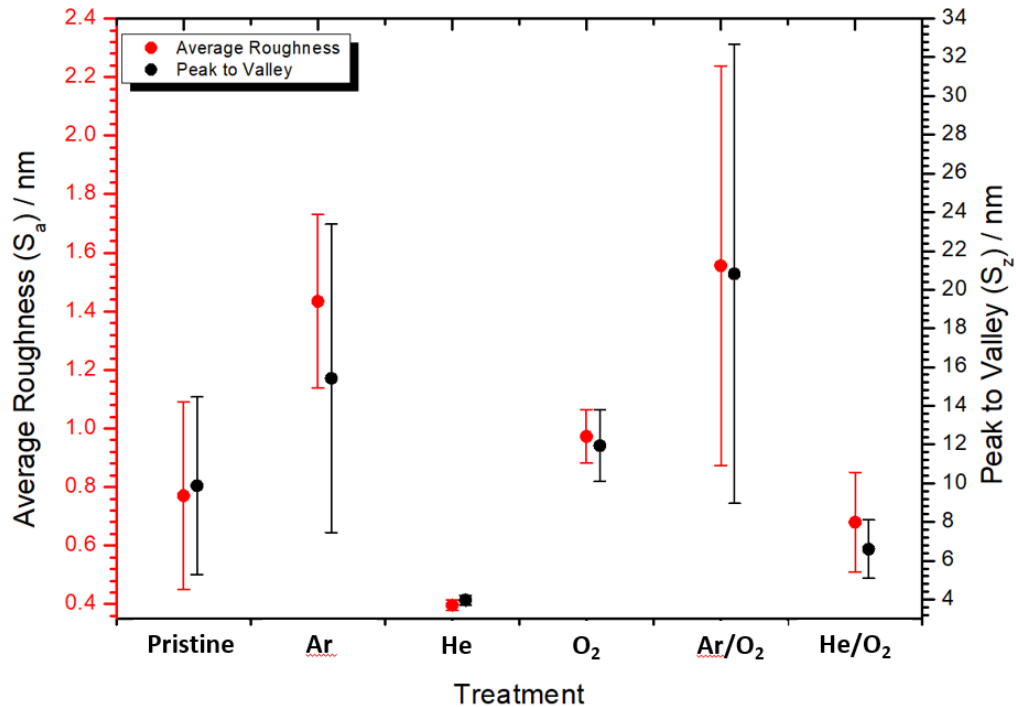
FIGURE 7.25: AFM roughness characteristics of FCP in gas phase. Marked smoothness of He is attributed to dissociation of C-F bonds and resultant double bond and cross-linking formation.

There was no detectable etch rate when exposed with an Ar plasma and this was also confirmed via optical observation at the surface post-etch. There was a measurable change in surface roughness however which suggests some manner of surface modification although it is less clear on how Ar affects this. Adding O_2 to Ar produces an etch rate of 3 nm min^{-1} with an error that overlaps with O_2 alone. This suggests that Ar contributes a negligible effect to the etch rate of FCP. The increased roughness characteristic with Ar however suggest some other form of surface interaction, the mechanism of which is not understood.

Etch Rates and Profile Measurements with a Carbon Neutralizer

The mixture of the discharge was He/O_2 whilst the power and pressure were varied. The treatment time was set at 20 minutes with lateral sweep.
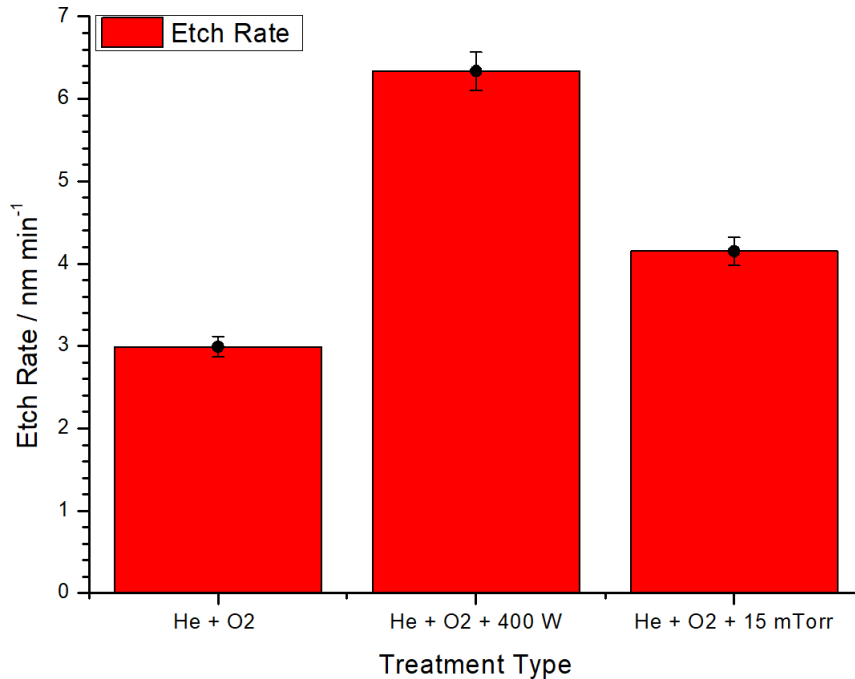
FIGURE 7.26: Etch rates of FCP with a carbon neutralizer.

The use of a carbon neutralizer (**Figure 7.26**) markedly reduces the etch rate of the He + O_2 mixture (compared to **Figure 7.24**) and this is thought to be due to a simultaneous reduction in UV photons and energy of neutrals. Doubling the power approximately doubles the etch rate (3 nm min^{-1} to 6 nm min^{-1}). This magnitude of etch rate increase was not seen in HCP. The transmission of the carbon neutralizer suggests that this increase is mainly due to O radicals. Halving the pressure causes an increase in etch rate but to a lesser degree. This again indicates the weak energy dependence of the neutral beam etching process (**Figure 7.17**).
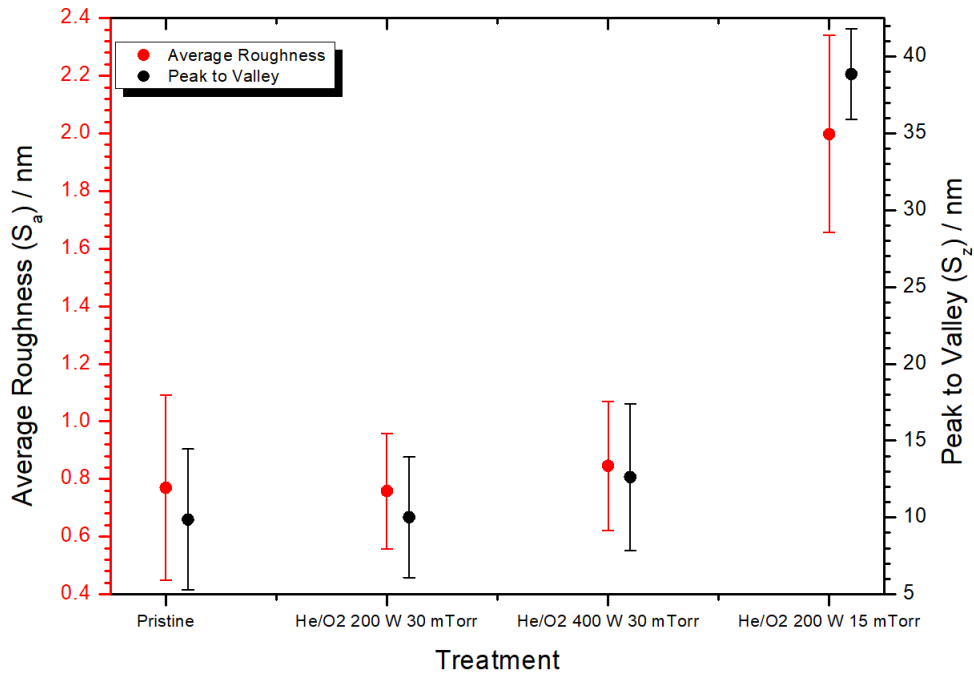
FIGURE 7.27: AFM roughness characteristics of FCP with carbon neutralizer

In **Figure 7.27**, there is no marked change in the roughness characteristic until the pressure is halved. The mechanism by which this occurred is not understood other than the increased particle energy having a more marked effect on the surface during bombardment. This change in roughness profile is reflected in the etch rate of about 1 nm min^{-1} when compared with He + O$_2$ at the standard pressure of 30 mTorr. The smoothness of the other profiles continue to indicate a more reactive etching mechanism.

Etch Rates and Profile Measurements with Wafer Neutralizer

The power of the discharge was set to 200 W, pressure to 30 mTorr treatment time was set at 20 minutes with lateral sweep.
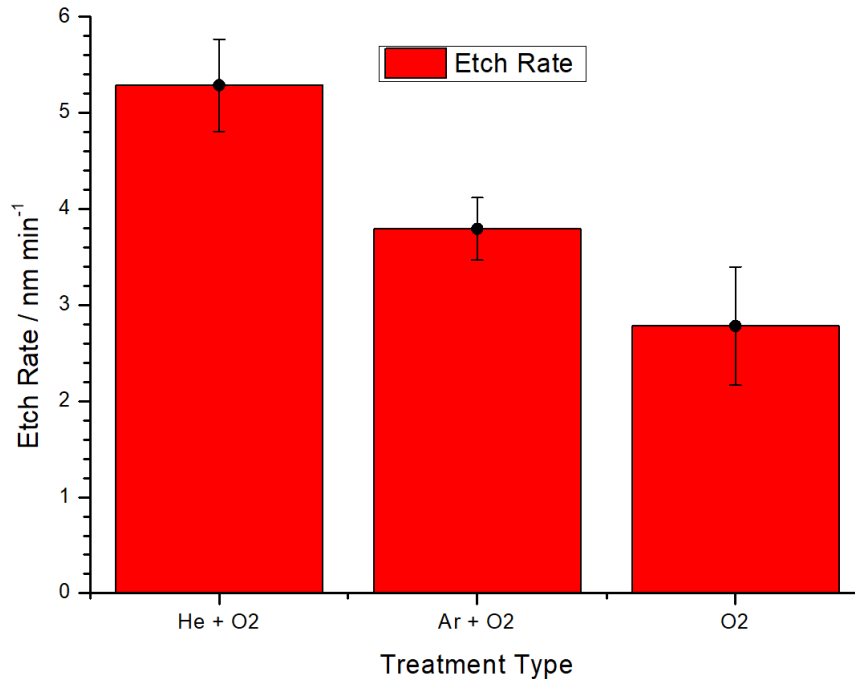
FIGURE 7.28: Etch rates of FCP with wafer neutralizer.

In **Figure 7.28**, it can be seen that etch rate of He + O_2 is 5.2 nm min^{-1}. This is larger than that measured in the gas phase (**Figure 7.24**) and carbon neutralizer (**Figure 7.26**). This is unexpected as the UV contribution has been removed. The reduction of the O_2 etch rate is also odd and seems to suggest a reduction in thermal neutrals. Why the wafer neutralizer potentially reduces the thermal contribution (**Section 7.1.2**) is not known. Ar + O_2 has visibly increased when compared to **Figure 7.24** which further disputes the O_2 measurement.

The roughness characteristics in **Figure 7.29** are the greatest indicator of the effect of bombarding, energetic neutrals. The noticeable increase in surface roughness (specifically Ar + O_2) indicate a mechanical etching mechanism where directed, energetic neutrals have deposited their energy in zones. Conversely, the uniform adsorption of diffuse reactive radicals in the

O_2 has ensured that the surface remains somewhat smooth.
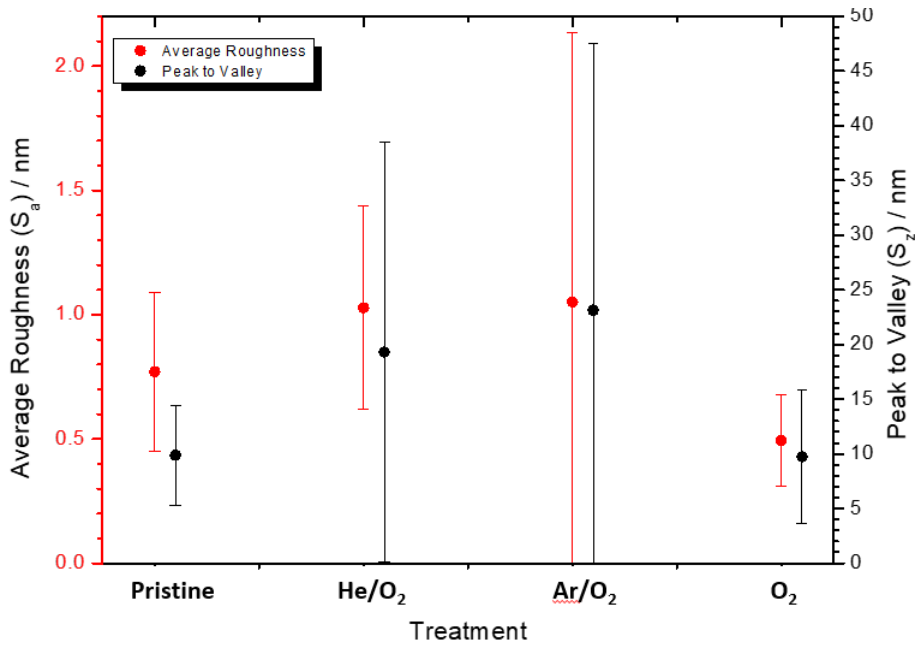
FIGURE 7.29: AFM roughness characteristics of FCP with a
wafer neutralizer.

The FCP roughness characteristics (**Figure 7.29**) indicate large variations in average surface roughness and peak-to-valley. The exception is O_2 which shows the expected lowered roughness profiles for a reactive and uniform neutral beam etching process.

Summary

The absorption of UV into the bulk of FCP dissociates C-F bonds and increases the surface energy of the substrate, leading to high etch rates. Etch rates in the carbon neutralizer respond more markedly to plasma parameters such as power and pressure. Doubling the power doubles the etch rate and it is thought that this is due to a combination of higher photon flux and the production of reactive species. Halving the pressure increases the etch rate suggesting that there is a small energy dependence of the bombarding neutral beam. In the wafer neutralizer, the etch rates were unexpected although increased roughness values suggested a mechanical etching mechanism from energetic neutrals. The combined etch rates and average surface

roughness profiles of both polymers are tabulated in **Table 7.7** and **Table 7.8**:

	Etch Rate / nm min^{-1}			Surface Roughness / S_a		
	Gas Phase	**Carbon**	**Wafer**	**Gas Phase**	**Carbon**	**Wafer**
Ar	0.192			0.096		
He	0.270			0.141		
O$_2$	1.473		1.195	0.155		0.095
Ar + O$_2$	0.493		1.116	0.36		0.084
He + O$_2$	0.707	1.074	1.423	0.298	0.073	0.096

TABLE 7.7: Etch rates and average surface roughness values
for the HCP polymer. Pristine roughness = 0.18483.

	Etch Rate / nm min^{-1}			Surface Roughness / S_a		
	Gas Phase	**Carbon**	**Wafer**	**Gas Phase**	**Carbon**	**Wafer**
Ar	0			1.434		
He	1.202			0.397		
O$_2$	3.455		1.531	0.973		0.494
Ar + O$_2$	3.051		2.087	1.556		1.051
He + O$_2$	4.501	1.047	2.909	0.680	0.758	1.027

TABLE 7.8: Etch rates and average surface roughness values
for the FCP polymer. Pristine roughness = 0.77019.

The complexity here is that the two polymers have distinctly different responses to plasma particle and UV exposure. HCP hardens in the presence of UV and this competes with simultaeneous etching mechanisms. In mixed discharges of UV photons, diffuse neutrals and energetic neutrals, the etch rate of HCP is suppressed and the roughness of the surface increases. The surface of HCP post etch is smoother if these contributions are separated or UV is mitigated by the presence of a carbon or wafer neutralizer. On the otherhand, UV exposure on FCP actually supplements etching mechanisms due to rapid photo-dissociation of C-F bonds. The effect of energetic neutral beams is ambiguous. In the Ar case, they do not transfer enough energy to the surface to etch and due to the similar masses of Ar and O$_2$, it is difficult to distinguish the contribution of the neutral beams in both the gas phase and wafer neutralizer based on etch rate alone. The increased surface roughness when Ar is added however seems to imply the directed neutrals do in fact have some significance in the surface physics.

7.3   X-ray Photoelectron Spectroscopy Results

The previous section has highlighted the effects of neutral beam and UV exposure from a physical point of view by measuring the etch rate and surface profile. Quantifying the neutral beam contribution was found to be non-trivial. It was concluded that UV interaction caused surface hardening via recombination of radicals and cross-linking within HCP, but encouraged higher etch rates in FCP via the dissociation of C-F bonds and the creation of defects which reacted very quickly to O_2 species. It is important to note that an increase in surface roughness suggested a mechanical etching mechanism (neutral beams) that was more abrasive and zonal. A decrease in surface roughness suggested a reactive mechanism (UV photons and adsorbing neutrals) which was uniform and removed material layer by layer. To further validate these claimss, a look at the chemical characteristics of the surfaces post-etch was undertaken.

X-ray Photoelectron Spectroscopy (XPS).

X-ray photoelectron spectroscopy (XPS) was performed on a Thermo Fisher Scientific K-alpha+ spectrometer at the Cardiff Hub of the EPSRC National facility for XPS. Samples were analysed using a micro-focused monochromatic Al x-ray source (72 W) over an elliptical analysis area of 600 microns. Data were recorded at pass energies of 150 eV for survey scans and 40 eV for high resolution scan with 1 eV and 0.1 eV step sizes respectively. Charge neutralization was achieved using a combination of low energy electrons and Ar ions. Data analysis was performed in CasaXPS using a Shirley type background and Scofield cross sections, with an energy dependence of -0.6.

This section illustrates the effects of UV radiation and O_2 chemistry on the surfaces of HCP and FCP substrates with focus on the following bond types mentioned in **Table 7.9**:

Bond	Binding Energy / eV	Bond Type	Bond Energy / eV
C - C	284.8	C - C	3.61
C = C	284.8 ± 0.5	C = C	6.36
C - H	284.8	C - H	3.73
C - O	286	C - O	4.28
C = O	289	C = O	7.76
O - C = O	290	C - O/C = O	$\sim 4.28/7.76$
CF_2	292	C - F	5.06
CF_3	294	C - F	5.06
O - C = $\underline{O}$	532	O = C	7.76
$\underline{O}$ - C = O	534	O - C	3.73

TABLE 7.9: Common Bonds and Bond Energies found in
Polymers [109].

7.3.1   HCP Results

It is supposed that some oxygen (**Figure 7.30 & 7.31**) is covalently bonded in the bulk of HCP from the outset. It is known that small amounts of O_2 are present during the deposition of HCP. Exposure to UV photons of maximum 10 eV of energy (vacuum UV photons of 21 eV cannot penetrate the glass) reduced the concentration of oxygen in the sample. Because the treated sample was also exposed to atmosphere, if this were just atmospheric surface oxygen, it would have been expected that the percentage of oxygen would naturally recover. It doesn't. Also, the percentage of oxygen is too high to simply be atmospheric. There is also no such nano structure that would provide a strong hydrophilic behavior such that de-absorption of the water in vacuum would be prevented. The wettability of water on the surface was also seen from eye and contact angles were observed to be large.
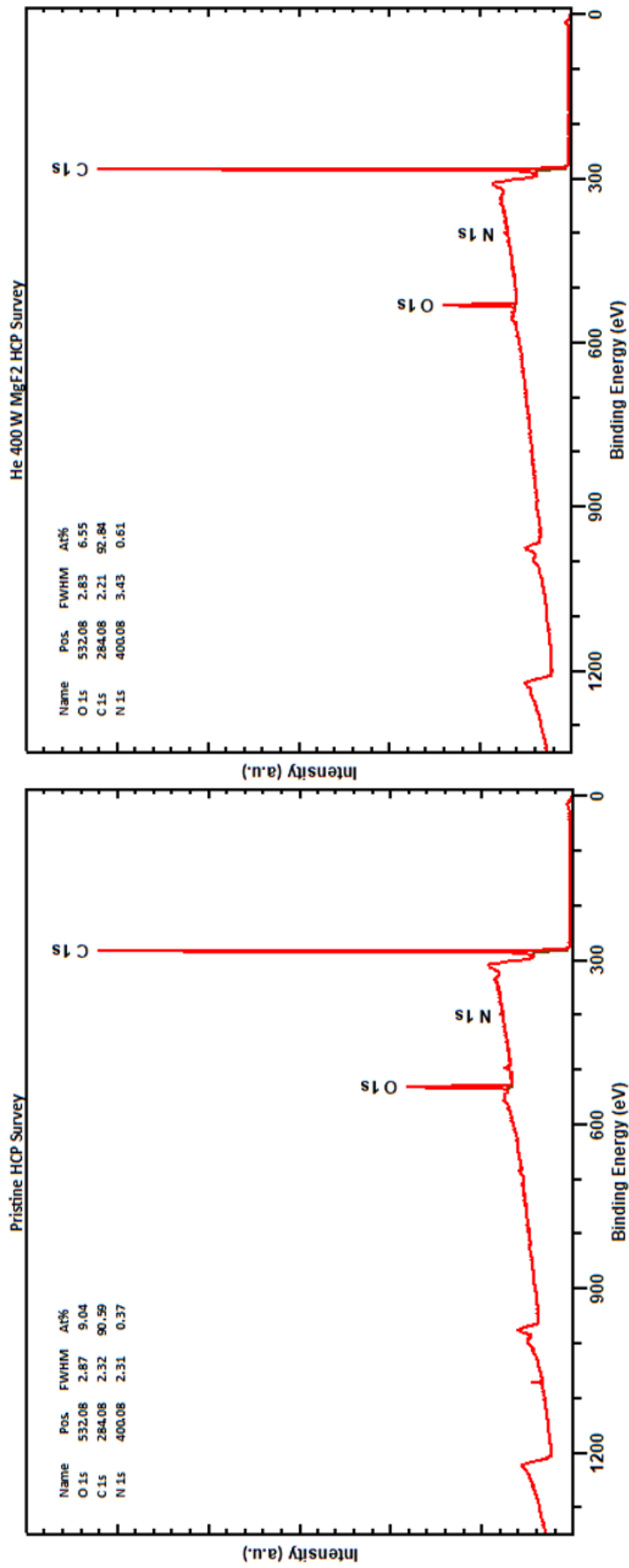
FIGURE 7.30: XPS survey comparison of pristine HCP and HCP underneath MgF₂ glass when exposed to a 400 W He plasma

FIGURE 7.31: XPS C1s spectra of HCP under different plasma conditions. 'Mesh = gas phase neutralization'.

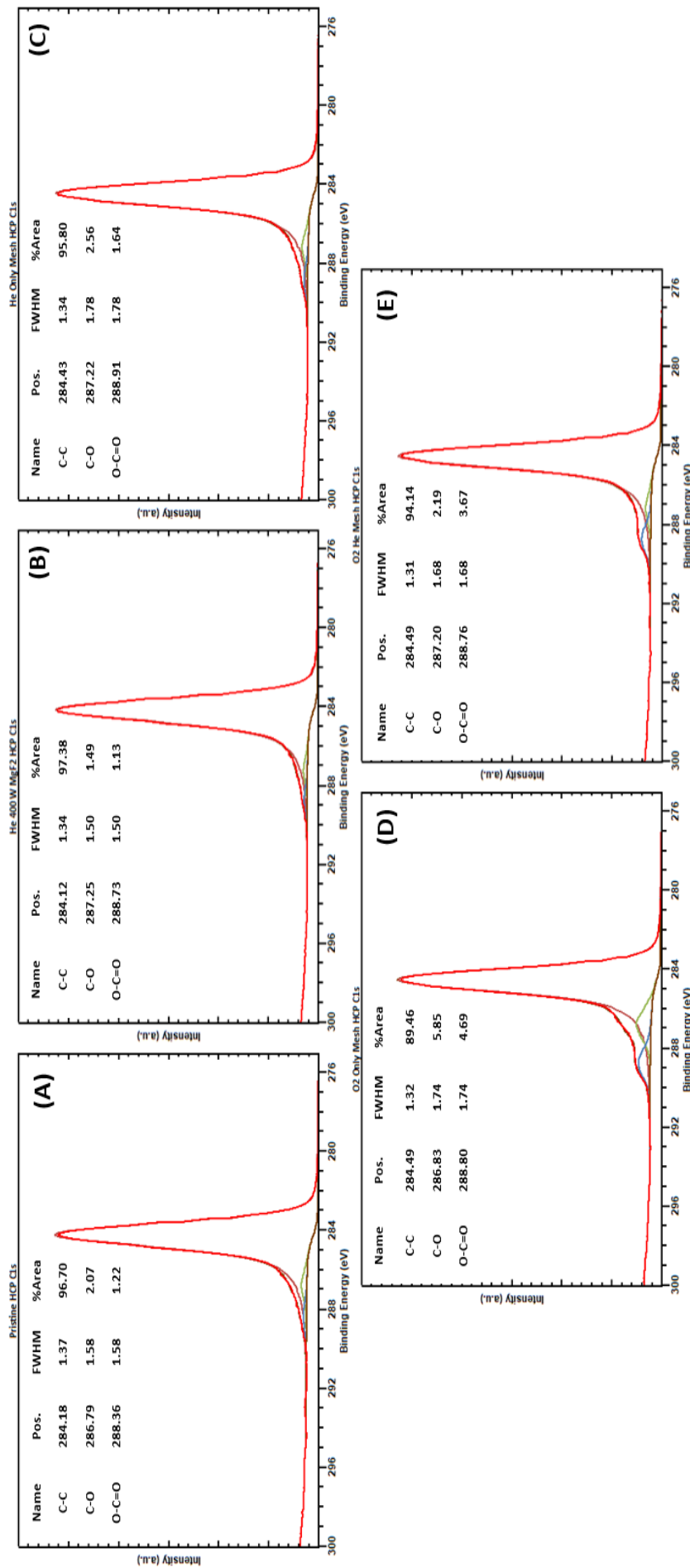**Figure 7.30** shows the survey spectra of the HCP substrate between pristine and soft UV exposure. Exposure to soft UV photons ($hv < 10$ eV) behind MgF_2 glass appears to have had the effect of reducing the percentage of carbon bonded to oxygen in the form of C-O and O-C=O. C-O has the binding energy range of 286 ± 1.5 eV whilst O-C=O is found in the range 287.8 ± 1.5 eV. Because it is such a small change (not up to 1% in any region), it is questionable as to whether there is a significant change in the C1s spectra, particularly as the etch rate (**Figure 7.15**) was not large. However, simple stochiometric ratios show that the oxygen content in the substrate had been reduced. $CO_{0.1}N_{0.004}$ in pristine compared to $CO_{0.07}N_{0.007}$ after soft UV exposure.

Upon full exposure to plasma emissions, **Figure 7.31** the change in the C1s spectra is marked. The increased presence of C-O and O-C=O when exposed to He (C) appears to suggest water impurities in the plasma which formed radicals on the surface of the substrate. OES of the plasma showed strong lines of OH and NO between 308 nm - 330 nm which suggests the formation of these radicals that attached themselves to the substrate surface. In a pure O_2 discharge (D), it can be seen that the presence of oxygen encourages the formation of double and single bonded carbon and oxygen in a reactive mechanism. The addition of He however (E) suppresses this, suggesting that the penetration of UV on the surface and into the bulk in an ultrafast time scale, drives cross-linking and hardening that prevents further implantation of oxygen and subsequent mass reduction (**Figure 7.13**).

Geyter *et al.* [110] has reported the effect of air, He and Ar plasma on polymer films, especially polypropylene which has a chemical structure closest to HCP. XPS results indicated the increase of C-O and O-C=O groups when under a He discharge and this was suggested to be the result of trace O_2 within the discharge. In **Figure 7.29** (B), any oxygen already present within the sample as an impurity would have formed cross-links or contributed to a uniform oxidative hardening of the substrate whilst trace

oxygen radicals in the discharge would have attempted surface reactions. This may explain the marked smoothing of the surface profile as seen in **Figure 7.14**.
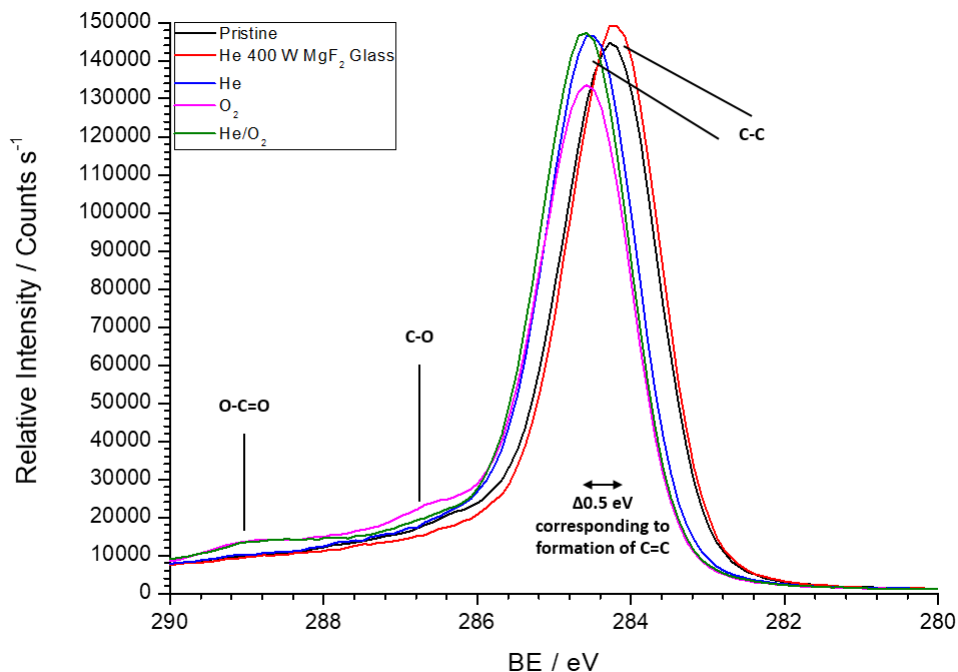
FIGURE 7.32: XPS comparison of HCP C1s spectra under different plasma conditions.

Figure 7.32 shows noticeable peak shifts of 0.5 eV suggesting the formation of C=C bonds in the bulk which only occur under full exposure of a plasma. This can happen due to UV photons penetrating the bulk and dehydrogenating the polymer structure to create alkyl radicals. The radicals may recombine to form C=C or carbonyl C=O groups in the presence of oxygen as seen by the O-C=O peak at ~ 289 eV. The lower carbon intensity in the O_2 plasma (pink trace) relates to greater mass reduction where the etch rate was significantly larger than any other gas mixture. This also followed an increase in C-O ~ 287 eV intensity. Addition of He appears to suppress this peak but does nothing to affect the production of C=O. This suggests that C-O is driven by chemistry and becomes suppressed when photo-driven cross-linking and double bond formation occur as they happen at a faster rate. The intensity of C-O bonds also appears to have been reduced when under UV exposure behind MgF_2 glass.
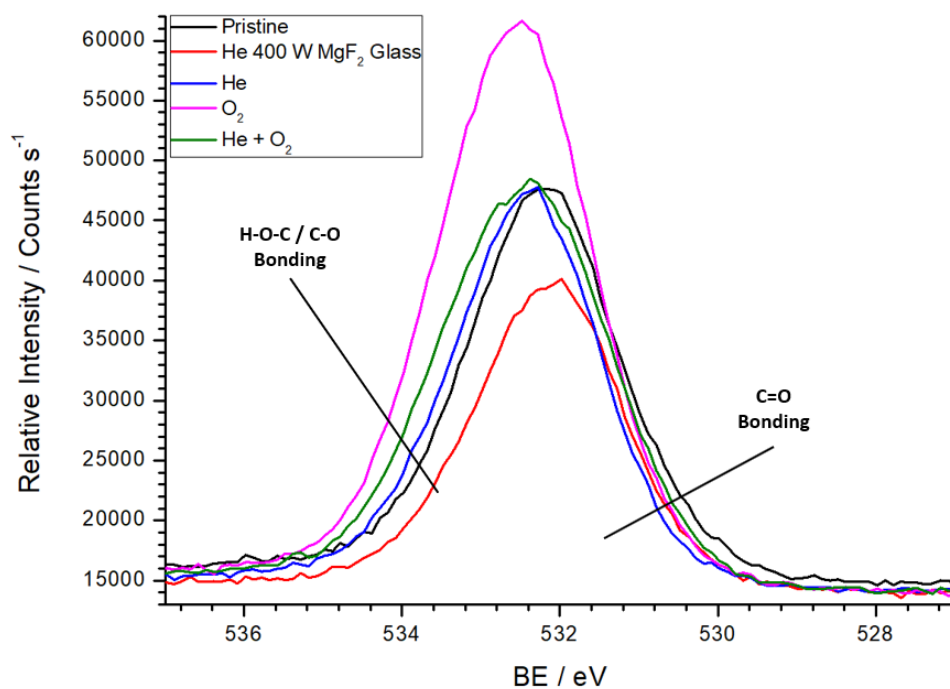
FIGURE 7.33: XPS comparison of HCP O1s spectra under different plasma conditions.

Individual comparison of the components of the O1s spectra was difficult due to the severe overlapping of the components. Hence, the peak shifts and intensity are displayed instead in **Figure 7.33**. **Figure 7.32** showed that any decrease in carbon was significant only in the pure O_2 discharge and this was related to mass reduction of the HCP substrate, most of which is carbon based. Exposure to oxygen (**Figure 7.33**) also increases the intensity on the condition that there are no energetic UV photons to suppress the implantation of oxygen via chemical reactions - as seen by the intensity of the O1s spectra (pink trace). This may relate to a passivation layer being formed on the sample during etching. The gradual shift of the O1s spectra indicates the formation of C-O and reduction of C=O especially in an O_2 discharge. Due to chemical implantation, this shift is marked in pure O_2 where more C-O type bonding is expected.

7.3.2   FCP Results

Compared to HCP, the exposure of FCP to UV has a more marked effect. It
can be seen that exposure to UV photons reduced the fluorine content by
about 8% (**Figure 7.32**). This resulted in a relative rise of all other atomic
species. This is assumed to be the dissociation of C-F bonds and therefore
reduction of fluorine from the substrate. The structure of FCP resembles
that of polytetrafluoride, with many instances of C-F, C-F_2 and C-F_3 bond-
ing with some small oxygen defect. The fluorine in the polarized CF_3 and
CF_2 bonds are typically further away from their central carbon atoms and
are therefore easier to dissociate.

It can be seen that the removal of species due to photo-dissociation is
more marked in the the FCP substrate than in HCP. Simple stochiometric ra-
tios (**Figure 7.34**) give $CF_{0.75}O_{0.06}N_{0.01}$ in pristine compared to $CF_{0.56}O_{0.1}N_{0.02}$
after soft UV exposure behind an MgF_2 glass. The surface of FCP becomes
very chemically active as indicated by the fact that N_2 in the venting gas
was able to embed itself on the substrate.
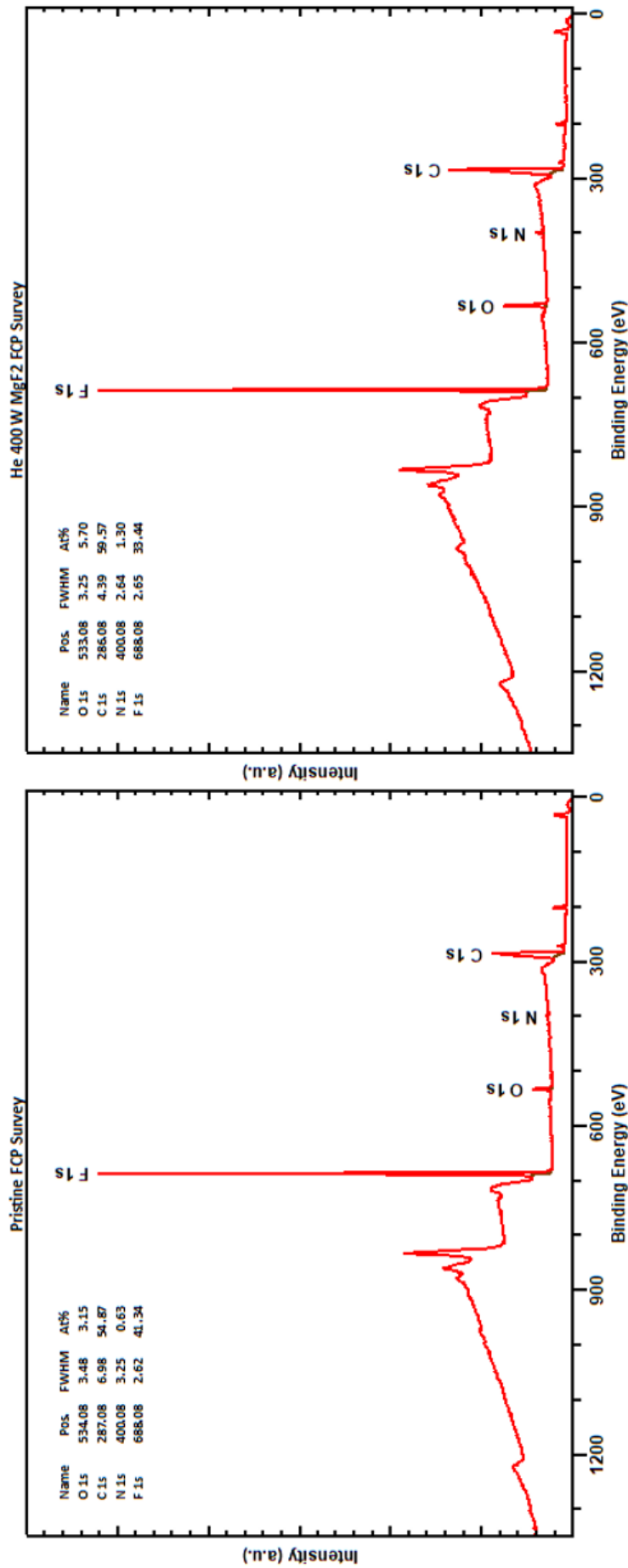
FIGURE 7.34: XPS survey comparison of pristine FCP and FCP underneath MgF$_2$ glass when exposed to a 400 W He plasma

Figure 7.35 illustrates the multi peak structure present in the C1s spectra of the FCP substrate. This indicates a high density of states with carbon existing in C-C bonding ($\sim$ 284.8 eV), C-O bonding ($\sim$ 286 eV), O-C=O ($\sim$ 288.5 eV) C=O bonding ($\sim$ 289 eV) and varied CF_2 and CF_3 states ($\sim$ 292 eV – 294 eV). Exposure to soft UV radiation of $hv \lesssim 10$ eV (B) was shown to visibly reduce the fluorine content. It can be seen that there is reduction of states relating to CF_2 and CF_3 indicating the dissociation of these bonds. C=O bonds also decreased in intensity irrespective of the type of treatment. It is speculated that the dissociation of the $C-F_x$ bonds creates fluorine radicals that also react with C=O bonds lowering their content.

Chemical composition relating to oxygen is particularly complex. The presence and absence of fluorine tends to induce large chemical shifts in other elements due to its reactivity and high electronegativity. The states of C-O and C=O both fall rapidly following plasma treatment (C, D & E) with the exception of UV behind MgF_2 glass where the C-O content actually rose. Conversely, oxygen contained in O-C=O rose markedly. Mittal *et al.* suggests that this is caused by the fast diffusion of discharge (and trace defect) oxygen into alkyl radical sites created by initial plasma exposure and the subsequent absence of fluorine [111].
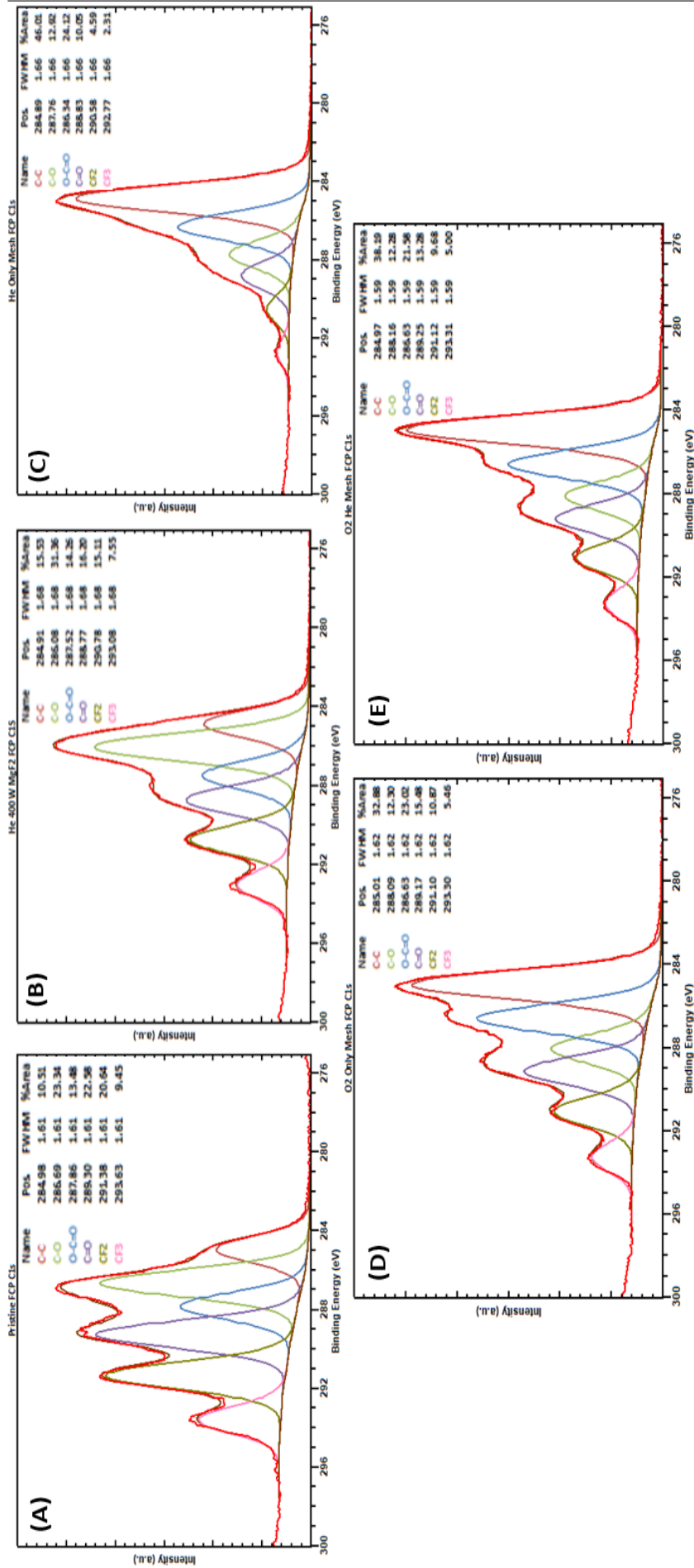
FIGURE 7.35: XPS C1s spectra of FCP under different plasma conditions.
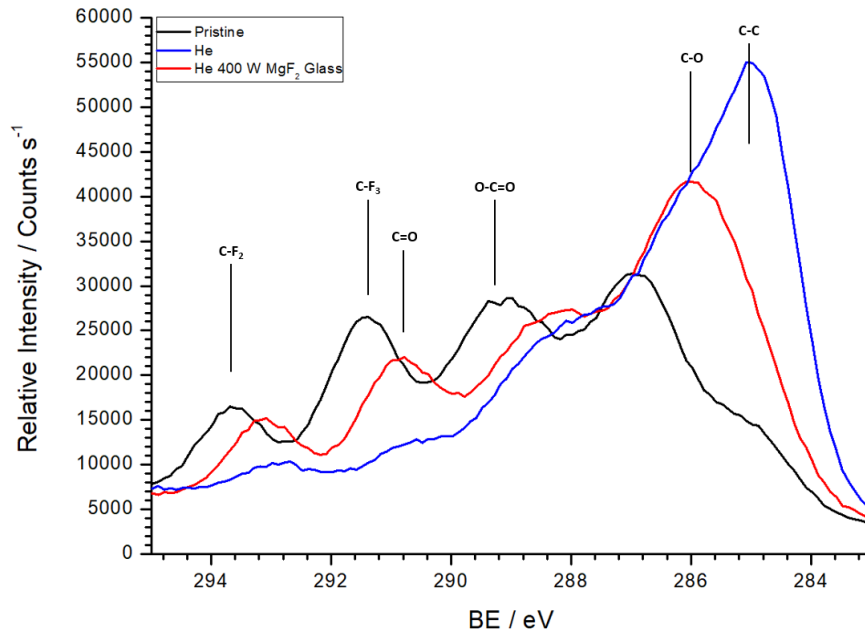
FIGURE 7.36: XPS comparison of FCP pristine and He/UV
C1s spectra.

The FCP polymer had a comparatively large etch rate when compared to HCP, as such it is more difficult to compare on intensity alone. **Figure 7.36** shows large increases of the 284.8 eV peak which is known for C-C/C-H bonding indicating that the absence of fluorine allows for the formation of these bonds. The exposure by UV is shown to visibly suppress the peaks at 292 eV/294 eV which indicates the dissociation of C-F bonds. This also follows with an increase of the C-O state when compared with the pristine sample. The previously highlighted percentage increases of O-C=O suggest that as the FCP substrate is being etched, a layer of oxide is built on the surface during the process. This has been mentioned in **Chapter 1** as a passivation mechanism.
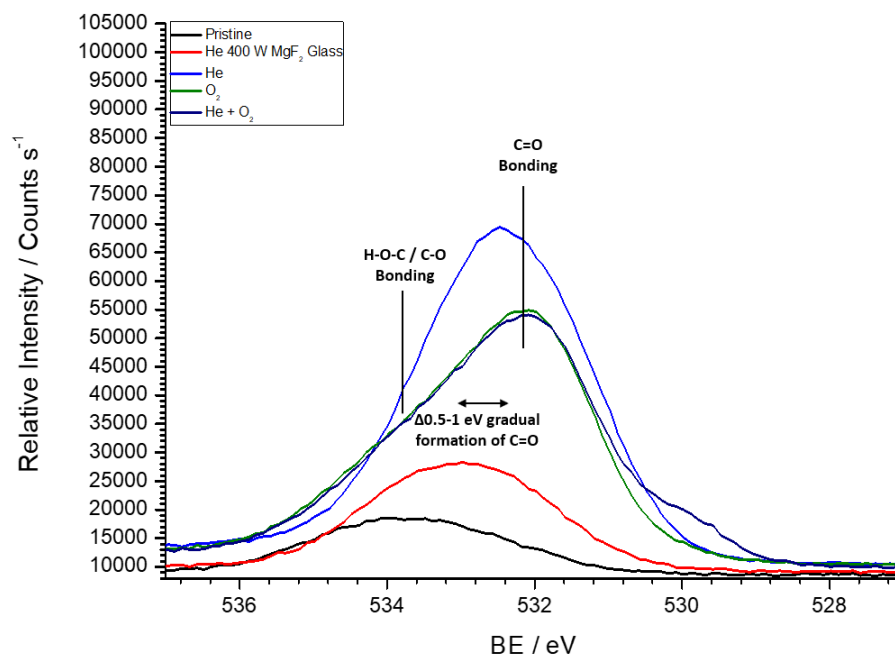
FIGURE 7.37: XPS comparison of FCP O1s spectra under
different plasma conditions.

In **Figure 7.37**, the general shift to the right of the peak following every plasma treatment indicates a growing formation of the C=O bond. Under strong UV radiation, chemical reaction and physical bombardment, the scission of C-F bonds creates alkyl radicals and reactive zones where oxygen contained in the discharge can diffuse to and create carboxyl and carbonyl groups. This 'oxidation' is speculated to be part of the formation of a passivation layer and the continued adsorption of oxygen encourages C=O bond formation. This is more marked with the exposure to pure O_2 plasmas, although the exposure to He is known to favour double bond and cross-link formation via other complex photo mechanisms.

7.4 Summary

The chemical properties of HCP and FCP were measured post-etch using XPS. It is found that complex chemistry on the surface and in the bulk of the polymers is driven by photon absorption. In the case of HCP, the exposure to UV rich plasma causes the dehydrogenation of the substrate to create alkyl radicals. These either recombine or react with oxygen in the discharge to form strong double bonds and cross-links which contribute to a smooth, hardened surface that is resistant to further etching. In the case of FCP, UV photons are instrumental in the dissociation of C-F bonds which markedly shift the energies of nearby elements due to its electronegativity. It was found that in the absence of fluorine, oxygen was able to diffuse through the bulk and react quickly with alkyl radicals to produce carboxyl and hydroxyl groups. Carbonyl C=O groups are suppressed. The increase of C-O whilst the material is being etched suggests the formation of a passivation layer which is known to be the result of an oxidized surface. Surface roughness profiles indicated a reactive etching mechanism causing smooth profiles, whilst rougher profiles were due to mechanical etching from fast, energetic neutrals.

VUV and UV photons were shown to have a marked effect on the surface properties by monitoring the etch rates and surface profiles post-etch. These effects came in the form of radicals forming on the substrate surface and recombining to form an oxidized structure that coincided with a suppressed the etch rate in HCP. However, the scission of C-F bonds and the creation of a chemically rich, oxygen structure coincides with the increased etch rate of an FCP polymer. There is still a requirement for neutral beam etching to have a reactive component and the XPS measurements show that much of the etch rate (especially on FCP) is due to the absorption of UV photons which enabled photochemistry on the substrate surface rather than physical, neutral bombardment.

Chapter 8

Conclusions and Future Work

8.1 Summary and Conclusions

The objective of this investigation was to study a source of energetic neutral particles and to characterize it. This was achieved in an optimized, bespoke experimental ICP run in CW. The nature of the plasma and the tailoring of neutral beams extracted from it was done using an EQP. It was shown that neutral beams can be formed by resonant charge-exchange and surface neutralization. It was also shown that these neutral beams could be applied in an etching protocol of polymer substrates in an industrial plasma etcher.

Chapter 2 formed a literature review on the historic investigations into a charge-free etching mechanism using neutrals beams. It was reviewed that research began by looking at the gas phase charge-exchange mechanism which transitioned into research using smaller plasma sources in a surface phase neutralization mechanism. Highlighted issues were centred around the lack of neutral beam characterization which resulted in a partial understanding of the neutral beam etching process.

Chapter 3 applied a transformer model to the bespoke ICP experiment and discussed the efficiency and structure of the plasma source. It was shown that a combination of coil geometry and the installation of a Faraday cage could reduce capacitive coupling such that the power transfer efficiency of RF into the plasma was predominantly inductive. The transfer of power was further discussed using an L-type matching network. It was

also shown that power losses due to resistive dissipation across the matching network and coil, although mitigated, remained unavoidable. Lastly, the creation of a modular neutral beam source based upon the gas phase charge-exchange mechanism was introduced.

Chapter 4 described the electromagnetic/electrostatic probes and optical measurements performed over a range of operational conditions in order to characterize the experimental ICP. It was shown that the increase of input power transitioned the plasma from a low density E-mode where capacitive coupling is dominant, to a high density H-mode where the inductive field dominates the plasma power absorption. Charged particle densities were measured and compared in both an electropositive Ar plasma and an electronegative O_2 plasma, performed with Hairpin, Floating Double and B-dot probes. The B-dot probe in particular enabled a mapping of the electromagnetic structure of the plasma which illustrated the uniformity of the ICP discharge and corroborated electron density values for high density operation. Simple OES was also undertaken to characterize the chemistry of an O_2 discharge and plasma imaging with an i-CCD camera to visualize the plasma emission structure was also undertaken. I-CCD imaging suggests that the plasma density is greatest at the axial centre and confirms the annular doughnut shape inferred by B-dot results.

Chapter 5 introduced the EQP as the main diagnostic instrument of the project and discussed its operation in both SIMS and RGA modes. Whilst RGA measured thermalized neutral gas, SIMS mode sampled external plasma ions from a discharge and characterized species by their masses and energies. The discussion of the unconventional use of a hybrid mode (SIMS + filaments) to measure fast neutral species was proposed and this was followed with a review of the EQP operation and COMSOL modeling to investigate various pecularities observed during operation. The COMSOL model was based upon the physical dimensions of the ion flight path and was reduced in complexity to monitor field effects and ion particle traces.

In RGA and hybrid modes, various and unavoidable electrostatic fields deflect external plasma ions off axis. However, there is no mechanism which can bring them back on axis.

Chapter 6 discussed the results of neutral energy measurements in various plasma operations and it was shown that neutral species follow the EDF's of their ions following charge-exchange. It was seen that the pressure variation of the neutralization volume suppressed the neutral beam flux into the EQP, but due to pressure measurement restrictions, no maximum of charge-exchange was detected. The measurements were validated via the discussion of electron filament variation which indicated that increasing the emission of electrons increased the amount of detected energetic neutrals. It was shown however that for the most energetic neutrals at plasma potential energy, most of them were captured by 100 μA. DEA was also used with the detection of the O^- to determine the energy of fast neutral O_2. It was shown that in the DEA mechanism, the two daughter particles carry away half the energy of the parent particle and this was seen in the EDF of O^- to be approximately half of the IEDF of O_2^+. Given that all transfer electrodes were polarized, there was no ambiguity in the use of O^- as a vector to determine the energy of charge-exchanged O_2. Neutral beam flux measurements were attempted using a planar ion flux probe on the residual ion current. It was concluded that due to differences in optimization between SIMS and RGA mode, measurement of a neutral beam flux using the EQP remains a task better suited to a simpler system.

Chapter 7 investigated the contribution of UV photons in the etching process and the general effectiveness of NBE on the mass reduction of polymer substrates and SiO_2. Preliminary etching trials produced etch rates of up to 30 nm min^{-1} in a single extractor setup, but this was much lower in a wafer neutralizer setup. This suggested a removal of the UV photon contribution, reactive thermalized neutrals, or both. Extraction of 0 eV - 150 eV neutral beams using a wafer neutralizer indicated very little energy

dependence of the etch rate. It was surmised that although NBE provides a charge-less, damage-free process, etch rates are low without some form of reactive contribution and this was measured to be absent with the wafer neutralizer. In particular, low sticking coefficients of energetic neutrals with surfaces mean that most of their energies are not deposited onto the surface. The investigation of UV photon contribution to improve the etch rate involved the use of a He plasma as a primary source of VUV and UV photons. It was found that for HCP, surface hardening and a suppression of the etch rate occurred. For FCP however, the etch rate was improved by as much as 1.5 nm min^{-1} when UV photons were combined with a neutral reactive species from an O_2 plasma. Furthermore, surface profile measurement on the substrates post-etch indicated a consistent smooth surface in the charge-less environment and especially when there was a photon contribution. This indicated that although NB etch rates are much lower compared to plasma ion assisted etching, their niche might be in the production of smooth features for surface finishing and pattern transfer. Validation of UV photon contribution was undertaken using XPS and it was seen that marked chemistry had occurred on the surface and within the bulk where there was a notable UV contribution. This concluded that NBE requires a reactive component for etch rates to be competitive.

8.2 Future Work Suggestions

Optical Emission Spectroscopy: Time resolved or Phase resolved [112] OES can play a key role in characterizing the plasma by identifying key fundamental chemical processes that occur in molecular discharges and can be translated into a more tailored protocol for NBE.

Plasma Modelling: A Global modelling code was used to benchmark previous diagnostic results. However, much of the physics was lost due to it being a volume averaged model. The employment of a 2D HPEM code [113] such as that used in [35] or Quantemol-VT [114] can not only model the complex mechanisms occuring in the discharge, but also the physics of the etching mechanism on the substrate features during etching. Modelling the feature profiles (possible in Quantemol-VT) allows enough perspective to continue to establish a neutral beam etching protocol.

COMSOL Modeling: It is a future work to be able to completely discriminate between the quantity of external plasma ions lost and ionized neutral species created in the cage region of the EQP. This requires more complex physical models such as the production of energetic neutral species from the inlet to determine the rate of ionization of neutrals within the cage region alongside the calculation of field effects that may affect their transit depending on where they are ionized. Using particle tracing techniques, it would be possible to monitor the transmission of ionized neutrals based upon their energies and where they were ionized within the cage. Future work could also involve using a wider range of particle energies and filament voltages where the 'response' of the system to particles with energy range $0 - 100$ eV could be quantified.

Neutral Energy Measurement: Although this research successfully measured energetic neutrals, further comparison is necessary as fast neutral energy is notoriously difficult to measure and becomes complicated in an

electrically dense environment such as the EQP. Laser Induced Fluoresence of energetic neutrals is a suggested method. Laser induced fluorescence has been used to monitor the radial flux profile of hydrogen in a helical system [115] and to determine the spatial distribution of injected neutrals in fusion plasmas [116]. Measurement of an energetic neutral velocity distribution would involve the monitoring of doppler shifted light, although this would require a more sophisticated experimental setup.

NBE Etching Contributions: During the etching of polymer substrates, it was surmised that the NBE mechanism lacked a high etch rate without the contribution of reactive thermalized neutrals. The contribution of these neutrals was never quantified however and results in a partial understanding of the full NBE mechanism. Ions could be swept before the extraction in order to finally distinguish the contribution of ions, fast neutrals, photons and thermalized neutrals. It was also mentioned in **Chapter 2** that directed energetic neutral beams in the energy range of 10 - 30 eV would be suitable for chargless etching without damage. Subsequent etching trials **Chapter 8** indicated a low etch rate with a low energy dependency with neutral energy < 100 eV. It would be a point of future work to investigate the NBE process > 100 eV in the hyperthermal regime.

Patterned Wafers: To fully characterize NBE post-etch, patterned wafers must be used. The surface profiles of HCP and FCP substrates were shown to have a reduction in roughness, it would be future work to investigate NBE of patterned wafers and then to characterize the vertical profiles and feature quality using SEM. This would lead to the fabrication transistors or integrated circuit components using the NBE process. These could then be performance tested. Kazuhiko *et al.* [117] reported on the fabrication of FinFETs using a NBE protocol on silicon wafers in 2006. This can be improved upon with further study of the surface physics and the discharge kinetics.

Appendix A

Hiden Analytical Schematics

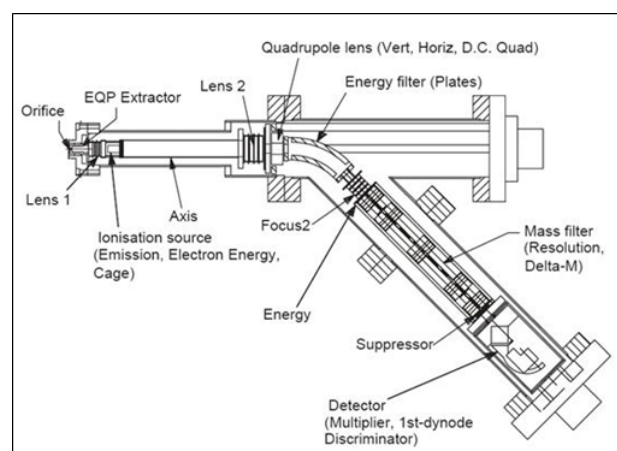FIGURE A.1: Hiden EQP Schematic 1. *Credit: Hiden Analytical*
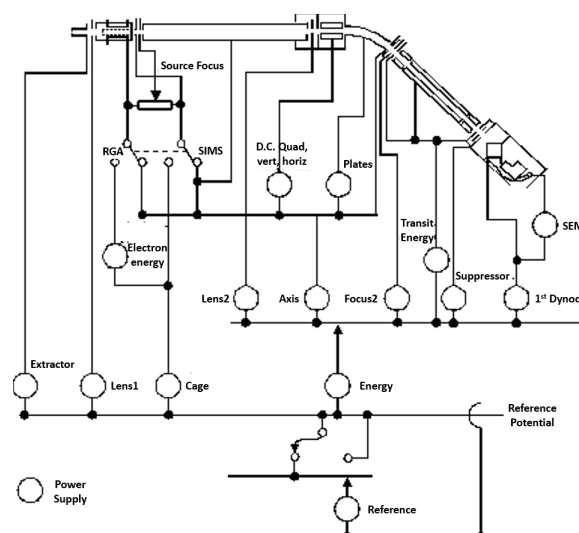

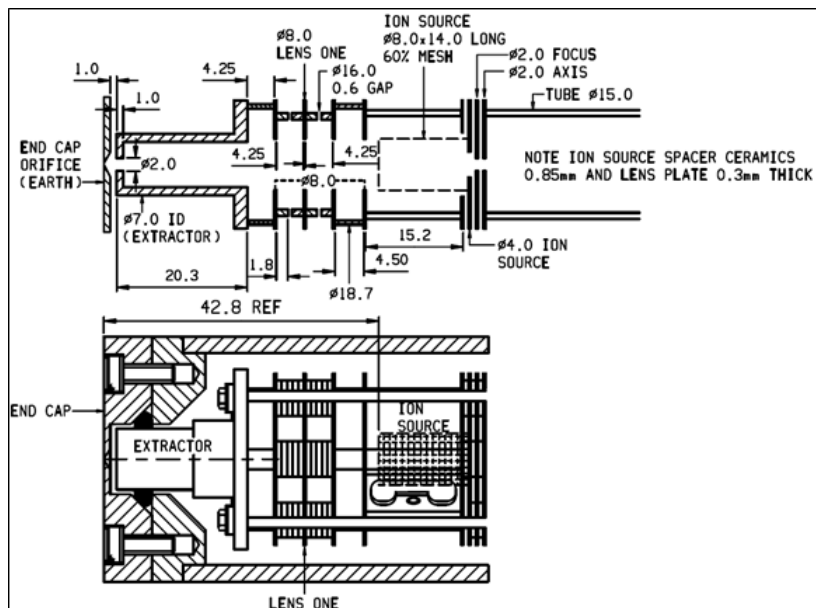FIGURE A.2: Hiden EQP Circuit Schematic. *Credit: Hiden Analytical*

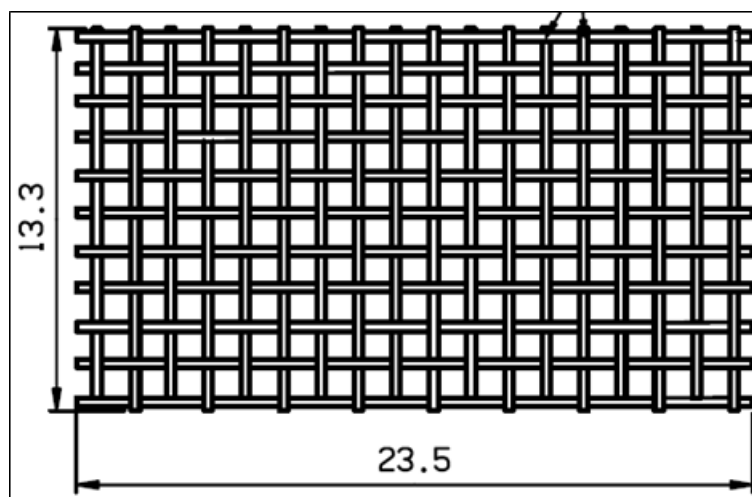FIGURE A.3: Hiden EQP Schematic 2. *Credit: Hiden Analytical*

FIGURE A.4: Hiden Cage Schematic. *Credit: Hiden Analytical*

All schematics were provided by Hiden Analytical are direct illustrations of the components of the Hiden 500 EQP system used in this research.

Bibliography

[1]   F. Duré and A. Lifschitz. "Modeling of the lithium based neutralizer for ITER neutral beam injector". In: *Chemical Physics* 398 (2012), 17–26. DOI: `10.1016/j.chemphys.2011.10.005`.

[2]   X. Peng, S. Wakeham, and A. Morrone. "Towards the sub-50nm magnetic device definition: Ion beam etching (IBE) vs plasma-based etching". In: *Vacuum* 83.6 (2009), 1007–1013. DOI: `10.1016/j.vacuum.2008.12.003`. URL: `http://www.sciencedirect.com/science/article/pii/S0042207X08005149`.

[3]   M. Diemer and S. Cooper. *Radio-activity induced by the oscillatory discharge, or, The subsequent radio-active emanation from substances exposed to the Tesla oscillatory discharge*. 1st ed. Andesite Press, 1903.

[4]   I. Langmuir. "Oscillations in Ionized Gases". In: *Proceedings of the National Academy of Sciences* 14.8 (1928), pp. 627–637. eprint: `http://www.pnas.org/content/14/8/627.full.pdf`. URL: `http://www.pnas.org/content/14/8/627.short`.

[5]   P. Chabert and N. Braithwaite. *Physics of radio-frequency plasmas*. Cambridge University Press, 2011.

[6]   M. Lieberman and A. Lichtenberg. *Principles of plasma discharges and materials processing*. Wiley-Interscience, 2005.

[7]   A. Garamoon, A. Samir, and F. Elakshar. "Electrical characteristics of a DC glow discharge". In: *Plasma Sources Science and Technology* 12.3 (2003), p. 417. URL: `http://stacks.iop.org/0963-0252/12/i=3/a=317`.

[8] B. B. Sahu and Jeon G. Han. "Electron heating mode transition induced by mixing radio frequency and ultrahigh frequency dual frequency powers in capacitive discharges". In: *Physics of Plasmas* 23.5 (2016), p. 053514. DOI: 10.1063/1.4952629.

[9] H. Goto, A. Lowe, and T. Ohmi. "Independent control of ion density and ion bombardment energy in a dual frequency excitation plasma". In: *Transactions of Semiconductor Manufacturing* 6.1 (1993). DOI: 10.1109/66.210658.

[10] W. Tseng and C. Tseng. "Effects of Gas Composition on Highly Efficient Surface Modification of Multi-Walled Carbon Nanotubes by Cation Treatment". In: *Nanoscale Research Letters* 4.3 (2008), pp. 234 –239. URL: http://doi.org/10.1007/s11671-008-9231-4.

[11] K. Sung and S. Pang. "Etching of Si with Cl_2 using an electron cyclotron resonance source". In: *Vacuum Science & Technology A: Vacuum, Surfaces and Films* 11 (1993), p. 1206. URL: http://avs.scitation.org/doi/abs/10.1116/1.578494.

[12] K. Sung, W. Juan, and S. Pang. "Dependence of etch characteristics on charge particles as measured by Langmuir probe in a multipolar electron cyclotron resonance source". In: *Journal of Vacuum Science & Technology A: Vacuum, Surfaces, and Films* 12.1 (1994), 69–74. DOI: 10.1116/1.578860.

[13] W. Hittorf. "On the Electricity of the Gases". In: *Annals of Physics* 257.1 (1884), pp. 90–139. ISSN: 1521-3889. DOI: 10.1002/andp.18842570105. URL: http://dx.doi.org/10.1002/andp.18842570105.

[14] A. P. Paranjpe. "Modeling an Inductively Coupled Plasma Source". In: *Vacuum Science & Technology A: Vacuum, Surfaces and Films* 12 (1994), p. 1221. URL: http://avs.scitation.org/doi/abs/10.1116/1.579299.

[15] *Semiconductor Industry Association, 2017*. 2017. URL: https://www.semiconductors.org/.

[16]   J. Coburn and H. Winters. "Ion- and electron-assisted gas-surface chemistry. An important effect in plasma etching". In: *Journal of Applied Physics* 50 (May 1979), pp. 3189–3196. DOI: `10.1063/1.326355`.

[17]   V. Donnelly and A. Kornblit. "Plasma etching: Yesterday, today, and tomorrow". In: *Vacuum Science & Technology A: Vacuum, Surfaces, and Films* 31 (Sept. 2013), pp. 050825–050825.

[18]   H. Toshiyoshi. *Fundamentals of Micromaching*. 2017. URL: `Hiroshi@ee.ucla.edu`.

[19]   L. LMeng, A. Xia, and L. Ming. "Fabricating GeO2passivation layer by N2O plasma oxidation for Ge NMOSFETs application". In: *Chinese Physics B* 23.6 (2014), p. 067701. DOI: `10.1088/1674-1056/23/6/067701`.

[20]   S. Murakawa and J. Mcvittie. "Mechanism of Surface Charging Effects on Etching Profile Defects". In: *Japanese Journal of Applied Physics* 33.Part 1, No. 4B (1994), 2184–2188. DOI: `10.1143/jjap.33.2184`.

[21]   V. Ishchuk, B. Volland, and M. Hauguth. "Charging effect simulation model used in simulations of plasma etching of silicon". In: *Journal of Applied Physics* 112.8 (2012), p. 084308. DOI: `10.1063/1.4759005`.

[22]   B. Ishchuk V.and Volland and I. Rangelow. "ViPER: simulation software for high aspect ratio plasma etching of silicon". In: *Microsystem Technologies* 20.10-11 (2013), 1791–1796. DOI: `10.1007/s00542-013-1926-5`.

[23]   K. Bogart, F. Klemens, and M. Malyshev. "Mask charging and profile evolution during chlorine plasma etching of silicon". In: *Journal of Vacuum Science & Technology A: Vacuum, Surfaces, and Films* 18.1 (2000), 197–206. DOI: `10.1116/1.582157`.

[24]   M. Boufnichel et al. "Profile control of high aspect ratio trenches of silicon. I. Effect of process parameters on local bowing". In: *Journal of Vacuum Science & Technology B: Microelectronics and Nanometer Structures* 20.4 (2002), p. 1508. DOI: `10.1116/1.1495505`.

[25] W. Pike. "Analysis of sidewall quality in through-wafer deep reactive-ion etching". In: *Microelectronic Engineering* 73-74 (2004), 340–345. DOI: 10.1016/s0167-9317(04)00122-4.

[26] M. Izawa, N. Negishi, and K. Yokogawa. "Investigation of Bowing Reduction in SiO2Etching Taking into Account Radical Sticking in a Hole". In: *Japanese Journal of Applied Physics* 46.12 (2007), 7870–7874. DOI: 10.1143/jjap.46.7870.

[27] S. Vitale, H. Chae, and H. Sawin. "Silicon etching yields in F2, Cl2, Br2, and HBr high density plasmas". In: *Journal of Vacuum Science & Technology A: Vacuum, Surfaces, and Films* 19.5 (2001), 2197–2206. DOI: 10.1116/1.1378077.

[28] A. Mahorowala, H. Sawin, and R. Jones. "Etching of polysilicon in inductively coupled Cl[sub 2] and HBr discharges. I. Experimental characterization of polysilicon profiles". In: *Journal of Vacuum Science & Technology B: Microelectronics and Nanometer Structures* 20.3 (2002), p. 1055. DOI: 10.1116/1.1481866.

[29] D. Economou. "Pulsed plasma etching for semiconductor manufacturing". In: *Journal of Physics D: Applied Physics* 47.30 (2014), p. 303001. URL: http://stacks.iop.org/0022-3727/47/i=30/a=303001.

[30] R. W. Boswell and D. Henry. "Pulsed high rate plasma etching with variable Si/SiO2selectivity and variable Si etch profiles". In: *Applied Physics Letters* 47.10 (1985), 1095–1097. DOI: 10.1063/1.96340.

[31] S. Samukawa. "Pulse-time-modulated electron cyclotron resonance plasma etching with low radio-frequency substrate bias". In: *Applied Physics Letters* 68.3 (1996), 316–318. DOI: 10.1063/1.116071.

[32] S. Banna, A. Agarwal, and G. Cunge. "Critical Review: Pulsed High-Density Plasmas for Advanced Dry Etching Processes". In: 30 (July 2012).

[33] H. Kim, M. Jeon, and A. Mishra. "Effect of source frequency and pulsing on the SiO2etching characteristics of dual-frequency capacitive coupled plasma". In: *Japanese Journal of Applied Physics* 54.1S (2014). DOI: 10.7567/jjap.54.01ae07.

[34] J. Seo, K. Kim, and K. Kim. "Characteristics of pulsed dual frequency inductively coupled plasma". In: *Japanese Journal of Applied Physics* 54.1S (2015), 01AA10. URL: http://stacks.iop.org/1347-4065/54/i=1S/a=01AA10.

[35] A. Agarwal, P. Stout, and S. Banna. "Recouping etch rates in pulsed inductively coupled plasmas". In: *Journal of Vacuum Science & Technology A: Vacuum, Surfaces, and Films* 29.1 (2011), p. 011017. DOI: 10.1116/1.3521315.

[36] S. Banna, A. Agarwal, and G. Cunge. "Pulsed high-density plasmas for advanced dry etching processes". In: *Journal of Vacuum Science & Technology A: Vacuum, Surfaces, and Films* 30.4 (2012), p. 040801. DOI: 10.1116/1.4716176.

[37] L. Dorf, J. Wang, and S. Rauf. "Atomic precision etch using a low-electron temperature plasma". In: *Advanced Etch Technology for Nanopatterning V* (2016). DOI: 10.1117/12.2222309.

[38] F. Shimokawa, H. Tanaka, and Y. Uenishi. "Reactive–fast-atom beam etching of GaAs using Cl_2 gas". In: 66 (Oct. 1989), pp. 2613 –2618.

[39] T. Mizutani and S. Nishimatsu. "Sputtering yield and radiation damage by neutral beam bombardment". In: 6 (June 1988), pp. 1417 –1420.

[40] T. Mizutani and T. Yunogami. "Neutral-Beam-Assisted Etching of SiO_2 – A Charge-Free Etching Process–". In: *Japanese Journal of Applied Physics* 29.10R (1990), p. 2220. URL: http://stacks.iop.org/1347-4065/29/i=10R/a=2220.

[41]   T. Yunogami, K. Yokogawa, and T. Mizutani. "Development of neutral-beam-assisted etcher". In: *Journal of Vacuum Science Technology* 13 (May 1995), pp. 952–958.

[42]   T. Tsuchizawa, Y. Jin, and S. Matsuo. "Generation of Electron Cyclotron Resonance Neutral Stream and Its Application to Si Etching". In: *Japanese Journal of Applied Physics* 33.4S (1994), p. 2200. URL: http://stacks.iop.org/1347-4065/33/i=4S/a=2200.

[43]   S. Samukawa, K. Sakamoto, and K. Ichiki. "High-Efficiency Low Energy Neutral Beam Generation Using Negative Ions in Pulsed Plasma". In: *Japanese Journal of Applied Physics* 40.10A (2001), p. L997. URL: http://stacks.iop.org/1347-4065/40/i=10A/a=L997.

[44]   S. Panda, D. J. Economou, and L. Chen. "Anisotropic etching of polymer films by high energy (100s of eV) oxygen atom neutral beams". In: *Journal of Vacuum Science Technology* 19 (Mar. 2001), pp. 398–404.

[45]   D. Lee, J. Bae, and S. Park. "Development of a low angle forward reflected neutral oxygen beam for materials processing". In: 398 (Nov. 2001), pp. 647–651.

[46]   M. Chung, D. Lee, and G. Yeom. "Study on the low-angle forward-reflected neutral beam etching system for SiO_2 etching". In: 420 (Dec. 2002), pp. 579–583.

[47]   S. Kim, S. Wang, and J. Lee. "Generation of low-energy neutral beam for Si etching". In: *Journal of Vacuum Science Technology* 22 (Sept. 2004), pp. 1948–1955. DOI: 10.1116/1.1774198.

[48]   S. Nam, D. Economou, and V. Donnelly. "Generation of Fast Neutral Beams by Ion Neutralization in High-Aspect-Ratio Holes: A Particle-in-Cell Simulation Study". In: *IEEE Transactions on Plasma Science* 35.5 (2007), pp. 1370–1378. ISSN: 0093-3813. DOI: 10.1109/TPS.2007.906439.

[49] K. Ichiki and M. Hatakeyama. "Characterization of neutral beam source using dc cold cathode discharge and its application processes". In: *Journal of Physics D: Applied Physics* 41.2 (2008), p. 024003. URL: http://stacks.iop.org/0022-3727/41/i=2/a=024003.

[50] Y. Hara, S. Takashima, and K. Yamakawa. "Characteristics of low energy atom and molecule beams generated by the charge exchange reaction". In: *Journal of Applied Physics* 103.5, 053301-053301-5 (Mar. 2008), pp. 053301–053301–5. DOI: 10.1063/1.2842402.

[51] Y. Hara, M. Hamagaki, and T. Mise. "Development of Neutral Beam Source Using Electron Beam Excited Plasma". In: *Japanese Journal of Applied Physics* 50.10R (2011), p. 106001. URL: http://stacks.iop.org/1347-4065/50/i=10R/a=106001.

[52] D. Marinov, Z. Otell, and M. Bowden. "Extraction and neutralization of positive and negative ions from a pulsed electronegative inductively coupled plasma". In: *Plasma Sources Science and Technology* 24.6 (2015), p. 065008. URL: http://stacks.iop.org/0963-0252/24/i=6/a=065008.

[53] T. Trottenberg, A. Spethmann, and J. Rutscher. "Non-electrostatic diagnostics for ion beams and sputter effects". In: *Plasma Physics and Controlled Fusion* 54.12 (2012), p. 124005. URL: http://stacks.iop.org/0741-3335/54/i=12/a=124005.

[54] Y. Iijima, T. Sato, and K. Hiraoka. "Analysis of Polyethyleneterephthalate Film Surface Sputtered with Ar Neutral and Ar Ion Beams". In: *Japanese Journal of Applied Physics* 33.11R (1994), p. 6325. URL: http://stacks.iop.org/1347-4065/33/i=11R/a=6325.

[55] R. Piejak, V. Godyak, and B. Alexandrovich. "A simple analysis of an inductive RF discharge". In: *Plasma Sources Science and Technology* 1.3 (1992), p. 179. URL: http://stacks.iop.org/0963-0252/1/i=3/a=006.

[56] V. Godyak, R. Piejak, and B. Alexandrovich. "Electron energy distribution function measurements and plasma parameters in inductively coupled argon plasma". In: *Plasma Sources Science and Technology* 11.4 (2002), p. 525. URL: http://stacks.iop.org/0963-0252/11/i=4/a=320.

[57] R. L. Stenzel. "Microwave resonator probe for localized density measurements in weakly magnetized plasmas". In: *Review of Scientific Instruments* 47 (May 1976), pp. 603–607. DOI: 10.1063/1.1134697.

[58] G. Hebner and I. Abraham. "Characterization of electron and negative ion densities in fluorocarbon containing inductively driven plasmas". In: *Journal of Applied Physics* 90 (Nov. 2001), pp. 4929–4937. URL: http://aip.scitation.org/doi/abs/10.1063/1.1410896.

[59] R. Piejak, J. J Al-Kuzee, and N. Braithwaite. "Hairpin resonator probe measurements in RF plasmas". In: *Plasma Sources Science and Technology* 14.4 (2005), p. 734. URL: http://stacks.iop.org/0963-0252/14/i=4/a=012.

[60] C. Corr, S. Gomez, and W. Graham. "Discharge kinetics of inductively coupled oxygen plasmas: experiment and model". In: *Plasma Sources Science and Technology* 21.5 (2012), p. 055024. URL: http://stacks.iop.org/0963-0252/21/i=5/a=055024.

[61] J. Wang, Y. Du, and X. Zhang. "E-H mode transition density and power in two types of inductively coupled plasma configuration". In: *Physics of Plasmas* 21.7 (2014), 073–502. DOI: 10.1063/1.4886147. URL: http://aip.scitation.org/doi/10.1063/1.4886147.

[62] Y. Zhang, J. Chen, and C. Song. "The study of influence of working pressure on mode conversion of argon radio-frequency inductively coupled plasma". In: *Vacuum* 132 (Oct. 2016), pp. 16–21. URL: http://www.sciencedirect.com/science/article/pii/S0042207X16302664.

[63] O. Johnson and M. Malter. "A Floating Double Probe Method for Measurements in Gas Discharges". In: *Physical Review* 80 (Sept. 1950), pp. 58–68.

[64] B. Annaratone, M. Allen, and J. Allen. "Ion currents to cylindrical Langmuir probes in RF plasmas". In: *Journal of Physics D: Applied Physics* 25.3 (1992), p. 417. URL: http://stacks.iop.org/0022-3727/25/i=3/a=012.

[65] V. Godyak and V. Demidov. "Probe measurements of electron-energy distributions in plasmas: what can we measure and how can we achieve reliable results?" In: *Journal of Physics D: Applied Physics* 44.23 (2011), p. 233001. URL: http://stacks.iop.org/0022-3727/44/i=23/a=233001.

[66] R. Piejak, V. Godyak, and B. Alexandrovich. "Validation of current density measurements with a B-dot probe". In: *Review of Scientific Instruments* 72 (Oct. 2001), pp. 4002–4004. DOI: 10.1063/1.1400146.

[67] R. Piejak, V. Godyak, and B. Alexandrovich. "The electric field and current density in a low-pressure inductive discharge measured with different B-dot probes". In: *Journal of Applied Physics* 81 (Apr. 1997), pp. 3416–3421. DOI: 10.1063/1.365026.

[68] R. Piejak, V. Godyak, and B. Alexandrovich. "Magnetic field distribution measurements in a low-pressure inductive discharge". In: *Journal of Applied Physics* 78.9 (1995), 5296–5301. DOI: 10.1063/1.359706. URL: http://aip.scitation.org/doi/10.1063/1.359706.

[69] M. Shiozawa and K. Nanbu. "Particle Modeling of Inductively Coupled Plasma and Radicals Flow to Predict Etch Rate of Silicon". In: *Japanese Journal of Applied Physics* 41.4R (2002), p. 2213. URL: http://stacks.iop.org/1347-4065/41/i=4R/a=2213.

[70] Y. Takao and N. Kusba. "Two-dimensional particle-in-cell Monte Carlo simulation of a miniature inductively coupled plasma source". In: *Journal of Applied Physics* 108.9 (2010), pp. 093 –309. URL: http:

//aip.scitation.org/doi/abs/10.1063/1.3506536?
journalCode=jap.

[71]   S. Anderson, N. Guibord, and M. Delaney. "Two-dimensional opti-
       cal emission imaging of a XeCl discharge in a microwave resonant
       cavity". In: *IEEE Transactions on Plasma Science* 30.1 (2002), 196–197.
       DOI: 10.1109/tps.2002.1003991.

[72]   M. J. Schabel et al. "Determination of electron temperature, atomic
       fluorine concentration, and gas temperature in inductively coupled
       fluorocarbon/rare gas plasmas using optical emission spectroscopy".
       In: *Journal of Vacuum Science Technology* 20 (Mar. 2002), pp. 555–563.
       DOI: 10.1116/1.1454126.

[73]   R. Laher and F. Gilmore. "Updated excitation and Ionization Cross
       Sections for Electron Impact on Atomic Oxygen". In: *Physical Chem-
       istry* 19.1 (1989), 278–304.

[74]   M. Bregnhoj and A. Blazquez-Castro. "Direct 765 nm Optical Ex-
       citation of Molecular Oxygen in Solution and in Single Mammalian
       Cells". In: *Physical Chemistry* 119.19 (2015), pp. 5422–5429. URL: http:
       //pubs.acs.org/doi/abs/10.1021/acs.jpcb.5b01727.

[75]   T. Chung and H. Kang. "Optical emission diagnostics with electric
       probe measurements of inductively coupled Ar/O2/Ar-O2 plasmas".
       In: *Physics of Plasmas* 19 (2012). URL: http://aip.scitation.
       org/doi/abs/10.1063/1.4765357?journalCode=php.

[76]   G. Kokkoris and A. Panagiotopoulos. "A global model for SF 6 plas-
       mas coupling reaction kinetics in the gas phase and on the surface of
       the reactor walls". In: *Journal of Physics D: Applied Physics* 42.5 (2009),
       p. 055209. URL: http://stacks.iop.org/0022-3727/42/i=
       5/a=055209.

[77]   L. Lallement, A. Rhallabi, and C. Cardinaud. "Global model and di-
       agnostic of a low-pressure SF 6 /Ar inductively coupled plasma".
       In: *Plasma Sources Science and Technology* 18.2 (2009), p. 025001. URL:
       http://stacks.iop.org/0963-0252/18/i=2/a=025001.

[78]   S. Rauf et al. "Model for a multiple-step deep Si etch process". In: *Vacuum Science & Technology* 20 (July 2002), pp. 1177–1190.

[79]   A. Pateau. "Modeling of inductively coupled plasma SF6/O2/Ar plasma discharge: Effect of O2 on the plasma kinetic properties". In: *JVacuum Science & Technology* 32 (2013), pp. 0734–2101.

[80]   J.K. Olthoff, R.J. Vanbrunt, and S. Radovanov. "Studies of Ion Kinetic-Energy Distributions in the Gaseous Electronics Conference Rf Reference Cell". In: *Research of the National Institute of Standards and Technology* 100 (July 1995), p. 383.

[81]   J. Benedikt and A. Hecimovic. "Quadrupole mass spectrometry of reactive plasmas". In: *Journal of Physics D: Applied Physics* 45.40 (2012), p. 403001. URL: http://stacks.iop.org/0022-3727/45/i=40/a=403001.

[82]   G. Trenchev and S. Kolev. "Modeling a Langmuir probe in atmospheric pressure plasma at different EEDFs". In: *Plasma Sources Science and Technology* 26.5 (2017), p. 055013. URL: http://stacks.iop.org/0963-0252/26/i=5/a=055013.

[83]   A. O. Brezmes and C. Breitkopf. "Fast and reliable simulations of argon inductively coupled plasma using COMSOL". In: *Vacuum* 116 (June 2015), pp. 65–72. DOI: 10.1016/j.vacuum.2015.03.002.

[84]   Y. Hara et al. "Si etching with reactive neutral beams of very low energy". In: *Journal of Applied Physics* 116.22, 223301 (Dec. 2014), p. 223301. DOI: 10.1063/1.4903974.

[85]   L. King and A. Gallimore. "Gridded retarding pressure sensor for ion and neutral particle analysis in flowing plasmas". In: *Review of Scientific Instruments* 68.2 (1997), pp. 1183–1188. DOI: 10.1063/1.1147881. URL: http://dx.doi.org/10.1063/1.1147881.

[86] A. van Blokland, T. Grimbergen, and H. van der Ven. "A mass-selective neutral particle energy analyzer with background rejection". In: *Review of Scientific Instruments* 63 (Mar. 1992), pp. 1978–1987. DOI: 10.1063/1.1143315.

[87] Y. Kusama et al. "Charge-exchange neutral particle measurement in MeV energy range on JT-60U". In: *Review of Scientific Instruments* 66 (Jan. 1995), pp. 339–341. DOI: 10.1063/1.1146405.

[88] T. Trottenberg, V. Schneider, and H. Kersten. "Measurement of the force on microparticles in a beam of energetic ions and neutral atoms". In: *Physics of Plasmas* 17.10 (2010), p. 103702. DOI: 10.1063/1.3489795. URL: http://dx.doi.org/10.1063/1.3489795.

[89] M. Stahl, T. Trottenberg, and H. Kersten. "A calorimetric probe for plasma diagnostics". In: *Review of Scientific Instruments* 81.2 (2010), p. 023504. DOI: 10.1063/1.3276707. URL: http://dx.doi.org/10.1063/1.3276707.

[90] S. Tinck, P. De Schepper, and A. Bogaerts. "Numerical Investigation of SiO2 Coating Deposition in Wafer Processing Reactors with SiCl4/O2/Ar Inductively Coupled Plasmas". In: *Plasma Processes and Polymers* 10.8 (2013), pp. 714–730. ISSN: 1612-8869. DOI: 10.1002/ppap.201300005. URL: http://dx.doi.org/10.1002/ppap.201300005.

[91] R. Udiljak, D. Anderson, and M. Lisak. "Improved model for multipactor in low pressure gas". In: *Physics of Plasmas* 11 (Oct. 2004), pp. 5022–5031.

[92] V. Laporta, R. Celiberto, and J. Tennyson. "Dissociative electron attachment and electron-impact resonant dissociation of vibrationally excited O2 molecules". In: *Physical Review A* 91 (Jan. 2015), p. 012701.

[93] K. Gope, V. Prabhudesai, and N. Mason. "Probing the resonant states of Cl 2 using velocity slice imaging". In: *Physics B: Atomic, Molecular and Optical Physics* 49.1 (2016), p. 015201. URL: http://stacks.iop.org/0953-4075/49/i=1/a=015201.

[94]   A. Phelps. "Cross Sections and Swarm Coefficients for Nitrogen Ions and Neutrals in N2 and Argon Ions and Neutrals in Ar for Energies from 0.1 eV to 10 keV". In: *Physical and Chemical Reference Data* 20 (May 1991), pp. 557–573.

[95]   S. Brown. *Basic Data of Plasma Physics: The Fundamental Data on Electrical Discharges in Gases*. 2nd ed. MIT Press, 1966.

[96]   R. Robinson. "Energetic binary collisions in rare gas plasmas". In: *Vacuum Science Technology* 16 (Apr. 1979), pp. 185–188. DOI: 10 . 1116/1.569903.

[97]   A. Matthews and S. Neuville. "Hard Carbon Coatings: The Way Forward". In: *MRSBulletin* 22.9 (1997), pp. 22–26. DOI: 10.1557.

[98]   J. Akinlami and A. Ashamu. "Optical properties of GaAs". In: *Semiconductors* 34.3 (2013), p. 032002. URL: http://stacks.iop.org/1674-4926/34/i=3/a=032002.

[99]   B. White, Q. Wang, and D. Economou. "Neutral oxygen beam stripping of photo resist on porous ultra low-k materials". In: (2003). URL: http://ieeexplore.ieee.org/document/1219739/.

[100] E. Bourdon. "Etching of a-C:H films by an atomic oxygen beam". In: *Vacuum Science & Technology A* 11.5 (1993), pp. 0734 –2101. URL: http://avs.scitation.org.libezproxy.open.ac.uk/doi/pdf/10.1116/1.578603.

[101] C. Chan, T. Ko, and H. Hiraoka. "Surface modification by plasmas and photons". In: *Surface Science Reports* 24 (May 1996), pp. 1–54.

[102] M. Fukasawa, Y. Miyawaki, and Y. Kondo. "Vacuum Ultraviolet and Ultraviolet Radiation-Induced Effect of Hydrogenated Silicon Nitride Etching: Surface Reaction Enhancement and Damage Generation". In: *Japanese Journal of Applied Physics* 51.2R (2012), p. 026201. URL: http://stacks.iop.org/1347-4065/51/i=2R/a=026201.

[103] M. Fukasawa, H. Matsugai, and T. Honda. "Wavelength Dependence of Photon-Induced Interface Defects in Hydrogenated Silicon Nitride/Si Structure during Plasma Etching Processes". In: *Japanese Journal of Applied Physics* 52.5S2 (2013), 05ED01. URL: http://stacks.iop.org/1347-4065/52/i=5S2/a=05ED01.

[104] S. Samukawa, B Jinnai, and F. Oda. "Surface Reaction Enhancement by UV irradiation during Si Etching Process with Chlorine Atom Beam". In: *Japanese Journal of Applied Physics* 46.1L (2007), p. L64. URL: http://stacks.iop.org/1347-4065/46/i=1L/a=L64.

[105] S. Grosse-Kreul, C. Corbella, and A. Keudell. "Surface Modification of Polypropylene (PP) by Argon Ions and UV Photons". In: *Plasma Processes and Polymers* 10 (Dec. 2013).

[106] S. Yoshimura, Y. Tsukazaki, and K. Ikuse. "Effect of light irradiation from inductively coupled Ar plasma on etching yields of SiO 2 film by CF 3 ion beam injections". In: *Physics: Conference Series* 232 (2010). DOI: 10.1088/1742-6596/232/1/012020.

[107] A. Urbanowicz, D. Shamiryan, and A. Zaka. "Effects of He Plasma Pretreatment on Low-k Damage during Cu Surface Cleaning with NH3 Plasma". In: *The Electrochemical Society* 157 (Jan. 2010). URL: http://jes.ecsdl.org/content/157/5/H565.abstract.

[108] *National Institute of Standards and Technology, 2017*. 2017. URL: https://physics.nist.gov/PhysRefData/Handbook/Tables/heliumtable2_a.htm.

[109] G. Beamson and D. Briggs. "High Resolution XPS of Organic Polymers: The Scienta ESCA300 Database". In: *Chemical Education* 70.1 (1993), A25. ISSN: 0257-8972. DOI: 10.1021/ed070pA25.5.

[110] N. De Geyter, R. Morent, and C. Leys. "Treatment of polymer films with a dielectric barrier discharge in air, helium and argon at medium pressure". In: *Surface and Coatings Technology* 201.16 (2007), pp. 7066–7075. ISSN: 0257-8972. DOI: https://doi.org/10.1016/j.

surfcoat.2007.01.008. URL: http://www.sciencedirect.com/science/article/pii/S0257897207000205.

[111] K. Mittal and M. Lyons. *Plasma Surface Modification of Polymers: Relevance to Adhesion*. 1st ed. CRC Press, 1994.

[112] T. Gans, C. Lin, and S. von der Gathen. "Phase-resolved emission spectroscopy of a hydrogen rf discharge for the determination of quenching coefficients". In: *Physical Review A* 67 (1 2003), p. 012707. DOI: 10.1103/PhysRevA.67.012707. URL: https://link.aps.org/doi/10.1103/PhysRevA.67.012707.

[113] M. Kushner. "Hybrid modelling of low temperature plasmas for fundamental investigations and equipment design". In: *Journal of Physics D: Applied Physics* 42 (2009), p. 194013.

[114] *Quantemol Virtual Tool, 2018*. 2018. URL: http://www.quantemol.com/products/quantemol-vt/.

[115] H. Takenaga, T. Nakao, and K. Uchino. "Evaluation of radial particle flux profile based on atomic hydrogen density measurements using laser induced fluorescence and emission at H alpha". In: *Nuclear Fusion* 35.1 (1995), p. 107. URL: http://stacks.iop.org/0029-5515/35/i=1/a=I09.

[116] R. Magee, M. Galante, and D. McCarren. "A two photon absorption laser induced fluorescence diagnostic for fusion plasmas". In: *Review of Scientific Instruments* 83.10 (2012). URL: [http://dx.doi.org/10.1063/1.4728092.

[117] E. Kazuhiko, N. Shuichi, and M. Meishoku. "Fabrication of a Vertical-Channel Double-Gate Metal-Oxide-Semiconductor Field-Effect Transistor Using Neutral Beam Etching". In: *Japanese Journal of Applied Physics* 45 (10 2006), pp. L279–L281. URL: http://stacks.iop.org/1347-4065/45/i=3L/a=L279.